

PHOTOELASTIC STUDIES OF CRACK PROPAGATION AND ARREST IN POLYMERS AND 4340 STEEL

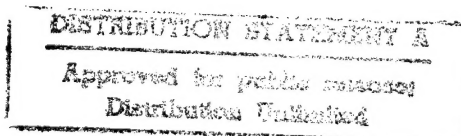
DEPARTMENT OF DEFENSE
PLASTICS TECHNICAL EVALUATION CENTER
ARRADCOM, DOVER, N. J. 07801

G. R. Irwin T. Kobayashi
W. L. Fourney J. T. Metcalf
J. W. Dally

University of Maryland

DEPARTMENT OF DEFENSE
PLASTICS TECHNICAL EVALUATION CENTER
ARRADCOM, DOVER, N. J. 07801

Prepared for
U. S. Nuclear Regulatory Commission



19960220 133

PLASTEC 33728

map 6-2

NOTICE

This report was prepared as an account of work sponsored by an agency of the United States Government. Neither the United States Government nor any agency thereof, or any of their employees, makes any warranty, expressed or implied, or assumes any legal liability or responsibility for any third party's use, or the results of such use, of any information, apparatus product or process disclosed in this report, or represents that its use by such third party would not infringe privately owned rights.

Available from
National Technical Information Service
Springfield, Virginia 22161
Price: Printed Copy \$12.00; Microfiche \$3.00

The price of this document for requesters outside of the North American Continent can be obtained from the National Technical Information Service.

Date: 9/9/95 Time: 3:54:04PM

Page: 1 Document Name: untitled

1 OF 1

DTIC DOES NOT HAVE THIS ITEM

-- 1 - AD NUMBER: D428600
-- 5 - CORPORATE AUTHOR: MARYLAND UNIV COLLEGE PARK DEPT OF MECHANICAL
ENGINEERING
-- 6 - UNCLASSIFIED TITLE: PHOTOELASTIC STUDIES OF CRACK PROPAGATION
AND ARREST IN POLYMERS AND 4350 STEEL
-- 9 - DESCRIPTIVE NOTE: 15 JUL 77 - 30 SEP 78
--10 - PERSONAL AUTHORS: IRWIN, G. R.; KOBAYASHI, T.; FOURNEY, W. L.;
METCALF, J. T.; DAILY, J. W.;
--11 - REPORT DATE: DEC 1978
--12 - PAGINATION: 330P
--15 - CONTRACT NUMBER: NRC-04-76-172
--18 - MONITOR ACRONYM: NUREG
--19 - MONITOR SERIES: CR-0542
--20 - REPORT CLASSIFICATION: UNCLASSIFIED
--22 - LIMITATIONS (ALPHA): APPROVED FOR PUBLIC RELEASE; DISTRIBUTION
UNLIMITED. AVAILABILITY: NATIONAL TECHNICAL INFORMATION SERVICE,
SPRINGFIELD, VA. 22161. PB29 508.
--33 - LIMITATION CODES: 1 24

**PHOTOELASTIC STUDIES OF
CRACK PROPAGATION AND ARREST
IN POLYMERS AND 4340 STEEL**

G. R. Irwin T. Kobayashi
W. L. Fourney J. T. Metcalf
J. W. Dally

Manuscript Completed: November 1978
Date Published: December 1978

University of Maryland
Mechanical Engineering Department
College Park, MD 20742

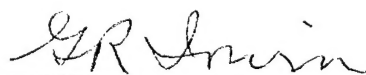
Prepared for
Division of Reactor Safety Research
Office of Nuclear Regulatory Research
U. S. Nuclear Regulatory Commission
Under Contract No. NRC-04-76-172

Signature Page

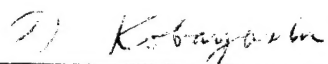
This report entitled "Photoelastic Studies of Crack Propagation and Arrest in Polymers and 4340 Steel" was prepared by the Department of Mechanical Engineering at the University of Maryland (College Park Campus) under Contract No. NRC-04-76-172 for the U. S. Nuclear Regulatory Commission. The research work described in this report was conducted from July 15, 1977 to September 30, 1978.

Messrs. C. Z. Serpan and E. K. Lynn of the Metallurgy and Materials Branch, Division of Reactor Safety Research served as technical monitors. In addition to the authors of the report, Messrs. M. Nutter and A. Howell assisted in performing many of the experiments, and several students A. Shukla, R. Chona, C. Sayre and T. Quigley performed the data analysis and figure preparation for this report.

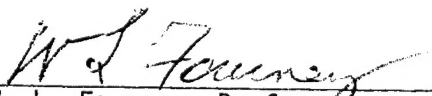
Respectfully submitted,



G. R. Irwin, Visiting Professor



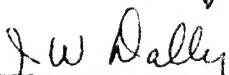
T. Kobayashi, Associate Professor



W. L. Fournery, Professor



J. T. Metcalf, Assistant Professor



J. W. Dally, Professor

Abstract

This report describes the progress made during the fourth year on a research program dealing with the dynamic characterization of fracture. The significant findings during the past year include:

(1) An evaluation of the BCL procedure for determining K_{IDm} , indicated that BCL reference curves predict velocities that are too high and predict values of the stress intensity factor which are too low. The deviations between the BCL predictions and experimental results are generally small (i.e. less than 10 per cent) and close estimates of K_{Im} can be obtained if a number of different determinations of K_{IDm} are averaged.

(2) An evaluation of the MRL procedure for determining K_{Ia} showed that K_{Ia} was within 4.5 per cent of the photoelastically determined value of K_{Im} .

(3) A new ultra high speed recording system was developed for recording dynamic fringe patterns in birefringent coatings.

(4) Studies of the stress intensity factor associated with propagating cracks in 4340 steel gave a \dot{a} vs K relation which compared favorably with results previously published by BCL.

(5) Comparisons of crack behavior in duplex specimens fabricated from plastic-plastic and steel-steel indicate that the processes of crack propagation, crack arrest and crack re-initiation are similar in both types of specimens.

(6) The investigation of crack propagation in ring specimens with mechanically simulated thermal stresses showed significant differences in the stress intensity factor associated with static

crack extension and dynamic crack propagation. Dynamic propagation occurs at much lower values of K than static crack extension.

(7) Studies of dynamic crack propagation in CT specimens (Homalite 100) fabricated with and without face grooves indicated that the effect of the face grooves is not significant on crack behavior.

(8) The physical and mechanical properties of Araldite B were determined and found to be in close agreement with the results published previously by Kalthoff et al.

(9) Methods for determining the stress intensity factor K from isochromatic fringe loops were improved by introducing two new techniques. First a dynamic correction factor was derived to account for the influence of crack tip velocity. Second, a full field method which utilizes multiple point isochromatic data to minimize the error in the K determination was developed.

TABLE OF CONTENTS

		<u>Page</u>
1.0	Introduction	1
2.0	Further Evaluation of Proposed Standard Procedures For Determining Arrest Toughness	4
2.1	BCL Procedure	5
2.2	Effect of the K vs a Relationship on the Reference Curves	7
2.3	Prediction of K vs a from BCL Procedure	9
2.4	K and Velocity Level Comparisons	13
2.5	Summary	15
2.6	MRL Procedure	16
2.7	Re-examination of the Results with Machine Loaded T-DCB Specimen	17
	2.7.1 Modulus of Elasticity	19
	2.7.2 Compliance Calibration	20
	2.7.3 Calibration of Material Fringe Value f_{σ}	22
	2.7.4 Re-examination of Machine-Loaded T-DCB Specimen	23
2.8	Examination of MRL Procedure with Transverse-Wedge- Loaded Compact Specimen (TWL-CS)	24
	2.8.1 Static Compliance Calibration	26
	2.8.2 Dynamic Photoelastic Observation of Crack Propagation and Arrest	29
2.9	Conclusions	36
3.0	Study of Crack Behavior in 4340 Steel with Bire- fringent Coatings	38

TABLE OF CONTENTS
(continued)

	<u>Page</u>
3.1 Introduction	38
3.2 Experimental Procedure	39
3.2.1 High Speed Camera	39
3.2.2 Flash Lamp System	40
3.2.3 Specimen and Loading Fixture	41
3.2.4 Method for Determination of the Stress Intensity Factor	42
3.3 Experimental Results	44
3.3.1 High-Speed Crack Propagation	46
3.3.2 Crack Arrest Phase	47
3.3.3 \dot{a} vs K Relationship	48
3.3.4 Crack Behavior in Transverse-Wedge-Loaded- Compact Specimen	49
3.4 Examination of the MRL and BCL Procedures	51
3.4.1 MRL Procedure	51
3.4.2 BCL Procedure	51
4.0 Comparison of Crack Behavior in Plastic and Steel Duplex Specimens	56
4.1 Introduction	56
4.2 Crack Behavior in Steel Duplex Specimen	57
4.3 Summary	62
5.0 A Dynamic Photoelastic Study of Crack Propagation in a Ring Specimen	65

TABLE OF CONTENTS
(continued)

	<u>Page</u>
5.1 Introduction	65
5.2 Review of Previous Work	66
5.2.1 Determination of Static K as a Function of Crack Length	67
5.2.2 Dynamic Crack Propagation in Monolithic Ring Specimens	67
5.2.3 Conclusions	69
5.3 Further Investigation of Monolithic Ring Specimens	69
5.3.1 Dynamic Experiments with Monolithic Rings	70
5.3.2 Conclusions and Discussion	74
5.4 Crack Propagation in Duplex Ring Specimens	75
5.4.1 Specimen Geometry and Material	76
5.4.2 Specimen Bonding Procedures	77
5.4.3 Experimental Procedure	78
5.4.4 Summary of Results for Duplex Ring Specimen	78
5.4.5 Conclusion	81
5.5 Conclusion and Discussion	82
6.0 Characterization of Effect of Damping on Crack Behavior	86
6.1 Introduction	86
6.2 Crack Behavior in Face-Grooved Specimens	87
6.2.1 Static Calibration of Stress Intensity Factor Analysis Method	87
6.2.2 Dynamic Crack Behavior in Face-Grooved Compact Specimen	89

TABLE OF CONTENTS
(continued)

	<u>Page</u>
6.3 Crack Behavior in a Fixed-Pin Compact Specimen	92
6.3.1 Static Calibration of the Stress Intensity Factor in the Fixed-Pin Compact Specimen	93
6.3.2 Dynamic Stress Intensity Factor in the Fixed-Pin Compact Specimen	93
7.0 Comparison of Crack Behavior in Araldite B and Homalite 100	99
7.1 Comparison of Mechanical Properties	99
7.1.1 Introduction	99
7.1.2 Experimental Procedure	99
7.1.2.1 Determination of f_{σ}	99
7.1.2.2 Static Tensile Test	101
7.1.2.3 Determination of Dynamic Values of E and ν	103
7.1.2.4 Dynamic Determination of Material Properties of Araldite B	106
7.1.2.5 Creep Characteristics of Homalite 100 and Araldite B	109
7.1.2.6 Viscoelastic Properties as a Function of Temperature	109
7.1.3 Summary of Mechanical Properties of Araldite B and Homalite 100	110
7.2 \dot{a} vs K Relationship for Araldite B and Homalite 100	112

TABLE OF CONTENTS
(continued)

	<u>Page</u>
7.2.1 Introduction	112
7.2.2 Experimental Procedures	112
7.2.2.1 Specimen Geometry	112
7.2.2.2 Loading System and Test Procedure	112
7.2.2.3 Data Analysis	113
7.2.3 Experimental Results	115
7.2.3.1 Compact Tension Specimen Results	115
7.2.3.2 SEN Specimen Results	116
7.2.3.3 R-DCB Specimen Results	117
7.2.4 \dot{a} vs K Relationship for Araldite B	117
7.3 Post Arrest Oscillations	118
7.3.1 Introduction	118
7.3.2 Post Arrest Studies	119
7.3.2.1 Test Procedure, Araldite B	119
7.3.2.2 Test Procedure, Homalite 100	119
7.3.3 Post Arrest Test Results	120
7.4 Fracture Surface Characteristics	121
7.4.1 Introduction	121
7.4.2 Procedure	122
7.4.3 Results	122
8.0 Parametric Aspects of Crack Tip Stress Fields	125

LIST OF TABLES

	<u>Page</u>
Table 2.1 Comparison of Predicted Velocities with Experimentally Measured Velocities.	15
Table 2.2 Summary of K_{Ia} Test Results.	18
Table 2.3 K_{Ia} Computation Data.	19
Table 2.4 Summary of Results for Compliance Tests on the T-DCB Specimen.	20
Table 2.5 Comparison of Three Equations for Determining K for the T-DCB Specimen.	21
Table 2.6 Comparison of Results for the Stress Intensity Factor (T-DCB Specimen).	22
Table 2.7 Summary of Results of MRL Procedure.	23
Table 2.8 Computational Factor as a Function of a/W .	25
Table 2.9 Static Compliance Calibration of MRL Design Transverse-Wedge-Loaded Compact Specimen (No. 281).	27
Table 2.10 Static Compliance Calibration of MRL Design Transverse-Wedge-Loaded Compact Specimen (No. 288).	28
Table 2.11 Stress Intensity Factor in Transverse-Wedge-Loaded Compact Specimen of MRL Design (No. 290).	30
Table 2.12 Stress Intensity Factor in Transverse-Wedge-Loaded Compact Specimen of MRL Design (No. 291).	31
Table 2.13 Stress Intensity Factor in Transverse-Wedge-Loaded Compact Specimen of MRL Design (No. 302).	32
Table 2.14 Stress Intensity Factor in Transverse-Wedge-Loaded Compact Specimen of MRL Design (No. 303).	33

LIST OF TABLES
(continued)

	<u>Page</u>
Table 2.15 Summary of MRL-TW-CS Test Results.	35
Table 3.1 Summary of Test Data for 4340 Steel.	45
Table 3.2 Summary of K_{Ia} Determined with the MRL Procedure for 4340 Steel.	53
Table 3.3 Summary of K_{IDm} and \dot{a} Determined with the BCL Procedure for 4340 Steel.	54
Table 5.1 Dynamic Values of f_g for a Wave Length of 492 mm.	77
Table 6.1 Comparison of Photoelastically Determined K with Calculated K for Face-Grooved Compact Specimen	88
Table 6.2 Stress Intensity Factor versus Crack Position in Face-Grooved Compact Specimen No. 311.	90
Table 6.3 Stress Intensity Factor versus Crack Position in Face-Grooved Compact Specimen No. 312.	91
Table 6.4 Stress Intensity Factor versus Crack Position in Face-Grooved Compact Specimen No. 369.	94
Table 6.5 Stress Intensity Factor versus Crack Position in Face-Grooved Compact Specimen No. 388.	95
Table 6.6 Stress Intensity Factor versus Crack Position in Face-Grooved Compact Specimen No. 367.	97
Table 6.7 Stress Intensity Factor versus Crack Position in Face-Grooved Compact Specimen No. 368.	98
Table 7.1 Summary of Data and Calculations, Edge Loaded Disc, Araldite B.	100

LIST OF TABLES
(continued)

	<u>Page</u>
Table 7.2 Material Properties for Araldite B.	102
Table 7.3 Summary of Data and Calculations Half Plane Model, Araldite B.	104
Table 7.4 Density of Araldite B.	105
Table 7.5 Dynamic Material Properties of Araldite B.	108
Table 7.6 Mechanical and Physical Properties.	111

LIST OF ILLUSTRATIONS

		<u>Page</u>
Fig. 2.1A	Reference curves for the R-DCB specimen (after BCL)	132
Fig. 2.1B	Reference curves for the CT specimen (after BCL)	133
Fig. 2.1B2	Reference curves for the CT specimen (after BCL)	134
Fig. 2.2	Geometry of the R-DCB specimen	135
Fig. 2.3	Geometry of the CT specimen	136
Fig. 2.4	The \dot{a} -K relation for Homalite 100	137
Fig. 2.5A	Comparison of the BCL reference curves with and without Γ type \dot{a} -K dependence, K_D/K_Q vs $\Delta a/a_0$	138
Fig. 2.5B	Comparison of the BCL reference curves with and without Γ type \dot{a} -K dependence, V/c_0 vs $\Delta a/a_0$	139
Fig. 2.6	Comparison of \dot{a} -K relation obtained using the BCL reference curve with results from photoelastic experiments. Homalite 100.	140
Fig. 2.7	Geometry of the CT specimen used at the University of Maryland.	141
Fig. 2.8	Comparison of \dot{a} -K relation obtained using the BCL reference curve with results of photo-mechanics experiments. Araldite B.	142
Fig. 2.9A	Comparison of \dot{a} -K relation obtained using the BCL reference curve with results of photoelastic experiments. Araldite B.	143

LIST OF ILLUSTRATIONS
(continued)

	<u>Page</u>
Fig. 2.9B Comparison of \dot{a} -K relation obtained using the corrected BCL Reference curve with torsional springs with results of photoelastic experiments. R-DCB Homalite 100.	144
Fig. 2.9C Comparison of \dot{a} -K relation obtained using the correct BCL reference curve without torsional springs with results of photoelastic experiments. R-DCB Homalite 100.	145
Fig. 2.10 Dimensions for the R-DCB specimen.	146
Fig. 2.11 Comparison of \dot{a} -K relation obtained using the BCL reference curve with results of photoelastic experiments. R-DCB Homalite 100.	147
Fig. 2.12 Comparison of \dot{a} -K relation obtained using the BCL reference curve with results from birefringent coating experiments CT 4340 steel.	148
Fig. 2.13 K_{Ia} as a function of $\Delta a/a_0$ for C-DCB Specimens.	149
Fig. 2.14 Geometry of MRL-CS specimen.	150
Fig. 2.15 Comparison of experimental and MRL EB Δ/p values as a function of a/W .	151
Fig. 2.16 K and a as a function of time (No. 290).	152
Fig. 2.17 K and a as a function of time (No. 291).	153
Fig. 2.18 K and a as a function of time (No. 302).	154
Fig. 2.19 K and a as a function of time (No. 303).	155

LIST OF ILLUSTRATIONS (continued)

	<u>Page</u>
Fig. 2.20 \dot{a} vs K relationship from Transverse-Wedge-Loaded Compact Specimen of MRL Design.	156
Fig. 2.21 K_{Ia} as a function of a_f/W .	157
Fig. 2.22 Displacement Record during the test for MRL-TWL-CS.	158
Fig. 2.23 Pin-displacement Load found as a Function of Time for T-DCB (No. 224).	159
Fig. 3.1 Experimental Apparatus Used to Photograph Birefringent Coatings.	160
Fig. 3.2 Diagram showing Flash Tube Power Supply and Synchronization Circuits.	161
Fig. 3.3 Dimensions of the Modified Compact Tension Specimen.	162
Fig. 3.4 Birefringent Coating on the M-CT Specimen.	163
Fig. 3.5 Specially Designed Loading Frame for Coated M-CT Specimen.	164
Fig. 3.6A Sequence of Isochromatic Fringe Patterns Showing the Propagating Crack.	165
Fig. 3.6B Sequence of Isochromatic Fringe Patterns Showing the Crack Arrest Phase of the Dynamic Event.	166
Fig. 3.7 Enlargement which Shows the Details of the Isochromatic Fringe Loop at the Crack Tip.	167

LIST OF ILLUSTRATIONS
(continued)

	<u>Page</u>
Fig. 3.8 Typical Data Extracted from the Isochromatic Fringe Loops.	168
Fig. 3.9 Stress Intensity Factor and Crack Length as a Function of Time for Model No. 333.	169
Fig. 3.10 Stress Intensity Factor and Crack Length as a Function of Time for Model No. 348.	170
Fig. 3.11 Stress Intensity Factor and Crack Length as a Function of Time for Model No. 349.	171
Fig. 3.12 Stress Intensity Factor and Crack Length as a Function of Time for Model No. 362.	172
Fig. 3.13 Stress Intensity Factor and Crack Length as a Function of Time for Model No. 375.	173
Fig. 3.14 Crack Velocity as a Function of Stress Intensity Factor for 4340 Steel.	174
Fig. 3.15 Fracture Surface Characteristics for Model Nos. 348 and 362.	175
Fig. 3.16 Fracture Surface Characteristics for Model Nos. 333 and 375.	176
Fig. 3.17 Comparison between Photoelastic and BCL Determination of the \dot{a} vs K Relation for 4340 Steel.	177
Fig. 3.18 K/K_Q vs a/W for Model No. 333.	178
Fig. 3.19 K/K_Q vs a/W for Model No. 348.	179
Fig. 3.20 K/K_Q vs a/W for Model No. 349.	180

LIST OF ILLUSTRATIONS
(continued)

	<u>Page</u>
Fig. 3.21 K/K_Q vs a/W for Model No. 362.	181
Fig. 3.22 K/K_Q vs a/W for Model No. 375.	182
Fig. 3.23 Influence of Loading Machine Compliance on the K/K_Q vs a/W Relation.	183
Fig. 3.24 Crack Arrest Toughness as a Function of Normal- ized Crack Jump Distance a_f/W for 4340 M-CT Specimens.	184
Fig. 3.25 Relation of \dot{a} to K_{Id} obtained using BCL Method of Data Analysis.	185
Fig. 4.1 Crack Position - Time Function Describing Crack Propagation Across the Duplex M-CT Specimen.	186
Fig. 4.2 Stress Intensity Factor as a Function of Time in a Duplex M-CT Specimen with Crack Reinitiation.	187
Fig. 4.3 Stress Intensity Factor as a Function of Time for a Duplex M-CT Specimen with a Brittle Adhesive Joint.	188
Fig. 4.4 Crack Extension - Time Records for the Duplex SEN Test No. DA-37.	189
Fig. 4.5 Crack Extension - Time Records for the Duplex SEN Test No. DA-38.	190
Fig. 4.6 Crack Extension - Time Records for the Duplex SEN Test No. DA-41.	191

LIST OF ILLUSTRATIONS
(continued)

	<u>Page</u>
Fig. 4.7 \dot{a} vs K Relationship for Homalite 100 (starter section) and KTE_2 (arrest section) and the Crack Propagation History in the Duplex Specimen.	192
Fig. 4.8 Schematic \dot{a} vs K Relationships for 4340 and A 533 B Steels at -11°C .	193
Fig. 4.9 Hardness Profiles for Electron Beam Welded A 533 B Specimen.	194
Fig. 5.1 Loading Fixture Attached to the Ring Specimen.	195
Fig. 5.2 Stress Intensity Factor K as a Function of Inner Pin Displacement d_i .	196
Fig. 5.3 Stress Intensity Factor K as a Function of Starter Crack Length to Width Ratio a_0/W .	197
Fig. 5.4 Stress Intensity Factor K as a Function of Time t for Models R-2 through R-5.	198
Fig. 5.5 Stress Intensity Facotr K as a Function of Crack Length to Width Ratio a/W for Model R-2 through R-5.	199
Fig. 5.6 Stress Intensity Factor K as a Function of Crack Velocity \dot{a} - Homalite 100 - 2nd Shipment and 3rd Shipment.	200
Fig. 5.7 Outer Pin Displacement as a Function of Time for Model R-6.	201

LIST OF ILLUSTRATIONS
(continued)

	<u>Page</u>
Fig. 5.8 Crack Tip Position a as a Function of Time t for Model R-6.	202
Fig. 5.9 Outer Pin and Starting Crack Point Displacement as a Function of Time for Model R-7.	203
Fig. 5.10 Crack Tip Position a as a Function of Time t for Model R-7.	204
Fig. 5.11 Inner Pin Displacement as a Function of Time for Model R-8.	205
Fig. 5.12 Crack Tip Position as a Function of Time for Model R-8.	206
Fig. 5.13 Stress Intensity Factor K as a Function of Time t for Models R-6 through R-8.	207
Fig. 5.14 Stress Intensity Factor K as a Function of a/W for Models R-6 through R-8.	208
Fig. 5.15 Static and Dynamic Stress Intensity Factor K as a Function of a/W .	209
Fig. 5.16 Static and Dynamic Stress Intensity Factor Square K^2 as a Function of a/W .	210
Fig. 5.17 Crack Jump Distance a^*/W as a Function of K_Q/K_{Im} .	211
Fig. 5.18 Stress Intensity Factor K as a Function of Crack Velocity \dot{a} for 4th Shipment of Homalite 100.	212
Fig. 5.19 Geometry of the Duplex Specimen.	213
Fig. 5.20 Stress Intensity Factor K as a Function of Crack Velocity for Araldite B.	214

LIST OF ILLUSTRATIONS
(continued)

	<u>Page</u>
Fig. 5.21 Crack Tip Position as a Function of Time for Model R-9.	215
Fig. 5.22 Crack Tip Position as a Function of Time for Model R-10.	216
Fig. 5.23 Crack Tip Position as a Function of Time for Model R-11.	217
Fig. 5.24 Stress Intensity Factor K as a Function of Time for Model R-9.	218
Fig. 5.25 Stress Intensity Factor K as a Function of Time for Model R-10.	219
Fig. 5.26 Stress Intensity Factor K as a Function of Time for Model R-11.	220
Fig. 5.27 Stress Intensity Factor K as a Function of a/W for Model R-9.	221
Fig. 5.28 Stress Intensity Factor K as a Function of a/W for Model R-10.	222
Fig. 5.29 Stress Intensity Factor K as a Function of a/W for Model R-11.	223
Fig. 5.30 Crack Tip Position as a Function of Time for Model R-12.	224
Fig. 5.31 Crack Tip Position as a Function of Time for Model R-13.	225
Fig. 5.32 Stress Intensity Factor as a Function of Time for Model R-12.	226

LIST OF ILLUSTRATIONS
(continued)

		Page
Fig. 5.33	Stress Intensity Factor as a Function of Time for Model R-13.	227
Fig. 5.34	Stress Intensity Factor as a Function of a/W for Model R-12.	228
Fig. 5.35	Stress Intensity Factor as a Function of a/W for Model R-13.	229
Fig. 5.36	Crack Jump Distance a^*/W as a Function of K_Q/K_{Im} .	230
Fig. 5.37	Stress Intensity Factor K as a Function of Crack Velocity \dot{a} for Araldite B.	231
Fig. 5.38	Comparison of Stress Intensity Factor K as a Function of Crack Velocity \dot{a} for Araldite B.	232
Fig. 6.1	Geometry of Face-Grooved Specimen.	233
Fig. 6.2	Typical Isochromatic Fringes Observed in the Face-Grooved Compact Specimen.	234
Fig. 6.3	Dynamic Stress Intensity Factor and Crack Position as a Function of Time for Model Nos. 311 and 312.	235
Fig. 6.4	Dynamic Stress Intensity Factor vs a/W for Model Nos. 311 and 312.	236
Fig. 6.5	Dynamic Stress Intensity Factor vs a/W for Model No. 144.	237
Fig. 6.6	Normalized Static Stress Intensity Factor vs. a/W for Various Machine Compliance (Ref. 6.2).	238

LIST OF ILLUSTRATIONS
(continued)

	<u>Page</u>
Fig. 6.7	ASTM E399 Compact Specimen and Load System. 239
Fig. 6.8	Static K/K_Q vs a/W for Fixed-Pin Compact Specimen. 240
Fig. 6.9	K/K_Q vs a/W for Fixed Pin Compact Specimen. 241
Fig. 6.10	K/K_Q vs a/W for Fixed-Pin Compact Specimen. 242
Fig. 6.11	G/G_Q vs a/W for Fixed-Pin Compact Specimen. 243
Fig. 7.1	Material Fringe Value as a Function of Time. 244
Fig. 7.2	Tension Test Specimen. 245
Fig. 7.3	X-Y Recorder Plot of Load vs Strain, Tension Test, Araldite B. 246
Fig. 7.4	Modulus of Elasticity as a Function of Temperature, Araldite B and Homalite 100 (2nd Shipment). 247
Fig. 7.5	Plate and Shear Wave Location with Time, Half Plane Model Test, Araldite B. 248
Fig. 7.6	Plate and Shear Wave, Half Plane Test No. 294, Araldite B. 249
Fig. 7.7	Fringe Order vs Strain to Obtain $\Delta\epsilon/\Delta N$, Test No. 472A, Araldite B. 250
Fig. 7.8	Material Fringe Variation with Loading Time, Araldite B. 251
Fig. 7.9	Elastic Modulus as a Function of Time, Araldite B and Homalite 100. 252

LIST OF ILLUSTRATIONS
(continued)

		Page
Fig. 7.10	Tangent δ and Complex Modulus E^* as a Function of Temperature and Frequency, Araldite B.	253
Fig. 7.11	Tangent δ and Complex Modulus E^* as a Function of Temperature and Frequency, Homalite 100 (1st Shipment).	254
Fig. 7.12	Tangent δ and Complex Modulus E^* as a Function of Temperature and Frequency, Homalite 100 (4th Shipment).	255
Fig. 7.13	Tangent δ and Complex Modulus E^* as a Function of Temperature, Araldite B and Homalite 100 (1st and 4th Shipments).	256
Fig. 7.14	Modified Crack Arrest Compact Specimen Geometry.	257
Fig. 7.15	Center Pin Loading SEN Specimen Geometry.	258
Fig. 7.16	Rectangular Double Cantilever Beam Specimen Geometry.	259
Fig. 7.17	Stress Intensity at Crack Tip, Test No. 287, Araldite B.	260
Fig. 7.18	Crack Tip Position and Stress Intensity Factor as a Function of Time, Test No. 287, Araldite B.	261
Fig. 7.19	Crack Tip Position and Stress Intensity Factor as a Function of Time, Test No. 293, Araldite B.	262
Fig. 7.20	Crack Tip Position and Stress Intensity Factor as a Function of Time, Test No. 313, Araldite B.	263

LIST OF ILLUSTRATIONS
(continued)

	<u>Page</u>
Fig. 7.21 Crack Tip Position and Stress Intensity Factor as a Function of Time, Test No. 314, Araldite B.	264
Fig. 7.22 Crack Tip Position and Stress Intensity Factor as a Function of Time, Test No. 308, Araldite B.	265
Fig. 7.23 Crack Tip Position and Stress Intensity Factor as a Function of Time, Test #309, Araldite B.	266
Fig. 7.24 Crack Tip Position and Stress Intensity Factor as a Function of Time, Test No. 331, Araldite B.	267
Fig. 7.25 Crack Tip Position and Stress Intensity Factor as a Function of Time, Test No. 332, Araldite B.	268
Fig. 7.26 Crack Velocity as a Function of Stress Intensity Factor, Araldite B.	269
Fig. 7.27 Normalized \dot{a} vs K Relationship, Homalite 100 and Araldite B.	270
Fig. 7.28 Post Arrest Oscillations in Stress Intensity Factor, R-DCB, Araldite B and Homalite 100.	271
Fig. 7.29 Normalized Energy Release Rate as a Function of Crack Velocity, Homalite 100 and Araldite B.	272
Fig. 7.30 Surface Features, Araldite B.	273
Fig. 7.31 Surface Features, Homalite 100.	274

1.0 Introduction

This is the fourth annual report which describes a research program dealing with characterization of several aspects of dynamic fracture. The program has several objectives which are listed below:

- Determine the relationship between crack velocity \dot{a} and stress intensity factor K for several different materials including Homalite 100, Araldite B, other epoxies and 4340 heat treated steel.
- Determine the influence of the type of fracture specimen on the \dot{a} vs K relationship.
- Independent evaluation of experimental procedures advanced by Battelle Columbus Laboratory (BCL) and Materials Research Laboratory (MRL) for determining crack arrest toughness.
- Investigation of crack propagation in thermally stressed ring specimens.
- Study the effect of damping on dynamic fracture behavior.
- Improve methods for determining the instantaneous stress intensity factor K from dynamic isochromatic fringe patterns.
- Provide consulting services for NRC.

The research program is one part of a large coordinated effort involving BCL (Hahn, Kanninen and Hoagland), MRL (Ripling and Crosley) and the Institut Für Festkörpermechanik (Kalthoff). The progress made in characterizing the various aspects of dynamic fracture and in developing a standardized test method for determining the arrest toughness of reactor vessel steel is due to the combined efforts of the four

laboratories and the free exchange of ideas, data, codes and experiences.

During the past four years several different research tasks have been completed which have provided the following conclusions:

(i) Showed that dynamic fracture could be represented by a relation between the crack velocity \dot{a} and the instantaneous stress intensity factor K over the entire range of dynamic fracture from crack arrest to crack branching.

(ii) Determined the \dot{a} vs K relation for several polymers including Homalite 100, Araldite B and two other epoxies.

(iii) Showed that the \dot{a} vs K relation was independent of the type of fracture specimen. Comparisons of the \dot{a} vs K relation determined from dynamic photoelastic results with SEN, R-DCB, C-DCB (both wedge and machine loading), M-CT and Ring type specimens indicated the arrest toughness was essentially independent of specimen geometry.

(iv) Examination of fracture behavior in duplex specimens indicated that the toughness and thickness of the material in the joint between the starter and arrest sections had a profound effect on the fracture behavior. It was shown that tough material in the joints will produce immediate crack arrest in even very thin joints. These experimental results imply that production of metallic duplex specimens by welding may be difficult since both the thickness and the toughness of the welded joint will have to be carefully controlled.

(v) Investigated crack propagation in ring specimens subjected to mechanically simulated thermal stresses. Ring specimens, monolithic and duplex, were studied to determine the K_Q values associated with crack arrest.

This report includes seven chapters in addition to the introduction. Chapter 2 which deals with an evaluation of the MRL and BCL standardized procedures for determining crack arrest toughness was written by W. L. Fournery and T. Kobayashi. The study of crack behavior in 4340 steel described in Chapter 3 was written by T. Kobayashi. A comparison of crack arrest characteristics in polymeric and mild steel specimens which is covered in Chapter 4 was written by T. Kobayashi. The results of experiments depicting crack propagation in monolithic and duplex ring specimens were described by A. Shukla and J. W. Dally in Chapter 5. Effects of damping, in polymeric specimens, on dynamic crack behavior is covered in Chapter 6 by T. Kobayashi. A comparison of dynamic fracture characteristics of Homalite 100 and Araldite B is given by J. Metcalf in Chapter 7. Finally, in Chapter 8 G. R. Irwin describes recent progress in improving methods for determining the instantaneous stress intensity factor from isochromatic fringe data.

CHAPTER 2

FURTHER EVALUATION OF PROPOSED STANDARD PROCEDURES FOR DETERMINING ARREST TOUGHNESS

Testing methods (2.1) for measuring crack arrest toughness have been proposed to the American Society for Testing Materials by a number of research groups involved with pressure vessel safety. In particular a cooperative testing program is currently being conducted under the auspices of ASTM committee E24.01.06. Two different means of predicting crack arrest toughness have been proposed.

Materials Research Laboratory (MRL) has proposed a method which uses the crack opening displacement (measured about a millisecond after crack arrest) and the final crack arrest length to predict the arrest toughness from an elasto-static equation.

Battelle Columbus Laboratories (BCL) has proposed a method which involves the specimen dynamics in the arrest toughness determination. BCL uses a finite difference computer code to generate reference curves which can be utilized to predict arrest toughness from a measurement of the initiation stress intensity (K_Q) and arrest length.

A cooperative test program has been initiated where both techniques are used to determine the arrest toughness of A533B reactor grade steel. A number of Laboratories (foreign and domestic) are participating in the cooperative program. The program will familiarize laboratories with the two different procedures and will permit an evaluation of the practability and reproductability of both techniques.

The Photomechanics Laboratory at the University of Maryland

has been investigating both procedures by using dynamic photoelasticity. Data obtained from a large number of tests involving R-DCB and M-CT specimen geometries have been used to evaluate the two procedures. The results of these two evaluations are described individually in the following subsections.

2.1 BCL Procedure

The BCL procedure utilizes a finite difference computer code to generate reference curves which are then used to predict crack arrest toughness. The computer code has been described in earlier references (2.2-2.4) and will not be discussed in detail here. The reference curves generated are presented in Fig. 2.1 and are for the specimens defined in Fig. 2.2 and 2.3. The reference curves for the R-DCB specimen are given in Fig. 2.1A and the reference curves for the CT specimen are given in Fig. 2.1B.

The experimental procedure for determining crack arrest toughness from the R-DCB specimen is described below. The specimen is loaded by slowly forcing a wedge between the loading pins in a relatively stiff loading system so that a single run-arrest event is produced. A stiff loading system is necessary to minimize the work done by the system on the test specimen during fast fracture and prior to the arrest of the crack. The load versus displacement across the slot at the specimen edge is recorded and the critical elastic displacement corresponding to the onset of rapid propagation is determined. The displacement existing after static equilibrium has been attained is recorded and the length of the arrested crack is measured. The K_Q value is

calculated from the critical displacement and initial crack length from elasto-static equations. Finally, the minimum value of dynamic toughness K_{IDm} and the corresponding velocity V are evaluated from the reference curves, Figure 2.1A. The reference curves show K_{ID}/K_Q (or K_{IDm}/K_Q) and V/c_0 as a function crack jump length $\Delta a/a_0$.

The reference curves are generated under conditions of rigid wedge loading and for the case where the crack velocity V is independent of K_{ID} . It is suggested by BCL that the reference curves can be used when the velocity varies with K_{ID} because this dependence seems to have a relatively small influence on the reference curves.

The reference curves may be used to interpret experimental data only if the following test conditions are met:

1. The specimen thickness $B > 0.3 (K_D/\sigma_y)^2$
2. The height H for the R-DCB specimen $H > 2.0 (K_Q/\sigma_y)^2$
3. The initial slot length $a_0 > 2.5 (K_Q/\sigma_y)^2$
4. The crack jump length Δa

$$B_N \leq \Delta a \leq (L-a_0-H) \text{ for the R-DCB}$$

$$B_N \leq \Delta a \leq (0.8W-a_0) \text{ for the CT}$$

Comparisons between the BCL numerical results and the results from experimental measurements have been limited. In a previous report (2.2) a comparison was made between experimental results for one R-DCB specimen and predictions made by the one-dimensional BCL computer code. For the K_Q used in the experiment, the comparison showed excellent agreement as the code accurately predicted crack arrest length, crack position with respect to time and the velocity of crack propagation.

To more thoroughly verify the BCL procedure an extensive series of comparisons have been made. In the first comparison, which is discussed in detail in Section 2.2, the effect of a velocity dependence on K_D was studied. The \dot{a} -K relationship for Homalite 100 was used as input to the one dimensional computer code and new reference curves were generated.

The second comparison involves the use of the BCL reference curves to generate \dot{a} -K relations for Homalite 100, Araldite B and 4340 steel. These results are then compared with \dot{a} -K relations determined by other methods in Section 2.3.

The final comparison involves checking the predicted and measured stress intensity factor and the crack velocity on a test by test basis. These comparisons are described in Section 2.4.

2.2 Effect of the K vs \dot{a} relationship on the reference curves.

The research group at BCL has reported (2.1) that while the reference curves were generated for the case where K_D was a constant for all crack velocities, these curves should also be valid in other cases. The inclusion of a K_D - \dot{a} dependence did not appear to significantly influence the reference curves. Since the K_D - \dot{a} dependence investigated by BCL was not as severe as the gamma shaped curve that governs the behavior of Homalite 100, it was decided to determine the change in the reference curves which would occur for this K_D - \dot{a} relation. This study was motivated by the fact that predictions made with the BCL program seemed to give good results with regard to K measured experimentally but appeared to be consistently in error in predicting velocity.

A subroutine which represented a hyperbolic fit to the $K - \dot{a}$ relationship for Homalite 100 given in Fig. 2.4 was utilized as input in the BCL one-dimensional computer code. The computations required to generate the desired reference curves for a uniform height DCB were conducted at BCL by Dr. Gehlen on a CDC computer. The results for the reference curves are presented in Fig. 2.5. The K_D/K_Q ratio as a function of the ratio of crack jump length to original crack length ($\Delta a/a_0$) is given in Fig. 2.5A. The nondimensional velocity V/c_0 (where c_0 is the bar wave speed) is given as a function of $\Delta a/a_0$ in Fig. 2.5B.

Three curves are presented in each figure. The solid line is a reproduction of the BCL reference curves (2.1). The curve identified by solid circles was obtained for the Γ type K dependence when the analytical beam on the elastic-foundation model includes torsional springs. The curve indicated by open circles represents results with the Γ type K dependence when no torsional springs are present in the analytical model.

It is evident from Fig. 2.5A that the BCL reference curve for determining K falls between the results obtained with and without torsional springs when the Γ type K dependence is included in the analysis. Reference to Fig. 2.5B shows that the Γ type K dependence markedly affects velocity prediction since results obtained with and without torsional springs both are lower than the BCL reference curve.

The maximum deviation in K_D/K_Q occurs at large jump distances and is 10.5 per cent for the case of torsional springs and 8.4 per cent without springs. In Fig. 2.5B the reference curve is higher than both curves that reflect the correct $K - \dot{a}$ dependence. Once again the

largest deviation is associated with large jump distances and is 9.5 per cent for the case of torsional springs and 28.6 per cent without springs.

2.3 Prediction of K vs \dot{a} from BCL Procedure

The BCL procedure was used to determine the K vs \dot{a} relationship for Homalite 100, Araldite B, and 4340 steel. If the procedure is sound, it should be possible to determine the correct K vs \dot{a} relationship for a material from measurements of crack jump distance and K_Q .

Results obtained from experiments conducted at the University of Maryland over the past three years were examined. For experiments where crack arrest had occurred within limits specified by BCL the crack jump length and K_Q were noted. This information was used in conjunction with the reference curves to determine a value of K_D and a corresponding value of velocity. In this manner, one point on the K_D vs \dot{a} relationship was established for each experiment. This procedure was repeated for all the data available and the corresponding points are shown on graphs of K vs \dot{a} determination using the photoelastic method.

The results in Fig. 2.6 correspond to experiments conducted with the modified compact tension (M-CT) specimens. The geometry for the M-CT specimen is given in Fig. 2.7 and the experiments are described in detail in reference 2.2. The three points shown predict a K vs \dot{a} curve with a slight backward lean; however, more experimental data would be needed before a definite trend could be established. The comparison of the two sets of results shows close agreement except for the slope of

the $K - \dot{a}$ relation.

Similar results obtained for Araldite B are presented in Fig. 2.8. The solid line represents photoelastic results which are described in another chapter of this report. The results identified with closed circles was determined by the BCL procedure with data from three M-CT specimens of the geometry defined in Fig. 2.7. Again the number of points is limited but the slight backward lean of the $\dot{a} - K$ curve is evident. For comparison purposes the results obtained by Kalthoff et. al. (2.5) with R-DCB specimens are also given. The crack jump length and K_Q values as given in Reference 2.5 were used with the BCL procedure to generate the results identified with the crosses in Fig. 2.8. The results from the Kalthoff data agree quite well with the Maryland results at low velocities. At higher velocities, the K values from the Kalthoff data are lower than the Maryland results.

Results for R-DCB specimens fabricated from Homalite 100 are presented in Fig. 2.9A-C, and the geometry of the R-DCB model is defined in Fig. 2.10. The experiments conducted to obtain these results are described in detail in reference 2.2. The solid curve presented in Fig. 2.9A-C was determined from photoelastic analysis of the data. The points shown in Fig. 2.9A were determined from BCL published reference curves. The agreement in K appears quite good with the exception of one test (no. 65). The vertical straight line in Fig. 2.9A represents the average of all K values determined from the BCL published curves (except for test no. 65) and agrees with the photoelastically determined value of K_{Im} . Test no. 65 is represented by the uppermost point. The results from that particular test are on the border line of being

accepted as valid according to BCL requirements. (The crack jump was 119 mm whereas the maximum crack jump to be considered valid is 106 mm). Earlier comparisons (2.2) between results for this experiment and the BCL predictions have shown excellent agreement from the standpoint of crack velocity crack position as a function of time, and total jump distance. With this favorable velocity comparison the test was considered valid for comparison relative to $K - \dot{a}$ relation.

The points shown in Fig. 2.9B were determined from the corrected reference curves given in Fig. 2.5 using the analytical model with torsional springs. Using the corrected curve caused the data points to be moved downward and to the left. Results obtained from the corrected curves with no torsional springs in the analytical model are presented in Fig. 2.9C. This corrected reference curve causes the points to be shifted down (in velocity) and to the right (in K level). The agreement is quite good for all points although the actual velocity from test 65 was on the order of 297 m/s (2.2) rather than the 232 m/s value predicted by the modified BCL reference curve.

As a matter of interest the result from test 259 (2.6) for a R-DCB specimen loaded with a relatively compliant system (Plastic pins and wedges) is also shown in Fig. 2.9A. The BCL code assumes a rigid loading system and the prediction for the compliant model by the BCL procedure are to the left of the correct K vs \dot{a} relationship.

Some of the results depicted in Fig. 2.9 were from tests conducted about 2 years ago by the Maryland group and load rather than displacement was recorded at that time. Frictional effects were difficult to account for accurately when calculating K_Q and introduce a possible

source of error in the comparisons. To eliminate this source of error it was decided to run a new series of R-DCB tests to utilize in evaluating the BCL procedure. The model geometry was the same as given in Fig. 2.10 and a fourth shipment of Homalite 100 was used to fabricate the specimens.

The tests were conducted as described in reference 2.2 except the crack opening displacement was recorded throughout the tests. This displacement was used to compute the value of K_Q . The K vs \dot{a} relationship for the new shipment of material was found to be significantly shifted to the right ($K_{Im} = .61 \text{ MNm}^{-3/2}$ compared to $K_{Im} = .38 \text{ MNm}^{-3/2}$). The K vs \dot{a} relationship as obtained by photoelastic measurement and by the BCL procedure are given in Fig. 2.11. The solid line represents the photoelastically determined function. The points represent predictions made from the BCL reference curves. The predicted "curve" falls to the left of the actual K vs \dot{a} relationship. Since the K vs \dot{a} relation for the fourth shipment of Homalite 100 is not the same as the K vs \dot{a} relation used in generating the corrected reference curves, the corrected curves are not applicable in this case. The trends, however, are probably the same. The model without torsional springs would produce a decrease in the velocity values and an increase in the K levels predicted. The model with springs would lower velocities and lower K levels.

The lowermost predicted point in Fig. 2.11 is just barely considered a valid test since the crack jump that occurred was only slightly larger than the specimen thickness ($\Delta a = 13.08 \text{ mm}$ compared to $B = 12.7 \text{ mm}$).

The two points identified with open circles in Fig. 2.11 represent

the results of the BCL procedure as applied to two tests in which the crack propagation occurred under "fixed grip" conditions. In these tests a fixed displacement was applied to the pins and they were rigidly locked in place so that no change in displacement could occur during crack propagation. This rigid loading system is more in line with the assumptions made by the BCL code. The points are shifted to the right when compared to results for non-fixed grip conditions. One of the two points falls on the photoelastic curve and the other to the right.

Results from the 4340 steel CT specimens of the MRL design are shown in Fig. 2.12. The details of the tests are described in a separate chapter of this report. A split photoelastic coating was applied to the surface of the 4340 samples and the K vs \dot{a} function was determined by a reflective photoelastic technique. Only three steel specimens used to determine the $K - \dot{a}$ relation resulted in arrest sufficiently far from the end of the specimen to be considered valid according to the BCL criteria. Of these three, the uppermost one, is borderline valid since the crack jump length was 76.45 mm when the maximum crack jump length permitted by the BCL procedure would be 75.44 mm. As has been the case with all these comparisons, the points determined from the BCL procedure lie to the left of the curve determined photoelastically, especially in the higher velocity region of the $K - \dot{a}$ relationship.

2.4 K and Velocity Level Comparisons

The K levels predicted from the BCL procedure are normally lower than those determined photoelastically. This is especially true at

the higher velocity values. Comparisons presented have shown that for K values the predictions are better when the corrected (for proper K vs \dot{a} input) BCL reference curve that assumes no torsional springs is used.

The velocities, actual and predicted, from various tests conducted at the University of Maryland are presented in Table 2.1. When possible, all three predicted velocities (BCL published curves, torsional spring reference curves and no torsional spring reference curves) are presented. It is apparent from these results that the published BCL curves give predicted velocities that are too large (Test 354 for example has a velocity of 214 m/s compared to a predicted value of 261 m/s). The analytical model with no torsional springs which was found to predict the K level most accurately appears to underestimate the velocities at higher values. The analytical model with torsional springs seems to predict the actual velocities closer than the other two reference curves.

TABLE 2.1
Comparison of Predicted Velocities with
Experimentally Measured Velocities

<u>Test</u>	<u>Actual</u>	<u>Predicted</u>		<u>BCL</u>
		<u>No Torsional Springs</u>	<u>Torsional Springs</u>	
354	214	---	---	261
65	297	232	294	325
66	66	108	109	109
124	43	133	133	133
258	97	106	105	105
352	92	---	---	104
357	285	---	---	316

Velocities given in m/s

2.5 Summary

Comparisons have been made between experimentally determined values of K and \dot{a} and predictions made utilizing the BCL procedure. The BCL reference curves are in disagreement by as much as 10 per cent at higher jump distances when compared to curves generated by using a correct K vs \dot{a} relationship as computer input.

The K vs \dot{a} curves determined from the BCL procedure at higher velocities seem to fall to the left of the relationships determined using photoelastic data.

Velocities as predicted from BCL published reference curves appear to be larger than values determined experimentally.

K_{Im} , if determined by averaging a significant number of separate K_{IDm} values, as predicted by the procedure, appears to give a good estimate of the experimentally determined value. The values utilized in the averaging must be from a number of tests which cover the entire range of crack speeds. This estimate will be slightly smaller than the value determined photelastically.

2.6 MRL Procedure

The crack arrest toughness measurement procedure proposed by Crosley and Ripling of Material Research Laboratory (MRL) is based on a static analysis of the run-arrest event. In this procedure, crack arrest toughness K_{Ia} is calculated from the load or the crack opening displacement at a specified location a short time (of the order of a millisecond for steel specimens) after a run-arrest segment of crack extension. The procedure is based on the assumption that the value of K about 1 ms after arrest differs only moderately from the value of K at arrest.

The proposed MRL procedure can be applied to two specimen geometries: namely, a machine-loaded tapered-double -cantilever-beam (T-DCB) specimen and transverse-wedge-loaded compact specimen (TW-CS). At the University of Maryland, the examination of the MRL procedure with a Homa-lite 100 T-DCB specimen was initiated in 1976 and the results were reported in ref. 2.2. The results obtained showed a deviation from the expected behavior in two different ways: 1) the values of K_{Ia} were higher rather than lower when compared with the photoelastically

determined arrest toughness values, K_{Im} ; and 2) the results for K_{Ia} were not dependent on the crack jump distance. Re-examination of the previously reported results and of material properties used in the analysis has been performed and the results are described in Section 2.7.

In the cooperative test program on crack arrest toughness measurement, which is now in progress, a TW-CS geometry is employed as a common test specimen. Examination of the MRL procedure with this TW-CS specimen has been performed, and the results are presented in Section 2.8.

2.7 Re-examination of the Results with Machine-Loaded T-DCB Specimen

A summary of results for K_{Ia} taken from ref. 2.2 is presented in Table 2.2. These results were obtained for Homalite 100 by using the MRL method of analysis. This method involves the determination of the strain energy release rate G from:

$$G_{Ia} = \frac{P_a^2}{2B} \frac{dC}{da} \quad (2.1)$$

where P_a is the load a short time after crack arrest
 dC/da is the slope of the compliance curve for the
 T-DCB specimen.

Table 2.2

Summary of K_{Ia} Test Results

Model No.	Specimen Thickness B (mm)	Load at Onset of Crack Propagation (N)	Load at Arrest P _a (N)	K_Q $(\text{psi}\sqrt{\text{in}})(\text{ftmm}^{-3/2})$	G_{Ia} $(\text{lb}/\text{in})(\text{N}/\text{m})(\text{psi}\sqrt{\text{in}})(\text{ftmm}^{-3/2})$	K_{Ia}	Initial Crack Length a (mm)	Crack Jump Distance Δa (mm)	$\frac{\Delta a}{a}$	$\frac{K_{Ia}}{K_Q}$			
169A	12.95	381	317	495	0.544	0.304	53.2	413	0.454	43.2	12.4	0.288	0.838
169B	12.95	336	301	438	0.481	0.274	48.0	392	0.431	60.6	8.1	0.134	0.896
170	13.03	406	338	527	0.579	0.344	60.2	439	0.482	40.3	10.8	0.267	0.832
172	13.67	423	316	535	0.588	0.286	50.1	400	0.440	39.4	12.7	0.323	0.748
174	13.51	449	311	572	0.629	0.281	49.2	397	0.436	58.1	28.9	0.498	0.693
224	12.90	445	309	580	0.637	0.289	50.6	402	0.442	54.8	25.8	0.471	0.694
225	12.45	449	298	596	0.655	0.279	48.8	395	0.434	55.3	31.8	0.596	0.662
				Average		405	0.446						

The arrest toughness K_{Ia} is given by;

$$K_{Ia} = \sqrt{g_{Ia} E} \quad (2.2)$$

where E is the modulus of elasticity given together with other material properties of Homalite 100 in Table 2.3.

TABLE 2.3

K_{Ia} Computation Data

Static Modulus of Elasticity, $E = 3680$ MPa

Slope of Compliance Curve, $\frac{dC}{da} = 1.37 \times 10^{-5} \text{ N}^{-1}$

Material Fringe Value $f_{\sigma} = 21.1$ MPa-mm/fringe

In order to study the reasons for the differences between the values of K_{Ia} and K_{Im} , three different aspects of the procedures previously used were re-examined. These include: 1) calibration of modulus elasticity, 2) compliance calibration, and 3) characterization of the material fringe value.

2.7.1 Modulus of Elasticity

The modulus of elasticity shown in Table 2.3 was determined from electrical strain gage data taken from a standard tensile specimen. Calibration of the value of modulus of elasticity was performed with the use of a Tuckerman Optical Extensometer. The average of 4 test results (3675, 3709, 3702, and 3695 MPa) was 3695 MPa. In the course of this study, it was also determined that the modulus of elasticity of Homalite

100 is essentially independent of time when the test temperature is below about 20°C, however, when test temperature is above 25°C, a significant creep behavior is observed. A detailed discussion of the temperature dependence of the modulus and the damping characteristics is presented in Chapter 7.

2.7.2 Compliance Calibration

The compliance calibration of a machine loaded T-DCB specimen was also repeated and the results of the second calibration are shown in Table 2.4. The results of $\frac{dC}{da} = 1.364 \times 10^{-5} \text{ N}^{-1}$ from this experiment agrees well with the previous result of $1.37 \times 10^{-5} \text{ N}^{-1}$. Comparison of experimental result for $\frac{KB\sqrt{h}}{P}$ with theoretical predictions by MRL and BCL are shown in Table 2.5. The experimental equation, determined from compliance calibration, falls between the MRL relation (Eq. 2.3) and the BCL relation (Eq. 2.4).

TABLE 2.4
Summary of Results for Compliance
Tests on the T-DCB Specimen

a (mm)	Load (N)	Pin-Displacement (mm)	Compliance (mm/N)
62.4	676	0.569	8.42×10^{-4}
75.3	698	0.705	10.10×10^{-4}
87.1	681	0.797	11.70×10^{-4}
99.9	663	0.895	13.50×10^{-4}

$$\frac{dC}{da} = 1.364 \times 10^{-5} \text{ N}^{-1}$$

TABLE 2.5
Comparison of Three Equations for Determining K
for the T-DCB Specimen

$$\frac{KB\sqrt{h}}{P} = 5.44 \quad \text{MRL Eq. (2.3)}$$

$$\frac{KB\sqrt{h}}{P} = 5.96 \quad \text{BCL Eq. (2.4)}$$

$$\frac{KB\sqrt{h}}{P} = \left(\frac{EBh}{2} \frac{dC}{da} \right)^{\frac{1}{2}} = 5.82 \quad \text{Empirical Eq. (2.5)}$$

where $E = 3695 \text{ MPa}$

$B = 13.23 \text{ mm}$

$\frac{dC}{da} = 1.364 \times 10^{-5} \text{ N}^{-1}$

$h = 101.6 \text{ mm}$

$B/B_N = 1$

Photographs of isochromatic fringe patterns taken during the compliance calibration of the T-DCB specimen were analyzed to obtain K. The photoelastically determined results for K are compared with the results obtained from Eq. 2.3 in Table 2.6. This comparison shows that on the average the value of K predicted by the MRL equation is 2 percent higher than the value of K determined using photoelastic data. Based on these findings it was decided to use Eq. (2.3) to determine K.

TABLE 2.6
Comparison of Results for the Stress
Intensity Factor (T-DCB Specimen)

a (mm)	P (N)	Photoelastic	MRL (Eq. 2.3)	Difference (%)
		K (MPa√m)	K (MPa√m)	
62	507	0.631	0.654	-4
	676	0.863	0.873	-1
75	498	0.616	0.643	-4
	698	0.907	0.901	+1
87	489	0.614	0.631	-3
	681	0.864	0.878	-2
100	503	0.631	0.649	-3
	663	0.906	0.856	+1

2.7.3 Calibration of Material Fringe Value f_{σ}

Re-calibration of the static material fringe value, f_{σ} , was performed with a disc under diametrical compression. The results showed that $f_{\sigma} = 24.2$ MPa-mm/fringe at a wave length of 492 nm. The dependence of f_{σ} on time was determined by continuously observing the change in the isochromatic fringe order in the disc as a function of time. The tests were conducted at two temperatures 16°C and 27°C, and detailed results are presented in Chapter 7. It was determined that f_{σ} was nearly independent of time at a temperature of 16°C; however, a significant time dependence was observed when the temperature was increased to 27°C.

The dynamic value of f_{σ} was obtained by using a bar subjected to impact loading. The procedure was described in detail in reference 2.2. This dynamic calibration gave $f_{\sigma} = 23.3$ MPa-mm/fringe, which was nearly the same as the static value of f_{σ} . Because of the close agreement, it was decided that the static value of f_{σ} can be used in the dynamic determination of K .

2.7.4 Re-examination of Machine-Loaded T-DCB Specimen

The data previously analyzed in Reference 2. for the machine-loaded T-DCB specimen was re-examined and the analytical procedure was modified to account for more accurate calibration of E and f_{σ} . Also, the MRL equation defined in Table 2.5 was used to determine K_{Ia} . The original data is listed in Table 2.7 together with the results for the arrest toughness K_{Ia} and the crack jump distance Δa .

TABLE 2.7
Summary of Results of MRL Procedure

Model No.	Specimen Thickness B (mm)	Load P_Q (N)	P_a (N)	Crack Jump Distance Δa (mm)	$\Delta a/a_0$	K_{Ia}/K_Q	K_{Ia} (MPa \sqrt{m})
169A	12.95	381	317	12.4	0.288	0.845	0.418
169B	12.95	336	301	8.1	0.134	0.957	0.397
170	13.03	406	338	10.8	0.267	0.797	0.443
172	13.67	423	316	12.7	0.323	0.803	0.394
174	13.51	449	311	28.9	0.498	0.748	0.393
224	12.90	445	309	25.8	0.471	0.720	0.409
225	12.45	449	298	31.8	0.596	0.688	0.409
231	13.20	449	316	23.5	0.423	0.730	0.408

The average value of K_{Ia} determined with the MRL equation was 0.409 MPa \sqrt{m} . The value of K_{Im} determined from photoelastic data analyzed with $f_{\sigma} = 24.2$ MPa-mm/fringe was 0.424 MPa \sqrt{m} . The photoelastically determined value of K_{Im} was about 4 per cent higher than the average value of K_{Ia} determined with the MRL equation.

The data of Table 2.7 is presented in Fig. 2.3 where K_{Ia} is shown as a function of $\Delta a/a_0$. It is apparent from this graph that K_{Ia} for Homalite 100 T-DCB specimens appear to show a slight dependence upon $\Delta a/a_0$ in the range of observation ($\Delta a/a_0 \leq 0.6$). The results of K_{Ia} from Araldite B, R-DCB specimens reported by Kalthoff et. al. are also shown in Fig. 2.3. The comparison shows that K_{Ia} for Araldite B, R-DCB specimens show a much stronger dependence upon $\Delta a/a_0$.

2.8 Examination of MRL Procedure with Transverse-Wedge-Loaded Compact Specimen (TWL-CS)

The MRL procedure of determining K_{Ia} with a TWL-CS type specimen involves measuring the crack opening displacement, Δ , at a specified location (0.25 W away from the load line) and calculating the value of K_{Ia} from the displacement shortly after arrest. Finally the crack length at arrest, Δ_f , and the appropriate value of Y are substituted into:

$$K_{Ia} = Y \Delta_f E \frac{1}{W} \frac{B}{B_N}^{\frac{1}{2}} \quad (2.6)$$

Where E is the Young's modulus

B is the specimen thickness

B_N is the net specimen thickness

W is the specimen length

The value of Y is a function of dimensionless crack length, a/W , and is given in Table 2.8. The procedure was applied to a specimen fabricated from Homalite 100. The geometry of the specimen used is shown in Fig. 2.14. It should be noted that face-grooves were not cut in the specimen and it was possible to photograph dynamic isochromatic fringe patterns near a crack tip. Without face-grooves, B_N is equal to B and Eq. 2.6 reduces to:

$$K_{Ia} = Y \Delta_f \frac{E}{W} \quad (2.7)$$

TABLE 2.8
The Computational Constant Y as a Function of a/W

a/W	Y	a/W	Y	a/w	Y
0.30	0.219	0.50	0.182	0.70	0.133
0.31	0.218	0.51	0.179	0.71	0.130
0.32	0.217	0.52	0.177	0.72	0.127
0.33	0.216	0.53	0.174	0.73	0.125
0.34	0.215	0.54	0.172	0.74	0.122
0.35	0.214	0.55	0.170	0.75	0.119
0.36	0.212	0.56	0.167	0.76	0.116
0.37	0.210	0.57	0.165	0.77	0.113
0.38	0.209	0.58	0.162	0.78	0.110
0.39	0.207	0.59	0.160	0.79	0.107
0.40	0.205	0.60	0.157	0.80	0.104
0.41	0.202	0.61	0.155	0.81	0.101
0.42	0.200	0.62	0.153	0.82	0.098
0.43	0.198	0.63	0.150	0.83	0.095
0.44	0.196	0.64	0.148	0.84	0.091
0.45	0.194	0.65	0.145	0.85	0.088
0.46	0.191	0.66	0.143	0.86	0.084
0.47	0.189	0.67	0.140	0.87	0.081
0.48	0.186	0.68	0.138	0.88	0.077
0.49	0.184	0.69	0.135	0.89	0.073

2.8.1 Static Compliance Calibration

Static compliance calibrations of MRL type compact specimen fabricated with Homalite 100 were performed to examine the validity of the function $Y(a/W)$ used in the equation for K_{Ia} . A Kaman displacement transducer (Model KD-2300-25) was mounted on the edge of the specimen at $0.25W$ ($W = 208.2$ mm) away from the load-line to measure crack opening displacement, Δ . The specimen was loaded with a fixture which pulled a half-pin while the other half-pin was held stationary. The applied load, P , was measured with a load cell. The experimental value of $EB \Delta/P$ was calculated and compared with the value of $EB \Delta/P$ taken from tables prepared by MRL. Results of the comparison are shown in Tables 2.9 and 2.10 and graphs of $EB \Delta/P$ as a function of a/W are shown in Fig. 2.15. It appears that the difference between the experimentally determined compliance $EB \Delta/P$ with the MRL value is approximately 26-29 percent when a/W is 0.3. However, as the value of a/W increases the difference becomes smaller. The reasons for this deviation are not known at this time.

TABLE 2.9

Static Compliance Calibration of MRL Design
Transverse-Wedge-Loaded Compact Specimen (No. 281)

a (mm)	a/W	P (N)	Δ (mm)	Δ/P (mm/N)	EB Δ/P (EXP)	EB Δ/P (MRL)	Difference %
63	0.30	400	0.152	3.81×10^{-4}	18.16	25.67	-29
73	0.35	445	0.216	4.85×10^{-4}	23.03	29.92	-23
83	0.40	200	0.127	6.35×10^{-4}	30.27	35.60	-15
94	0.45	222	0.165	7.44×10^{-4}	35.46	43.06	-18
104	0.50	211	0.216	1.02×10^{-4}	48.62	53.22	-9
114	0.55	245	0.330	13.50×10^{-4}	64.35	67.04	-4
125	0.60	245	0.406	16.60×10^{-4}	79.12	86.67	-9
136	0.65	178	0.432	24.30×10^{-4}	115.80	116.04	-0.2

B = 12.90 mm

W = 208.2 mm

E = 3695 MPa

TABLE 2.10

Static Compliance Calibration of MRL Design

Transverse-Wedge-Loaded Compact Specimen (No. 288)

a (mm)	a/W	P (N)	Δ (mm)	Δ/P (mm/N)	EB Δ/P	EB Δ/P (MRL)	Difference %
62	0.30	107	0.043	4.02×10^{-4}	18.96	25.67	-26
72	0.35	107	0.059	5.51×10^{-4}	26.07	29.92	-13
83	0.40	---	---	---	---	35.60	---
94	0.45	107	0.090	8.41×10^{-4}	39.87	43.06	-7
104	0.50	107	0.114	10.70×10^{-4}	50.73	53.22	-5
114	0.55	107	0.140	13.10×10^{-4}	62.10	67.04	-7
125	0.60	107	0.151	17.90×10^{-4}	84.86	86.67	-2
135	0.65	107	0.257	24.00×10^{-4}	113.78	116.04	-2

B = 12.83 mm

W = 208.2 mm

E = 3695 MPa

2.8.2 Dynamic Photoelastic Observation of Crack Propagation and Arrest

Dynamic photoelastic observations were made with a Cranz-Schardin camera of crack propagation in a specimen loaded in accordance with the MRL procedure. Tables 2.11 through 2.14 summarize the results. Results of these photoelastic experiments which show both K and the crack length a as a function of time are given in Figs. 2.16 to 2.19. Examination of these results indicate that an oscillation of K occurred during propagation and after crack arrest. The K vs \dot{a} relationship shown in Fig. 2.20 indicates that $K = 0.42 \text{ MPa}\sqrt{\text{m}}$ at arrest.

TABLE 2.11
Stress Intensity Factor in Transverse-Wedge-Loaded
Compact Specimen of MRL Design (No. 290)

Frame No.	Time (μ sec)	a (mm)	\dot{a} (m/s)	K (MPa \sqrt{m})
2	58	87	237	0.556
3	88	93	237	0.502
4	125	102	237	0.472
5	151	109	237	0.497
6	176	115	237	0.509
7	200	121	237	0.492
8	228	127	232	0.477
9	258	134	210	0.458
10	284	140	207	0.449
11	307	145	190	0.420
12	351	150	160	0.399
13	380	154	137	0.435
14	404	159	117	0.459
15	439	162	63	0.412
16	503	164	--	0.414

B = 12.7 mm (0.498)

W = 208.2 mm

a_0 = 74 mm

a_f = 165 mm

TABLE 2.12
Stress Intensity Factors in Transverse-Wedge-Loaded
Compact Specimen of MRL Design (No. 291)

Frame No.	Time (μ sec)	a (mm)	\dot{a} (m/s)	K (MPa \sqrt{m})
2	58	85	157	---
3	90	90	140	0.421
4	124	94	137	0.434
5	148	97	128	0.465
6	176	101	128	0.466
7	202	105	143	0.443
8	225	109	143	0.406
9	254	112	107	0.459
10	283	115	83	0.438
11	312	116	62	0.439
12	350	118	0	0.451
13	381	118	0	0.452
14	405	118	0	0.452
15	445	118	0	0.435
16	499	118	0	0.416

B = 12.5 mm

W = 208.2 mm

$a_o = 71$ mm

$\Delta_o = 0.284$ mm

$a_{f1} = 118$ mm

$a_{f2} = 145$ mm

$a_o/W = 0.34$

$a_{f1}/W = 0.57$

$a_{f2}/W = 0.70$

$\gamma = 0.215$

$\gamma = 0.165$

$\gamma = 0.133$

TABLE 2.13
Stress Intensity Factor in Transverse-Wedge-Loaded
Compact Specimen of MRL Design (No. 302)

Frame No.	Time (μ sec)	a (mm)	\dot{a} (m/s)	K (MPa \sqrt{m})
3	53	89	158	0.433
4	81	93	133	0.437
5	124	98	133	0.431
6	147	102	47	0.436
7	186	105	47	0.439
8	195	109	47	0.449
9	227	111	47	0.422
10	254	112	37	0.411
11	283	113	0	0.410
12	307	113	0	0.428
13	333	113	0	0.428
14	360	113	0	0.424
15	385	113	0	0.446
16	415	113	0	0.444

B = 12.7 mm

W = 208.2 mm

a_0 = 74.0 mm

a_{f1} = 113 mm

a_{f2} = 134.9 mm

TABLE 2.14
Stress Intensity Factor in Transverse-Wedge-Loading
Compact Specimen of MRL Design (No. 303)

Frame No.	Time (μ sec)	a (mm)	\dot{a} (m/s)	K (MPa \sqrt{m})
4	66	89	122	0.384
5	109	94	130	0.424
6	132	98	133	0.443
7	147	100	133	0.426
8	180	103	133	0.450
9	228	109	90	0.436
10	254	111	57	0.408
11	279	112	35	0.388
12	304	113	0	0.410
13	331	113	0	0.437
14	358	113	0	0.439
15	384	113	0	0.424
16	412	113	0	0.413

B = 12.9 mm

W = 208.2 mm

$a_0 = 74$ mm

$a_{f1} = 113$ mm

$a_{f2} = 125$ mm

From the measurement of crack opening displacement, Δ , at a specified distance ($0.25W$ from the load line), and crack arrest position, the MRL crack arrest toughness, K_{Ia} , was calculated. The results are summarized in Table 2.15. An average value of K_{Ia} based on seven determinations was $0.41 \text{ MPa}\sqrt{\text{m}}$. A graph showing K_{Ia} and a_f/W is presented in Fig. 2.21 and indicates that the K_{Ia} value is dependent upon the crack jump distance.

It should be noted that crack re-initiation and re-arrest was observed in three of four experiments. Furthermore it was observed that the time required for the crack opening displacement to stabilize exceeded five ms. This fact is demonstrated in Fig. 2.22 where an oscilloscope trace is compared with the X-Y recorder trace of the displacement as a function of time. This behavior was also observed in the T-DCB specimen. In T-DCB specimen about 15-20 ms were required for the oscillation to damp out as is indicated in Fig. 2.23. Examination of pin-displacement and load change as a function of time clearly indicates that the load stabilizes to the static value before the pin-displacement reaches the final value. That is, the load exhibits a significant oscillation; however, the mean value of the load oscillation quickly approaches the static value. Considering the slow response of the specimen with regard to the crack opening displacement, it is critical to provide sufficient time for a specimen to stabilize after crack arrest; otherwise, the K_{Ia} value, computed with a crack opening displacement representing the transient state, may not be accurate.

TABLE 2.15

Summary of MRL-TW-CS Test Results

Test No.	a_o (mm)	Δ_o (mm)	K_o (MPa \sqrt{m})	a_{f1} (mm)	Δ_{f1} (mm)	K_{Ia} (MPa \sqrt{m})	a_{f2} (mm)	Δ_{f2} (mm)	K_{Ia} (MPa \sqrt{m})
290	74	0.37	0.65	165	0.43	0.37	--	--	--
291	74	0.30	0.52	118	0.32	0.43	145	0.38	0.41
302	75	0.30	0.52	113	0.30	0.42	133	0.30	0.37
303	74	0.30	0.52	113	0.30	0.42	125	0.35	0.42

W = 208.3 mm

2.9 Conclusions

MRL procedure applied to the TW-CS specimen has been examined by comparing K_{Ia} determined using this procedure with K_{Im} determined photo-elastically. The average value of $K_{Ia} = 0.406 \text{ MPa}\sqrt{\text{m}}$, and $K_{Im} = 0.425 \text{ MPa}\sqrt{\text{m}}$. The difference between K_{Ia} and K_{Im} is 4.5 percent which is within expected error. Although the average of K_{Ia} was close to K_{Im} , the individual determinations of K_{Ia} appear to be more strongly dependent upon $\Delta a/W$ in the TW-CS specimen than with T-DCB specimen.

The slow response of the crack opening displacement should be taken into consideration in determining K_{Ia} value.

References

- 2.1 "Prospectus For a Cooperative Test Program on Crack Arrest Toughness Measurements", Subcommittee on Dynamic Testing/Dynamic Initiation - Crack Arrest Task Group, December 1977.
- 2.2 "Photoelastic Studies of Crack Propagation and Crack Arrest", Irwin, et. al. NUREG Report for Nuclear Regulatory Commission by the University of Maryland Photomechanics Laboratory, September 1977.
- 2.3 "Critical Experiments, Measurements and Analyses to Establish a Crack Arrest Methodology for Nuclear Pressure Vessel Steels", Hahn, et. al., BMI-1937, Battelle Report, August 1975.
- 2.4 "Critical Experiments, Measurements and Analyses to Establish a Crack Arrest Methodology for Nuclear Pressure Vessel Steels", Hahn, et. al., BMI-NUREG-1959, Battelle Report, October 1976.
- 2.5 "Measurements of Dynamic Stress Intensity Factors for Fast Running and Arresting Cracks in Double-Cantilever-Beam Specimens", J. F. Kalthoff, J. Bienert, and S. Winkler, Fast Fracture and Crack Arrest - ASTM STP 627, June 1976.
- 2.6 "Influence of Loading System on Crack Propagation and Arrest Behavior in DCB Specimens", W. L. Fournery and T. Kobayashi, 11th National Symposium on Fracture Mechanics, June 1978.

3. Study of Crack Behavior in 4340 Steel with Birefringent Coatings

3.1 Introduction

At the University of Maryland, brittle birefringent polymers and dynamic photoelasticity have been extensively utilized to study crack propagation and arrest, and to aid in the development of test specimens and procedures for standardized crack arrest toughness measurements.

In the past four years this approach has permitted the:

- 1) Establishment of K vs \dot{a} curves for three polymers [3.1,3.2],
- 2) The dynamic effects to be characterized for six different specimen geometries [3.3],
- 3) The determination of the effect of a tough adhesive line on crack arrest [3.4],
- 4) The examination of the proposed ASTM standard crack arrest toughness measurement procedure [3.5].

Although the study of crack behavior in birefringent and brittle polymers with dynamic photoelasticity has contributed a great deal to the understanding of dynamic fracture, the development of the method of direct determination of the stress intensity factor and the investigation of dynamic crack behavior in steel are more significant objectives in the crack arrest program. At the University of Maryland, extensive effort has been made during this past year to develop a birefringent coating method suitable for studying fracture of steels.

The use of birefringent coatings to study dynamic fracture has been attempted previously [3.6,3.7]. However, in these investigations a continuous sheet of birefringent coating covered the entire specimen surface. This procedure caused uncertainty as to whether the photoelastic response in the coating was dominated by the fracture of the

base material or by the plastic deformation and fracture of the coating [3.8]. A split birefringent coating technique - a separate sheet of birefringent coating on either side of the anticipated crack path - has been developed at the University of Maryland which alleviates problems encountered by previous investigators. The method has been applied to the proposed ASTM compact specimen fabricated from oil quenched and tempered 4340 steel. The \dot{a} vs K relationship and K_{Im} value were established for this steel. The MRL and BCL crack arrest analysis procedures [3.9] were also used to determine crack arrest toughness and the results obtained were compared with the results from direct photoelastic measurements. This chapter describes the development of the experimental procedures for birefringent coatings, the results of the experiments on 4340 steel, and a comparison of photoelastic results with those obtained with the MRL and BCL procedures.

3.2 Experimental Procedure

The experimental apparatus, which is shown in Fig. 3.1, included an ultra-high speed camera, flash lamp system, loading fixture and specimen. Details pertaining to the experimental apparatus and the method of data analysis are presented in the following subsections.

3.2.1 High Speed Camera

The camera employed in this experiment was a Cordin model 330A continuous writing, simultaneous streak and framing camera. When used in the framing mode, the camera is capable of recording 80 frames with an image size of 15 mm by 21 mm on 35 mm film at a framing rate up to 2×10^6 fps. The selection of framing rate depends upon the crack

behavior (i.e., high-speed propagation, crack arrest, or post arrest) and the duration of the flash system, since the test was conducted with an open shutter. For the results reported here, the framing rate was approximately 330,000 fps.

The exposure time for the Cordin camera is a function of frame rate and the width of the framing stop. For these experiments the exposure time is estimated to be about 1 μ sec. The film employed was Kodak 2495 RAR high-speed negative 35 mm film. This film is medium grained with an orthochromatic emulsion that has good resolving power. As it is sensitive to light of wave lengths below 600 nm, a Kodak No. 8 filter was used to block the light with wave lengths below 500 nm. Thus, the wave length of the light used to record the fringe patterns peaked at 550 nm with a band of about 100 nm.

3.2.2 Flash Lamp System

Photographing dynamic isochromatic fringe patterns in the birefringent coatings with the Cordin Model 330A framing camera required a high-intensity, short-duration light. A special Xenon flash lamp circuit was designed to satisfy this requirement. The circuit diagram of the flash lamp presented in Fig. 3.2 shows three capacitors (121 μ F--5KVDC each) connected with an inductive coil (5.7 μ H). The capacitors are charged to 3.4 KV with a 5 KVDC power supply. Two 4-inch long Xenon flash lamps (EGG type FX81C-4) are connected in series to the capacitor bank. The firing of the lamps is initiated by applying a 25 KV trigger pulse produced by an EGG type TM11-A trigger module. The flash lamp system develops sufficient intensity to expose the film (Kodak 2495 RAR) within 15-20 μ s after receiving a trigger signal, and

the duration of this intensity is about 200 μ s.

Synchronization between the firing of the flash lamps and initiation of crack propagation was achieved with a conductive paint line placed at the tip of the machined initial crack and by a pulse-forming circuit. When the conductive paint line was broken by the crack propagation, a 20 VDC pulse 50 ns in duration was produced. This pulse triggered the EGG TM11-A which initiated the firing of the lamps. An examination of the time required for the system to respond indicated that less than 10 μ s delay occurred between the initiation of the crack and firing of the lamps.

3.2.3 Specimen and Loading Fixture

The specimen material was a hot-rolled, annealed, vacuum degassed, aircraft quality 4340 steel. The specimen shown in Fig. 3.3 was machined from a 27 mm x 210 mm x 210 mm plate. The geometry of the specimen was in accordance with the MRL specification for the co-operative test program. A machined specimen was then subjected to the following heat treatment: one hour at 900°C, oil quenching, and tempering at 370°C. One face of the heat-treated specimen was sanded and cleaned for bonding with a birefringent coating.

The birefringent coating material selected was 2 mm thick polycarbonate sheet (PS-1) with reflective backing manufactured by Photoelastic, Inc. Two pieces of coating 75 mm x 110 mm in size were prepared. The edges of the coating which were to be placed along the face groove of the specimen were machined to have the same slope as the groove face as shown in Fig. 3.4. The coating was bonded to the

specimen with Hysol EA 9810 structural high strength epoxy adhesive.

The specimen was loaded by a transverse wedge and split pin in the specially designed loading fixture as illustrated in Fig. 3.5. The wedge was forced between the two halves of the split pin with a hydraulic cylinder until crack initiation occurred. The crack opening displacement during the test period was monitored with an eddy current displacement transducer (Kaman Model KD-2300-2S) mounted at a position $0.25W$ away from the load line as specified in the MRL procedure. The signal from the displacement transducer was recorded with a digital memory oscilloscope (Nicolet, Inc. Model Explorer III). The crack opening displacement was used to calculate the stress intensity factor, K_Q , associated with crack initiation and the stress intensity factor after crack arrest K_{Ia} by employing the MRL procedure [3.9].

3.2.4 Method for Determination of the Stress Intensity Factor

Typical high-speed photoelastic results showing the isochromatic fringe patterns in the birefringent coating on the face-grooved 4340 steel specimen (Test Nq362) are shown in Fig. 3.6A and B. The fringe patterns in Fig. 3.6A are for the propagating crack and the patterns in Fig. 3.6B are for the crack arrest phase. The enlargement of one of the photograph (Frame 23) is shown in Fig. 3.7. The crack position and the stress intensity factor was determined from the isochromatic loops in a three step process. First, the over-deterministic method developed by Sanford and Dally [3.11] was used to compute the stress intensity factor in the coating. The Sanford and Dally technique is a numerical method of least square fitting of the theoretical

stress intensity factor K to an isochromatic loop with a fringe order N . Ten sets of data (N_i, r_i, θ_i) were taken from the isochromatic fringe loops as shown schematically in Fig. 3.8. Reading of the data and data processing was performed with the use of a digitizer (Talso, Inc. Model BL 611-B) interfaced with a programmable calculator (HP-9815A). The values of K_I , K_{II} and σ_{ox} were printed out after every iteration and the calculation was terminated when convergence was observed (normally after about five iterations).

The second step in the process is to convert the K for the birefringent coating to K for the steel. This was accomplished by relating the stresses in the steel to stresses in the coating as described in Reference 3.12 to obtain:

$$K^S = \frac{E^S}{E^C} \frac{1+\nu^C}{1+\nu^S} K^C \quad (3.1)$$

where E is the modulus of elasticity and

ν is Poisson's Ratio and the

superscripts s and c refer to steel and coating respectively.

Der, et al [3.8], examined the validity of the above equation by mounting the birefringent coating on one side of the crack path Homalite 100 specimens. The comparison of K determined with Eq. 3.1 to analyze isochromatic loops in the coating with K determined directly from isochromatic fringes in the Homalite 100 indicated a good agreement.

The third step in the analysis was to account for the effect of face grooves on the determination of K from the specimens employed in this study. Studies with face-grooved Homalite 100 specimens (see

Chapter 6) showed that the effect of the grooves was to increase K by a factor F so that

$$K^G = FK \quad (3.2)$$

where

$$F = \sqrt{B/B_N} \quad (3.3)$$

B is the specimen thickness

B_N is the net thickness

G is a superscript identifying the K associated with grooved specimens

Adjusting Eq. (3.1) to account for the effect of the grooves gives

$$(K^S)^G = \frac{E^S}{E^C} \frac{1+\nu^C}{1+\nu^S} K^C \sqrt{B/B_N} \quad (3.4)$$

In the analysis the following material constants were used

$$E^S = 206.9 \text{ GPa}$$

$$E^C = 2.48 \text{ GPa}$$

$$\nu^S = 0.30$$

$$\nu^C = 0.36$$

$$f_{\sigma}^* = 6.69 \text{ MPa-mm/fringe}$$

3.3 Experimental Results

Sixteen specimens were tested, and successful recording of isochromatic fringe patterns associated with a running crack and/or an arrested crack was observed in five experiments (Nos. 333, 348, 349, 362 and 375). A valid crack opening-displacement record was obtained in four additional models (Nos. 315, 351, 371 and 380). The test results for the nine tests which produced usable data are summarized in Table 3.1. In the table, the symbol Δ represents crack opening

*Note the static material fringe value for polycarbonate has been used because no data is currently available on the dynamic value.

displacement measured at $0.25 \bar{W}$ from the load-line as specified by the MRL procedure. The subscript o corresponds to crack initiation and the subscript f to crack arrest. The values of K_Q based on the MRL Eq. 2.3 are also shown in Table 3.1.

Table 3.1
Summary of Test Data for 4340 Steel

Model No.	a_o (mm)	Δ_o (mm)	a_f (mm)	Δ_f (mm)	K_Q (MPa \sqrt{m})
315	64	0.42	100	0.495	50.8
333	65	0.90	--	--	108.4
348	57	1.02	--	--	126.3
349	60	0.83	165	--	102.3
351	61	0.71	132	0.92	86.7
362	60	0.85	148	1.26	104.8
371	60	0.64	148	1.25	79.3
375	59	0.58	124 130	0.76(1st) 0.81(2nd)	72.3
380	58	0.50	95	0.61	61.9

In the following sub-sections the results of dynamic photoelastic analysis are presented, and in Section 3.4 the results of interpreting the data with the MRL and BCL analyses are presented and compared with the photoelastic results.

3.3.1 High-Speed Crack Propagation

Results showing the stress intensity factor K and the crack position a as a function of time are shown in Fig. 3.9 for Model No. 333. The crack propagated at an essentially constant velocity $\dot{a} = 780$ m/s during the observation period, and did not arrest in this specimen. The stress intensity factor, on the other hand, showed an oscillation about a monotonically decreasing mean value.

Results of K and a as a function of time are presented in Fig. 3.10 for Model No. 348. Crack propagation in this specimen was similar to that observed in Model No. 333 since the crack extended across the specimen without arresting at a velocity ranging from 730 to 664 m/s. As the crack approached the far end of the specimen, \dot{a} decreased but the crack did not arrest. Again, the stress intensity factor exhibited an oscillation about a monotonically decreasing mean value. While scatter exists in the experimental determination of K , it is believed that the oscillations do occur. Early observations indicate that variations in K which occur at high velocities do not markedly affect the crack tip velocity.

Results from another high-speed propagation experiment (Model No. 349) shown in Fig. 3.11 indicate that the crack propagated across the specimen at a velocity ranging from 779 m/s to 602 m/s. In this specimen crack arrest occurred with $a_f = 165$ mm which was only 5 mm away from the end of the specimen. The stress intensity factor again appears to show a strong oscillation about a monotonically decreasing

mean value. The measurement of K from isochromatic fringe loops was terminated when the crack tip reached to within 20 mm of the end of the specimen.

3.3.2 Crack Arrest Phase

Results of K and a as a function of time for Model No. 362 are presented in Fig. 3.12. Early in the observation period, the crack propagated at a constant velocity of 624 m/s, and the stress intensity factor was nearly constant at $75 \text{ MPa}\sqrt{\text{m}}$. The crack then experienced cyclic deceleration and acceleration with a decreasing mean value of \dot{a} during the time period between 80 and 140 μs . During this period, the stress intensity factor also exhibited a cyclic oscillation with decreasing mean values from $72 \text{ MPa}\sqrt{\text{m}}$ to about $55 \text{ MPa}\sqrt{\text{m}}$. The first crack arrest was observed at $t = 140 \mu\text{s}$. The stress intensity factor at crack arrest was $52 \text{ MPa}\sqrt{\text{m}}$. The stress intensity factor increased after the crack arrest and when $K = 62 \text{ MPa}\sqrt{\text{m}}$ the crack reinitiated. The time duration of the first crack arrest was only 15 μsec .

After reinitiation, the stress intensity factor again decreased until $K = 52 \text{ MPa}\sqrt{\text{m}}$ and the second crack arrest was observed at $t = 175 \mu\text{s}$. Crack extension between the first and second crack arrest was only about 3 mm. After the second crack arrest, K increased again. The stress intensity reaching a value of $62 \text{ MPa}\sqrt{\text{m}}$ before the second crack reinitiation occurred at $t = 208 \mu\text{s}$. The third and final crack arrest was observed after an additional crack extension of 3 mm, and the stress intensity factor was $52 \text{ MPa}\sqrt{\text{m}}$. During the rest of the observation period the stress intensity factor appeared to decrease.

The results from the third specimen shown in Fig. 3.13 indicate that the initial velocity of the crack was 450 m/s and the velocity decreased monotonically to zero. The stress intensity factor exhibited one oscillation early in the propagation phase and then a monotonic decay. Analysis of the isochromatic loops in the last half of the event was not performed due to the development of mode II loading.

3.3.3 \dot{a} vs K Relationship

The results of the stress intensity factor (K) and crack velocity \dot{a} shown in Figs. 3.9 to 3.13 have been tabulated and graphed in Fig. 3.14 to establish the \dot{a} vs K relationship for 4340 steel. The data contain considerable scatter; however, they tend to group into three categories. The data from Model Nos. 348 and 362 cover a wide range of crack velocities and the relationship between \dot{a} and K for these specimens is closely represented by the solid line in Fig. 3.14. The data from Model Nos. 333 and 349 cover a very small range of crack velocities and they seem to indicate a different \dot{a} vs K relationship as shown by the dotted line. Finally, the data from Model No. 375 appear to show still another \dot{a} vs K relationship indicated by the broken line. Further examination of the dynamics of crack propagation in this specimen (discussed in the section 3.3.4) indicates that unusual behavior of the crack propagation in Model 375.

The examination of fracture surfaces of the various models indicated that the surfaces of Model Nos. 348 and 362 are quite similar and have a coarse grainy structure as shown in Fig. 3.15. The fracture surfaces of Models Nos. 333 and 375 on the other hand are of extremely

smooth with fine grained textures as shown in Fig. 3.16. Clearly, the fracture characteristics of these two sets of models are different and this fact explains the differences in the \dot{a} vs K observed in Fig. 3.14.

The photoelastically established \dot{a} vs K relationships shown in Fig. 3.14 are compared with the \dot{a} vs K relationship reported by BCL in Report BMI-1937 in Fig. 3.17. The BCL \dot{a} vs K curve shows excellent agreement with the photoelastic results shown by the solid line in Fig. 3.14. In order to further verify the agreement, it is recommended that the microstructure and hardness of the Model Nos. 348 and 362 and the BCL specimens be compared.

3.3.4 Crack Behavior in Transverse-Wedge-Loaded-Compact Specimen

In order to study the behavior of cracks in the proposed ASTM crack arrest compact specimen, a graph of K/K_Q vs a/W was made for Model Nos. 333, 348, 349, 362 and 375. The results are shown in Figs. 3-18 to 3-22. Examination of these figures shows the following behavior:

- 1) Characteristic oscillation in K/K_Q as a function of a/W exist. For example, maxima in K/K_Q at $a/W = 0.6, 0.73, \text{ and } 0.85$ and minima in K/K_Q at $a/W = 0.67 \text{ and } 0.81$.
- 2) The oscillation of K/K_Q vs a/W appears to follow the static curve of K/K_Q vs a/W computed under the assumption that the compliance of the specimen is twice of the loading machine compliance. The effect of the loading machine compliance was analyzed by Crosby and Ripling of the Material Research Laboratory and presented in the Third Annual Report for the

Electrical Power Research Institute (RP 303-1, MRL #752).

The results of loading machine compliance on K/K_Q and the experimental results for the compact specimen obtained by the MRL are shown in Fig. 3.23. It is of interest to note that the MRL experimental results for compact specimens loaded transversely with a 3-piece wedge also show that the compliance of the specimen is twice that of the machine.

The MRL results and the photoelastic results shown in Figs. 3.18-3.22 point to the following serious problems:

- 1) It is apparent from the photoelastic results that interaction between the loading system and the specimen is occurring even during rapid crack propagation. The consideration of this interaction is essential for the analysis of dynamic crack behavior in the specimen. For this reason the BCL procedure may produce incorrect results if this interaction is not taken into account (see Section 3.4 for further discussion).
- 2) In comparing the dynamic crack arrest toughness with the static stress intensity factor, the static stress intensity factor should include the influence of the interaction between the loading system and the specimen. Without this consideration the dynamic crack arrest toughness may appear to be substantially higher than the static stress intensity factor computed under a rigid loading system assumption.

Finally, in the previous section it was noted that the \dot{a} vs K relationship for Model No. 375 requires further explanation. The inconsistent behavior of this model is again apparent in the results presented in Fig. 3.22. The behavior of K/K_Q for $a/W < 0.67$ for this specimen appears to be unreasonable unless a substantial energy transfer occurred from the loading system to the specimens. Further study is necessary on this point.

3.4 Examination of the MRL and BCL Procedures

3.4.1 MRL Procedure

The data given in Table 3.1 was used with the MRL procedure to determine the values of K_{Ia} which are shown in Table 3.2. The average of seven values of K_{Ia} was $55.9 \text{ MPa}\sqrt{\text{m}}$ which is about 8 per cent higher than K_{Im} determined by the photoelastic method. The agreement is considered to be reasonable since further refinement of the photoelastic results may be necessary.

The dependence of K_{Ia} on the crack jump distance, is shown in a graph of K_{Ia} vs a_f/W presented in Fig. 3.24. Although some scatter in K_{Ia} values is evident, the dependence of K_{Ia} on a_f/W was small. As discussed in the previous section, specimen No. 375 which produced two low data points in Fig. 3.24 appeared to have received a slightly different heat treatment, and the fracture of specimen No. 315 also appeared to be fine grained.

3.4.2 BCL Procedure

The data shown in Table 3.1 were also used with the BCL procedure to obtain K_{ID} and \dot{a} as indicated in Table 3.3. It is to be noted, that the computation of K_Q was not in accordance with the BCL procedure which specifies measuring displacement on the split pin loading device or at the end of the specimen at $0.172 \bar{W}$ distance from the load-end. The K_Q values shown in the table were calculated with the MRL procedure. It is also noted, that the results for Model Nos. 362, 371 and 375 are open to question since the crack jump distance for Nos. 362 and 371 exceeded a validity criterion of $B_N < \Delta a < 0.8W - a_0$ specified in the

BCL procedure. Finally, one of the results for No. 375 was for the second arrest following reinitiation.

Utilizing the results for K_{ID} and \dot{a} shown in Table 3.3, gave the BCL version of the \dot{a} vs K relationship presented in Fig. 3.25. These results show that K is $50 \text{ MPa}\sqrt{\text{m}}$ and is independent of \dot{a} when $\dot{a} < 600 \text{ m/s}$. When $\dot{a} > 600 \text{ m/s}$, the stress intensity factor increases with an increase in the crack velocity. Comparison of the BCL version of the \dot{a} vs K relationship with the photoelastically determined results shows that the BCL curve has a much steeper slope than the photoelastically derived curve. This difference may be due to the interaction between the specimen and the loading system. As shown in the previous section, the photoelastic results of K/K_Q vs a/W indicate that additional energy is supplied from the loading system to the specimen during crack propagation. This added energy is equivalent to raising the level of K_Q . If the additional energy supply during the crack propagation is taken into account, the BCL curve will shift to the right and will show a better agreement with the photoelastic results.

One major problem associated with the use of BCL procedure is the difficulty in estimating the interaction between the loading system and the amount of additional energy flow from the loading system to the specimen. The photoelastic results clearly demonstrate the importance of this problem. Further detailed study of the interaction between the loading system and the specimen and its implications in the case of the BCL procedure is recommended.

Table 3.2
Summary of K_{Ia} Determined with the
MRL Procedure for 4340 Steel

Model No.	a_o (mm)	Δ_o (mm)	K_Q (MPa \sqrt{m})	a_f (mm)	Δ_f (mm)	K_{Ia} (MPa \sqrt{m})
315	64	0.42	50.8	100	0.495	46.2
351	61	0.71	86.7	132	0.92	58.6
362	60	0.85	104.8	148	1.26	58.8
371	60	0.64	79.3	148	1.25	58.3
375	59	0.58	71.5	124	0.76	55.5 (1st)
				130	0.81	55.1 (2nd)
380	58	0.50	61.9	95	0.61	58.7

Average $K_{Ia} = 55.7$

Table 3.3
Summary of K_{IDm} and \dot{a} Determined With the
BCL Procedure for 4340 Steel

Model No.	a_o (mm)	a_f (mm)	$\Delta a/W$	K_Q (MPa \sqrt{m})	K_{IDm} (MPa \sqrt{m})	\dot{a} (m/s)
315	64	100	0.21	50.8	41.7	105
351	61	132	0.42	86.7	59.0	630
362	60	148	0.52	104.8	63.9*	730
371	60	148	0.52	79.3	48.4*	730
375	59	124	0.38	71.5	50.1	525
		130	0.42	71.5	48.6**	630
380	58	95	0.22	61.9	50.1	263

* Jump distance was too large to meet a valid test criterion.

** Second arrest

References

- 3.1 Kobayashi, T. and Dally, J. W., in Fast Fracture and Crack Arrest, ASTM STP 627, G. T. Hahn and M. F. Kanninen, Eds., American Society for Testing and Materials, 1977, pp. 257-273.
- 3.2 Kobayashi, T., and Dally, J. W., "A System of Modified Epoxies for Dynamic Photoelastic Studies of Fracture", Experimental Mechanics, Vol. 17, No. 10, 1977, pp. 367-374.
- 3.3 Kobayashi, T., Dally, J. W., and Fourney, W. L., "Influence of Specimen Geometry on Crack Propagation and Arrest Behavior", a paper presented at the 6th International Conference on Experimental Stress Analysis, September 1978, Munich, FRG.
- 3.4 Dally, J. W., and Kobayashi, T., "Crack Arrest in Duplex Specimens", International Journal of Solids Structures, Vol. 14, 1978 pp. 121-129.
- 3.5 Kobayashi, T., and Dally, J. W., "A Photoelastic Evaluation of the Method of Measuring Crack Arrest Toughness with a Tapered DCB Specimen", to be published in Metal Digest, Paper No. 78-Mat-15.
- 3.6 Van Elst, H. C., Dynamic Crack Propagation, G. C. Shih, ed., Noordhoff International Publishing, Leyden 1972, pp. 283-332.
- 3.7 Daniel, I. M. and Rowlands, R. E., Experimental Mechanics, Vol. 15, December 1975, pp. 449-457.
- 3.8 Der, V. K., Barker, D. B., and Holloway, D. C., to appear in Mechanics Research Communications.
- 3.9 Crosley, P. B., and Ripley, E. J., "Guidelines for Measuring K_{Ia} with a Compact Specimen", in Prospectus for a Cooperative Test Program on Crack Arrest Toughness Measurement under the auspices of ASTM E24.03.04.
- 3.10 Hogland, R. G., Gehler, P. C., Rosenfield, A. R., Kannien, M. F. and Hahn, G. T., "Proposed Tentative Method of Test for Fast Fracture Toughness and Crack Arrest Toughness", in Prospectus for a Cooperative Test Program on Crack Arrest Toughness Measurement, under the auspices of ASTM E24.03.04.
- 3.11 Sanford, R. J. and Dally, J. W., "A General Method for Determining Mixed-Mode Stress Intensity Factors from Isochromatic Fringe Patterns", to appear in Engineering Fracture Mechanics Journal.
- 3.12 Zandman, F., Redner, S., and Dally, J. W., Photoelastic Coatings, SESA Monograph No. 3, Iowa State University Press, 1977.

4. Comparison of Crack Behavior in Plastic and Steel Duplex Specimens

4.1 Introduction

During the third year of the research program at the University of Maryland, crack behavior in plastic duplex specimens was studied extensively with the use of dynamic photoelasticity (4.1). Major findings are summarized below:

1) The influence of the joint between the starter and arrest sections on fracture behavior is profound. The joint can produce crack arrest, crack branching, crack blunting and splitting along the joint. The factors which control fracture behavior include K_{Ic} , K_{Im} , and K_{Ib} for all three materials including the starter, joint and arrest sections. Also, the thickness of the joint is important in the fracture behavior.

2) When a very tough adhesive joint is used in polymeric models, the joint serves to arrest the cracks. The cracks arrest abruptly upon penetrating about 0.01 to 0.02 mm into the adhesive. After arrest, the K value increases rapidly with respect to time as kinetic energy in the duplex specimen is converted to strain energy. If K reaches a sufficiently high level, the crack will reinitiate in the adhesive and extend into the arrest section of the duplex specimen. This is demonstrated in Fig. 4.1 and Fig. 4.2 where crack position and the stress intensity factor are shown as a function of time.

If K is not sufficiently large for reinitiation, the crack remains at arrest and the K field at the crack tip oscillates at a frequency which depends upon the geometry of the fracture specimen.

3) When a brittle adhesive is used in a thin joint between two sections, no tendency for arrest is observed when the crack enters the joint. Results presented in Fig. 4.3 show that the crack propagates without pause across the thin and brittle joints. However, for relatively thick joints the crack will branch, divide the energy available, and produce arrest when the crack reaches the second interface.

In all cases, arrest at the joint affects the dynamic behavior of the specimen by producing very large oscillations in K . Fabricating metallic duplex specimens by welding may produce similar fracture behavior as the welded joint and the heat affected region may act as a tough third material between the starter and the arrest sections. It is reasonable to anticipate crack halt, stable crack arrest, crack branching, weld splitting or violent K oscillation in metallic duplex specimens depending upon the properties of the welded joint.

During this year, available information on crack behavior in the metallic duplex specimens was gathered and crack behavior in steel duplex specimens was analyzed and compared with that observed in plastic specimens.

4.2 Crack Behavior in Steel Duplex Specimen

The crack behavior in four duplex SEN specimens fabricated with starter sections of 4340 hardened to R_c 45-48 and welded to arrest sections A533B steel was reported in reference 4.2. Results showing crack extension as a function of time for three of the four specimens have been reproduced in Figs. 4.4 to 4.6. Inspection of Fig. 4.4 shows that the crack was travelling at about 850 m/s in the 4340 starter section

before it penetrated into the weld zone. The graph of crack extension with respect to time clearly indicates that the crack arrested in the weld zone or heat affected zone for a period of 60 μ s. The crack then reinitiated in the arrest section (A 533 B) at a speed of 366 m/s. Similar crack behavior where the crack travels at a high speed in the starter section of 4340 steel, and then arrests or halts when the crack penetrates into the weld or heat-affected zone is evident in Figs. 4.5 and 4.6. The arrest period varies from 30 μ s to 60 μ s, and the crack reinitiates in the arrest section of A 533 B material at much lower speed.

Results from the fourth test (DA-45) in reference 4.2 was not considered since data show crack extension as a function of time after the crack reached the weld line was not available.

The results presented for metallic duplex specimens in Figs. 4.4 to 4.6 indicate a close resemblance to the crack behavior observed in the plastic duplex specimens. Considering this close resemblance, it is plausible that the stress intensity factor in the steel duplex SEN specimen followed a pattern similar to that observed in plastic duplex specimens (i.e. see results shown in Fig. 4.2). At this point, further explanation of the change in the stress intensity factor shown in Fig. 4.2 is provided by using the a vs K relationship for each material which is given for Homalite 100 (starter section) and KTE_2 (arrest section) in Fig. 4.7. In the figure, the values of K_{IC} for Homalite 100, KTE_2 and the adhesive material are also shown. The processes of crack propagation, arrest, reinitiation and re-arrest are shown in the same figure. The crack initiated in the starter section

(Homalite 100) at the K_Q value of $1.47 \text{ MPa}\sqrt{\text{m}}$. (See point 1). Initially, the crack accelerated rapidly to the point 2, however, since the compact specimen exhibits a decreasing K as the crack length increases, both the stress intensity factor and the crack velocity decreased along the \dot{a} vs K curve from point 2 to point 4. The photoelastic observation of the plastic duplex specimen was initiated at point 3. At point 4, the propagating crack reached the adhesive joint material and encountered a material with a toughness K_{Id} of $1.2 \text{ MPa}\sqrt{\text{m}}$. The stress intensity factor at this instant was $0.59 \text{ MPa}\sqrt{\text{m}}$ which was too low to penetrate through the adhesive joint and crack arrest occurred (points 4 to 5).

While the crack was at arrest, the stress intensity factor increased from points 5 to 6. The reinitiation of the crack took place when the stress intensity factor exceeded the rapid loading toughness K_{Id} of the adhesive which was $1.2 \text{ MPa}\sqrt{\text{m}}$. It is noted that the reinitiation was controlled by the adhesive toughness rather than the rapid loading toughness for the KTE_2 material (arrest section) of $0.9 \text{ MPa}\sqrt{\text{m}}$. The increase of the K during the arrest is considered to be due to the conversion of kinetic energy to strain energy immediately after arrest and also due to the energy flow from the loading system to the specimen during the arrest period.

After the crack reinitiation at point 6, the crack jumps to point 7 on the \dot{a} vs K curve for KTE_2 material. With further extension the crack decelerates along the \dot{a} vs K curve from point 7 to point 8 where the second arrest was observed.

As demonstrated above, the behavior of the crack in the duplex specimen can be fully explained with the use of the \dot{a} vs K relationships

for the materials in the starter and arrest sections. It is also important to note that the toughness of K_{Id} of the adhesive joint controls crack reinitiation and that a large increase in the stress intensity factor during crack arrest at the joint is possible. The study indicated that the maximum stress intensity factor during the arrest could exceed the K_Q value. This fact indicates that substantial energy flow from the loading system to the specimen occurs during the arrest period.

At this point, it is of interest to examine the results of the BCL duplex SEN specimens with the use of typical \dot{a} vs K relationships shown in Fig. 4.8. The \dot{a} vs K relationship for 4340 was determined from photoelastic measurements described in Chapter 3. These results were used for -11°C test condition since the temperature dependence of 4340 material employed appeared to be small. The \dot{a} vs K relationship for A 533 B steel at -11°C was constructed from the available information in Refs. 4.2 and 4.3; however, at this time, the curve should be taken merely as a schematic presentation.

The K_Q values for the three tests with metallic duplex specimens were 104-107 $\text{MPa}\sqrt{\text{m}}$. When the crack jump occurs, (from point 1 to point 2) the crack initially propagates at a velocity of about 850 m/s as indicated by the location of point 2 on the \dot{a} vs K relationship for 4340 steel. As the crack propagates, it extends into a lower K field and shifts from point 2 to point 3 on the \dot{a} vs K relation. The small change in the crack velocity is also indicated by the crack extension vs time relation shown in Fig. 4.4. At point 3, the crack reaches the

the weld zone or heat affected zone of the duplex specimen. Study of the hardness profile across the electron beam weld zone indicated that elevated hardness ($R_c = 50$) was observed in the weld zone as shown in Fig. 4.9 (Ref. 4.2). This suggests that the fracture toughness of the welded zone may be substantially lower than that of either the original materials. If this is the case, a significant crack tip blunting may occur due to surface roughening as observed in the plastic duplex sample. When the crack finally reaches the A 533 B material, the stress intensity factor indicated by the point 3 is below K_{Im} for A 533 B, and crack arrest occurred (from point 3 to point 4).

During the arrest period, the stress intensity factor increased rapidly as indicated in the plastic sample (see Fig. 4.2). When the stress intensity factor reached the magnitude indicated by point 5, crack reinitiation occurs and the crack propagates at the velocity indicated by point 6 on the \dot{a} vs K curve for A 533 B. With continued crack extension, the stress intensity factor decreased and crack arrest occurred at point 7.

The processes described above appear to explain the crack behavior observed in the three metallic duplex specimens.

It is of interest to note that when the K_Q level is increased so that K at point 3 is higher than the K required for reinitiation at point 5, crack arrest at the weld zone will not occur. In this case, a distinct crack velocity will occur, as shown in the Fig. 4.8 (points 10 to 11), when the crack penetrates through the weld zone into the A 533 B arrest section.

From the above consideration, it is apparent that the reinitiation fracture toughness shown by point 5 ($K_{Id} \approx 100 \text{ MPa}\sqrt{\text{m}}$) plays a significant role on the crack behavior in the metal duplex specimen. When the stress intensity factor at the time of entry into the weld zone is below K_{Id} , crack arrest occurs. The crack velocity after reinitiation will be about 350 m/s, and is influenced by the value of K_Q or the stress intensity factor at point 3. The crack pause time is controlled by the difference in the stress intensity factors between points 5 and 3.

For those cases where crack arrest is not observed yet distinct crack velocity changes occur at the weld zone, the minimum crack velocity would be 350 m/s. It is interesting to note in these cases that the \dot{a} vs K relationship for A 533 B material or other tough material could be obtained by measuring the change in the crack velocity and the \dot{a} vs K relationship for 4340 material.

Additional data is available to substantiate the statement regarding the minimum observable crack velocity. BCL has provided for 20 additional crack extension-time graphs for metallic duplex specimens. In 18 cases, a distinct change in crack velocity occurred as the crack crosses the weld line. The minimum crack velocity observed in these 18 cases was 340 m/s.

4.3 Summary

The results from the study of crack behavior in plastic duplex specimens were compared to observations of crack propagation in steel duplex specimens. It is apparent that, although the properties and

behaviors of plastics are quite different from those of metallic materials, the processes of crack propagation, crack arrest, and crack reinitiation are identical in both types of duplex specimens. It is thus concluded that, with proper selection of plastic materials for starter sections, arrest sections and adhesive joints, it is possible and practical to simulate crack behavior in metal duplex specimens. Also, it would be possible to simulate crack behavior through weld lines in other structures.

REFERENCES

- 4.1 Irwin, G. R., Dally, J. W., Kobayashi, T., Fourny, W. L., and Etheridge, J. M., "Photoelastic Studies of Crack Propagation and Crack Arrest", NUREG-0342, NRC-5, 1977.
- 4.2 Hahn, G. T., Gehlen, P. C., Hoagland, R. G., Kanninen, M. F., Marschall, C. W., Popelar, C., Rosenfield, A. R. and Simon, R., "Critical Experiments, Measurements and Analyses to Establish a Crack Arrest Methodology for Nuclear Pressure Vessel Steels", BMI-NUREG 1966, Feb. 1977.
- 4.3 Hoagland, R. G., Rosenfield, A. R., Gehlen, P. C. and Hahn, G. T., "A Crack Arrest Measuring Procedure for K_{Im} , K_{Id} and K_{Ia} Properties," Fast Fracture and Crack Arrest, ASTM STP 627, G. T. Hahn and M. F. Kanninen, etc. American Society for Testing and Materials, 1977.

5. A Dynamic Photoelastic Study of Crack Propagation in a Ring Specimen

5.1 Introduction

This study considers the behavior of a crack propagating in a ring specimen subjected to a mechanically simulated thermal stress field. Particular emphasis was placed on the arrest behavior of the crack as it propagated from the tension into the compression region of this self-equilibrated stress field.

The study is motivated by the possibility of crack initiation and propagation in pressure vessels due to thermal stresses produced by a loss-of-coolant-accident (LOCA). Previous work at Oak Ridge National Lab (ORNL) by Cheverton, et. al. [5.1] has shown the applicability of linear elastic fracture mechanics in predicting crack initiation in cylindrical pressure vessels subjected to thermal stress fields. However, the behavior of the crack after initiation has not been explored and questions arise regarding the arrest of the crack as it propagates from the high tensile stress region near the inside wall of the pressure vessel into the compressive region in the central region of the wall.

Some insight can be gained regarding crack propagation into self equilibrated thermal stress fields by performing a dynamic photoelastic analysis. Photoelasticity provides whole field data during the propagation period which contains the instantaneous stress intensity factor, the crack tip position, and the change in the state of the stress across the section due to crack movement. Also, by using duplex specimens observations of crack propagation from a region of low toughness to a

region of high toughness can be made.

The model used in this investigation was a ring with an inside radius $r_i = 101.6$ mm and an outside radius $r_o = 228.6$ mm. The thermal stresses were mechanically simulated by using a mechanical deformer following a procedure introduced by Durrelli and Barriage [5.2]. Dynamic isochromatic fringe patterns were recorded with a Cranz-Schardin high-speed camera. The results obtained show energy lost during propagation, the arrest of the crack, oscillations of the stress intensity factor after arrest and reinitiation of the crack. Numerical results which have been obtained should provide a data base for verifying computer codes which are currently being developed to treat the problems of crack propagation in pressure vessels subject to thermal stresses.

5.2 Review of Previous Work

A dynamic photoelastic analysis was performed to study crack propagation in five monolithic ring specimens. The ring specimens were loaded with a specially designed mechanical deformer, Fig. 5.1, which separated and rotated a slit cut into the ring to produce a combination of tension and bending which simulated a steady state thermal stress.

The loading system and the model were calibrated to obtain a relation between the stress intensity factor K_Q associated with a blunt crack tip and the pin displacement as shown in Fig. 5.2. The loading system was also evaluated by using a ring without a crack. It was observed that the ratio of outer and inner pin displacement and the ratio of the fringe orders N_o/N_i at the outer and inner boundaries were constant ($d_o/d_i = 2.5$, $N_o/N_i = 0.53$ for $x/w = 0.38$) as the slit opening

was varied. It was also observed that the central region of the ring specimen was not affected by the clamping action of the grips. Based on these findings the deformer was considered adequate to simulate steady state thermal stresses in the ring specimens.

5.2.1 Determination of Static K as a Function of Crack Length

The influence of crack length on the stress intensity factor K was determined. Static experiments were conducted where the crack length was increased in increments and the pin displacements were held constant. The stress intensity factor K was measured for the blunt crack from the isochromatic fringe loops. The determination of K-a was made with four different pin displacements and the results obtained are shown in Fig.

5.3. It was observed that K increases with crack length until $a/w = 0.2$. For $a/w > 0.2$, K decreases monotonically tending toward zero as the crack tip approaches the outer boundary.

5.2.2 Dynamic Crack Propagation in Monolithic Ring Specimens

Ring specimens were used to study crack propagation in a two-dimensional, self-equilibrated thermal stress field. The fracture specimens were loaded to a specified value of K_Q by applying a pre-determined displacement to the pins of a mechanical deformer. The ratio of K_Q/K_{Im} was varied between 1.2 and 3.0 in the series of experiments to cover the range of crack behavior of interest.

Five dynamic photoelastic experiments (R-1 to R-5) were performed with monolithic ring specimens. The isochromatic fringe loops associated with the crack tip were analyzed using a simplified version of Etheridge's

[5.3] three parameter method. A dynamic correction due to Irwin and Rossmanith [5.4] was made in the determination to account for the effect of crack velocity on K .

The photoelastic data gave the values of K , a and \dot{a} as a function of time. The results for K as a function of time are shown in Fig. 5.4 and 5.5. Inspection of Fig. 5.4 indicates that K decreased monotonically with time until the crack arrested. After the arrest, K increased as the available kinetic energy was converted to strain energy. When K increased to K_{Id} the crack reinitiated. The results for model R-5 in Fig. 5.4, show the increase in K after arrest.

These results show that K increased about 16 percent after the crack arrested. If the variations in K are treated as vibrations, the amplitude of the oscillations would be about 8 percent of K_{Im} . These oscillations are probably produced due to the dynamics of the specimen and interaction of the loading system. The exact magnitude of the amplitude of the oscillation is difficult to measure because the scatter in the experimental results is of the same order.

Reference to the K - a/w data shown in Fig. 5.5 indicates that K also decreases monotonically with crack length. Indeed, it is remarkable that results from all four experiments (R-2 to R-5) are in close correspondence indicating that K - a/w relationship appears to be nearly independent of K_Q/K_{Im} .

Finally, a relation between the crack velocity \dot{a} and stress intensity factor K was established as shown in Fig. 5.6. The results indicated a terminal velocity of $\dot{a}_T = 356$ m/s and $K_{Im} = 0.36$ MPa \sqrt{m} for the second shipment of Homalite 100 and a terminal velocity of 340 m/s and $K_{Im} = 0.52$

MPa \sqrt{m} for the third shipment of Homalite 100.

5.2.3 Conclusions

A dynamic photoelastic study of crack propagation in ring specimens subjected to mechanically simulated thermal stresses showed that the instantaneous stress intensity factor decreased monotonically with both crack extension and time until crack arrests. This behavior was quite different from that of static stress intensity factor which increased with increasing crack length until $a/w = 0.2$, and then decreased monotonically toward zero for $a/w > 0.2$.

Oscillations in K during propagation phase were not observed in the ring specimen. Oscillations did occur after crack arrest with a peak to peak amplitude of about 16 percent.

The $K-\dot{a}$ relation was determined from the ring specimen for two different shipments of Homalite 100. The results obtained for $K_{Im} = 0.36$ MPa \sqrt{m} and $\dot{a}_T/c_2 = 0.29$ compared favorably with results obtained from R-DCB, C-DCB, M-CT and SEN specimens fabricated from the same shipment (2nd of Homalite 100). Results from the third shipment of Homalite 100 with the ring specimen gave $K_{Im} = 0.52$ MPa \sqrt{m} and $\dot{a}_T/c_2 = 0.26$.

5.3 Further Investigation of Monolithic Ring Specimens

Additional experiments were performed with monolithic rings to study displacement at the loading pins during crack propagation. The purpose was to determine if energy was added to the ring specimens through the loading pins during the propagation phase. The displacement was measured at the inner and outer pins by using eddy current

displacement transducers (Kaman Model No. KD-2300-2S).

5.3.1 Dynamic Experiments with Monolithic Rings

Three dynamic tests were performed with monolithic rings to further investigate dynamic crack propagation in rings and to measure changes in displacement at the loading pins during propagation. As any movement of the loading pins produces a change in energy in the system, it was decided to lock the system after applying the initial displacement of the pins. This was accomplished by clamping the two halves of the de-former together as illustrated in Fig. 5.1.

In the first experiment (R-6), the outward displacement measured during crack propagation at the outer pins was about 0.001 in (0.025 mm) as shown by the oscilloscope trace in Fig. 5.7. This displacement was about 1 percent of the initial displacement given to the pins. After arrest the pins oscillate with a frequency of about 500 Hz. If the load in the pins remains constant, the energy added to the system due to this outward displacement is 1.6 percent of the initial energy.

Other data obtained from this experiment is given below. The specimen was loaded until $K_Q/K_{Im} = 2.15$ and the fracture surface indicated the crack jump $a/w = 0.82$ before the first arrest. The final arrest of the crack occurred at $a/w = 0.95$. The results indicate that $\dot{a} = 305$ m/s shortly after initiation. The velocity decreased to 25 m/s in 475 μ s just prior to arrest. The crack tip position as a function of time is shown in Fig. 5.8.

In experiment R-7, the displacements were measured at the outer pins and across the starting crack. The signal output from the

displacement transducers was stored on a magnetic disc in a digital scope (NIC series 2090). The data was reproduced on an X-Y recorder and is shown in Fig. 5.9. During the propagation period (about 500 μ s), the displacement measured across the starter crack remained essentially constant. The small fluctuations which are evident in Fig. 5.9 are electronic noise produced by the high electro-magnetic field associated with firing the camera. In the post arrest period, the displacement increases to a maximum value of 0.009 in (0.229 mm) at about 2 ms after initiation.

The displacement at the outer pins increased from the beginning and was about 0.006 in (0.152 mm) prior to crack arrest. This was about 6 percent of the initial displacement given to the pins. It corresponds to an energy increase of 12 percent of the initial energy provided the load in the pins remains constant. After arrest, the displacement continued to increase until it reached a maximum value of 0.0157 in (0.399 mm) at about 1.8 millisecond after initiation. This maximum increase of 0.0157 in. is 14 percent of initial displacement and corresponds to an energy increase of about 28 percent. After the arrest, the displacement decreased in an oscillatory fashion with a frequency of 600 Hz. The large displacements observed in this experiment indicate that the system was not locked properly. Apparently the clamp became loose prior to test.

Other data obtained from this test is as follows. The value of K_Q/K_{Im} used was 1.96 and the crack first arrested at 0.756 a/w from the inner boundary. The final arrest of the crack occurred at 0.92 a/w. The results indicate that $\dot{a} = 305$ m/s after initiation. The crack

velocity decreased to 17 m/s in a period of 425 μ s prior to arrest. The crack tip position as a function of time is shown in Fig. 5.10.

In experiment R-8 the displacement was measured at the inner pins. It was observed that the displacement changed by only 0.0003 in (0.0075 mm) during the propagation period as shown in Fig. 5.11. This displacement was about 0.75 percent of initial displacement. Again, if the load is considered to be a constant in the pins, this displacement corresponds to an energy increase of 1.5 percent of the initial energy. After the arrest the displacement increased steadily to 0.005 in (0.127 mm) in 1.5 ms after initiation.

Other results from this experiment show that the crack first arrested at $a/w = 0.66$. The final arrest occurred at $a/w = 0.85$. The value of K_Q/K_{Im} used in this experiment was 1.76 and the results indicate $\dot{a} = 244$ m/s after initiation. The velocity dropped to 76 m/s in a period of 380 μ s prior to arrest. The crack tip position as a function of time is shown in Fig. 5.12.

The photoelastic data obtained from these tests were analyzed to determine K , a and \dot{a} as shown in Tables A-1 to A-3. The value of K was obtained using Dally's ten point computer program [5.5]. The results obtained were corrected for velocity effects using Irwin's [5.4] dynamic correction factor. The stress intensity factor K is shown as a function of time t and position a/w in Fig. 5.13 and 5.14. These results show that the value of K decreases monotonically both with time and crack length during the propagation period. It is interesting to note that the dynamic value of K is almost independent of the initial value of K_Q .

A comparison of the K - a/w relation for statically extended cracks and dynamically running cracks is shown in Fig. 5.15. It is evident from this comparison that considerable difference exists between the stress intensity factor associated with a statically positioned crack and a crack which achieves the same position by dynamic propagation. Moreover, this difference increases as the value of K_Q is increased.

The comparison of the static and dynamic K in Fig. 5.15 shows that only a fraction of the total energy is dissipated at the crack tip.

The value of \mathcal{G} can be calculated from the equation

$$\mathcal{G} = \frac{K^2}{E}$$

where

E is modulus of elasticity

K is stress intensity factor.

The value of K^2 is plotted as a function of a/w in Fig. 5.16 for both the static and dynamic values of K . The area below the static and dynamic curves gives an estimate of the energy loss due to the fracture process. The computations show that the energy dissipated during the dynamic propagation was 54 J/m^2 and the energy associated with the static crack extension was 120 J/m^2 . Thus, the fraction of energy lost in dynamic propagation was 45 percent of the static energy.

The fracture surfaces from these experiments showed striations which were the shape of a thumb nail indicating the positions of crack arrest. The distance from the inner boundary to the location of the striation was measured for each specimen to give the crack jump distance as a function of K_Q/K_{Im} . The results shown in Fig. 5.17 indicate that

it becomes increasingly difficult to drive the crack into the ring as a/w becomes large.

Finally, the data from the last three experiments permitted a relation between the crack velocity \dot{a} and stress intensity factor K to be established for the 4th shipment of Homalite 100. The results showed a terminal velocity of 305 m/s and an arrest value of $K_{Im} = 0.5 \text{ MPa}\sqrt{\text{m}}$ as shown in Fig. 5.18.

5.3.2 Conclusions and Discussion

The measurement of displacement at the loading pins with a locked deformer indicated that the pins were essentially stationary during crack propagation. The movement was less than 1 percent of the initial displacement during the propagation phase. If the load in the pins is assumed to be constant this small pin movement corresponds to an energy increase of about 2 percent. If the model is not locked the displacement increases to about 6 percent during the propagation phase and 14 percent in the post arrest period. This corresponds to a maximum energy increase of 12 percent in the propagation phase and of 28 percent in the post arrest period.

A significant difference was observed between the stress intensity factor associated with a statically positioned crack and a crack which achieves the same position by dynamic propagation. The comparison shows that dynamic fracture involves significantly less energy than static fracture.

The K - \dot{a} relation determined for the 4th shipment of Homalite 100 showed $K_{Im} = 0.50 \text{ MPa}\sqrt{\text{m}}$ and $\dot{a}_T = 305 \text{ m/s}$. These results compared

favorably with the third shipment of Homalite 100 but differed from the results of 2nd shipment. Thus, it is evident that the fracture characteristics of Homalite 100 depend upon the manufacturing process.

The crack jump distance from initiation to first arrest is a function of K_Q/K_{Im} which can be approximated by

$$\frac{a}{w} = 0.9325 + \frac{0.1465}{0.85 - K_Q/K_{Im}}$$

for $1 < K_Q/K_{Im} < 2$. It appears that $K_Q/K_{Im} \approx 3$ will be required to completely drive the crack across the ring if the initial crack length is $a/w = 0.08$.

5.4 Crack Propagation in Duplex Ring Specimens

Duplex ring specimens were used to study crack propagation as a crack travels from a region of low toughness material to a region of higher toughness material which is placed in the compression zone.

There are several advantages of utilizing duplex type specimens in experiments designed to characterize the dynamic fracture. The specimen with its brittle start section requires lower loads for crack initiation and the initiation can be more closely controlled. Because of the lower loads there are fewer specimen malfunctions due to excessive plastic deformation or branching at the crack tip. Finally, the use of specimen material which is sometimes expensive or difficult to procure is minimized by employing relatively small arrest sections in the duplex specimen.

Dynamic experiments were conducted with duplex ring specimen and

the influence of the fracture toughness variation on the crack jump distance was studied. The experimental procedure and the observed results are described in this section of Chapter 5.

5.4.1 Specimen Geometry and Material

The duplex specimen described in Fig. 5.19 consists of two sections: a starter section fabricated from a brittle material (Homalite 100) and an arrest section fabricated from a tougher material (Araldite B or KTE₂). The width of the two sections was determined from the fracture toughness-temperature curves given in ORNL reports (5.1). The widths of the starter and arrest sections were 38 mm and 89 mm respectively.

In the duplex-ring specimen, the starter section was fabricated from Homalite 100, which is a brittle polyester with low initiation toughness. The complete K versus \dot{a} curve for this material has been obtained by Kobayashi and Dally [5.8]. Two different materials were used in the arrest section. In the first series of tests, Araldite B was employed as the arrest material. The complete K versus \dot{a} curve for this material was obtained by Kobayashi and Metcalf and is shown in Fig. 5.20. In the second series of tests, the material employed in the arrest section was a specially formulated, tough epoxy (KTE₂) which contained 100 pph accelerator 398 (Jefferson Chemical Co.). This tough epoxy exhibited a K_{IC} of 0.9 MPa \sqrt{m} . The complete K versus \dot{a} curve for KTE₂ was determined by Irwin et. al. [5.6]. The materials used in the starter and arrest sections were tested using the Hopkinson bar method to determine the dynamic material fringe value f_G as shown in Table

5.1

TABLE 5.1

Dynamic Values of f_{σ} for a Wave Length of 492 nm

Material	f_{σ}	f_{σ}
Homalite 100 (3rd shipment)	117 psi-in/fringe	20.49 KPa-m/fringe
Araldite B	58 psi-in/fringe	10.16 KPa-m/fringe
KTE ₂	106 psi-in/fringe	18.55 KPa-m/fringe

5.4.2 Specimen Bonding Procedure

The edges of the starter section and the arrest section were machined and bonded along a joint line which was perpendicular to the direction of the starter crack. The adhesive used for bonding was a DETA cured epoxy, prepared by mixing 100 pph of Shell Epon 828 with 11 pph of Dow Chemical DETA. The mixture was placed in a vacuum chamber for 5-10 minutes to remove all the entrapped air. The edges of the two sections were thoroughly cleaned and a thin layer of adhesive applied. The two sections were bonded and maintained vertical for 24 hours. The dead weight of the starter section was used as a compressive load during the curing process. The surfaces of the specimen were then faced and polished to provide a uniform and smooth transition from the starter section to the arrest section.

A thin layer of adhesive (0.18 mm) was used for bonding, to minimize the opportunity for crack branching at the adhesive joint. Irwin et. al. [5.7] have discussed in detail the influence of adhesive

thickness on crack propagation.

5.4.3 Experimental Procedure

A starter crack 9 mm long was saw cut into the specimen, and the crack tip was rounded off to support high values of K_Q . After applying a predetermined displacement to the pins to obtain the required value of K_Q , the crack was initiated by drawing a sharp blade across the crack tip.

The isochromatic data obtained shows that the crack propagates with a high velocity in the starter section until it encounters the adhesive joint where it arrests abruptly. After the crack arrests in the adhesive, the value of K_Q increases until it is sufficient to reinitiate the crack. Depending upon the initial value of K_Q , the crack may either come to a final arrest in the arrest section or may completely fracture the specimen, without arrest. Sufficiently high values of K_Q ($1.9 < K_Q/K_{Im} < 2.7$) were used to ensure that reinitiation of the crack occurred at the adhesive joint.

5.4.4 Summary of Results for Duplex Ring Specimen

A total of five experiments were conducted to study the crack propagation in duplex-type ring specimens. In the first three experiments, Araldite B was used as the arrest material, and in the other two experiments KTE₂ was used. The isochromatic fringe loops associated with the crack tip were analyzed using a simplified version of Etheridges [5.3] three-parameter method. In all five experiments, the crack arrested in the arrest section.

In the first three experiments (R-9, R-10, R-11) performed with Araldite B as the arrest material, the value of K_Q was varied between $1.00 \text{ MPa}\sqrt{\text{m}}$ and $1.25 \text{ MPa}\sqrt{\text{m}}$. The crack arrested in all three experiments. The photoelastic data obtained from these tests were analyzed and the crack tip position as a function of time is shown in Figures 5.21, 5.22, and 5.23 for experiments R-9, R-10 and R-11, respectively.

In experiment R-9, the crack exhibited a constant velocity of 280 m/s after initiation. The velocity decreased to 173 m/s before it came to an abrupt stop at the adhesive joint. It remained arrested at the adhesive joint for a period of 165 μs , and then reinitiated into the arrest section at a constant velocity of 340 m/s. As the crack moved into the compression zone, the velocity decreased until it was again arrested at $a/w = 0.81$. The crack reinitiated and came to a final arrest at a position $a/w = 0.93$.

The crack in experiment R-10 propagated at a constant velocity of 340 m/s in the starter section, and then abruptly arrested at the adhesive joint. After reinitiation, the crack propagated into the arrest section and the crack velocity decreased from 204 m/s to 64 m/s in 300 μs . The crack was first arrested at a position of $a/w = 0.87$ and then reinitiated and propagated through the specimen.

In experiment R-11 the crack also propagated at a constant velocity of 340 m/s in the starter section until it abruptly arrested at the adhesive joint. The crack reinitiated and propagated into the arrest section at a velocity of 263 m/s. The velocity then decreased to 38 m/s before the crack was arrested at $a/w = 0.90$. The final arrest came at

$a/w = 0.99$.

The isochromatic fringe loops associated with the crack tip were analyzed to give the values of stress intensity factor K shown in Tables A-4 to A-6. The value of K is shown as a function of time and a/w , for each experiment, in Figures 5.24 to 5.29.

The results indicated that the value of stress intensity factor initially increased in the starter section and then decreased monotonically as the crack approached the adhesive joint. This behavior was observed in both experiments R-9 and R-11. In experiment R-10, the value of K showed a continuous decrease from the time of initiation. After arrest at the adhesive joint, the value of K increased as the kinetic energy in the specimen was converted into strain energy. The value of K increased until the crack reinitiated. The reinitiation value of K at the adhesive joint was observed to be about $1.3 \text{ MPa}\sqrt{\text{m}}$ in experiment R-9. In the arrest section, K decreased monotonically with slight oscillations until final arrest.

The last two tests were performed with KTE_2 as the arrest material. The trend of the results was the same as that obtained in tests with Araldite B. It was realized that with KTE_2 the crack would arrest for quite high values of K_Q ($K_Q/K_{Im} \approx 3.5$) since its toughness is so high.

The values of K_Q in experiments R-12 and R-13 were $1.37 \text{ MPa}\sqrt{\text{m}}$ and $1.25 \text{ MPa}\sqrt{\text{m}}$, respectively. The cracks in these experiments propagated at constant velocities of 340 m/s and 305 m/s, respectively after initiation and then came to an abrupt stop at the adhesive joint. After reinitiation, the velocity decreased monotonically in both the

experiments until the crack came to an arrest. The crack first arrested at $a/w = 0.90$ in experiment R-12 and at $a/w = 0.87$ in experiment R-13. The crack length as a function of time for experiments R-12 and R-13 is shown in Figures 5.30 and 5.31, respectively.

As observed in the Araldite B experiments, the value of K in the KTE_2 experiments was found to increase initially in the starter section and then to decrease monotonically until the crack reached the adhesive joint. After reinitiation into the arrest section, K decreased monotonically until the crack was arrested. The arrest value of K for KTE_2 was observed to be $0.77 \text{ MPa}\sqrt{\text{m}}$. Values of K for experiments R-12 and R-13 are shown in Tables A-7 and A-8, respectively. The stress intensity factor was plotted as a function of time and of a/w and these results are shown in Figures 5.32 to 5.35.

The influence of the toughness of the arrest material on the crack jump distance was studied. Crack jump distance was plotted as a function of K_Q for both series of tests and is shown in Figure 5.36. It was observed that crack jump distance decreases as the toughness of the material is increased.

5.4.5 Conclusion

A study of the behavior of a propagating crack as it travels from a region of low toughness to a region of higher toughness was made using duplex ring specimens. It was observed that as the toughness of the material in the compression zone is increased, the crack jump distance decreases for the same initial value of K_Q . This shows that the crack would arrest in the specimen for higher values of K_Q if the toughness

in the compression zone was increased.

The photoelastic data from experiments R-9, R-10 and R-11 were used to establish the relation between the stress intensity factor K and the crack velocity \dot{a} for Araldite B, which is shown in Fig. 5.37. From the curve, $K_{Im} = 0.6 \text{ MPa}/\sqrt{\text{m}}$ and $\dot{a}_T = 340 \text{ m/s}$. These results are in good agreement with the relation obtained by Kobayashi and Metcalf, as shown in Fig. 5.38.

5.5 Conclusion and Discussion

A dynamic photoelastic study of crack propagation in ring specimens subjected to mechanically simulated thermal stresses showed that the instantaneous stress intensity factor decreased monotonically with both crack extension and time until crack arrests. This behavior was quite different from that of the static crack extension where K increased with increasing crack length until $a/w = 0.2$, and then decreased monotonically toward zero for $a/w > 0.2$. This significant difference gives a clear indication that static stress analysis will not be applicable in determining K associated with a crack which is propagating in a dynamic stress field.

A comparison between the static and dynamic values of K for the same pin displacement shows that dynamic fracture involves significantly less energy than static fracture.

Measurement of pin displacement during the propagation phase shows that the energy added to the model by the outward movement of pins was about 2 percent of the initial energy provided the system was properly locked. If the model was not locked the energy added increased to about

10 percent during the propagation phase.

The $K-\dot{a}$ relation was determined from the ring specimen for three different shipments of Homalite 100. The results obtained for the second shipment of Homalite 100, $K_{Im} = 0.36 \text{ MPa}\sqrt{\text{m}}$ and $\dot{a}_T/c_2 = 0.29$, compared favorably with results obtained from R-DCB, C-DCB, M-CT and SEN specimens fabricated from the same shipment (second) of Homalite 100. Results from the third shipment of Homalite 100 with the ring specimen gave $K_{Im} = 0.52 \text{ MPa}\sqrt{\text{m}}$ and $\dot{a}_T/c_2 = 0.26$. The fourth shipment of Homalite 100 showed $K_{Im} = 0.5 \text{ MPa}\sqrt{\text{m}}$ and $\dot{a}_T/c_2 = 0.25$. The results for the third and fourth shipment compare quite well but differ from the results of the second shipment. Thus, it is quite evident that the fracture characteristics of Homalite 100 depend upon the manufacturing process.

The crack jump distance in monolithic ring specimens from initiation to first arrest is a function of K_Q/K_{Im} which can be approximated by

$$a/w = 0.9325 + \frac{0.1465}{0.85 - K_Q/K_{Im}}$$

for $1 < K_Q/K_{Im} \leq 2$. It appears that $K_Q/K_{Im} \approx 3$ will be required to completely drive the crack across the ring if the initial crack length is $a/w = 0.08$.

The behavior of a crack propagating from a region of low toughness to a region of high toughness was studied using duplex specimens. The dynamic value of K was found to increase initially and then to decrease in the starter section. The value of K kept decreasing till the crack was abruptly arrested at the adhesive joint. At the adhesive joint K increased till reinitiation occurred in the arrest section. The value of K decreased monotonically in the arrest section until the crack

finally arrested.

A relation between K and \dot{a} was established for Araldite B from duplex specimens and is shown in Fig. 5.37. This gave $K_{Im} = 0.6 \text{ MPa}\sqrt{\text{m}}$ and $\dot{a}_T = 340 \text{ m/s}$. These values compared well with the values obtained by Kobayashi and Metcalf as shown in Fig. 5.38.

It was observed, that, as the toughness of the material in the arrest section is increased, the crack jump distance decreases for the same value of K_Q . The crack jump distance as a function of K_Q for duplex specimens is shown in Fig. 5.36.

REFERENCES

- 5.1 R. D. Cheverton, "Pressure Vessel Fracture Studies Pertaining to a PWR-LOCA-ECC Thermal Shock, Experiments TSE 1 and TSE 2", ORNL, September 1976.
- 5.2 J. B. Barriage and A. J. Durelli, "Application of a New Deformeter to Two-Dimensional Thermal Stress Problems", SESA proceedings, Vol. XIII, No. 2.
- 5.3 J. M. Etheridge, "Determination of the Stress Intensity Factor from Isochromatic Fringe Loops", Doctor of Philosophy Dissertation, University of Maryland, 1976, Thesis Advisor: J. W. Dally.
- 5.4 H. P. Rossmanith and G. R. Irwin, "The Dynamic Correction for the K Determination", Interim Report to the Nuclear Regulatory Commission, March 1978.
- 5.5 Sanford, R. J. and Dally, J. W., "A General Method for Determining Mixed-Mode Stress Intensity Factors From Isochromatic Fringe Patterns", to appear in Engineering Journal of Fracture Mechanics.
- 5.6 G. R. Irwin, et al, "A Photoelastic Characterization of Dynamic Fracture", NUREG-0072, December 1976.
- 5.7 G. R. Irwin, et al, "Photoelastic Studies of Crack Propagation and Crack Arrest", Report prepared for U. S. Nuclear Regulatory Commission under Contract No. AT(49-24)-0172, September 1977.
- 5.8 Kobayashi, T., and Dally, J. W., "The Relation Between Crack Velocity and the Stress Intensity Factor in Birefringent Polymers," ASTM STP 672, Symposium on Fast Fracture and Crack Arrest, 1977.

6. Characterization of Effect of Damping on Crack Behavior

6.1 Introduction

Dynamic fracture behavior is known to be influenced by mechanisms of energy dissipation. Indeed, an energy balance forms the basis of fracture mechanics; however, little is known about the role of damping and energy loss in crack propagation, crack arrest and post arrest behavior.

Energy dissipation is caused not only by internal material damping, but also by the specimen geometry. The latter cause of energy dissipation may be of particular importance in the analysis of crack behavior in large, complex structures such as nuclear pressure vessels. In the case of small laboratory test specimens, low magnitude stress waves generated at the onset of and during crack propagation are reflected by the nearby boundaries and return to interact with a crack. Furthermore, some of the initial strain energy may be converted into kinetic energy during an early phase of crack propagation. Later, this kinetic energy acts to increase the stress intensity factor when it is converted back into strain energy in the final phase of crack propagation. In a large, complex structure such as a nuclear pressure vessel, stress waves generated at the crack tip may not return to the crack tip and interact with a propagating or arrested crack. This energy which is lost may alter the dynamic behavior of a crack. Analysis of the effect of damping on crack behavior can be accomplished by careful consideration of the energy balance during crack propagation and after crack arrest. Experiments of three different types were performed to study the effects of

damping and energy losses.

First, crack behavior in a face-grooved compact specimen was studied and the results were compared with those from the specimens without face-grooves. Second, the investigation involved tests to observe crack behavior in a fixed-pin compact specimen. In these tests, the loading-pins were firmly fastened, after loading to a desirable level, to eliminate energy exchange between the specimen and the loading system. Finally, in the third series of tests, post-arrest crack behavior in the compact specimen was observed. In all cases, the strain energy release rate, G , was determined during the crack propagation and after crack arrest.

6.2 Crack Behavior in Face-Grooved Specimens

It is believed that introduction of face-grooves along the crack path may contribute to energy damping by providing a means for dispersing stress waves which are propagating in the specimen. Dynamic photoelastic tests were conducted to observe the crack behavior in the CLL-compact specimen with face-grooves and the results were compared with those from the specimen without face-grooves. The geometry of the face-grooved specimen is shown in Fig. 6.1. Note that the depth of the face-grooves was 12.5 percent of the plate thickness on both faces of the specimen.

6.2.1 Static Calibration of Stress Intensity Factor Analysis Method

Introduction of face-grooves complicate the analysis of the photoelastic isochromatic fringes since they block the passage of light near

the crack tip, and distort the isochromatic fringe patterns near the groove. A typical isochromatic fringe pattern showing fringe loop distortion in the face-grooved CLL-CS is shown in Fig. 6.2.

Initial analysis of the isochromatic fringe loops was made by neglecting the existence of face grooves. Polar coordinates of ten points on the fringe loops were taken from the fringe loops, and the Newton-Raphson technique coupled with least square method was used to determine K . The results obtained with this method are shown in the column designated by K_{photo} in Table 6.1. The stress intensity factor was also determined by employing the MRL procedure where K is related to the crack opening displacement at $0.25 W$ away from the load line

Table 6.1
Comparison of Photoelastically Determined K with
Calculated K for Face-Grooved Compact Specimen

Frame No.	a/W	K_{photo} (MPa \sqrt{m})	K_{cal}^* (MPa \sqrt{m})	K_{cal}/K_{photo}
1	0.40	0.612	0.641	1.05
2	0.45	0.534	0.574	1.07
3	0.50	0.518	0.591	1.14
4	0.55	0.532	0.614	1.15
5	0.60	0.515	0.583	1.13
6	0.65	0.513	0.590	1.15
7	0.70	0.488	0.557	1.14
8	0.75	0.494	0.565	1.14

* K_{cal} was obtained with the MRL equation.

$W = 203 \text{ mm}$

The results of the computation are shown in the column K_{cal} in Table 6.1. It is interesting to note in this table that $K_{cal}/K_{photo} = 1.14$ when $a/W > 0.5$. Since $\sqrt{B/B_N}$ is also equal to 1.14 in this face-grooved CT specimen, the correction for the effect of face-grooves could be written as

$$K = [B/B_N]^{1/2} K_{photo} \quad (6.1)$$

6.2.2 Dynamic Crack Behavior in Face-Grooved Compact Specimen

Two tests were performed to study dynamic crack behavior in the face-grooved specimen. The results are summarized in Tables 6.2 and 6.3. Graphs of the stress intensity factor and crack position as a function of time are presented in Fig. 6.3. The corresponding graph of K vs a/W for the two specimens is given in Fig. 6.4. An examination of these results shows that an oscillation in K occurs. The oscillation behavior was compared with that of a non face-grooved specimen (Model No. 144) shown in Fig. 6.5. The comparison shows that no significant difference was observed during the propagation of the crack. As information of the post-arrest behavior of the crack in the specimen No. 144 was not obtained, it is impossible to evaluate the effect of face-grooves on energy lost due to damping after crack arrest.

Table 6.2
Stress Intensity Factor vs Crack Position
in Face-Grooved Compact Specimen No. 311

Frame No.	Time (μ s)	a/W	K _{photo} (MPa \sqrt{m})	K (MPa \sqrt{m})
1	10	0.425	0.485	0.559
2	31	0.438	0.501	0.578
3	54	0.456	0.489	0.564
4	82	0.476	0.500	0.577
5	118	0.501	0.489	0.561
6	143	0.512	0.488	0.564
7	166	0.521	0.471	0.543
8	190	0.527	0.477	0.550
9	224	0.540	0.454	0.524
10	257	0.547	0.463	0.534
11	295	0.549	0.454	0.524
12	331	0.550	0.486	0.560
13	353	0.555	0.471	0.541
14	404	0.555	0.446	0.514
15	446	0.555	0.470	0.542
16	478	0.555	0.482	0.556

$a_o = 65.3 \text{ mm}$
 $a_{f1} = 112.8 \text{ mm}$
 $a_{f2} = 156.9 \text{ mm}$

$a_o/W = 0.32$
 $a_f/W = 0.77$

$W = 203 \text{ mm}$
 $\sqrt{B/B_N} = 1.153$

Table 6.3
Stress Intensity Factor vs Crack Position
in Face-Grooved Compact Specimen No. 312

Frame No.	Time (μ s)	a/W	K _{photo} (MPa \sqrt{m})	K (MPa \sqrt{m})
1	12	0.404	0.487	0.559
2	32	0.415	0.492	0.564
3	53	0.426	0.498	0.571
4	83	0.435	0.492	0.564
5	118	0.443	0.480	0.551
6	143	0.446	0.482	0.533
7	166	0.451	0.541	0.621
8	193	0.457	0.483	0.554
9	224	0.461	0.490	0.562
10	258	0.461	0.487	0.559
11	295	0.461	0.483	0.554
12	330	0.461	0.473	0.543
13	333	0.461	0.496	0.569
14	375	0.461	0.487	0.559
15	419	0.461	0.483	0.554
16	450	0.461	0.479	0.549

W = 203 mm

a₀ = 65.3 mm

a_f = 93.7 mm

a₀/W = 0.322

a_f/W = 0.462

$\sqrt{B/B_N} = 1.147$

6.3 Crack Behavior in a Fixed-Pin Compact Specimen

One complexity in the analysis of dynamic crack propagation, particularly from the total energy balance viewpoint, is the energy exchange due to the interaction between the specimen and the loading system during crack propagation and after crack arrest. Fournery and Kobayashi (6.1) studied the influence of compliance of the loading wedge and pins on the crack behavior in the R-DCB specimen. One experiment was performed with a plastic wedge and plastic pins and another with an aluminum wedge and steel pins. The results indicated that the crack jump distance with the plastic pins and wedge was large by a factor of two than the crack jump distance with metallic pins and wedge. These experiments clearly demonstrated that a substantial transfer of energy from the loading system to the specimen occurred during crack propagation.

Additional evidence which signifies the importance of the interaction between the loading system and the specimen was provided by Crosley and Ripling (6.2) when it was noted that significant load train compliance is still present even with transverse wedge loading. A summary of the results presented by Crosley and Ripling, is shown in Fig. 6.6.

The energy exchange due to the interaction between the loading system and the specimen also complicates the analysis of post arrest behavior of the stress intensity factor. The stress intensity factor after post arrest oscillation is always compared with the static stress intensity factor. However, this static stress intensity factor must

be determined with appropriate consideration of the interaction between the load system and the specimen.

In order to eliminate the complication due to the interaction between the loading system and the specimen, a fixed-pin compact specimen was utilized in the test. The specimen geometry and the loading system are shown in Fig. 6.7. An ASTM E399 compact specimen fabricated from Homalite 100 was employed. Two 50 mm diameter aluminum pins were used for loading, and two 12.5 mm diameter steel threaded rods were inserted into holes at the ends of the loading pins. After introducing the specified pin displacement with the inner nuts on the threaded rods, the loading pins were firmly locked on the threaded rods by tightening outer nuts. The crack was then initiated with a solenoid activated knife which sharpened the crack tip.

6.3.1 Static Calibration of the Stress Intensity Factor in the Fixed-Pin Compact Specimen

Two experiments were conducted to study the static stress intensity factor as a function of crack position in the fixed-pin compact specimen. The results are tabulated in Tables 6.4 and 6.5, and a graph of K/K_Q vs a/W is shown in Fig. 6.8. These results are used to analyze the dynamic results which are presented later.

6.3.2 Dynamic Stress Intensity Factor in the Fixed-Pin Compact Specimen

Two experiments were performed to examine the dynamic stress intensity factor as a function of time and position in the fixed-pin compact specimen. The results are tabulated in Tables 6.6 and 6.7, and a graph of K/K_Q vs a/W is given in Fig. 6.9. The static K/K_Q vs a/W

curve is also shown in this figure. It is of particular interest to note that the dynamic stress intensity factor oscillates about the monotonically decreasing static stress intensity curve. Initially, the dynamic stress intensity factor is below the static value; however, in the later phase of propagation, the dynamic stress intensity factor becomes higher than the static value. During propagation, the dynamic stress intensity factor is nearly the same as the static value since the oscillations are small. After crack arrest, the oscillation in K continued and the value of K decreased slightly.

Table 6.4
Static Stress Intensity Factor vs a/W for
Fixed Pin Compact Specimen (No. 369)

a/W	K ($\text{MPa}\sqrt{\text{m}}$)	K/K_Q
0.30	1.00	1.00
0.37	0.85	0.85
0.43	0.72	0.72
0.50	0.63	0.63
0.56	0.61	0.61
0.61	0.58	0.58

$W = 203 \text{ mm}$

Table 6.5
Static Stress Intensity Factors vs a/W for
Fixed Pin Compact Specimen (No. 388)

a/W	K (MPa \sqrt{m})	K/K_Q
0.31	1.03	1.00
0.35	0.91	0.88
0.40	0.88	0.85
0.50	0.69	0.67
0.55	0.65	0.63
0.60	0.59	0.57
0.65	0.56	0.54
0.70	0.48	0.47

$W = 203 \text{ mm}$

The oscillation behavior of K was very similar to that noted by Kalthoff et. al. (6.3) in a study of R-DCB specimens fabricated from Araldite B. However, the deviation of the dynamic stress intensity factor from the static value was found to be much less in the fixed-pin compact specimen than in R-DCB. This fact indicates that the dynamic effect in the fixed-pin compact specimen is much less than that in R-DCB.

Examination of energy balance during crack propagation and after crack arrest, can be achieved from graphs of b/b_Q vs a/W which are shown in Fig. 6.10. When the dynamic stress intensity factor was

below the static value, the area was designated by the letter A and when the dynamic stress intensity factor was above the static one, the area was designated by the letter B. The areas A and B are approximately equal indicating that energies required for dynamic crack propagation is essentially the same as that required for static crack extension.

References

- 6.1 Fourney, W. L. and Kobayashi, T., "Influence of Loading System on Crack Propagation and Arrest Behavior in a DCB Specimen" to appear in ASTM STP.
- 6.2 Crosley, P.B., and Ripling, E. J., Third Annual Report for Electrical Power Research Institute, Project RP 303-1, "Crack Arrest Studies" MRL No. 752.
- 6.3 Kalthoff, J. F., et. al., "Dynamic Stress Intensity Factors for Arresting Cracks in DCB Specimens," Fast Fracture and Crack Arrest ASTM STP 627, 161-176 (July 1977).

Table 6.6

Dynamic Stress Intensity Factor and Crack
Position as a Function of Time - Specimen No. 367

Frame No.	Time (μ sec)	a (mm)	K ($\text{MPa}\sqrt{\text{m}}$)	a/w	K/K _Q
1	5	73.9	--	0.36	--
2	15	78.8	0.74	0.39	0.72
3	45	85.7	0.70	0.42	0.68
4	75	92.0	0.66	0.45	0.64
5	115	100.5	0.66	0.50	0.64
6	145	106.6	0.68	0.53	0.66
7	170	112.7	0.70	0.56	0.68
8	200	119.4	0.66	0.59	0.64
9	240	127.1	0.56	0.63	0.54
10	270	131.5	0.55	0.65	0.53
11	305	134.4	0.55	0.66	0.53
12	335	136.8	0.55	0.67	0.53
13	360	137.8	0.51	0.68	0.50
14	390	137.8	0.55	0.68	0.53
15	415	137.8	0.56	0.68	0.54
16	440	137.8	0.56	0.68	0.55

$$K_Q = 1.03 \text{ MPa}\sqrt{\text{m}}$$

Table 6.7
Dynamic Stress Intensity Factor and Crack
Position as a Function of Time - Specimen No. 368

Frame No.	Time (μ sec)	a (mm)	K ($\text{MPa}\sqrt{\text{m}}$)	a/w	K/ K_Q
1	9	82.2	0.62	0.40	0.70
2	36	86.6	0.59	0.43	0.67
3	67	90.0	0.61	0.44	0.69
4	101	95.6	0.63	0.47	0.72
5	133	101.7	0.63	0.50	0.72
6	163	106.7	0.58	0.53	0.66
7	190	110.0	0.54	0.54	0.61
8	217	112.0	0.55	0.55	0.63
9	257	112.0	0.54	0.55	0.61
10	284	112.0	0.52	0.55	0.59
11	318	112.0	0.54	0.55	0.61
12	349	112.0	0.54	0.55	0.61
13	377	112.0	0.50	0.55	0.57
14	403	112.0	0.51	0.55	0.58
15	443	112.0	0.55	0.55	0.63
16	458	112.0	0.49	0.55	0.56

$$K_Q = 0.88 \text{ MPa}\sqrt{\text{m}}$$

7.0 Comparison of Crack Behavior in Araldite B and Homalite 100

7.1 Comparison of Mechanical Properties

7.1.1 Introduction

Araldite B is an epoxy type polymer which has been selected to complement the use of Homalite 100 in dynamic photoelastic studies of crack arrest. The properties of Araldite B have been documented previously (ref. 7.1); however, due to variations between shipments or batches, a series of static and dynamic tests were conducted to determine its material properties. The material properties of Homalite were previously determined and published in references (7.2 and 7.3). The properties to be determined by this series of tests are: material fringe values (f_{σ} and f_{ϵ}), modulus of elasticity (E), Poisson's ratio (ν), and density (ρ).

7.1.2 Experimental Procedure

7.1.2.1 Determination of f_{σ}

The material fringe value is determined by loading a disc in diametrical compression in a polariscope over a period of time. The 76.2 mm diameter disc was machined from a 10 mm thick sheet of Araldite "B" (First Shipment). The load was applied at $t = 0$ and the fringe order at the center of the disc was measured using the Tardy compensation method. The duration of the test was approximately 24 hours, with the fringe order measurements made at various intervals during this period. The data and results for f_{σ} as a function of time are listed in Table 7.1, shown graphically in Fig. 7.1. It is noted that over almost four time decades there is a decrease in f_{σ} of approximately 10 per cent, which is not uncommon for photoelastic materials.

Table 7.1

Summary of Data and Calculations, Edge Loaded Disc
Araldite "B", D = 76.2 mm, h = 10 mm, P = 1021 N

TIME (t) (s)	Log t	N	$f_{\sigma}^* = \frac{8P}{\pi ND}$ (psi-in/fringe)
10	1.00	3.10	62.7
20	1.30	3.12	62.3
70	1.85	3.18	61.1
120	2.08	3.19	60.9
150	2.18	3.21	60.6
230	2.36	3.23	60.2
500	2.70	3.25	59.8
1100	3.04	3.27	59.5
2000	3.30	3.30	58.9
4700	3.67	3.32	58.6
10,520	4.02	3.36	57.9
71,120	4.85	3.46	56.2
91,000	4.96		

* Sodium Light, $\lambda = 589.3 \text{ nm}$

$$\frac{\text{psi-in}}{\text{fringe}} = 0.176 \frac{\text{N-mm}}{(\text{mm})^2} = 176 \text{ kPa} \cdot \text{mm}$$

7.1.2.2 Static Tensile Test

A simple tension test of a specimen machined from an 8 mm thick sheet Araldite "B" was conducted to determine the static values of Young's modulus, Poisson's Ratio, and to check the material fringe value previously obtained. Axial and transverse strain gages were mounted on the front and back surfaces of the specimen defined in Fig. 7.2, at the center of the gage length. The gages used were two element rectangular rosettes produced by Micro Measurements as EA-06-0627-350, $R = 350 \Omega$ gage factor 2.07. The specimen was loaded in a universal testing machine which was calibrated just prior to its use. The specimen was loaded at a rate of 1 mm/min and the axial and transverse strains and the load were monitored on two different X-Y recorders. Typical results used to calculate E and ν (static values) are shown in Fig. 7.3. Next, the tension specimen was fitted with a polarizer and analyzer, and a beam of light from a He-Ne laser was transmitted through the specimen at the strain gage location. The light intensity was measured by a photodiode and recorded as a function of load on an X-Y recorder. This data was used to obtain E , ν , f_ϵ and f_σ as presented in Table 7.2.

The value of the modulus of elasticity obtained from this test was about 8 per cent higher than expected, so additional tensile tests were conducted to check the modulus of elasticity and to evaluate the effect of temperature. In this set of tests, Tuckerman optical strain gages were used to check the output of the resistance strain gages. Test specimens were machined from Araldite B and Homalite 100 (second and third shipments) to the approximate dimensions of Fig. 7.2. The

specimen was mounted in a load frame, the Tuckerman strain gages mounted, front and rear, and the resistance strain gages connected to two separate bridges. The specimen was then loaded in increments, and the strains recorded after each load increment. The test was performed as rapidly as possible to eliminate time as a variable. The temperature of the laboratory was varied from 16°C to 29°C for the Homalite 100 (second shipment) specimen and from 23.5°C to 28°C for the Araldite B specimen to determine temperature sensitivity. The modulus of elasticity was calculated from load and strain data, and Poisson's ratio calculated from the ratio of transverse to axial strain. It was noted that the Tuckerman optical strain gage output matched that of the resistance strain gages to within two per cent.

TABLE 7.2

Material Properties for Araldite B

Modulus of Elasticity (static)	$E = 533,000 \text{ psi}$
Poisson's Ratio (static)	$\nu = 0.374$
Strain Fringe Value (static)	$f_{\epsilon} = 186 \text{ } \mu\text{in/in} - \text{in/fringe}$
	$f_{\sigma} = 72.2 \frac{\text{psi-in}}{\text{fringe}} @ \lambda = 632.8 \text{ nm}$
	$f_{\sigma} = 56.1 \frac{\text{psi-in}}{\text{fringe}} @ \lambda = 492.0 \text{ nm}$
	$f_{\sigma} = 67.2 \frac{\text{psi-in}}{\text{fringe}} @ \lambda = 589.3 \text{ nm}$

The test data and results are tabulated in Tables E-1 through E-7 (see Appendix) and a graph of modulus of elasticity as a function of temperature is presented in Fig. 7.4. From these results it is evident that at a temperature of 24°C, the modulus of elasticity is 485,000 psi (3,340 MPa) for Araldite B which is in good agreement with Ref. (1). Also it is clear from Fig. 7.4 that both Homalite 100 and Araldite B are temperature sensitive, the former more so than the latter. This fact is confirmed in tests described later in Section 7.1.2.6.

7.1.2.3 Determination of Dynamic Values of E and ν

A half-plane model loaded by a point charge of explosive was used to determine the dynamic values of E and ν . A 380 mm by 635 mm sheet of 8 mm thick Araldite "B" was used for the half-plane model. The dynamic fringe patterns were recorded with a Cranz-Schardin multiple spark camera operating at 57,000 frames per second. Time delays were added to the camera circuit so that the observation period was 500 μ s. The explosive charge was 125 mg of Lead Azide, which was triggered simultaneously with the camera. The time for each of the sixteen frames was measured from an intensity-time trace of the light output from the camera. The location of the dilatational and shear waves for each photograph was measured and the data obtained is shown in Table 7.3. Results obtained for the velocities are shown in Table 7.3 and Fig. 7.5. Also a typical photograph showing wave propagation in the half-plane and the Von Schmidt angle is shown in Fig. 7.6.

The density of Araldite "B" was measured on a Kraus Jolly Balance and found to be $.0001145 \text{ lb-s}^2/\text{in}^4$ (See Table 7.4). Dynamic values of E and ν are calculated from the following relationships:

$$\text{Shear Modulus} \quad \mu = \rho c_2^2 \quad \rho = .0001145 \frac{\text{lb-s}^2}{\text{in}^4} \quad (7.1)$$

$$\text{Poisson's Ratio} \quad \nu = \frac{(c_1/c_2)^2 - 2}{(c_1/c_2)^2} \quad (7.2)$$

$$\text{Elastic Modulus} \quad E = 2(1 - \nu)\mu \quad (7.3)$$

TABLE 7.3

Summary of Data and Calculations, Half Plane Model
Araldite "B" (380 x 635 x 8 mm)

FRAME NUMBER	TIME (μs)	$f(c_1)$ (in)	$f(c_2)$ (in)
1	28.5	2.74	
2	37.0	3.30	
3	44.0	3.91	
4	53.0	4.65	
5	61.0	5.30	
6	68.8	5.97	3.00
7	78.5	6.65	3.45
8	87.0	7.30	3.78
9	98.4	8.19	4.35
10	107.5		4.76
11	116.3		5.16
12	127.5		5.65

$$c_1 = 78,900 \text{ in/s} \quad (2004 \text{ m/s})$$

$$c_2 = 45,100 \text{ in/s} \quad (1156 \text{ m/s}) \quad \rho = .0001145 \frac{\text{lb-s}^2}{\text{in}^4}$$

$$\mu = \rho c_2^2 = 233,000 \text{ psi} \quad (1,610 \text{ MPa})$$

$$\nu = \frac{\kappa^2 - 2}{\kappa^2} = .35 \quad , \quad \kappa = c_1/c_2 = 1.75$$

$$E = 2(1 + \nu)\mu = 629,000 \text{ psi} \quad (4,340 \text{ MPa})$$

TABLE 7.4
Density of Araldite "B"

	f(Weight in Air)	f(loss of Weight in Water)
1	10.23	8.37
2	10.19	8.32
3	10.20	8.31
4	10.20	8.29
5	10.23	8.32
AVG	10.21	AVG 8.32

$$\text{SPECIFIC GRAVITY} = \frac{10.21}{8.32} = 1.227$$

$$\rho_{\text{WATER}} @ 70^{\circ}\text{F} = 1.936 \frac{\text{SLUGS}}{\text{FT}^3}$$

$$\rho_{\text{ARALDITE "B"}} = \frac{1.936 \times 1.227}{12^4} = .0001145 \frac{\text{lb-s}^2}{\text{in}^4}$$

7.1.2.4 Dynamic Determination of Material Properties of Araldite B

The dynamic properties of Araldite B including modulus of elasticity (E_D), Poisson's ratio (ν), and the photoelastic fringe order value (f_{σ_d}) were determined using a modified Hopkinson bar method.

The bar specimen was machined to 9.5 x 9.5 x 510 mm size from Araldite B sheet stock, and strain gages were mounted along the length, 125 mm apart. The gages used were FAET-06D-35-S6 ohms. These gages are miniature two-element rectangular rosettes which were mounted to the top and bottom of the bar to eliminate bending response. The gages were connected to two different bridges to measure axial and transverse strain separately. Calibration resistances were switched across in one arm of each bridge to give a calibration deflection related to strain on the oscilloscope. The bar was fitted with a soft aluminum attenuator at the point of impact of a sharp projectile from an air gun. A throw-off bar similar to the impact bar was loosely mounted at the reflection end to prevent reflection of the tensile wave. A He-Ne laser used as a light source transmitted a beam through the bar between one pair of strain gages, a polarizer and analyzer were placed on each side of the bar. A photodiode monitored the intensity of light from the polariscope. This air gun apparatus is more completely described in Ref. (7.3). The data was recorded on two channel time base oscilloscopes and a Nicolet digital oscilloscope. The first oscilloscope was used to record axial strain at the two gage locations to measure bar wave velocity. The Nicolet digital oscilloscope simultaneously measured both the output of the photodiode (fringe order) and the axial strain at the same location. The second oscilloscope was used to record axial and

transverse strain at one gage location in the determination of dynamic Poisson's ratio. All three scopes were triggered by the projectile as it passes a series of magnetic pickups just prior to impact. Prior to triggering, zero and calibration readings were recorded.

The bar wave velocity was calculated by comparing the distance between the two strain gage locations, five inches, with the time required for the bar wave to traverse this distance, as recorded by the first oscilloscope. The bar wave velocity thus calculated was approximately 15 per cent lower than the dilatational wave velocity measured by the half plane test described previously. The dynamic modulus of elasticity was calculated from the bar wave velocity and the material density. This value of dynamic elastic modulus is approximately 15 per cent lower than the value obtained from the half plane test, however, it does agree with Ref. 1 and is considered an accurate value. The dynamic fringe order value f_{σ} was calculated using the expression:

$$f_{\sigma} = Eh \left(\frac{\Delta \epsilon}{\Delta N} \right) \quad (7.4)$$

where $\Delta \epsilon / \Delta N$ is the slope of a graph of axial strain as a function of fringe order number, Fig. 7.7. The data for this graph was obtained from a print-out of the Nicolet digital oscilloscope, which is considered a much more accurate method of obtaining this information than the previously used method of measuring from a photograph using proportional dividers or a travelling microscope. The dynamic material fringe value was for the He-Ne laser light, but was converted to wave lengths associated with sodium light and the spark light (492 nm) used with the Craz-Schardin camera by:

$$(f\sigma)_1 = \frac{\lambda_1}{\lambda_2} (f\sigma)_2 \quad (7.5)$$

The results of this experiment are summarized in Table 7.5. The dynamic value of f_σ (sodium light) is shown together with static determinations obtained from the disc calibration to give the variation in material fringe value over nine time decades in Fig. 7.8.

TABLE 7.5

Dynamic Material Properties of Araldite B

Bar Wave Velocity $c_0 = 67,000 \text{ in/s}$ (1,702 m/s)

Dynamic modulus of Elasticity $E_D = c_0^2 \rho$ $\rho = .0001145 \frac{\text{lb-s}^2}{\text{in}^4}$

$E_D = 530,000 \text{ psi}$ (3,650 MPa)

Dynamic Fringe Value $(f_{\sigma_d}) = Eh \left(\frac{\Delta \epsilon}{\Delta N} \right)$ $h = 0.375 \text{ in}$ (9.53 mm)

$$\frac{\Delta \epsilon}{\Delta N} = 365$$

$(f_{\sigma_d}) = 72.5 \frac{\text{psi-in}}{\text{fringe}}$ (12.70 MPa-mm/Fringe) @ 632.8 nm

67.5 $\frac{\text{psi-in}}{\text{fringe}}$ (11.82 MPa-mm/Fringe) @ 589.3 nm

56.4 $\frac{\text{psi-in}}{\text{fringe}}$ (9.88 MPa-mm/Fringe) @ 492.0 nm

7.1.2.5 Creep Characteristics of Homalite 100 and Araldite B

A series of tension tests for Araldite B and Homalite 100 were conducted with the load applied over a long period of time to determine the relative rate sensitivity of the two photoelastic materials. The tension specimens of Araldite B and Homalite 100, (second and third shipments) were mounted in a load frame, the Tuckerman strain gages attached and zeroed, and a load of 262 lbs. applied. The strain gages were monitored over a period from one to 10^5 seconds and the modulus of elasticity determined as a function of time. The data obtained is shown in Tables E-8 to E-10 in the appendix and the modulus of elasticity is given as a function of time in Fig. 7.9. From these results it is evident that Homalite 100 is more rate sensitive than Araldite B at room temperature.

7.1.2.6 Viscoelastic Properties as a Function of Temperature

Polymeric materials exhibit viscoelastic properties, and a phase lag or phase angle δ occurs between stress application and strain response. The tendency for a material to behave in this manner is time and temperature dependent. To evaluate the viscoelastic characteristics a series of tests were made using specimens of Araldite B (1st shipment) and Homalite 100 (1st and 4th shipment) in a Dynamic Viscoelastometer, Rheovibron DDV-III-C. Test specimens were machined to approximately 1 mm x 6 mm x 70 mm and were cycled in the Rheovibron at frequencies of 3.5 Hz and 110 Hz, with a temperature range from -120°C to 125°C . The low temperatures were achieved with a liquid nitrogen cooled chamber, and the high temperatures with electric heaters. The extreme temperature

ranges are of academic interest only. The temperature range of real concern is the extreme seasonal temperature range of the laboratory which is 16°C to 26°C.

The Rheovibron gives the energy loss factor, tangent δ directly. It also gives the specimen extension which can be used with the instrument constants and the specimen dimensions to determine the complex (dynamic) modulus E^* . Both Tangent δ and E^* are plotted as a function of temperatures in Fig. 7.10 through 7.12. These results show typical viscoelastic behavior as measured by tangent δ , with a local maximum at about -60°C, then a relatively constant value until a sharp increase occurs at temperatures above room temperature. The dynamic modulus E^* , which is also a function of temperature, exhibits a gradual decrease in value with increasing temperature, and a much sharper decline at higher temperatures. Both materials, Araldite B and Homalite 100, are sensitive to frequency or the rate of load application. Since 110 Hz more nearly approximates the dynamic rate of load application, a comparison of the two material at this frequency is shown in Fig. 7.13.

7.1.3 Summary of Mechanical Properties of Araldite B and Homalite 100

The results of all experiments for Araldite B and Homalite 100 are shown in Table 7.6. The properties of Araldite B are the results of the experiments described in this chapter. The values for mechanical properties for Homalite 100 are those previously reported in Ref. 7.3 and repeated here for comparison.

From the results it is evident that photoelastically, Araldite B is more sensitive than Homalite 100. Also, the modulus of elasticity

of Homalite 100 is more temperature and rate sensitive than that of Araldite B.

TABLE 7.6
Mechanical and Physical Properties

		Homalite 100 (First Shipment)	Araldite "B" (First Shipment)
c_1	(in/s) : (m/s)	84,700 : 2150	78,900 : 2004
c_2	(in/s) : (m/s)	48,600 : 1230	45,100 : 1156
E_s	(psi) : (GPa)	560,000 : 3.86	485,000 : 3.34
E_D	(psi) : (GPa)	700,000 : 4.83	530,000 : 3.65
μ_D	(psi) : (GPa)	267,000 : 1.84	233,000 : 1.16
ν		0.31	0.37
ρ	(lb-sec ² /in ⁴) : (KG-sec ² /m ⁴)	0.000112 : 122	0.0001145 : 125
K_{Im}	(psi√in) : (MPa√m)	380 : 0.42	606 : 0.67
f_{σ_s}	(psi-in/fringe) : (MPa-mm/fringe)		
	@ 632.8 nm	143 : 25.1	72.2 : 12.6
	@ 589.3 nm	132 : 23.2	67.2 : 11.8
	@ 492.0 nm	110 : 19.3	56.1 : 9.82
f_{σ_D}	(psi-in/fringe) : (MPa-mm/fringe)		
	@ 632.8 nm	161 : 28.2	72.5 : 12.7
	@ 589.3 nm	150 : 26.3	67.5 : 11.8
	@ 492.0 nm	125 : 21.9	56.4 : 9.9

7.2 \dot{a} vs K Relationship for Araldite "B" and Homalite 100

7.2.1 Introduction

The \dot{a} vs K relationship is believed to be a material property and is considered in this comparison of properties of Araldite B and Homalite 100. To characterize the complete \dot{a} vs K relationship, crack propagation at all possible velocities must be induced in photoelastic specimens and the corresponding stress intensity factor measured. The results of these experiments give \dot{a} vs K which is compared with Homalite 100.

7.2.2 Experimental Procedures

7.2.2.1 Specimen Geometry

The three specimen configurations used to collect data for the \dot{a} vs K relationship were the MCT, SEN and R-DCB. Specimen geometry for the three configurations are shown in Figs. 7.14 to 7.16. Photoelastic models were prepared from 8 millimeter thick Araldite B (first shipment) following the same laboratory procedure as used for Homalite 100. The initial crack is a saw cut of length a_0 , and a silver paint conductive line was applied at the end of the starter crack for time synchronization.

7.2.2.2 Loading System and Test Procedure

The modified compact tension specimens were loaded along the crack line with a split D and transverse wedge arrangement as the specimen is suspended in a load frame. A load transducer is placed in the loading mechanism and a displacement transducer is mounted at the top of the specimen. Both transducers are monitored by an oscilloscope which

triggered at the beginning of the experiment. The loading device is completely described in Ref. 7.2.

The specimen and load frame are set up in a light field polariscope in a Cranz-Schardin spark gap camera (light of wave length $\lambda = 492.0$ nm). The specimen was loaded to the specified level of $K_Q > K_{Ic}$ and the crack initiated by drawing a sharp knife across the starter crack. As the crack initiates, the conductive line is broken and a pulse forming circuit produces a triggering signal which initiates the experiment. A two-channel oscilloscope monitoring load and displacement is triggered together with a four channel delay generator which initiates the Cranz-Schardin camera. Sixteen photographs of dynamic isochromatic fringes are recorded during the crack propagation and arrest event. The timing of the sixteen sparks was monitored by a high frequency photo diode (Lite-Mike) and recorded on an oscilloscope. The instantaneous stress intensity factor is determined from the dynamic isochromatic fringe patterns for each photograph.

7.2.2.3 Data Analysis

Typical dynamic isochromatic fringe loops for a compact tension specimen are shown in Fig. 7.17. From photographic enlargements, the fringe order N and position parameters r and θ are measured. The loop radius r is measured from the crack tip to the loop and the angle θ is the direction along which r is measured. The angle θ is measured from the direction of crack propagation, positive counterclockwise. The manual method of measuring r and θ is to place a transparent polar grid over the photograph, centered at the crack tip, and measure r with

proportional dividers at five predetermined angles. To improve accuracy, loops of maximum radius between 2 and 5 millimeters are used and two loops of the same order, one on each side of the crack tip are measured, giving a total of ten data points. This data is fed into a computer programmed to solve the equation:

$$\begin{aligned}
 f(K_I, K_{II}, \sigma_{ox}) = & \frac{1}{2\pi r_m} \{ [K_I \sin \theta_m + 2K_{II} \cos \theta_m]^2 + [K_{II} \sin \theta_m]^2 \} \\
 & + \frac{2\sigma_{ox}}{\sqrt{2\pi r_m}} \sin \frac{\theta_m}{2} [K_I \sin \theta_m (1 + 2\cos \theta_m) + K_{II} (1 + 2\cos^2 \theta_m + \cos \theta_m)] \\
 & + \sigma_{ox}^2 - (N_m f \sigma / h)^2 = 0
 \end{aligned}$$

by the method of least squares and the Newton-Raphson method. This program was developed by Sanford and Dally Ref. (7.4) and adapted to the University of Maryland Computer. A better method of measuring r and θ is being adapted by the Photomechanics Laboratory utilizing the recently acquired Talos X-Y scanner and Hewlett-Packard 9815 A calculator. Using this method five arbitrary points which include r_{max} are selected at random on each of two isochromatic loops and the radius r and position angle θ are automatically measured and recorded by the X-Y scanner. This method is faster and more accurate than the manual method and is expected to reduce experimental error significantly. In either case, the computer solution for K_I (plane strain) is the stress intensity factor K which is used in the \dot{a} vs K relationship for Araldite B.

The location of the crack tip is measured from the photograph using proportional dividers to establish the crack tip position (a), and

time is given by scanning the output of the digital oscilloscope. The crack length, a , is graphed as a function of time, and the crack velocity, \dot{a} , is the slope of this a - t curve. Thus, the corresponding values of \dot{a} and K are determined and graphed to obtain the \dot{a} - K relationship.

7.2.3 Experimental Results

7.2.3.1 Compact tension Specimen Results

Five modified compact tension (M-CT) specimens with test numbers 286, 287, 293, 313 and 314 were tested. The first specimen, #286, was loaded to a low value with $K_Q = 0.64 \text{ MPa}\sqrt{\text{m}}$. In this test the crack ran only a few millimeters at very low velocity. This test was not considered valid because of difficulty in measuring the crack tip location. To save material, the specimen was reworked and used again for test #287. This time it was loaded to an intermediate value of $K_Q = 2.09 \text{ MPa}\sqrt{\text{m}}$ and the crack ran through the specimen at a high velocity.

Two specimens, #287 and #293 exhibited the full range of velocity and results of a vs t and K vs t are shown in Fig. 7.18 and 7.19. The data used has been summarized in the Appendix in Tables E-11 and E-12. It can be seen from the results of Fig. 7.18 that velocity may be constant (293) or decreasing (287) depending on the initial value of K_Q . The dynamic stress intensity factor K , as shown in Fig. 7.19 oscillates with time as can be expected by the dynamic nature of the experiments. As long as the crack is running, K is greater than K_{Im} and is relatively constant at low crack velocity. At high crack velocity, (293) K varies from 1.01 to 2.08 $\text{MPa}\sqrt{\text{m}}$, which is in accordance with the expected shape

of the \dot{a} vs K relationship.

The other two compact tension experiments in this series, #313 and #314 were intended to characterize arrest and post arrest behavior. Prior to initial arrest, low crack velocities were recorded and corresponding K values calculated. Results for a vs t and K vs t are shown in Figs. 7.20 and 7.21 and the data recorded in Tables E-13 and E-14 in the Appendix.

7.2.3.2 SEN Specimen Results

Two center pin loaded single edge notched (CPL-SEN) specimens were used for experiments #308 and #309. Specimen #308 was loaded to $K_Q = 0.79 \text{ MPa}\sqrt{\text{m}}$ and the crack initiated. Results for a vs t given in Fig. 7.22 shows velocity increasing from 150 m/sec to a maximum of 350 m/sec. Results for K vs t given on the same figure show an increasing K field with $K = 0.74 \text{ MPa}\sqrt{\text{m}}$ at $t = 29 \text{ }\mu\text{s}$ after crack initiation to a maximum of $1.27 \text{ MPa}\sqrt{\text{m}}$ at $t = 460 \text{ }\mu\text{s}$.

Specimen #309 was loaded to a higher value of K_Q , $1.02 \text{ MPa}\sqrt{\text{m}}$ and the crack initiated. The results for a vs t and K vs t shown in Fig. 7.23, indicates that the crack velocity was higher than for experiment #308 ranging from 277 m/s to a maximum of 353 m/s. The corresponding K field was $1.03 \text{ MPa}\sqrt{\text{m}}$ at $t = 28 \text{ }\mu\text{s}$ after initiation and increased to $K = 1.66 \text{ MPa}\sqrt{\text{m}}$ at $t = 458 \text{ }\mu\text{s}$. The data used for Figs. 7.22 and 7.23 are tabulated in Tables E-15 and E-16. The results of experiments 308 and 309 contribute additional information to the K vs \dot{a} relationship in the intermediate and high velocity portion of the curve.

7.2.3.3 R-DCB Specimen Results

Two rectangular double cantilever beam (R-DCB) specimens (#331 & 332) were tested to provide additional data in the low velocity range of the K vs \dot{a} relationship. Specimen #331 was loaded to a low value of $K_Q = 0.64 \text{ MPa}\sqrt{\text{m}}$ and a low velocity crack was initiated for post arrest studies. It can be seen from the a vs t and K vs t graphs given in Fig. 7.24, that the crack velocity was never more than about 10 m/s with the K value almost constant at a mean value of about $0.6 \text{ MPa}\sqrt{\text{m}}$. Late in the event with $t = 850 \text{ }\mu\text{s}$, K increased to $0.64 \text{ MPa}\sqrt{\text{m}}$ and the crack reinitiated and ran a short distance further.

Specimen #332 was loaded to $K_Q = .69 \text{ MPa}\sqrt{\text{m}}$ and a low velocity crack was initiated which ran for approximately 6 mm before arrest. The results for a vs t and K vs t given in Fig. 7.25 show a higher velocity with a maximum of 86 m/s, decreasing until arrest occurs. The corresponding K recorded started at $0.66 \text{ MPa}\sqrt{\text{m}}$ at $t = 180 \text{ }\mu\text{s}$, and oscillated in a decreasing K field to $0.55 \text{ MPa}\sqrt{\text{m}}$ at arrest. The data used in Figs. 7.24 and 7.25 is shown in Tables E-17 and E-18. These two tests will be further analyzed for the discussion of post arrest behavior of Araldite B, however, for the period of time that the crack was propagating the \dot{a} and K values are useful in augmenting other data for the \dot{a} vs K relationship.

7.2.4 \dot{a} vs K Relationship for Araldite B

The \dot{a} vs K Relationship for Araldite B is shown in Fig. 7.26. The results show a characteristic vertical or near vertical stem at low crack velocity, and a nearly horizontal extension at high crack

velocity. All the data points obtained are shown, while there is some deviation the scatter is within the range of experimental error. The results are from experiments using three specimen geometries, modified compact tension, SEN and R-DCB. The stress intensity factor measured by R-DCB specimens was six to ten per cent lower than corresponding values achieved from modified compact tension specimens. This is within expected experimental accuracy, therefore there is not strong evidence to indicate that a separate \dot{a} vs K relationship exists for each specimen geometry. A point of interest in the \dot{a} vs K relationship for Araldite B is that it shows a positive slope at the lower values of crack velocity and this slope decreases rapidly as crack velocity increases. To compare the \dot{a} vs K relationship of Araldite B to that of Homalite 100, a normalized form of the relationship was used, as shown in Fig. 7.27. Here the difference in slope of the near vertical stem shows up clearly. With Homalite 100 the stress intensity factor is virtually constant over half the crack velocity range, while for Araldite B the stress intensity factor increases by thirteen per cent in the same portion of the crack velocity range.

7.3 Post Arrest Oscillations

7.3.1 Introduction

The dynamic nature of crack propagation and crack arrest manifests itself in oscillations in the stress intensity factor during crack propagation and after crack arrest. The magnitude and decay of post arrest oscillation of stress intensity factor are presented graphically by showing stress intensity factor as a function of time in post arrest

studies of Araldite B and Homalite 100. These results may be analyzed on a qualitative basis to observe the damping properties of each material.

7.3.2 Post Arrest Studies

7.3.2.1 Test procedure, Araldite B

Two post arrest tests were successfully conducted with Araldite B, test nos. 331 and 332. These tests were conducted using R-DCB specimens machined from 8 mm thick sheets. The Cranz-Schardin camera was used to record data. The specimens were mounted in a load frame for which the load was applied by a hydraulic cylinder moving a wedge vertically between two one inch diameter pins. The load frame and specimen were placed in a light field polariscope in the Cranz-Schardin camera. The specimen was loaded to a low value of K_Q and a low crack velocity and crack arrest were achieved over a relatively long time period, approximately 1000 μ seconds.

7.3.2.2 Test Procedure, Homalite 100

Two post arrest tests for Homalite 100 previously reported in Ref. (7.3) were selected for comparison with the two post arrest tests for Araldite B. Test specimens 5A and 6 were R-DCB specimens machined from Homalite 100 sheet stock, and were tested using substantially the same test procedure as described above, with one exception. Time delays were placed in the Cranz-Schardin camera timing circuit to extend the total time of the observation period.

7.3.3 Post Arrest Test Results

The results of post arrest test nos. 331 and 332 for Araldite B are shown in Fig. 7.24 and 7.25. The data utilized here is summarized in Tables E-17 and E-18. The results of tests of Models 5A and 6 for Homalite 100 are taken from Ref. 7.3, and a typical comparison of results, Model 332 compared with model 6 is shown in Fig. 7.28.

Post arrest oscillations in the stress intensity factor were observed in these experiments using R-DCB specimens of Homalite 100 and Araldite B. The oscillations in stress intensity factor are small, on the order of five per cent, which is about the same as the experimental accuracy of these experiments. Therefore, quantitative conclusions on post arrest oscillations from these test results cannot be made. It is interesting to note, however, that similar oscillations appear in both pre and post arrest experiments. From the dynamic nature of these experiments, it is reasonable to expect that the pre-arrest variations in stress intensity factor would carry over into the post-arrest phase, with the test specimen providing a medium for damping. This behavior should be more evident after abrupt crack arrest, than after gradual crack arrest. On this premise it is possible to draw qualitative conclusions from post arrest behavior as related to the specimen material. Homalite 100 appears to show more damping than Araldite B. Also, it is evident from Fig. 7.28 that reinitiation is accompanied by a rise in stress intensity factor. Finally, it can be seen that abrupt arrest is followed by greater oscillations than those following gradual arrest.

7.4 Fracture Surface Characteristics

7.4.1 Introduction

A normalized representation of the \dot{a} vs K relationship for Araldite B and Homalite 100 shown in Fig. 7.27, provides a basis to compare the behavior of the two materials. The most noticeable difference in the two curves lies in the vertical stem at low to intermediate crack velocity. In Homalite 100 it is nearly vertical, while for Araldite B, it shows a large positive slope which decreases rapidly as crack velocity increases. The reason for this difference lies in the rate of energy dissipation at the crack tip. Energy dissipation is measured by the strain energy release rate G as modified for the dynamic situation by Freund [7.5] as follows:

$$G_v = \frac{(1-\nu^2)K^2}{E} A(d) \quad (7.7)$$

where ν = Poisson's ratio

K = dynamic stress intensity factor

E = Young's Modulus

$$\text{and } A(d) = \frac{b^2 d^2 (1-a^2/d^2)^{1/2}}{(1-\nu)[4d^2(d^2-a^2)^{1/2}(d^2-b^2)^{1/2} - (2d^2-b^2)^2]}$$

where $a = (c_1)^{-1}$

$b = (c_2)^{-1}$

$c = (\dot{a})^{-1}$

The dynamic strain energy release rate was calculated for Homalite 100 and Araldite B, and normalized with respect to the static strain energy release rate. This ratio is shown as a function of crack velocity in

Fig. 7.29. These results indicate that for the first half of the crack velocity range for Homalite 100, the strain energy release rate increases a small amount, five per cent, while for Araldite B the increase is almost forty per cent in the same crack velocity range. The reason for the increased capability for fracture energy dissipation in Araldite B over Homalite 100 may be found from a study of the features of the surface of the fracture zone. Examination of the fracture surface shows, even to the naked eye, that striations and crazing appear in varying amounts. A closer examination under the microscope reveals all features of the fracture zone.

7.4.2 Procedure

Specimens of Homalite 100 (first shipment) previously fractured in crack propagation experiments were selected for a crack velocity range of from 90 m/s to 402 m/s and a corresponding stress intensity factor range of $0.422 \text{ MPa}\sqrt{\text{m}}$ to $0.875 \text{ MPa}\sqrt{\text{m}}$. SEN specimens numbers 308 and 309 of Araldite B were selected to give a similar range in crack velocity from 260 m/s to 356 m/s and a corresponding stress intensity factor range of $0.89 \text{ MPa}\sqrt{\text{m}}$ to $1.55 \text{ MPa}\sqrt{\text{m}}$.

These specimens were viewed by a Unitron series N microscope at a magnification of 50 diameters and photographed using incident light on the fracture surface.

7.4.3 Results

Typical photographs taken during the microscopic examination of fracture surfaces are shown in Fig. 7.30 for Araldite B and 7.31 for Homalite 100. Each photograph is identified by magnitude of crack

velocity and instantaneous stress intensity factor. Note that crack travel is left to right and increasing crack velocity and stress intensity is also left to right. It is clear from Fig. 7.30 for Araldite B that some striations and crazing are present at the maximum crack velocity. However, what is more important is the presence of small parabolic shaped patterns which increase in size and density with increasing stress intensity factor. These parabolic shaped markings on the fracture surface are the results of crack nucleation ahead of the main crack front, which join as the crack progresses through the specimen. The parabolic shape is explained by Wolock and Newman [7.6] in their study of fracture topography at the confluence of the main crack front as it intersects the secondary circular crack front emanating from the crack nucleation point. This fracture mechanism effectively increases the fracture zone size and permits greater energy dissipation. These parabolic shaped patterns were not observed in the study of the fracture zone of Homalite 100 (Fig. 7.31). Only striations and crazing at maximum crack velocity were observed. It is concluded that the effective increase in fracture zone size with attendant increase in energy dissipation is the reason why \dot{a} vs K relationship differs between Araldite B and Homalite 100. It is also noted that the \dot{a} vs K relationship for Araldite B more nearly matches that of steel.

References

- 7.1 Clark, A.B.J., and Sanford, R.J., "A Comparison of Static and Dynamic Properties of Photoelastic Materials", Proc. SESA, Vol. 20, No. 1, 1963, pp. 148-151.
- 7.2 Irwin, G.R., Dally, J.W., Kobayashi, T. and Etheridge, J.M., "A Photoelastic Study of the Dynamic Fracture Behavior of Homalite 100", NRC Report 75/107, Contract No. AT(49-24)-074, September 1975.
- 7.3 Irwin, G.R., Dally, J.W., Kobayashi, T., Fourny, W. L., Etheridge, J.M., "A Photoelastic Characterization of Dynamic Fracture", U.S. Nuclear Regulatory Commission Report, NUREG-0072, December 1976.
- 7.4 Sanford, R.J., and Dally, J.W., "A General Method for Determining Mixed-Mode Stress Intensity Factors From Isochromatic Fringe Patterns", to appear in Engineering Journal of Fracture Mechanics.
- 7.5 Freund, L.B., "Crack Propagation in an Elastic Solid Subjected to General Loading - II. Non-Uniform Rate of Extension", Journal of the Mechanics and Physics of Solids, Vol. 20, 1972, p. 141.
- 7.6 Wolock, I., and Newman, S.B., "Fracture Topography", Fracture Processes in Polymeric Solids, Bernard Rosen, Editor, Interscience Publishers, New York, 1964.

8. Parametric Aspects of Crack Tip Stress Fields

During the period, September 1977 to September 1978, investigations of rapid fracturing at the University of Maryland were assisted by Dr. H.-P. Rossmanith, Technical University of Vienna. Support for his work was divided between a fellowship from the Max Kade Foundation, NSF funding (fracturing of rock), and NRC funding for this project. Only a brief summary will be given here. A detailed report of this year of postdoctoral study has been prepared by Rossmanith with some assistance from G. R. Irwin and others, particularly numerous numerical computations by a student, R. Chona. Certain inferences from this work appear reasonably clear and have an important bearing on our crack arrest project tasks. These inferences are related mainly to optimization of K value determinations from isochromatic fringe patterns and to possible influences of specimen size and geometry upon crack extension behaviors.

During the fall of 1977, Dally directed attention to certain unusual fracture behavior features observed when a plate of Homalite 100 was tested using explosive loading pressure in a central hole. The crack speed prior to crack division was much larger than the crack speed before branching observed using SEN specimens of Homalite 100. When crack division occurred, multiple and closed spaced branching produced an appearance termed "candelabra" by Dally. These observations provided the incentive for a detailed study by Rossmanith in search of explanations. The investigation included a careful review of dynamic crack tip stress fields which led to computations and conclusions which are of interest to the NRC project.

In this discussion, the crack tip region is considered in two-

dimensional fashion. The origin of the x, y coordinate system remains at the crack tip with the y -axis normal to the crack. Positions in the stress field are also denoted by polar coordinates, r, θ , where θ is measured from the x -axis. A relatively simple crack tip stress field solution is available if it is allowable to assume a fixed crack speed. In terms of K determinations from flash photographs of isochromatic fringes near a crack tip, one can proceed as follows. A graph of crack speed from time differences between photographs can be used to assign a particular crack speed to each photograph. Measurements of r and θ may then be made for positions of known fringe order. These measurements, along with computations based upon the available crack stress field solution permit K determinations. It is necessary to make the r, θ measurements far enough away from the crack tip (an indistinct region) for purposes of measurement accuracy. However, the measurement region must remain close enough to the crack tip so that the fixed crack speed assumption has an adequate degree of validity.

The solution method has been discussed in previous reports. The method employs a basic stress function which is regarded as a truncated power series of terms proportional to $r^{(n-\frac{1}{2})}$. In addition, one assumes that a uniform stress, σ_{ox} , can be added to σ_x . For many purposes, it has seemed that only the first (singularity) term of the series, which is proportional to the parameter, K , along with the parameter, σ_{ox} , are needed in the stress field representation used for K determination. Efforts have been made to improve K determinations by including an additional parameter by using the stress function term which is proportional to \sqrt{r} . Whether the stress function singularity term should be

augmented by the addition of one or two additional terms of the power series is uncertain. It is clear that the K dominated singularity term would be in itself adequate if the crack size and lateral specimen dimensions were sufficiently large.

The influence of crack speed on the stress field is usually discussed in terms of the ratio of crack speed \dot{a} to shear wave speed, \dot{a}/c_2 . The values of this ratio observed with Homalite 100 have been less than about 0.33 with the exception of the center-hole explosive test noted above. The fact that the velocity ratio always appears in the stress equations in the form $(\dot{a}/c_2)^2$ suggested early in our work that calculations might be simplified by dropping terms proportional to higher powers of the velocity ratio. However, this practice invites judgement errors. One of the initial conclusions from the Rossmanith studies was that calculations based upon the exact fixed-speed solution are readily suited for computer programming and may as well be used in the exact form. Currently dynamic corrections to K determinations, based upon the static solution, are being made using the improved accuracy which can be obtained in this way.

The most obvious influence of specimen geometry on the near-crack-tip isochromatics is the tilt angle of the main isochromatic loops. This is chiefly controlled by the relative size of the parameter, σ_{ox} . When σ_{ox} is negative (compressive), the position on the main fringe loop where r is maximum has an angle, θ_m , which is less than 90° . The crack tip isochromatics (in the measurement region) have this appearance for end loaded SEN specimens. In the case of DCB specimens, σ_{ox} is positive (tensile) and θ_m is larger than 90° . For compact tension

specimens, the θ_m values do not differ greatly from 90° suggesting relatively small σ_{ox} values. The largest tilts of θ_m away from 90° occur with DCB specimens. For these the θ_m values are in a range where small changes of θ_m cause large changes of K . The judgement choice of crack tip location then becomes relatively important to accuracy of the determination of K . When the main fringe loops lean strongly backward, as for DCB specimen tests, the variation of maximum shear stress with θ at a fixed r value has a minimum for θ between 0 and 90° . In this region a new set of isochromatics termed notch-fringes appear in the measurement region. In previous K determinations measurements have been limited to values of r and θ at the main loop position of maximum r value. However, the notch-fringes provide equally convenient measurement points. Exploratory trials were made of K determinations based upon the minimum r point of a well defined notch fringe. The results of these trials could be made consistent with the K results from main loop measurements only by shifting the crack tip location. It was concluded that K determinations should be based upon a group of measurement points within the measurement region selected on the basis of clarity of the measurement point and that the crack tip location should be adjusted toward optimum fit to the assumed stress field. A similar conclusion was reached independently by Dally and Sanford as a result of studies conducted at the Naval Research Laboratory.

Although the influence of the crack speed on the isochromatic pattern differs with the value of σ_{ox} , in general the dynamic effect near the crack tip is to moderately increase the main fringe loop θ_m values. Correspondingly the θ value near the crack tip where the

principal tensile stress in largest shifts from the static analysis location of 60° to a larger angle. Progressive crack extension occurs by the forming and joining of advance separations. It is natural to associate the roughness of flat tensile fracturing, which increases with increase of crack speed, with the tendency of advance separations to form out-of-plane relative to the average plane of the crack. A second aspect of the dynamic stress field which is relevant to the same line of thought is the existence of a region ahead of the crack tip within which the largest tension is more nearly parallel to x than parallel to y . Within this region, the expected orientation of a planar type advance separation would be unfavorable for purposes of the joining action of progressive fracturing. This feature also becomes larger in terms of size and principal stress ratio with increase of crack speed. These tendencies toward increase of fracture roughness, coupled with the increase with K of the fracture process zone, lead to crack division at large enough values of K and crack speed. Depending upon the size of the fracture process zone, the above roughening tendencies can be reduced by negative σ_{ox} or emphasized by a positive σ_{ox} .

In the common applications of fracture mechanics, one assumes that crack extension behavior is governed by a single parameter. The test specimen crack tip region is assumed to model the service component crack tip region if the parameter K (or J) is the same for each. However the validity of this method of model testing depends upon the size of the fracture process zone relative to the size of the singularity zone dominated by the single parameter, K (or J). The size of the singularity zone depends upon specimen geometry, dimensions (crack,

size, net ligament size, beam height, etc.), and loading. A plausible explanation for the high velocity prior to branching which was observed with center-hole explosive loading of Homalite 100 is the unusually large negative σ_{ox} value applicable to this test. For the mechanically loaded specimens of Homalite 100, the high velocity region of the \dot{a} versus K curves show enough scatter so that it is difficult to say whether variations of σ_{ox} introduce a significant data trend. However, judging from fracture surface roughness, the fracture process zone in Homalite 100 is small in comparison to that for the metallic specimens used in crack arrest toughness testing. It is concluded that singularity zone sizes for various specimen geometries and dimensions should be estimated and employed in laboratory testing.

It is of interest to note that similar conclusions are developing in studies of crack extension using elastic-plastic analysis. In a July 31, 1978 report for an EPRI project at General Electric Research Laboratory (C. F. Shih et al, Report SRD-78-116), calculations were made of the H-R-R singularity zone size associated with J for several specimen geometries. It was concluded that the singularity zone size was substantially larger for notched-bend and compact specimens than for center-cracked specimens. This was thought to furnish a plausible explanation for the tendency of the center-cracked specimen crack to turn and follow a path at an angle of about 45° to the line of the initial crack.

As a final aspect of studies by Rossmanith, thermodynamic principals applicable to fracturing were reviewed rather carefully by Rossmanith and Irwin. It was concluded that, if values of \dot{a} and K are

measured for steady continuing crack extension, with only moderate acceleration (negative or positive), a graph of \dot{a} versus \dot{L} should not possess a negative slope. It was noted that a vertical low velocity stem in a graph of \dot{a} versus K implies a positive slope of \dot{a} versus \dot{L} due to the trend with crack speed of the proportionality constant between K^2 and \dot{L} .

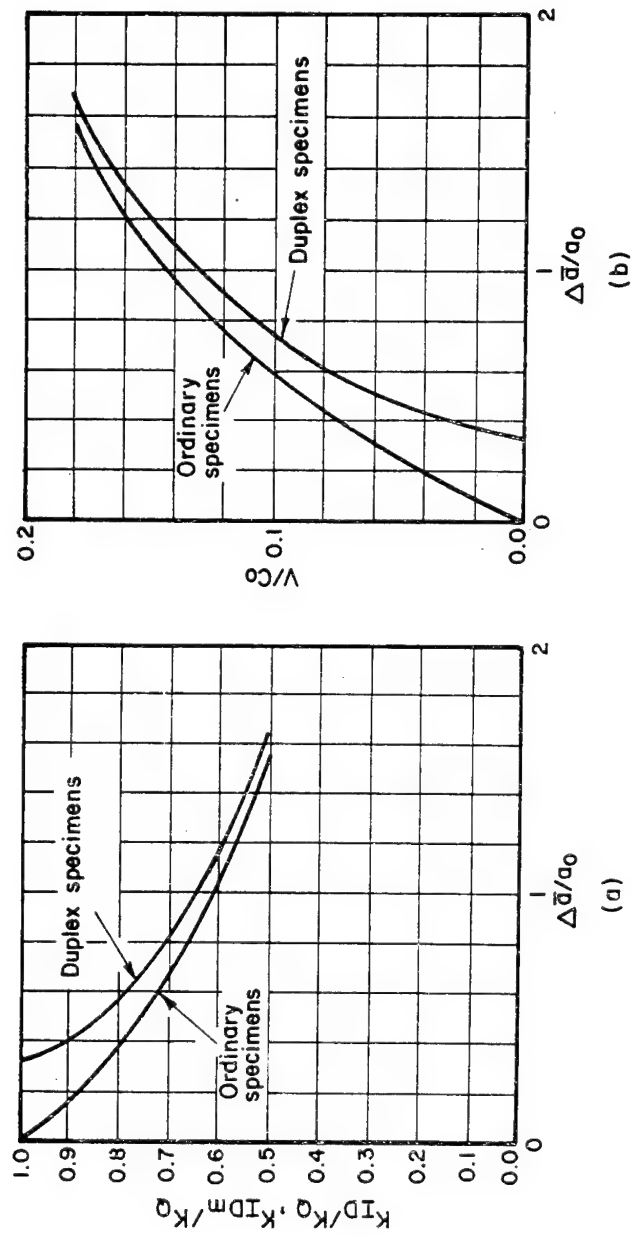


Fig. 2.1A Reference curves for the R-DCB specimen (after BCL)

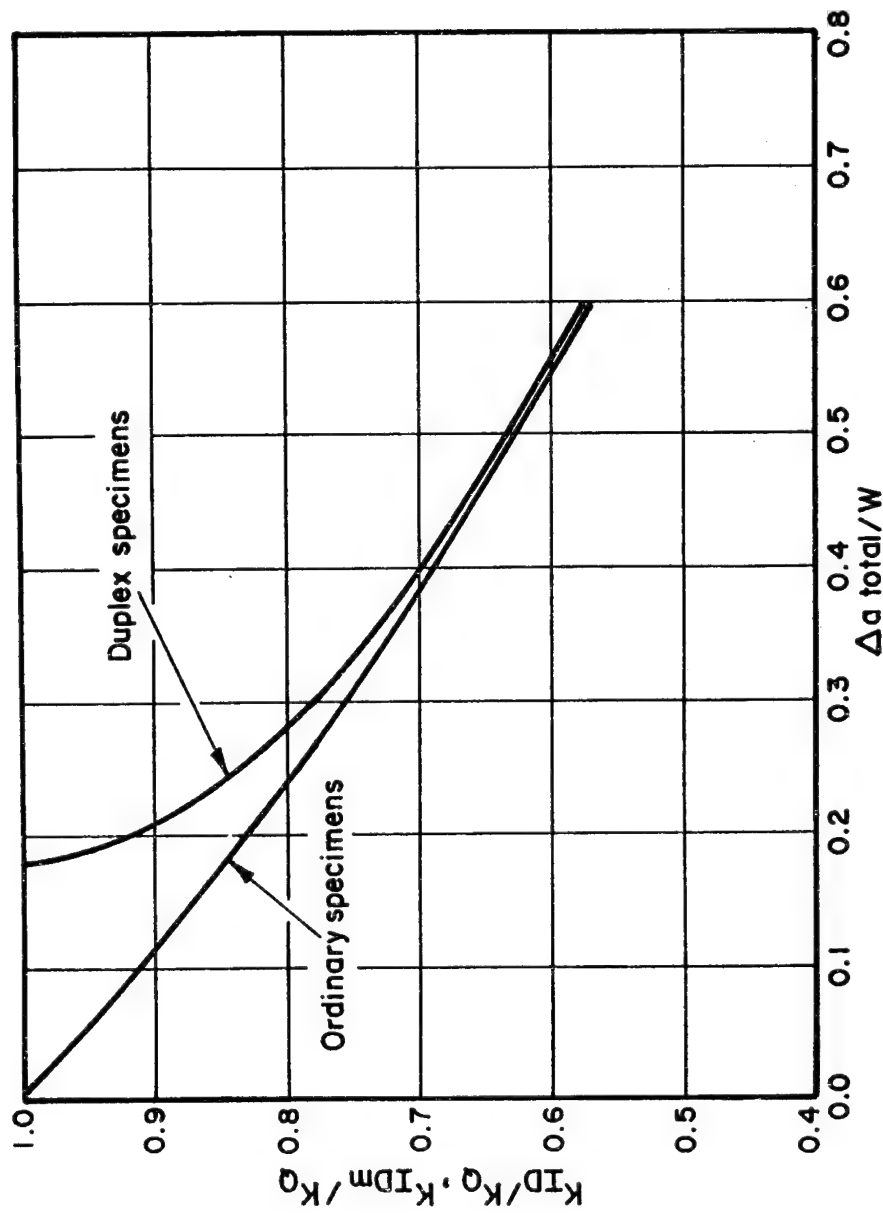


Fig. 2.1B1 Reference curves for the CT specimen (after BCL)

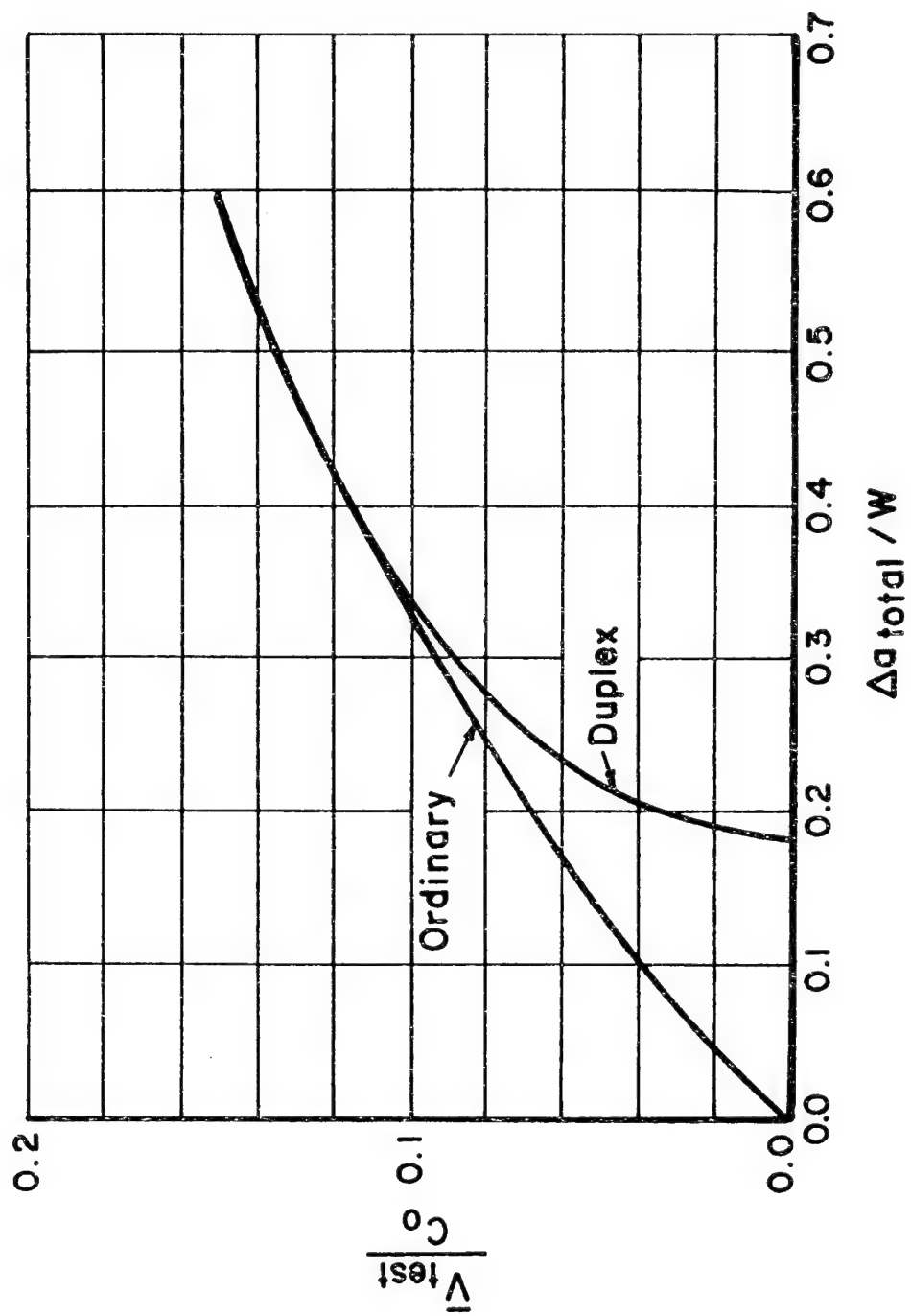


Fig. 2JB2 Reference curves for the CT specimen (after BCL)

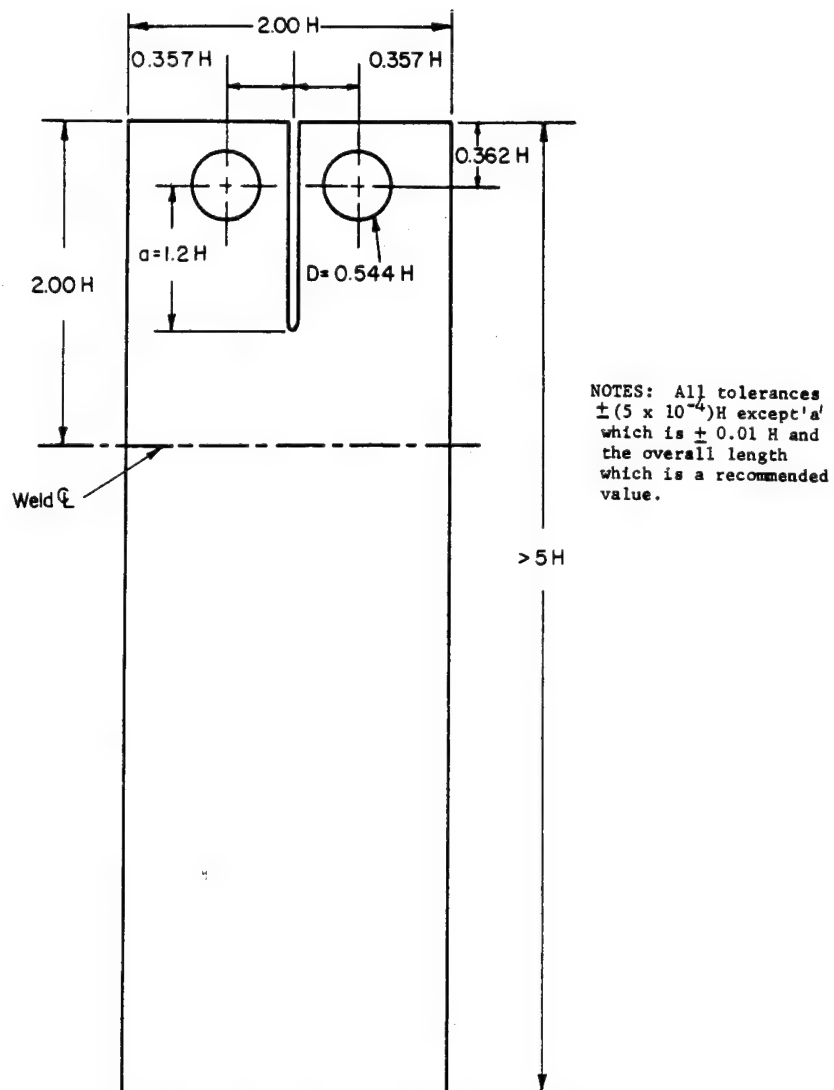


Fig. 2.2 Geometry of the R-DCB specimen

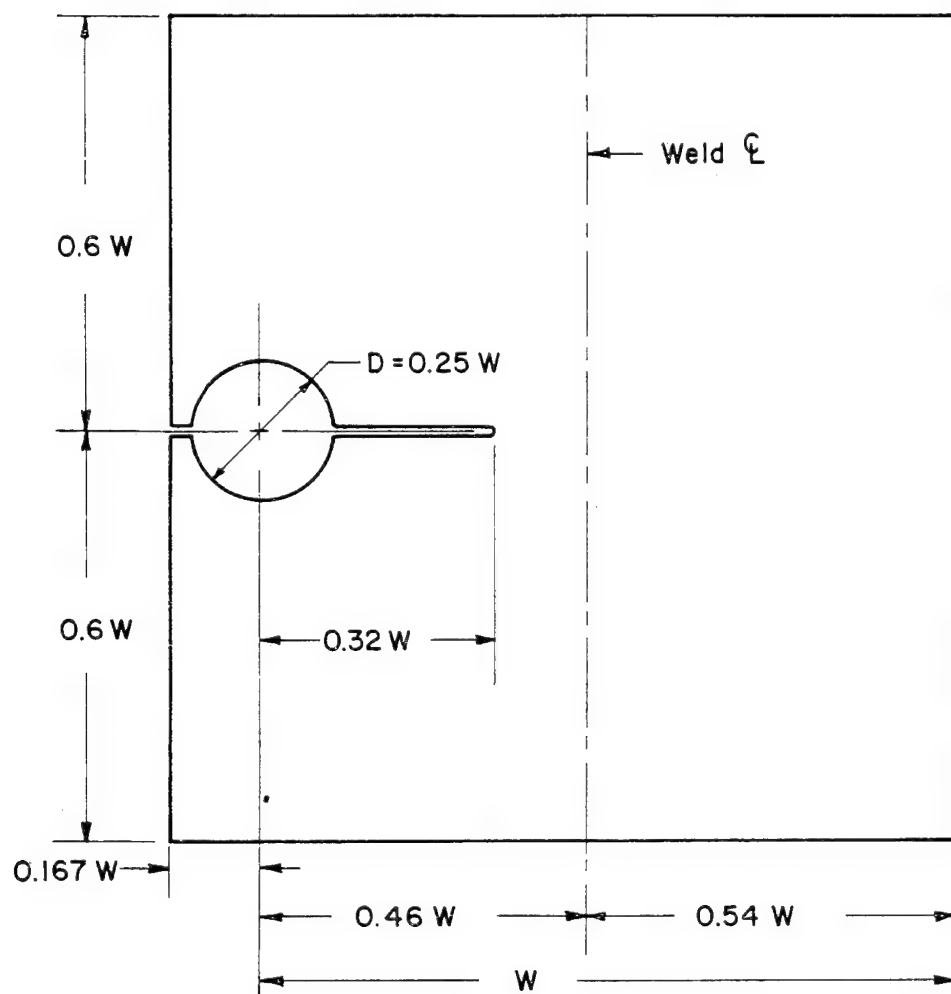


Fig. 2.3 Geometry of the CT specimen

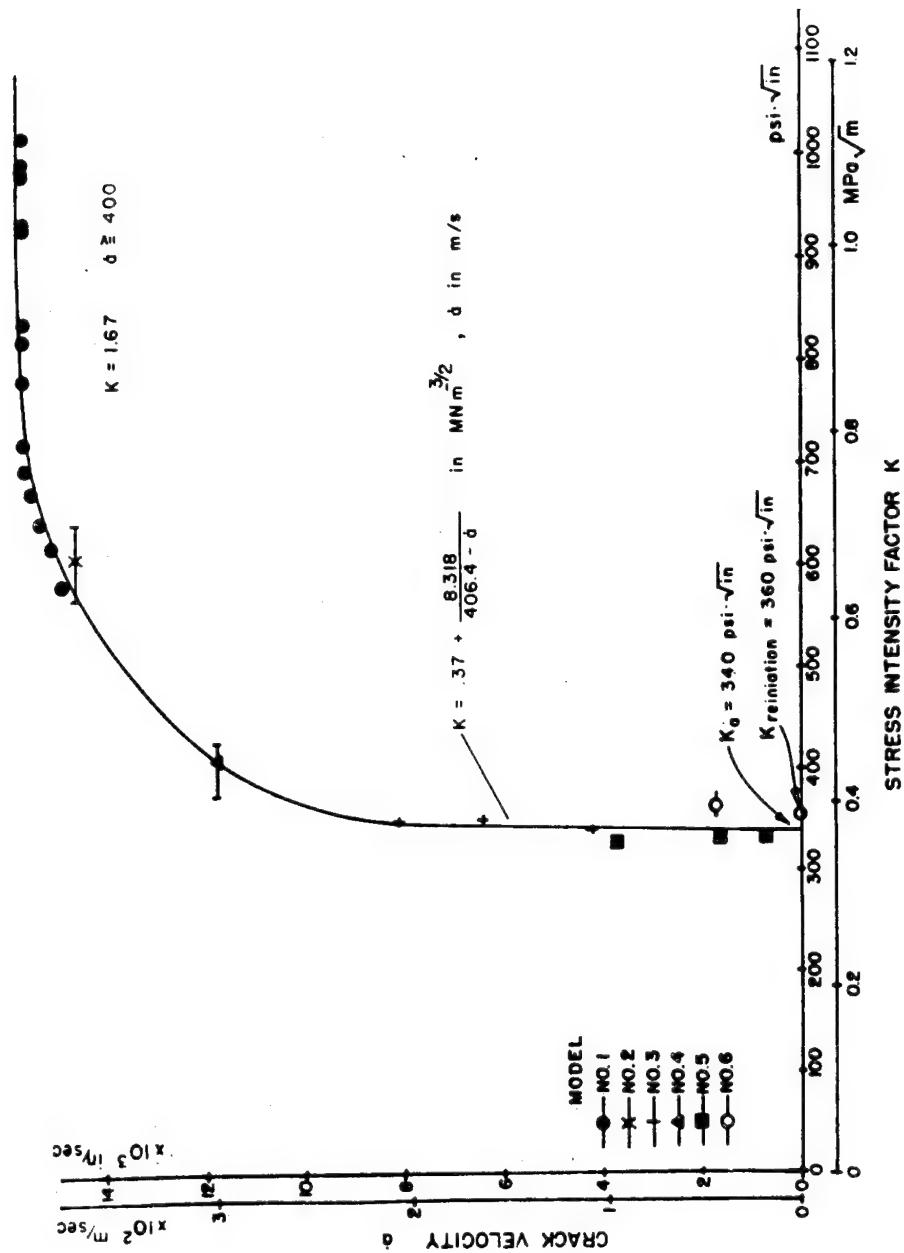


Fig. 2.4 The \dot{a} - K relation for Homalite 100

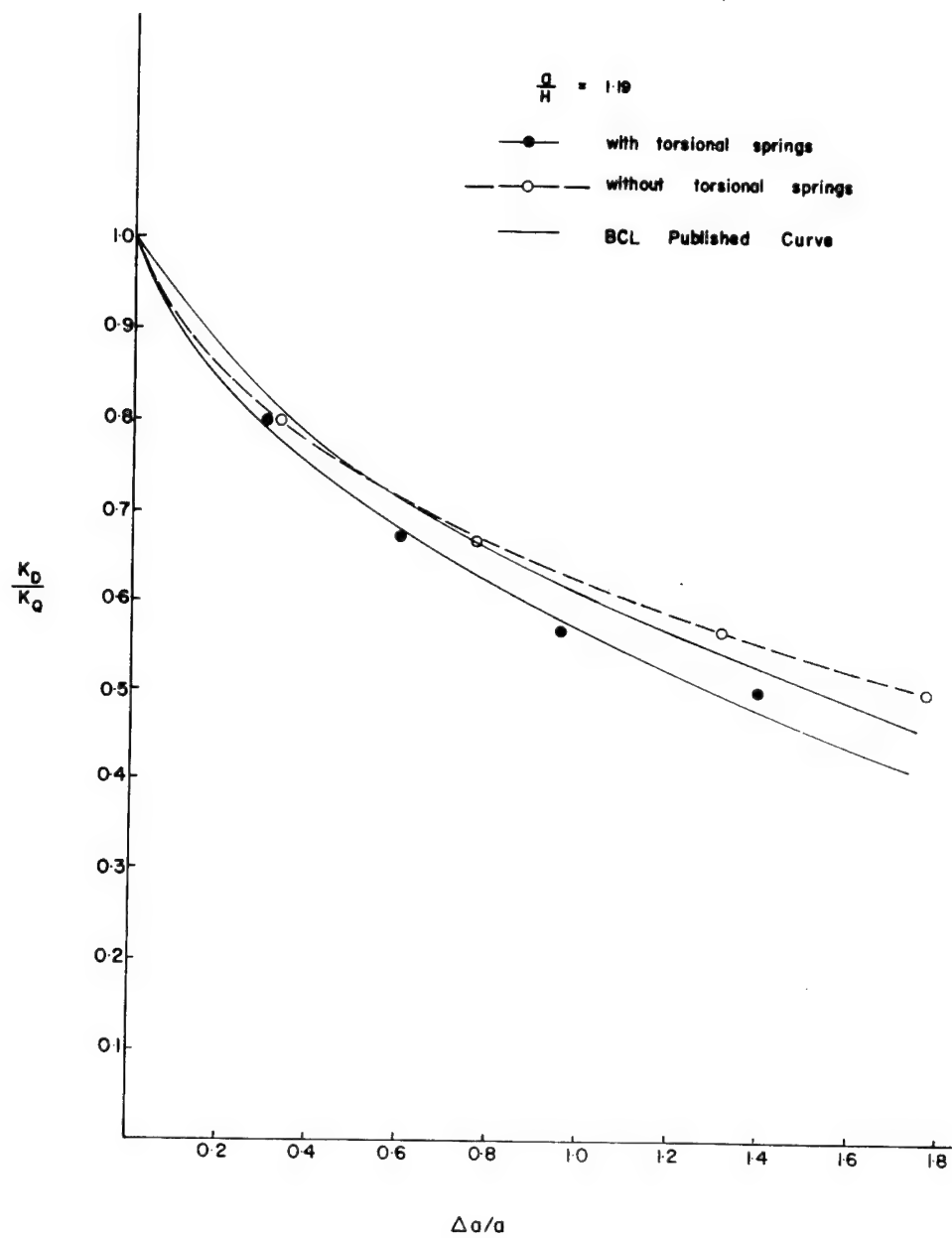


Fig. 2.5A Comparison of the BCL reference curves with and without \dot{a} -K dependence, K_D/K_Q vs $\Delta a/a_0$

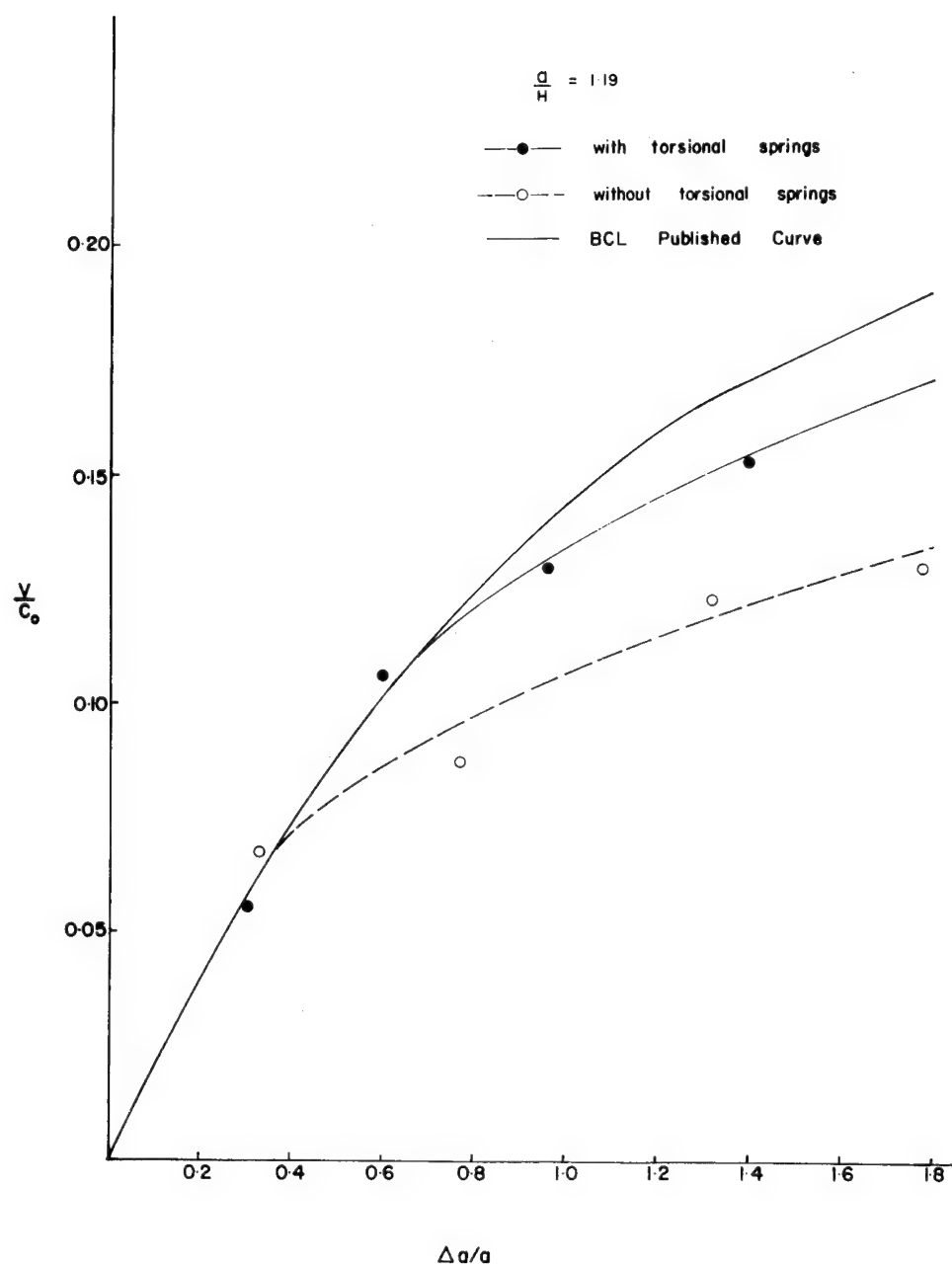


Fig. 2.5B Comparison of the BCL reference curves with and without Γ type \dot{a} -K dependence, V/c_0 vs $\Delta a/a_0$

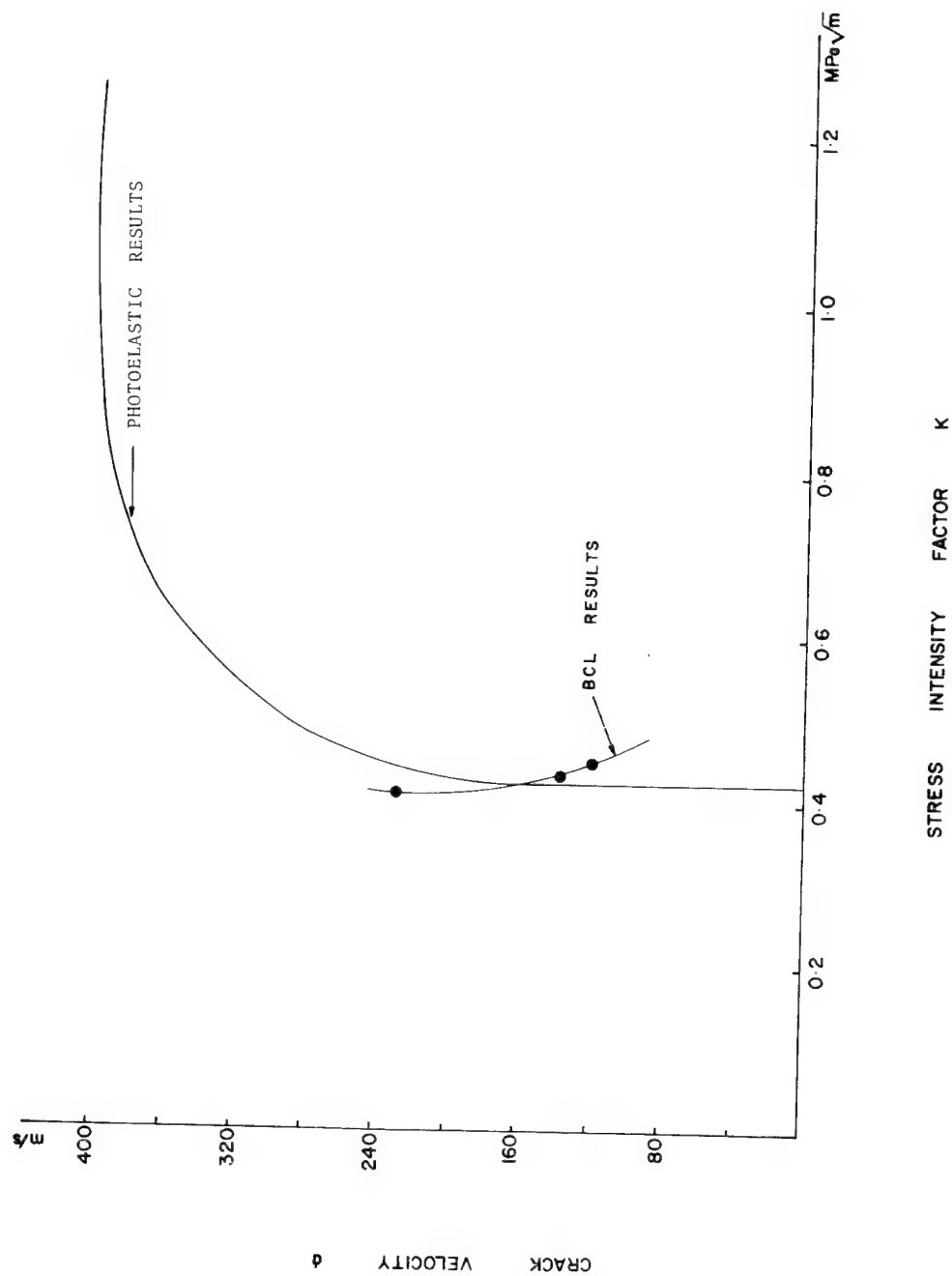
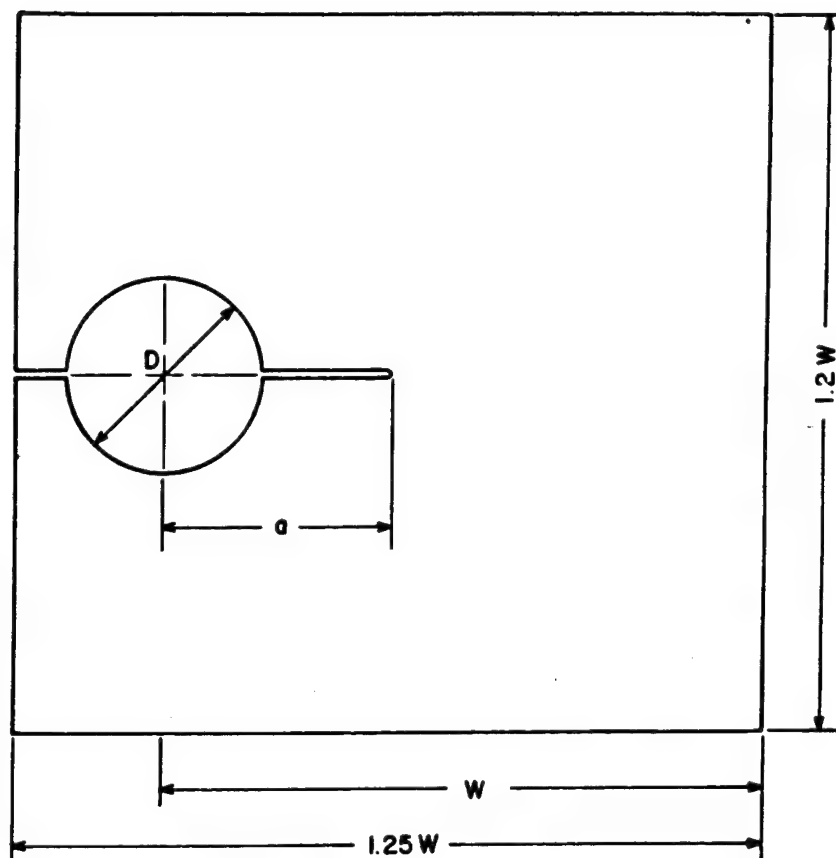


Fig. 2.6 Comparison of \dot{a} -K relation obtained using the BCL reference curve with results from photoelastic experiments. Homalite 100.



$$W = 203\text{mm} \quad a = (0.3-0.5)W$$

$$D = 76\text{mm}$$

Fig. 2.7 Geometry of the CT specimen used at the University of Maryland.

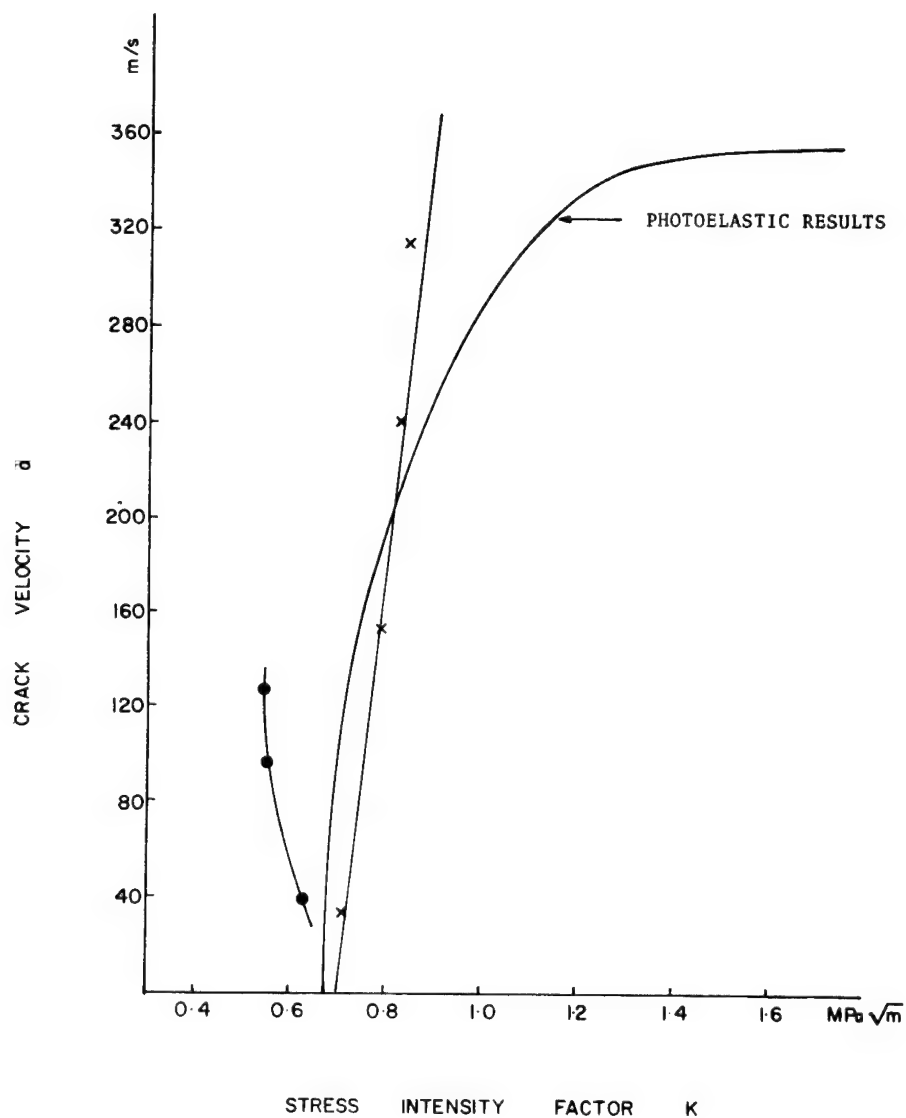


Fig. 2.8 Comparison of \dot{a} - K relation obtained using the BCL reference curve with results of photomechanics experiments. Araldite B.

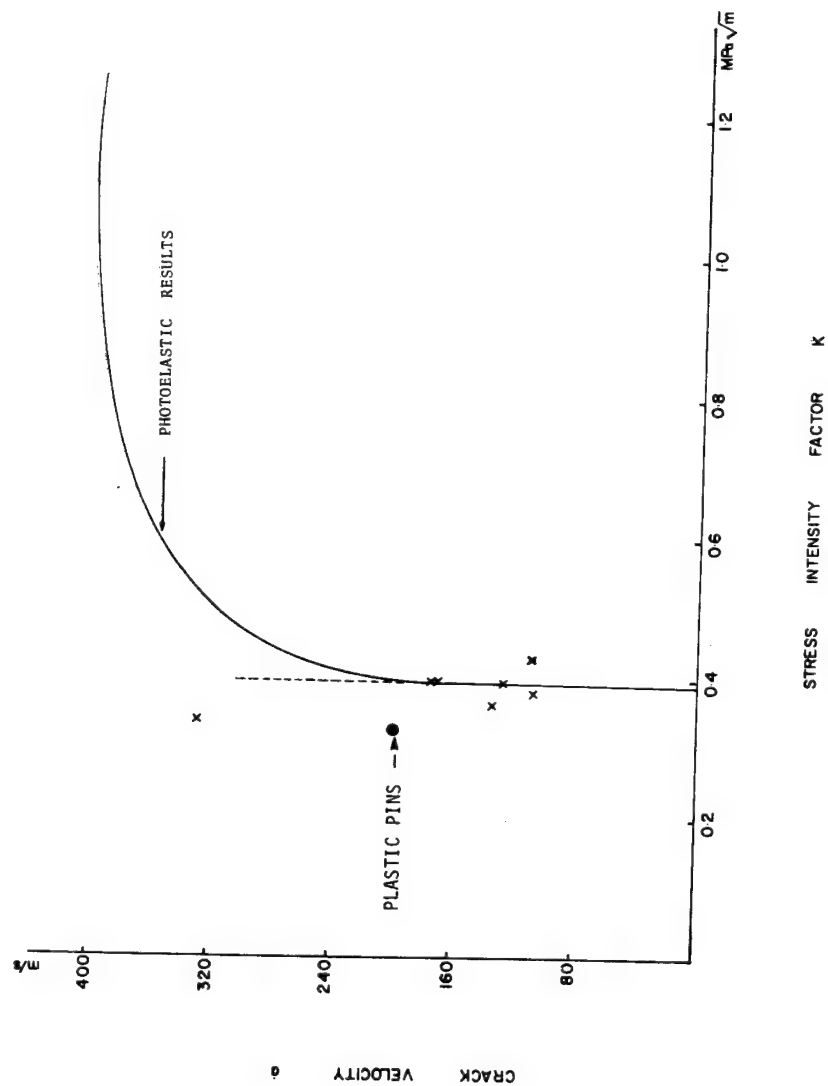


Fig. 2.9A Comparison of \dot{a} - K relation obtained using the BCL reference curve with results of photoelastic experiments. Araldite B.

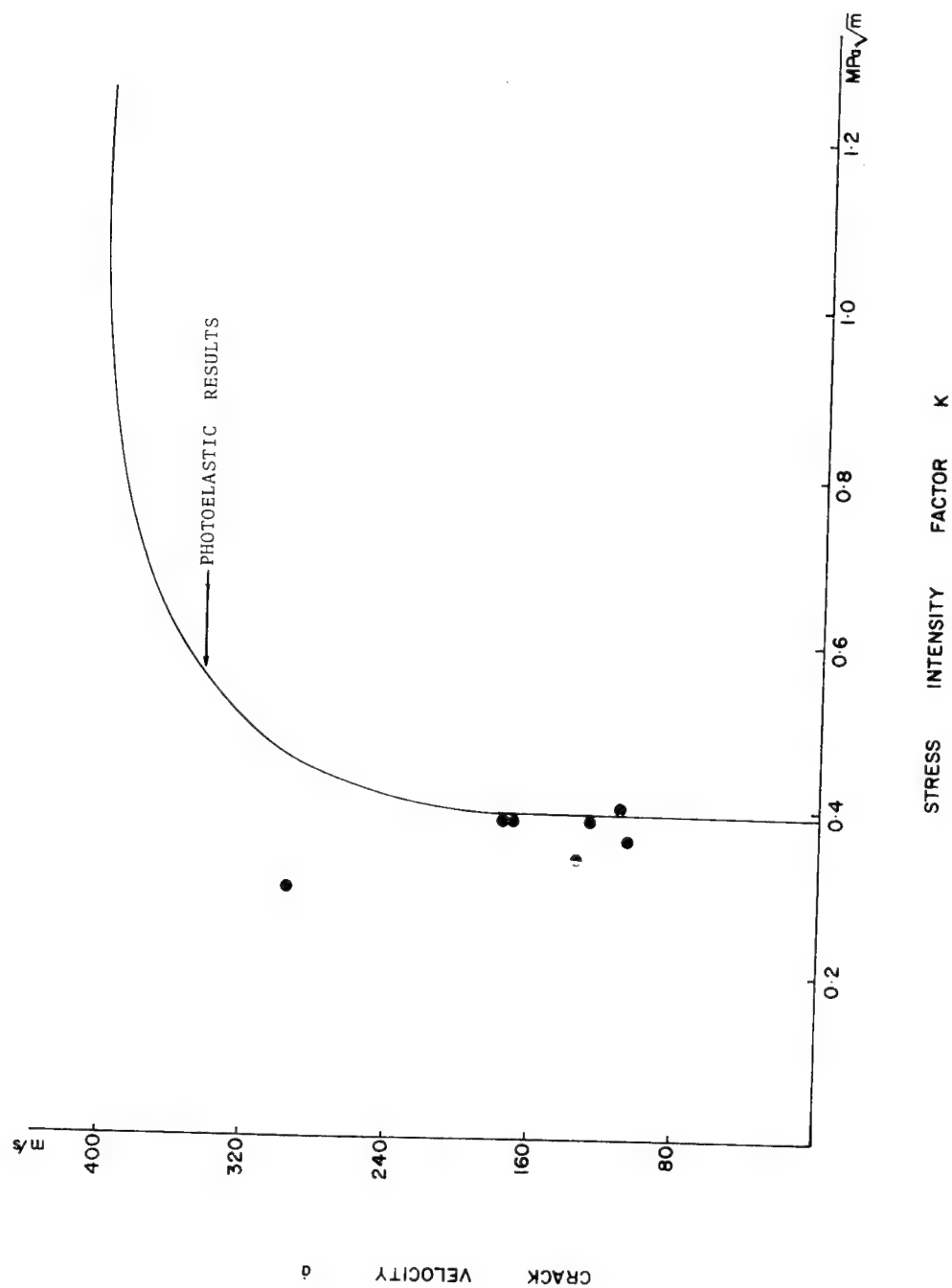


Fig. 2.9B Comparison of \dot{a} - K relation obtained using the corrected BCL Reference curve with torsional springs with results of photoelastic experiments. R-DCB Homalite 100.

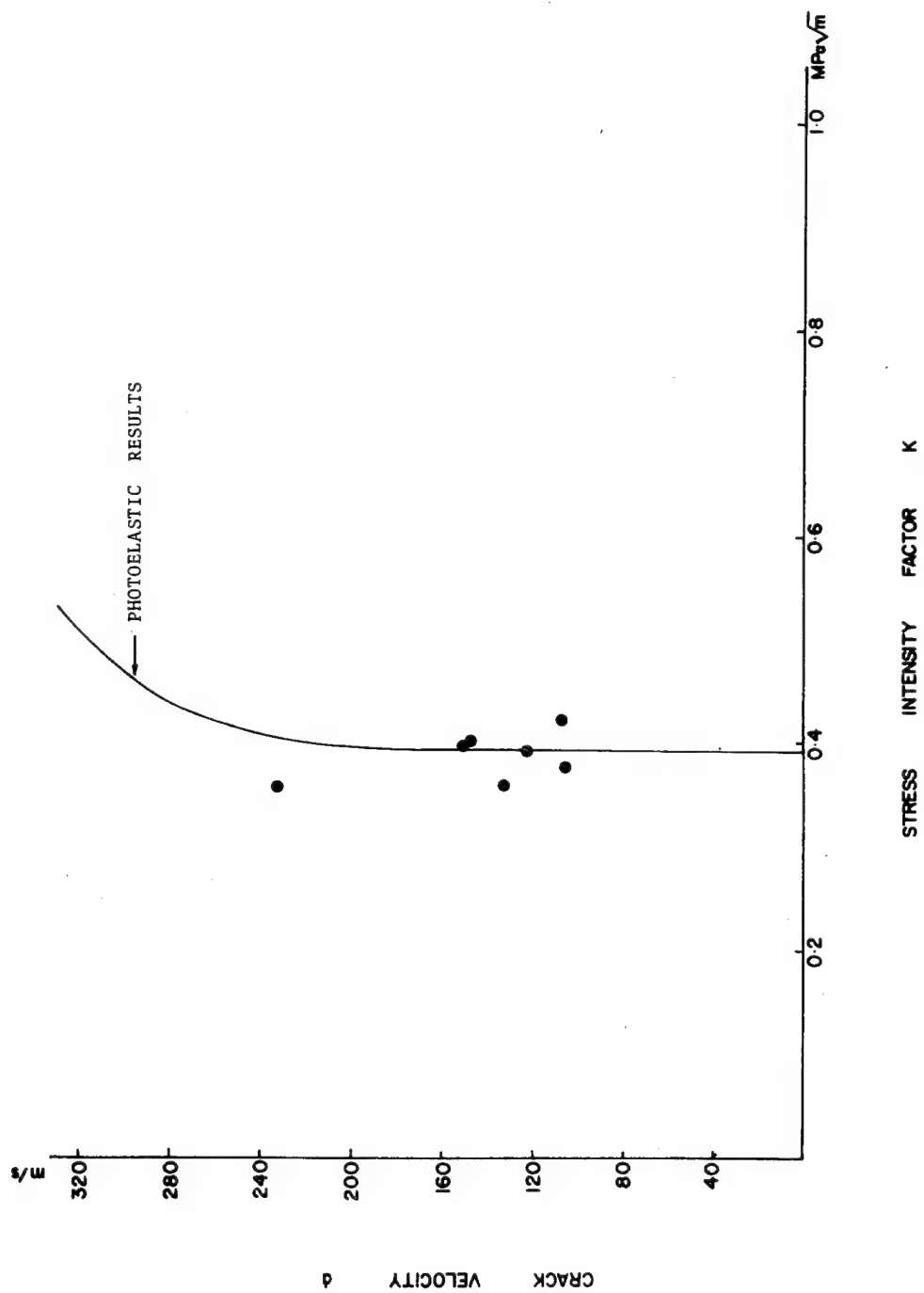
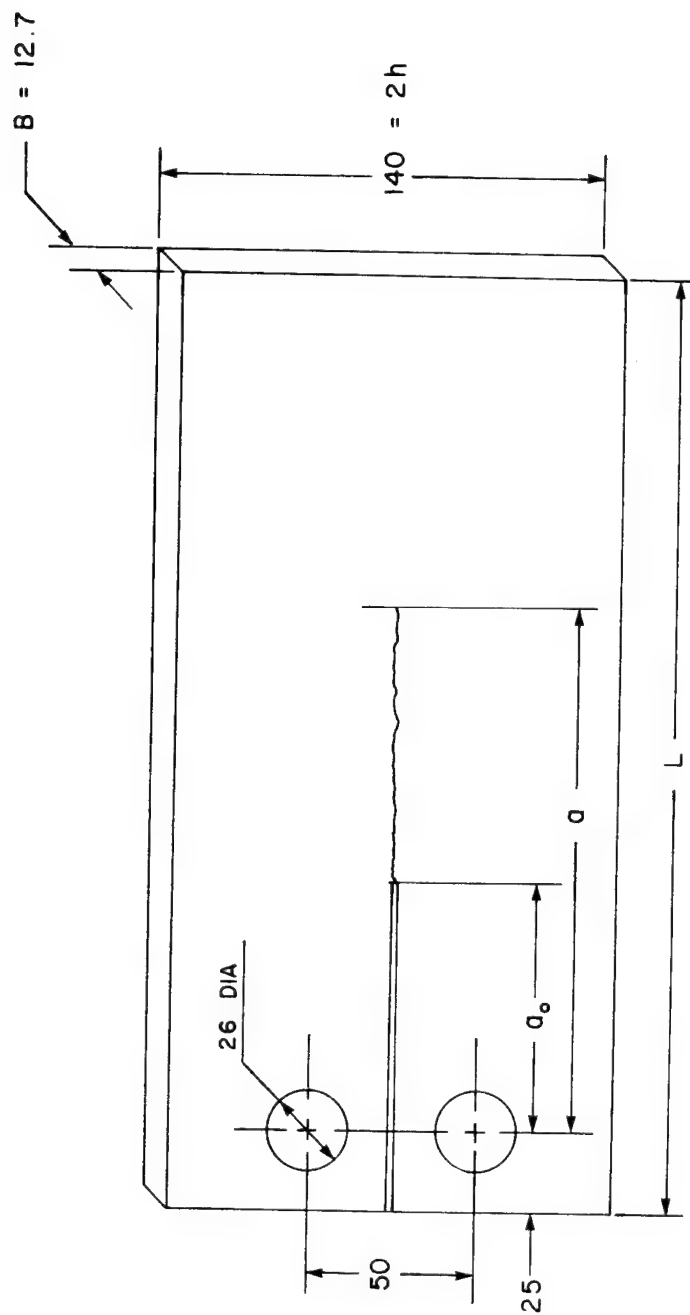


Fig. 2.9C Comparison of \dot{a} - K relation obtained using the correct BCL reference curve without torsional springs with results of photoelastic experiments. R-DCB Homalite 100.



SPECIMEN GEOMETRY

Fig. 2.10 Dimensions for the R-DCB specimen.

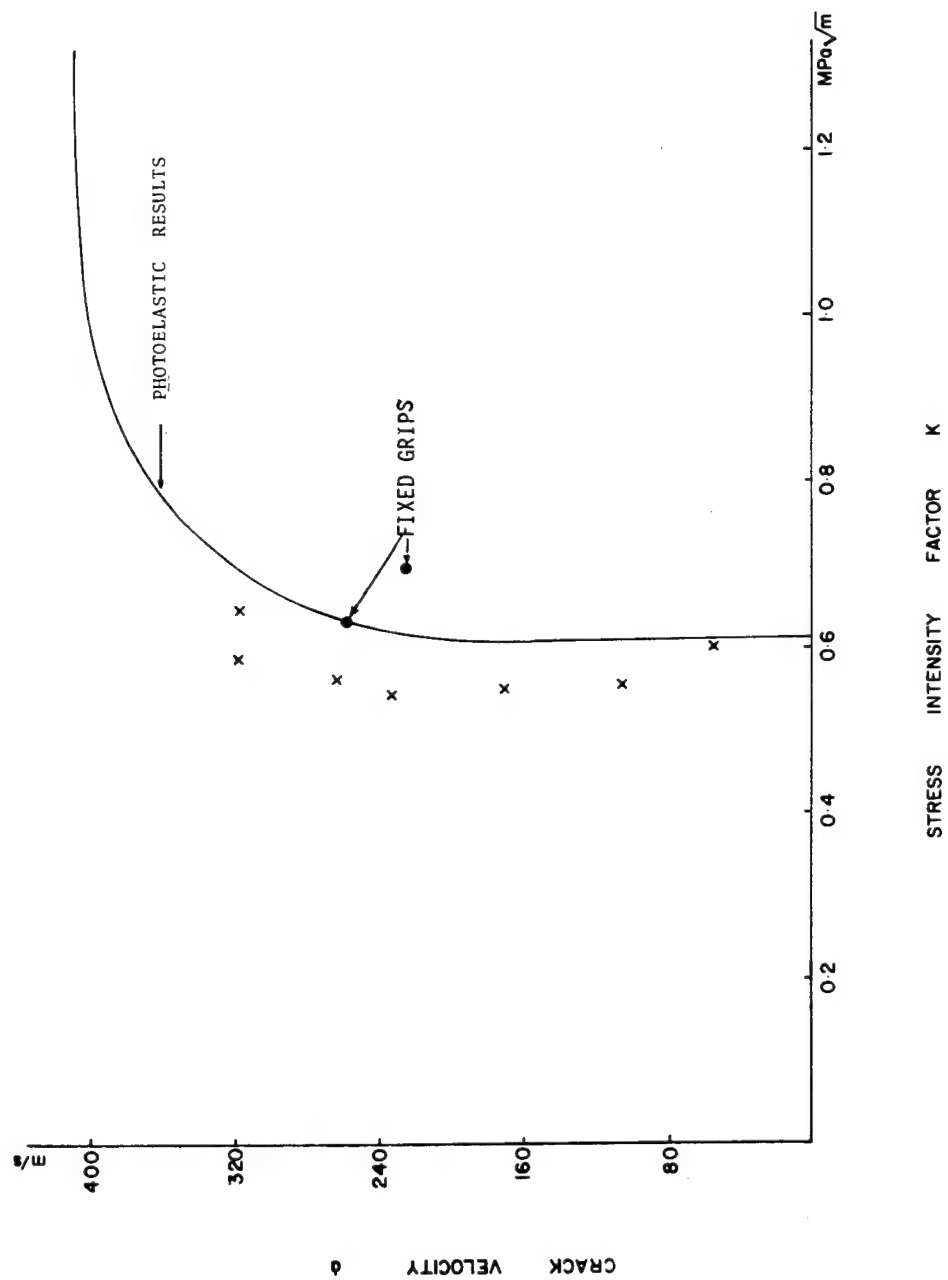


Fig. 2.11 Comparison of \dot{a} - K relation obtained using the BCL reference curve with results of photoelastic experiments. R-DCB Homalite 100.

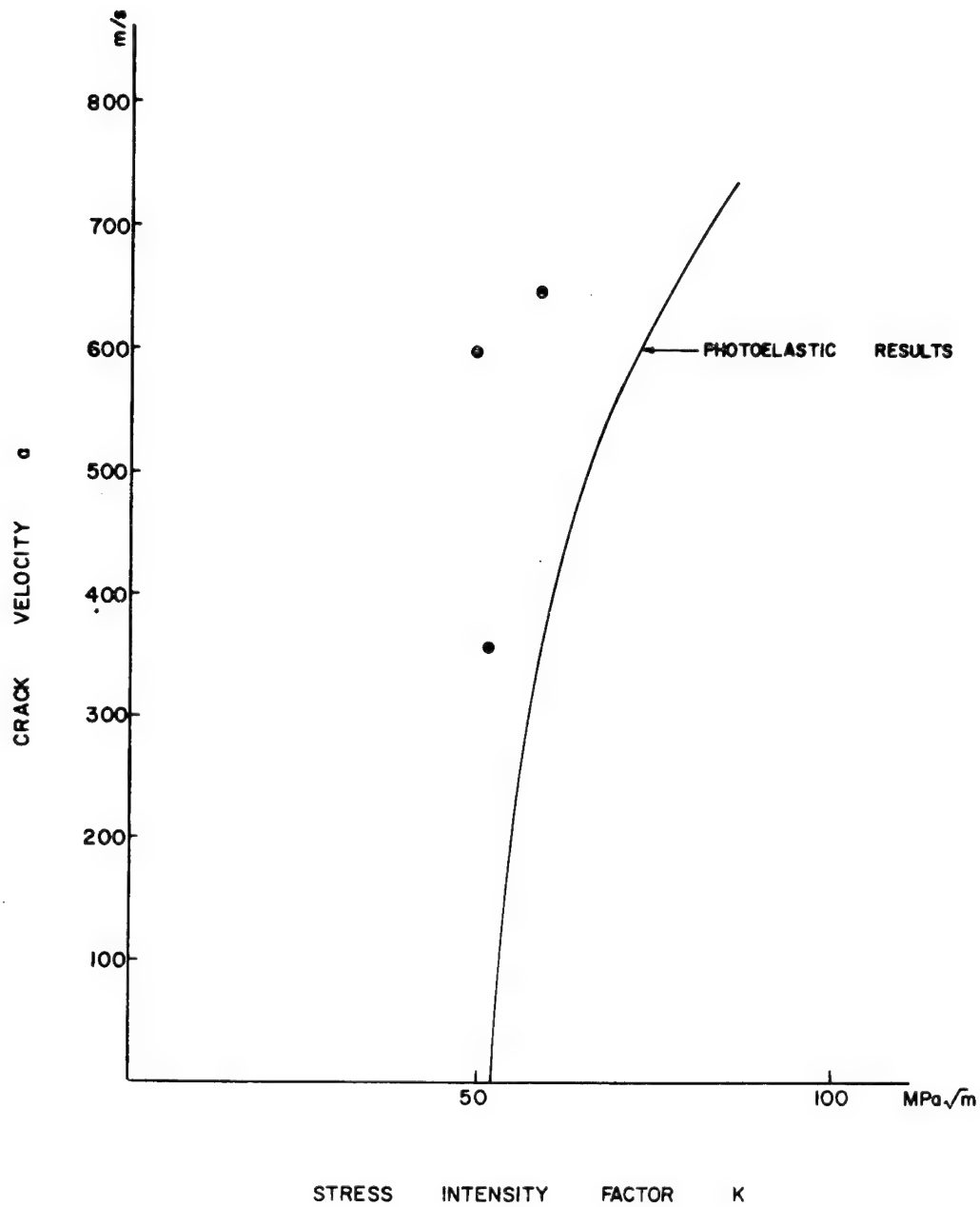


Fig. 2.12 Comparison of \dot{a} - K relation obtained using the BCL reference curve with results from birefringent coating experiments CT 4340 steel.

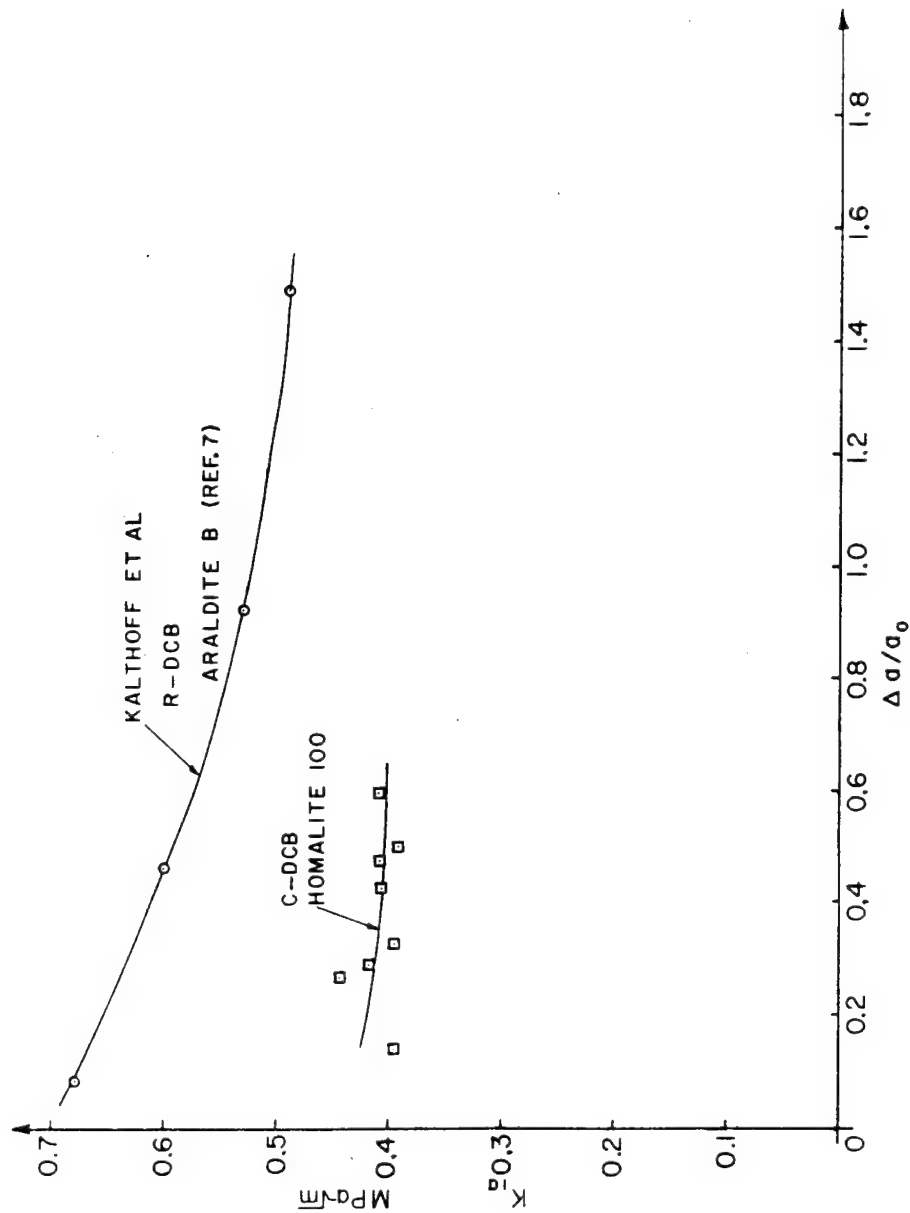


Fig. 2.13 K_{Ia} as a function of $\Delta a/a_0$ for C-DCB Specimens.

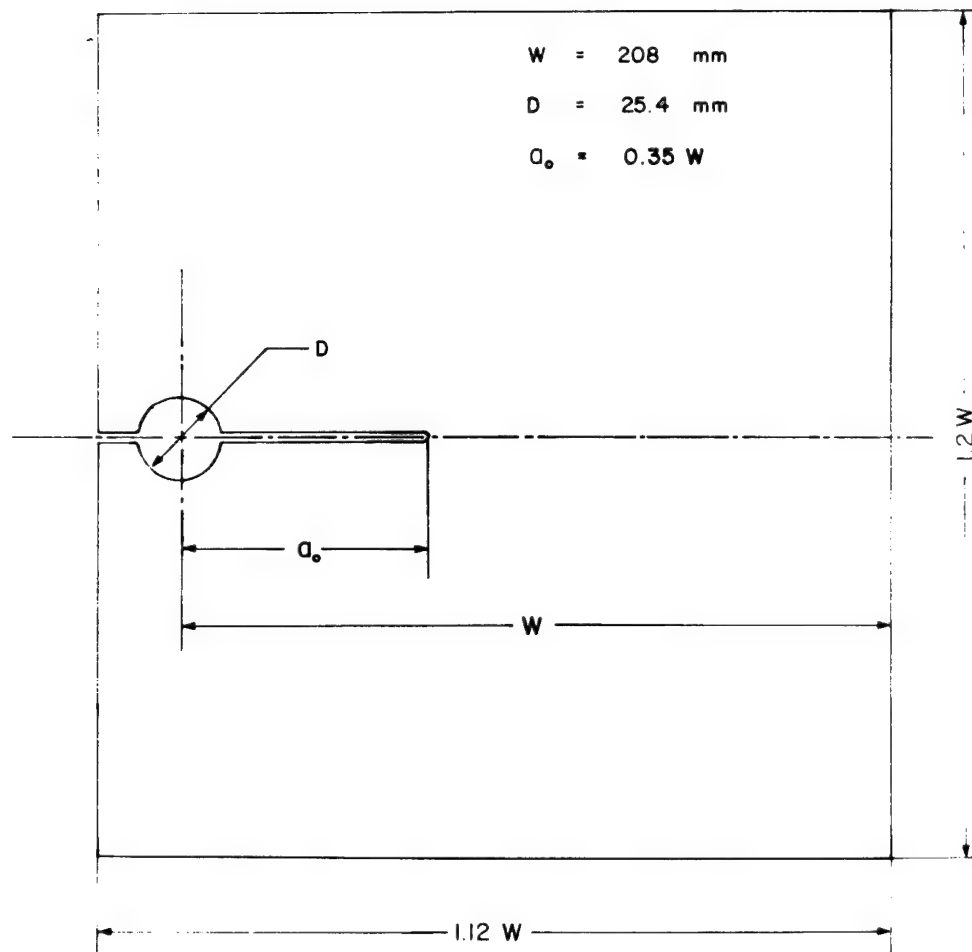


Fig. 2.14 Geometry of MRL-CS specimen.

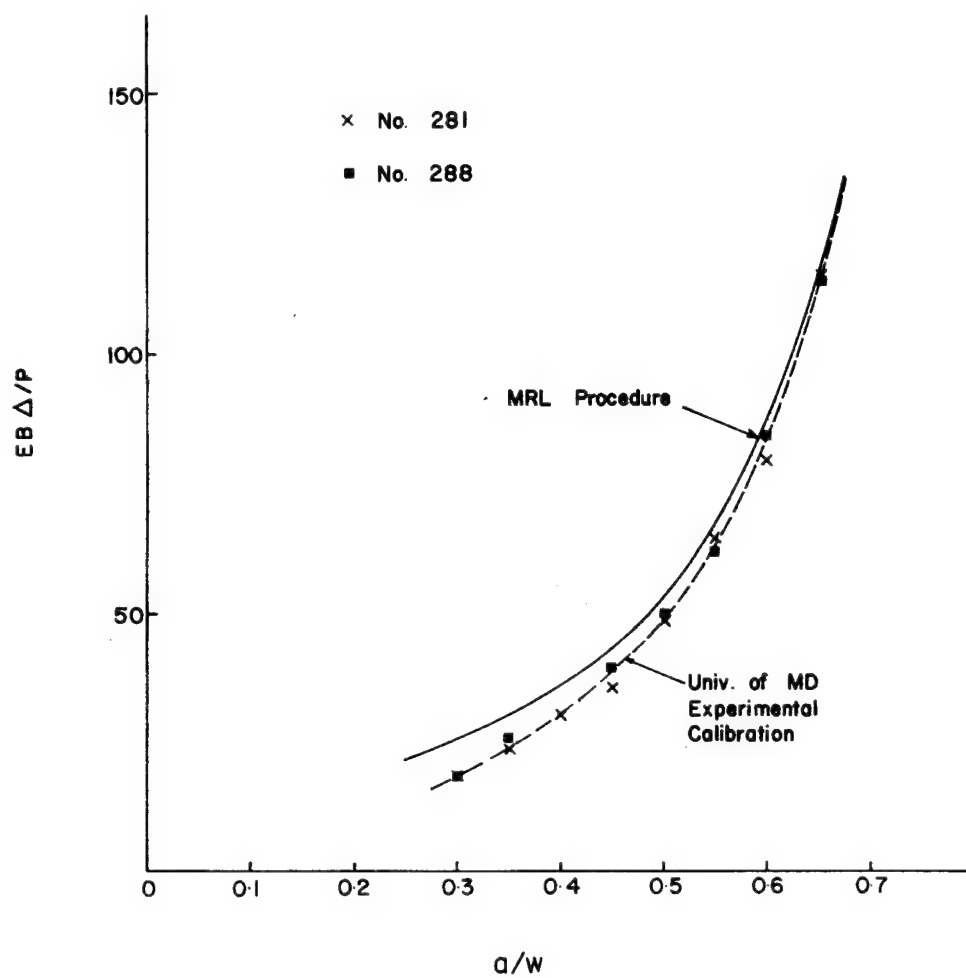


Fig. 2.15 Comparison of experimental and MRL $EB \Delta/p$ values as a function of a/W .

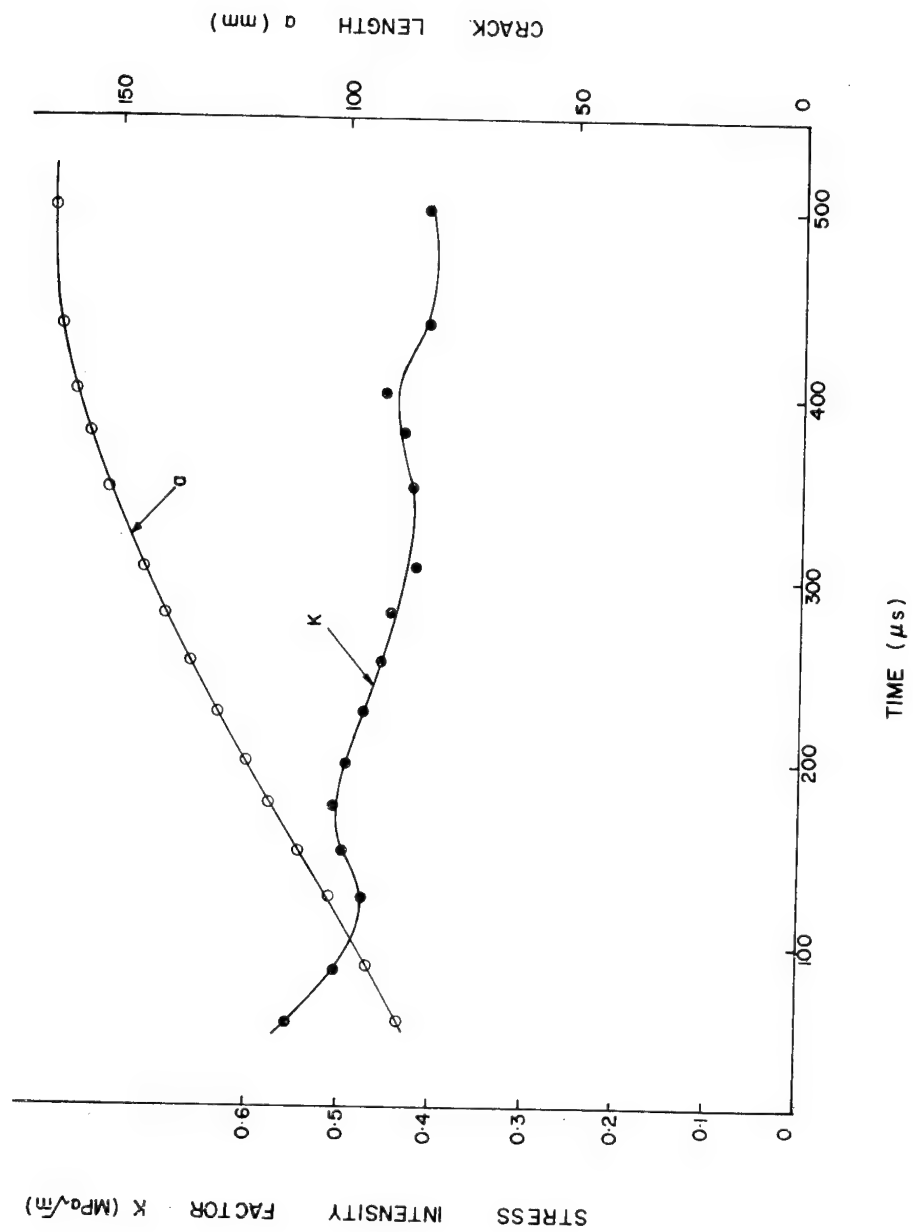


Fig. 2.16 K and a as a function of time (No. 290).

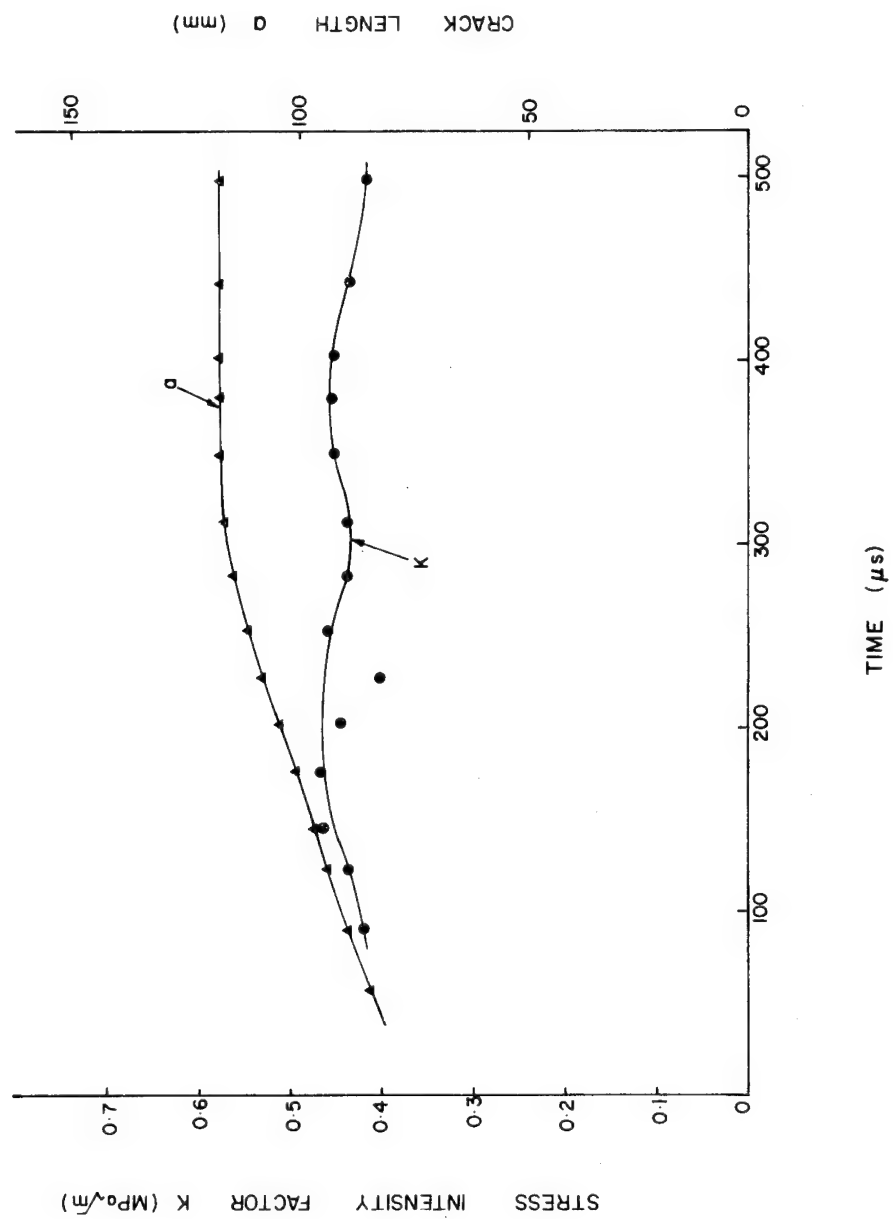


Fig. 2.17 K and a as a function of time (No. 291).

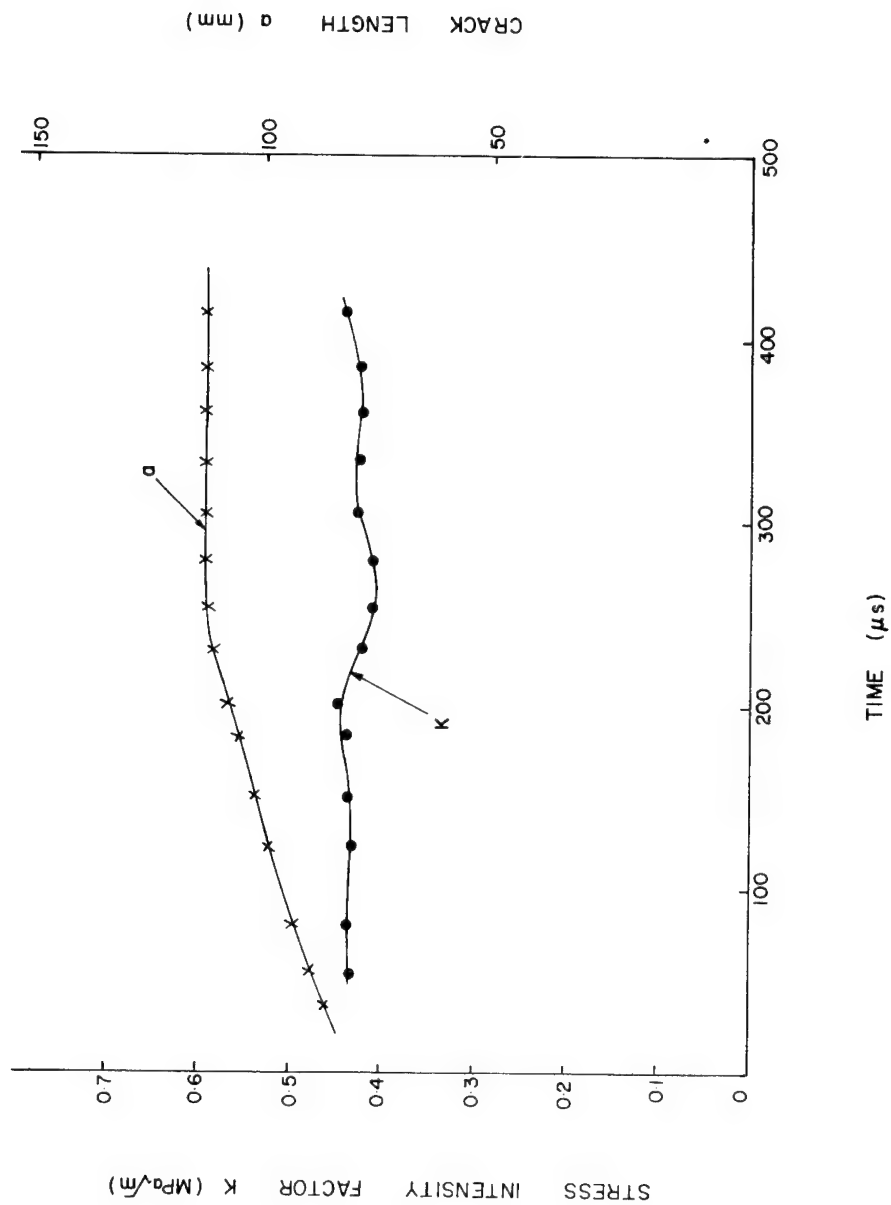


Fig. 2.18 K and a as a function of time (No. 302).

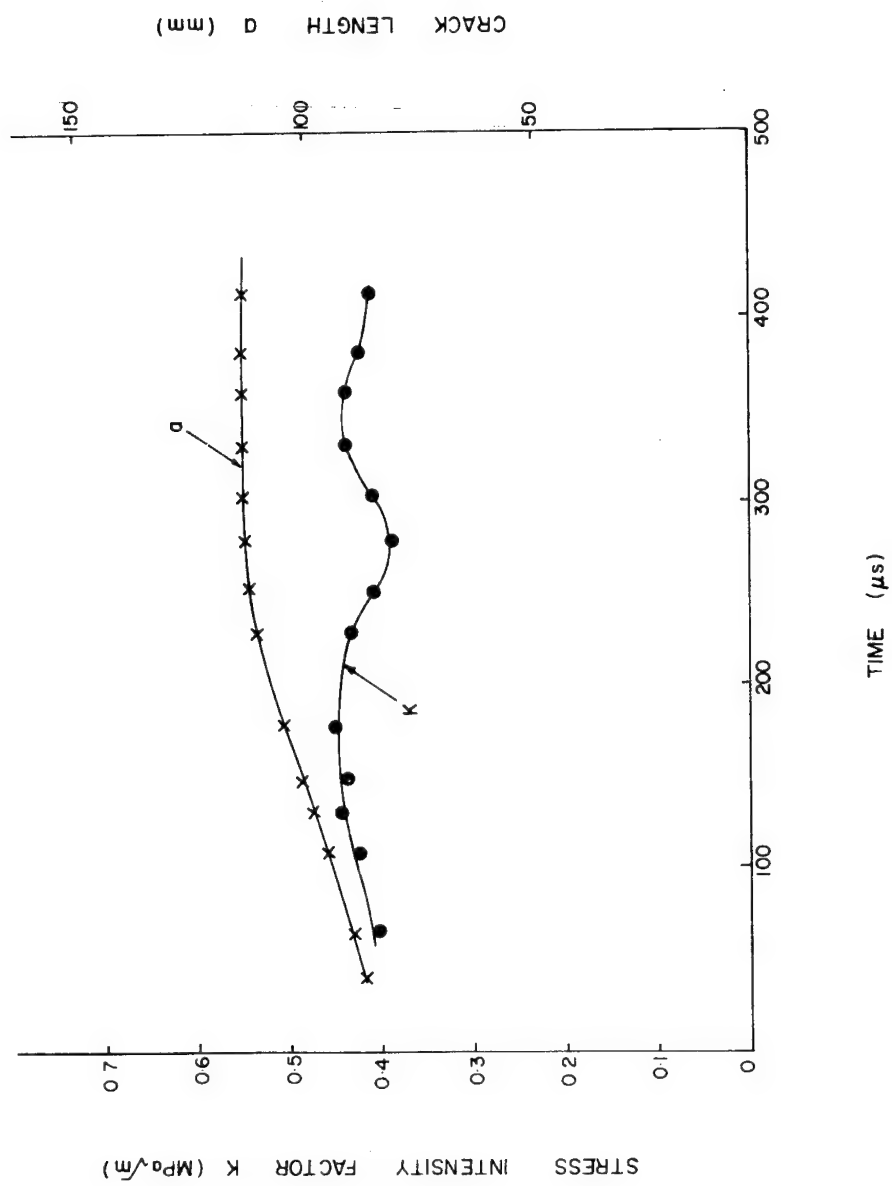


Fig. 2.19 K and a as a function of time (No. 303).

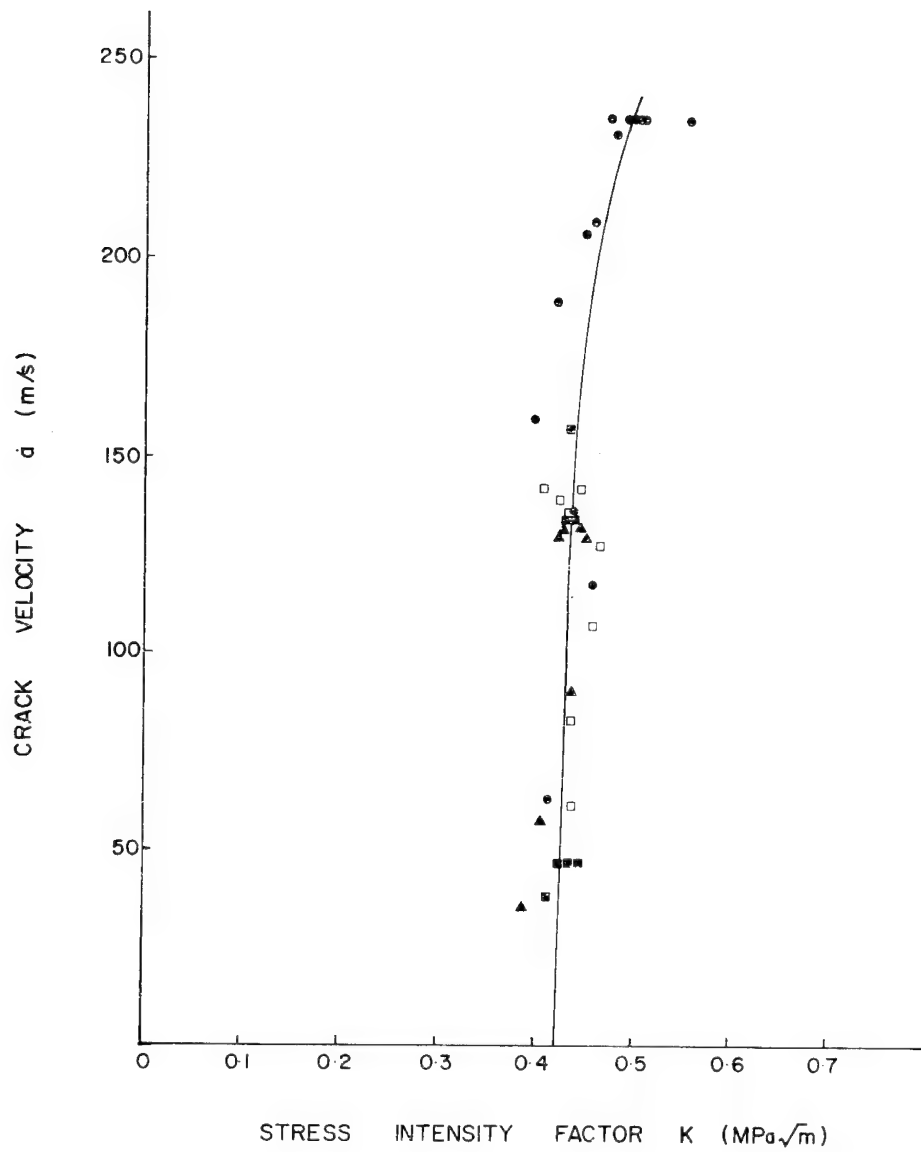


Fig. 2.20 \dot{a} vs K relationship from Transverse-Wedge-Loaded Compact Specimen of MRL Design.

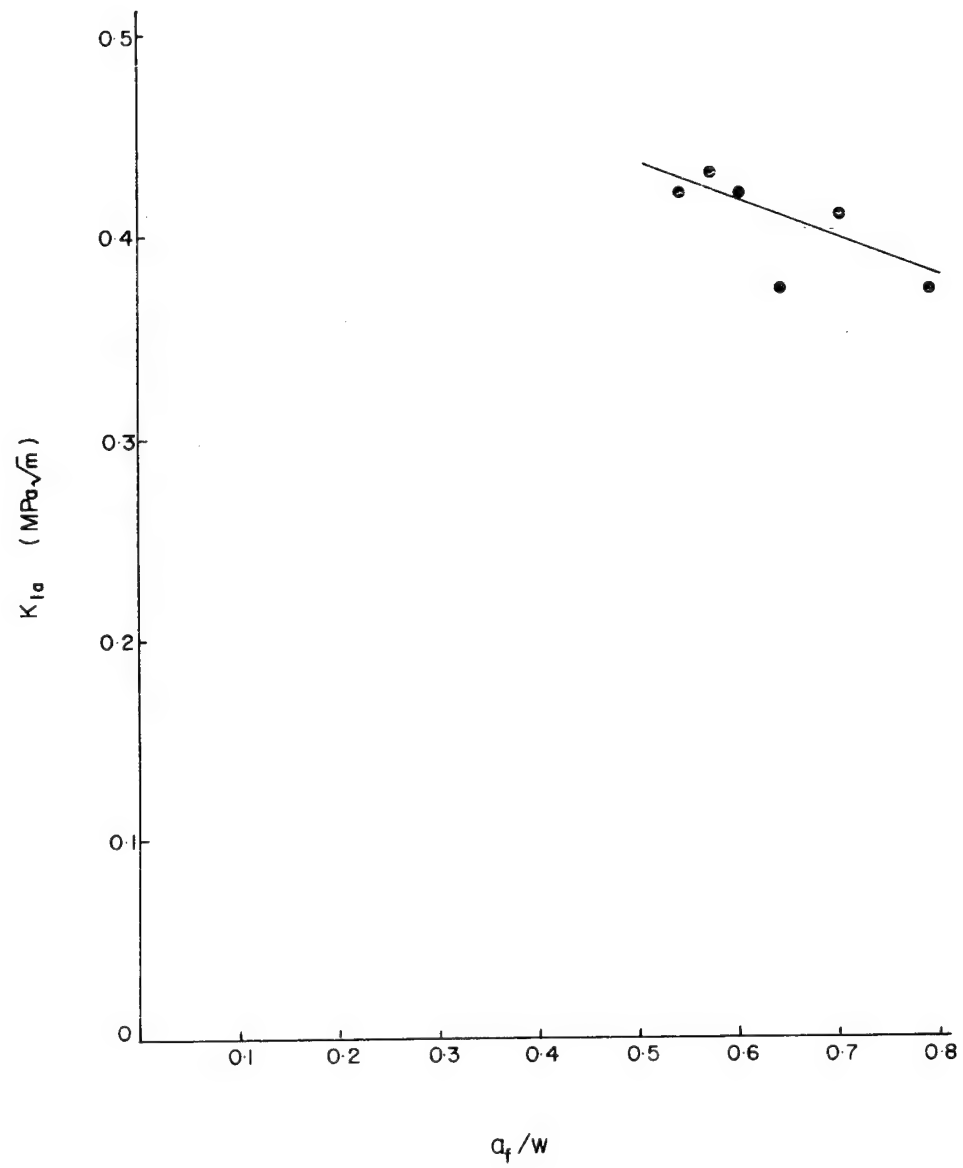


Fig. 2.21 K_{Ia} as a function of a_f/W .

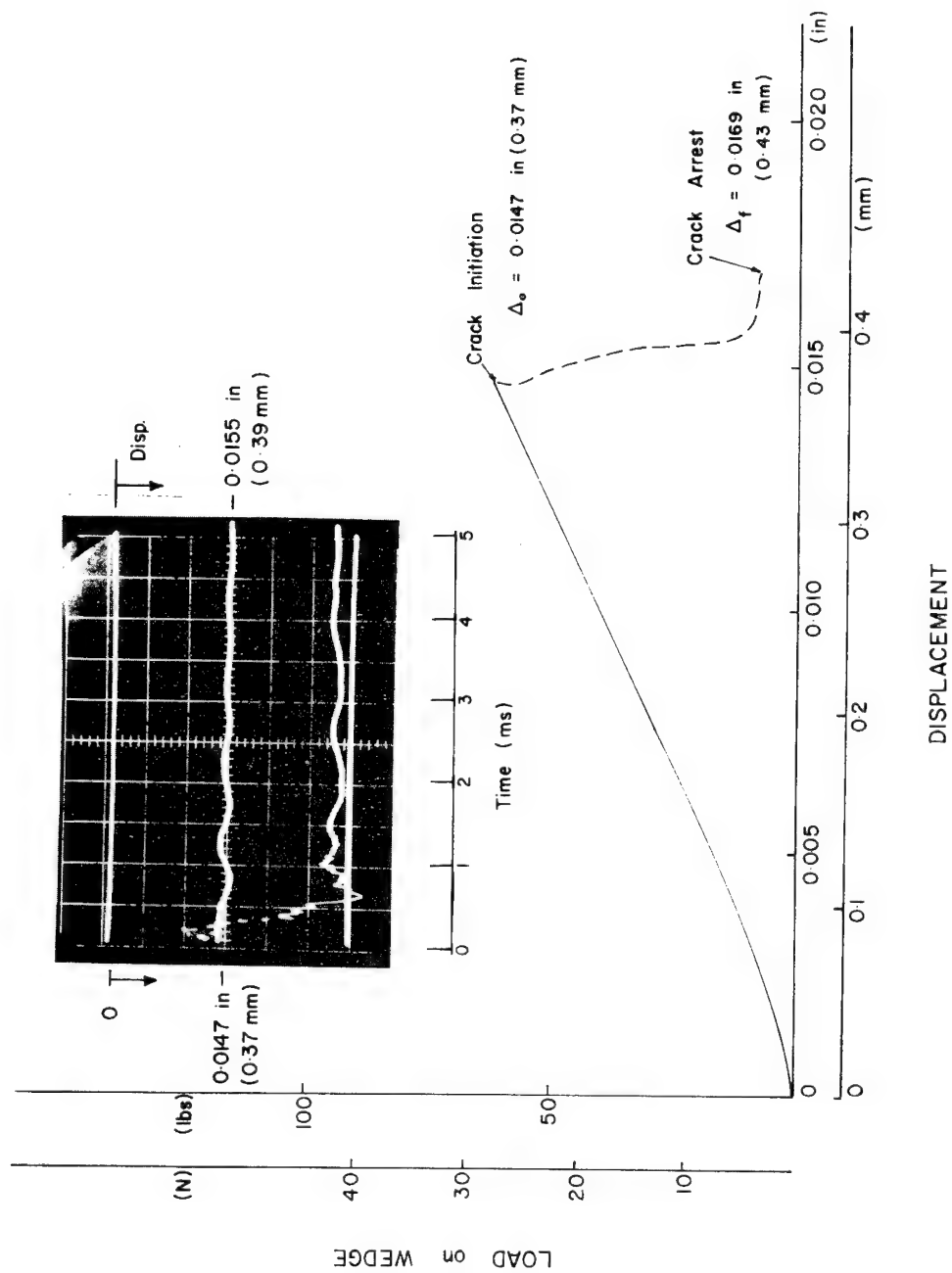


Fig. 2.22 Displacement Record during the test for MRL-TWL-CS.

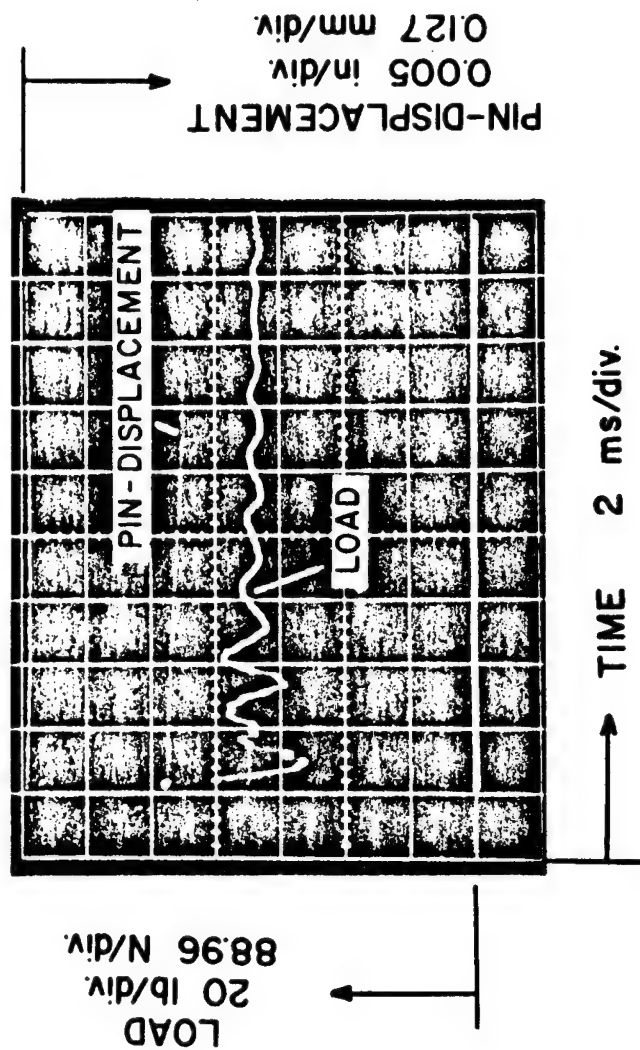


Fig. 2.23 Pin-displacement Load found as a Function of Time for T-DCB (No. 224).

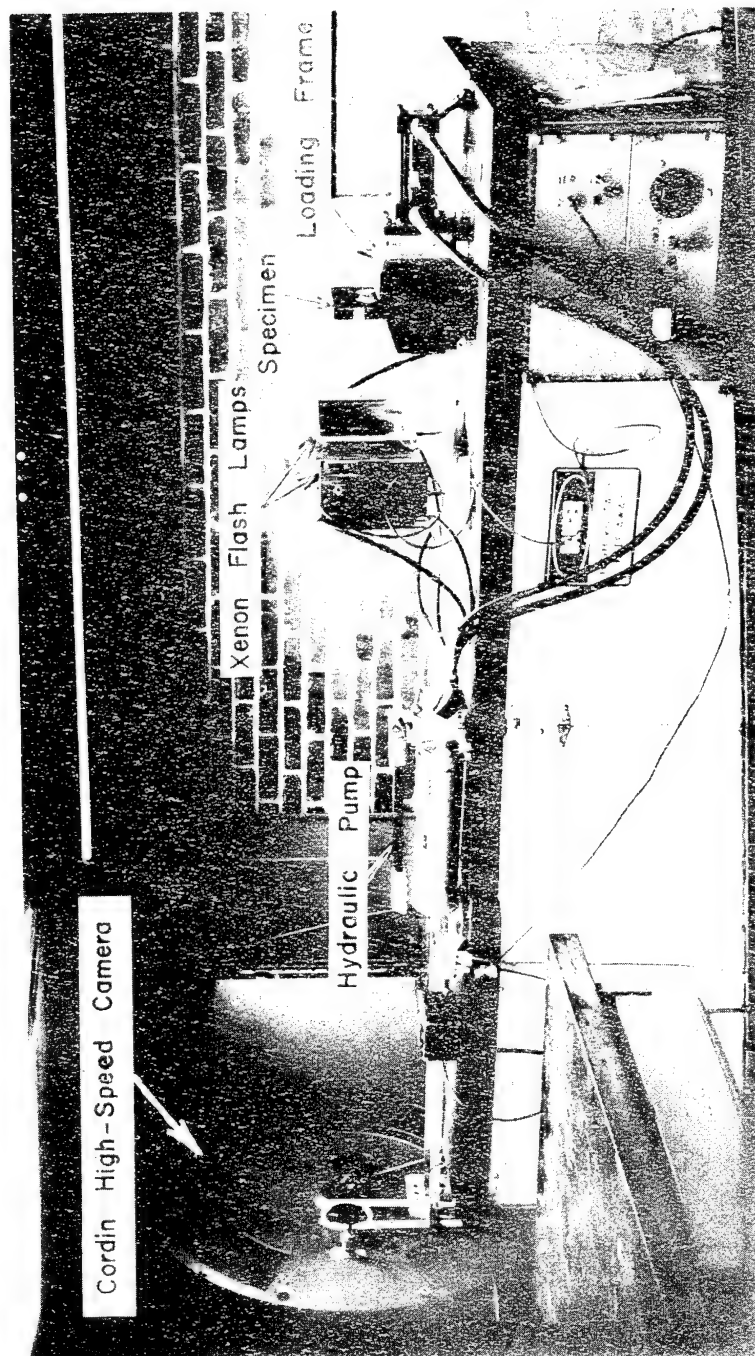


Fig. 3.1 Experimental Apparatus Used to Photograph Birefringent Coatings.

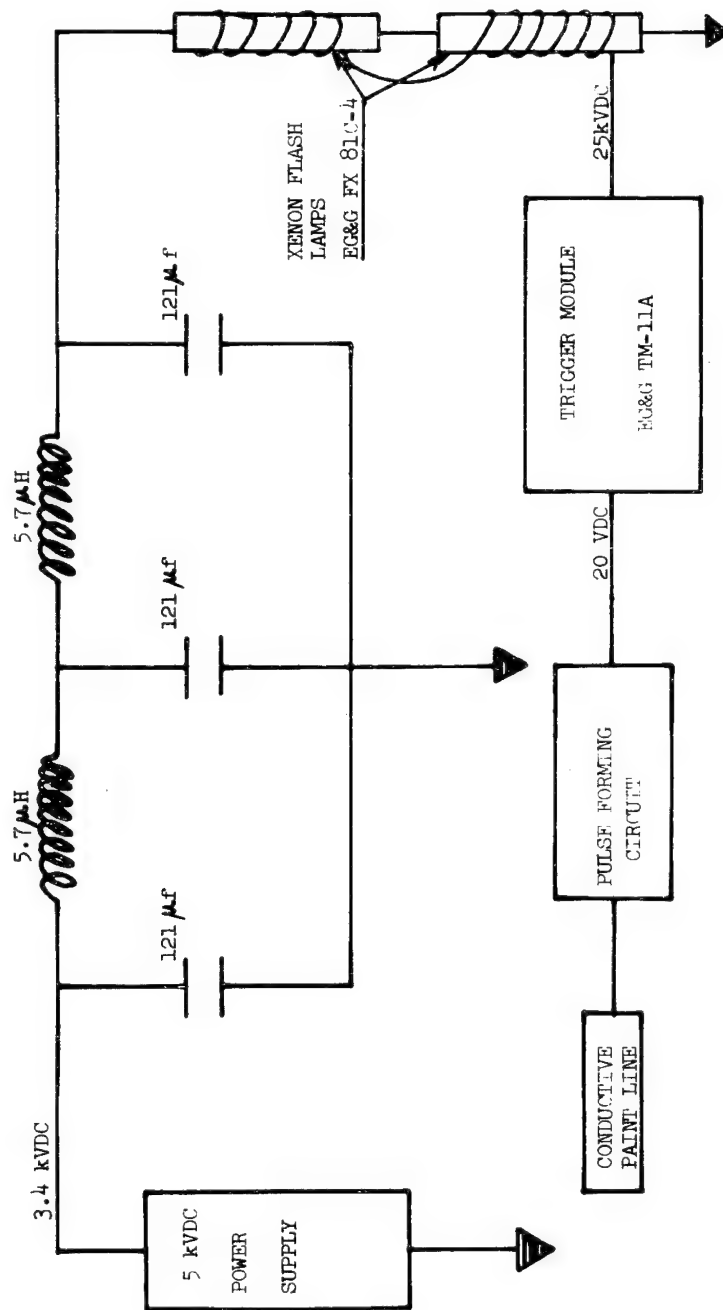


Fig. 3.2 Diagram showing Flash Tube Power Supply and Synchronization Circuits.

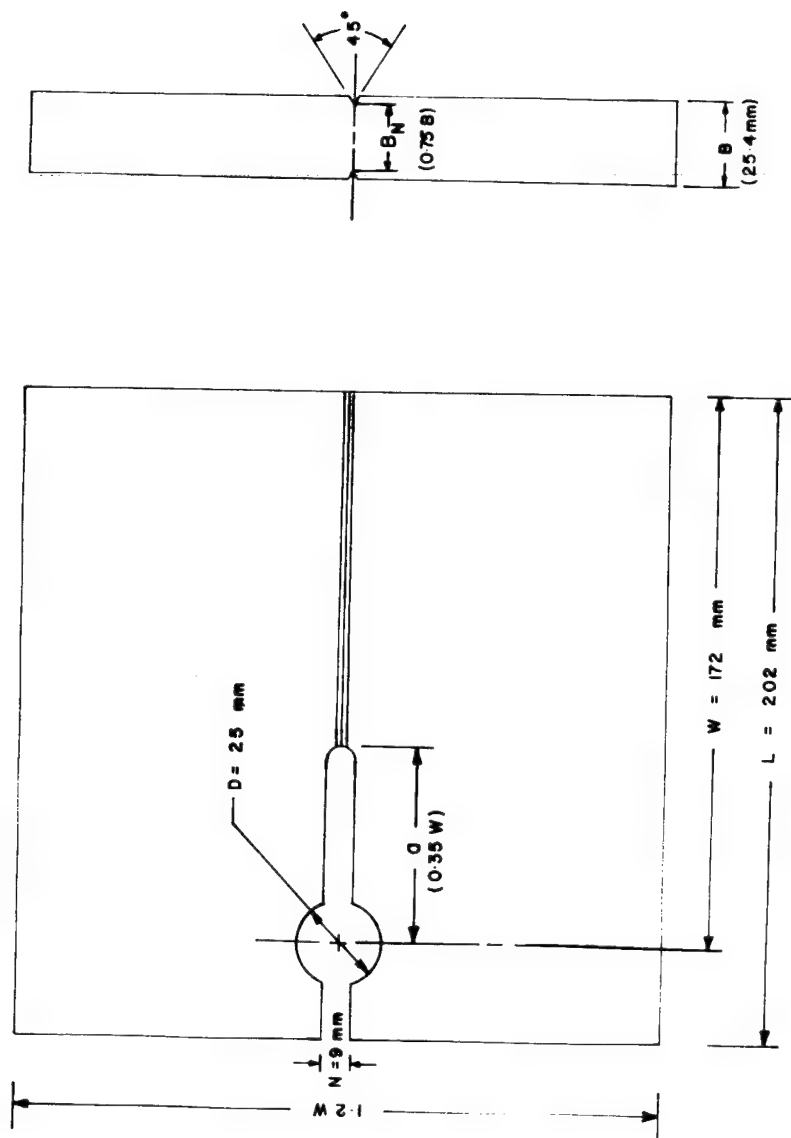


Fig. 3.3 Dimensions of the Modified Compact Tension Specimen.

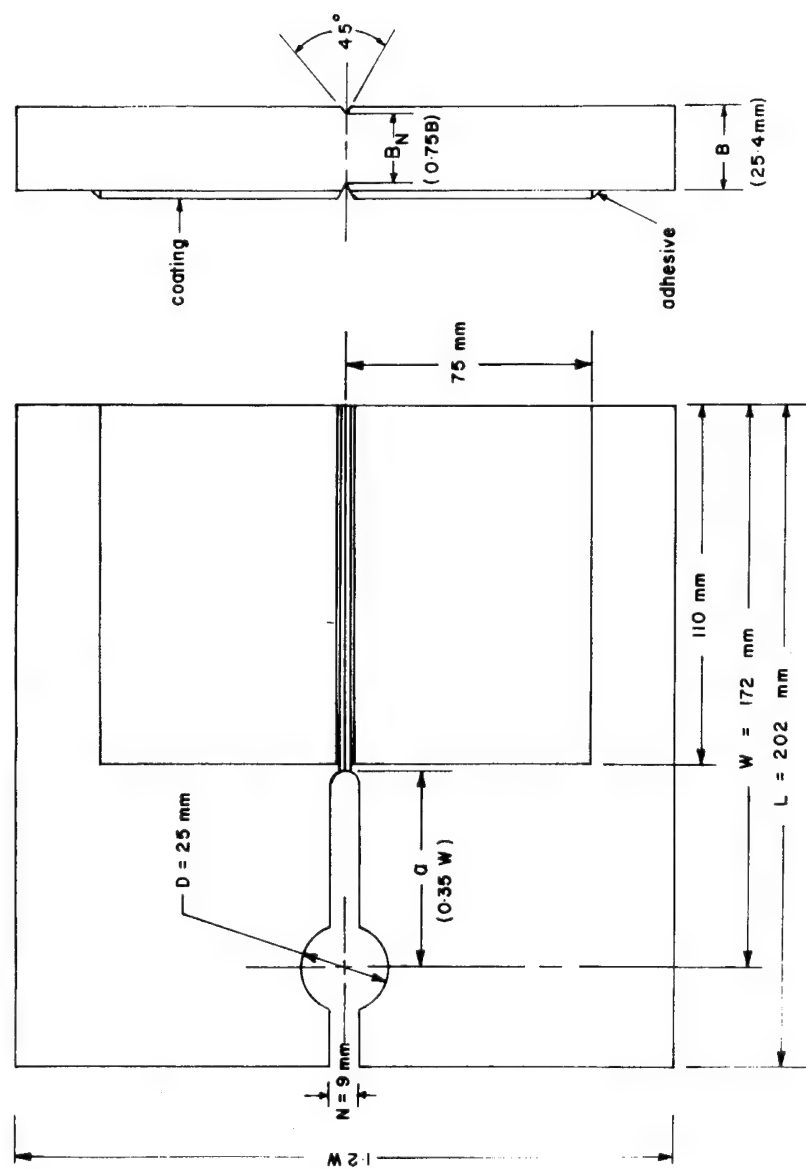


Fig. 3.4 Birefringent Coating on the M-CT Specimen.



Fig. 3.5 Specially Designed Loading Frame for Coated M-CT Specimen.

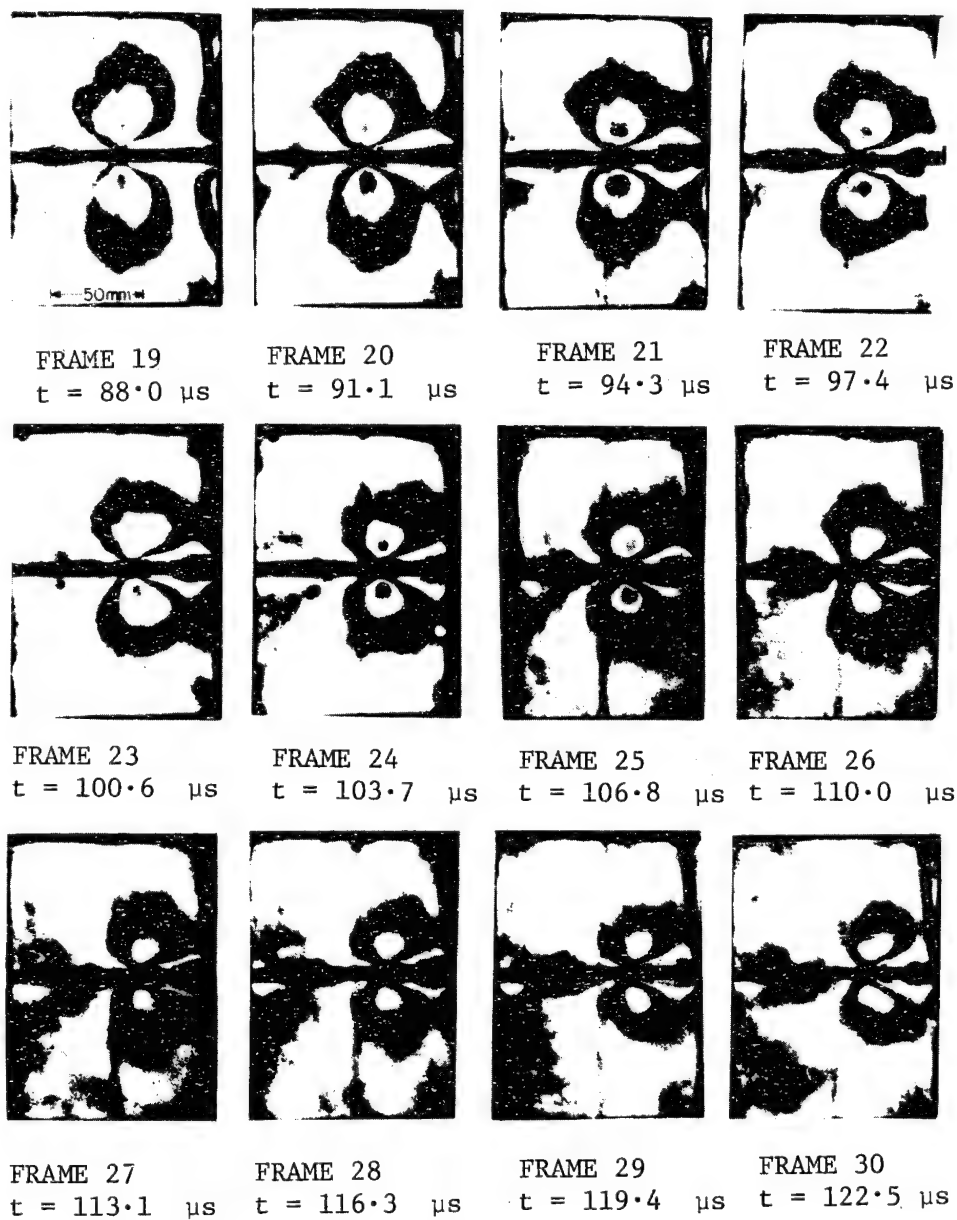


Fig. 3.6A Sequence of Isochromatic Fringe Patterns Showing the Propagating Crack.

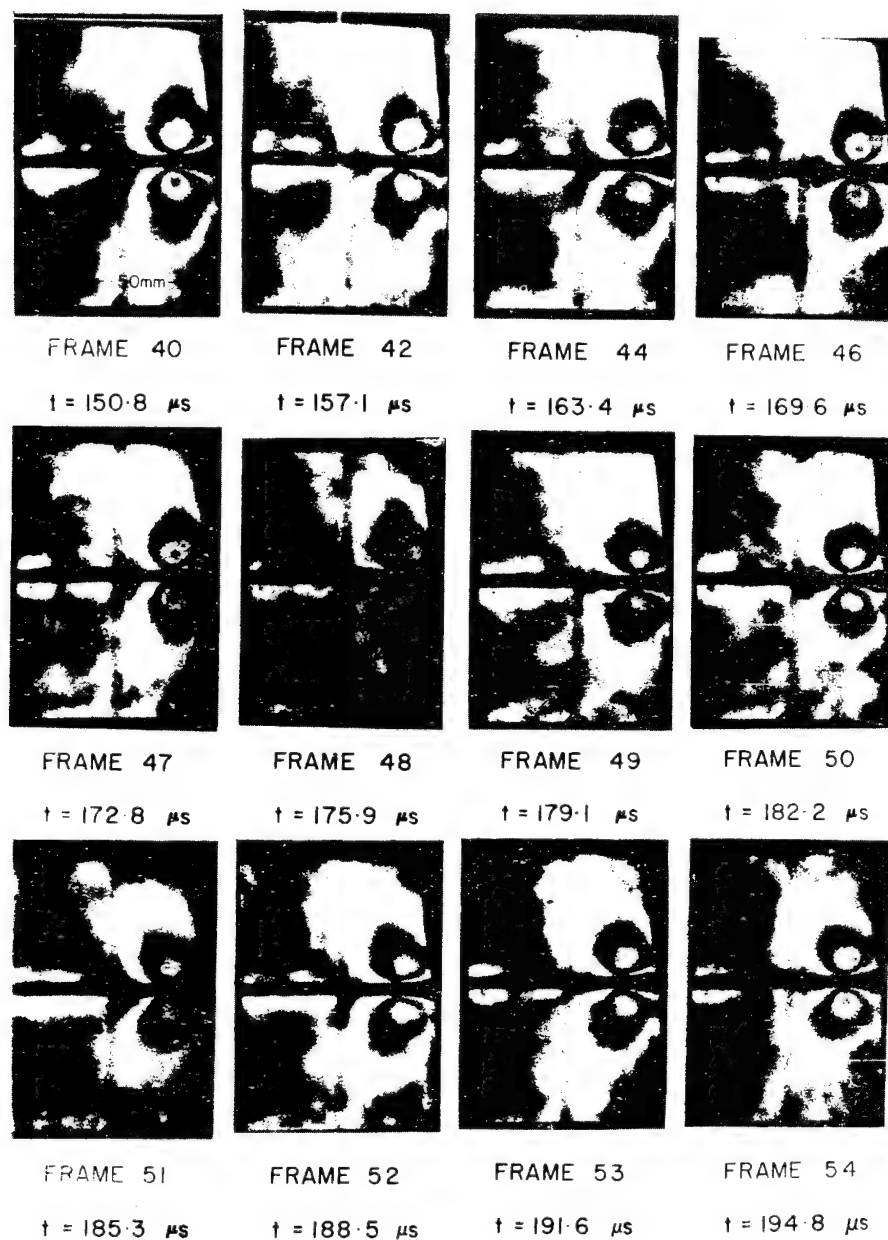


Fig. 3.6B Sequence of Isochromatic Fringe Patterns Showing the Crack Arrest Phase of the Dynamic Event.

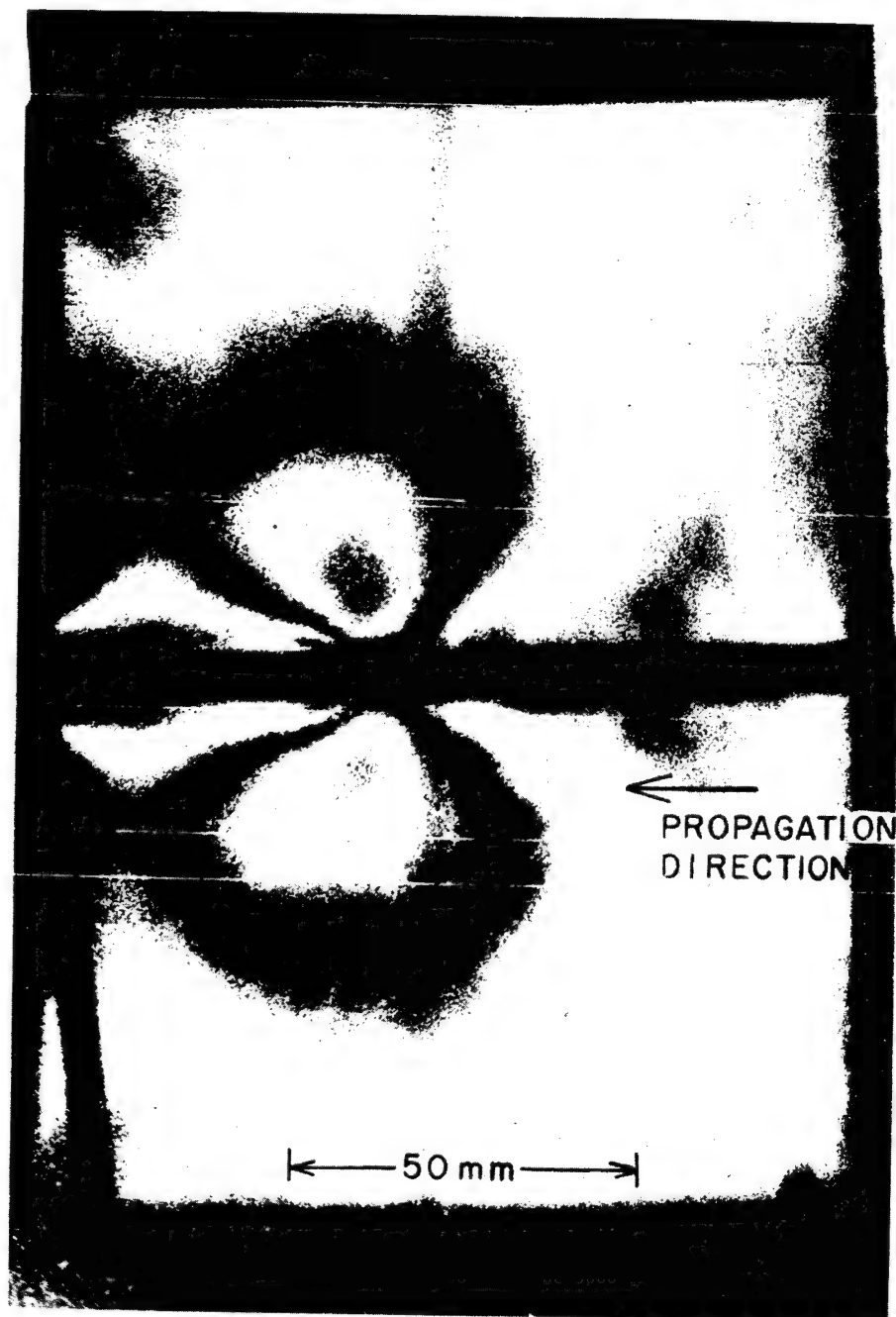


Fig. 3.7 Enlargement which Shows the Details of the Isochromatic Fringe Loop at the Crack Tip.

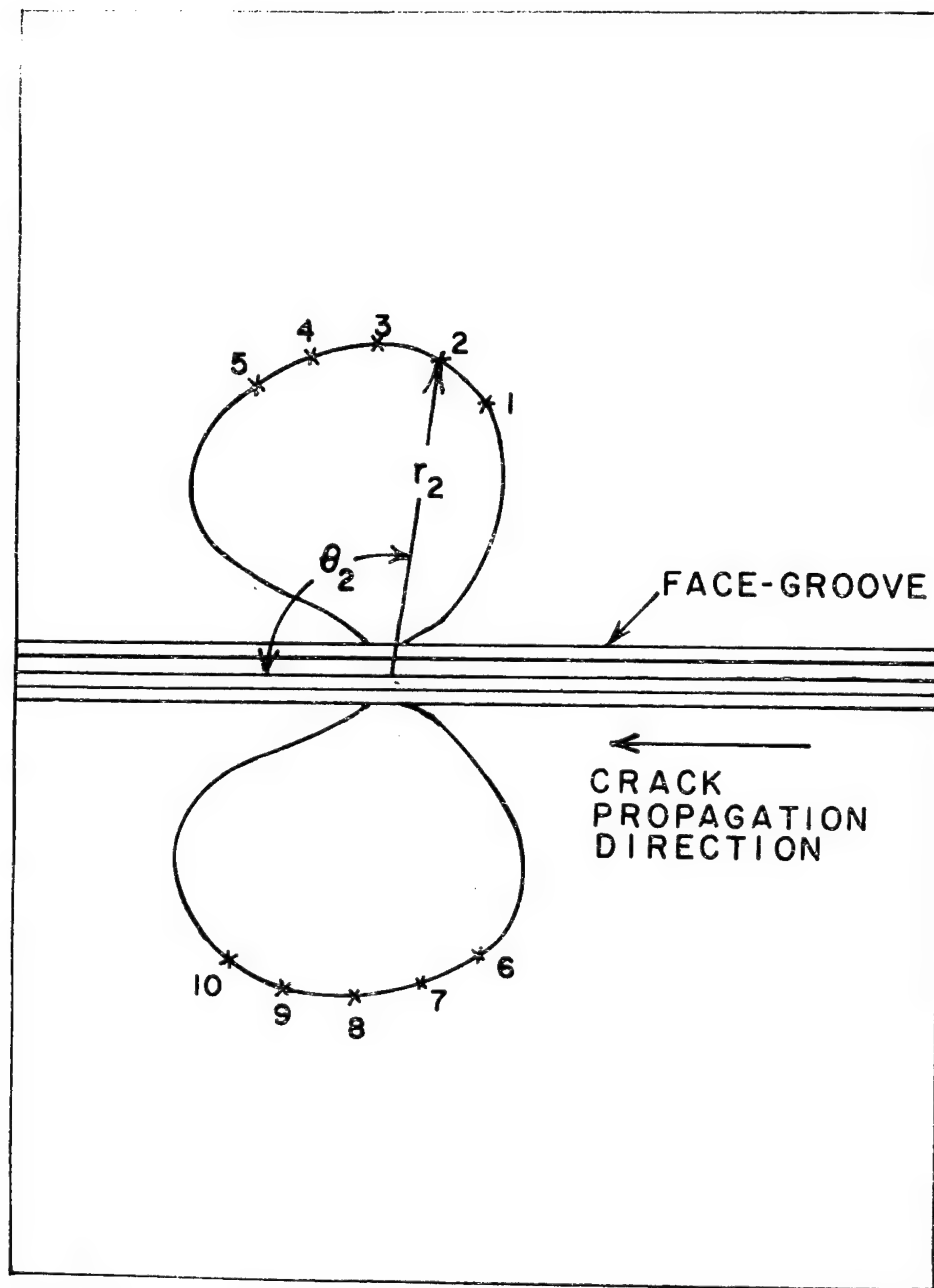


Fig. 3.8 Typical Data Extracted from the Isochromatic Fringe Loops.

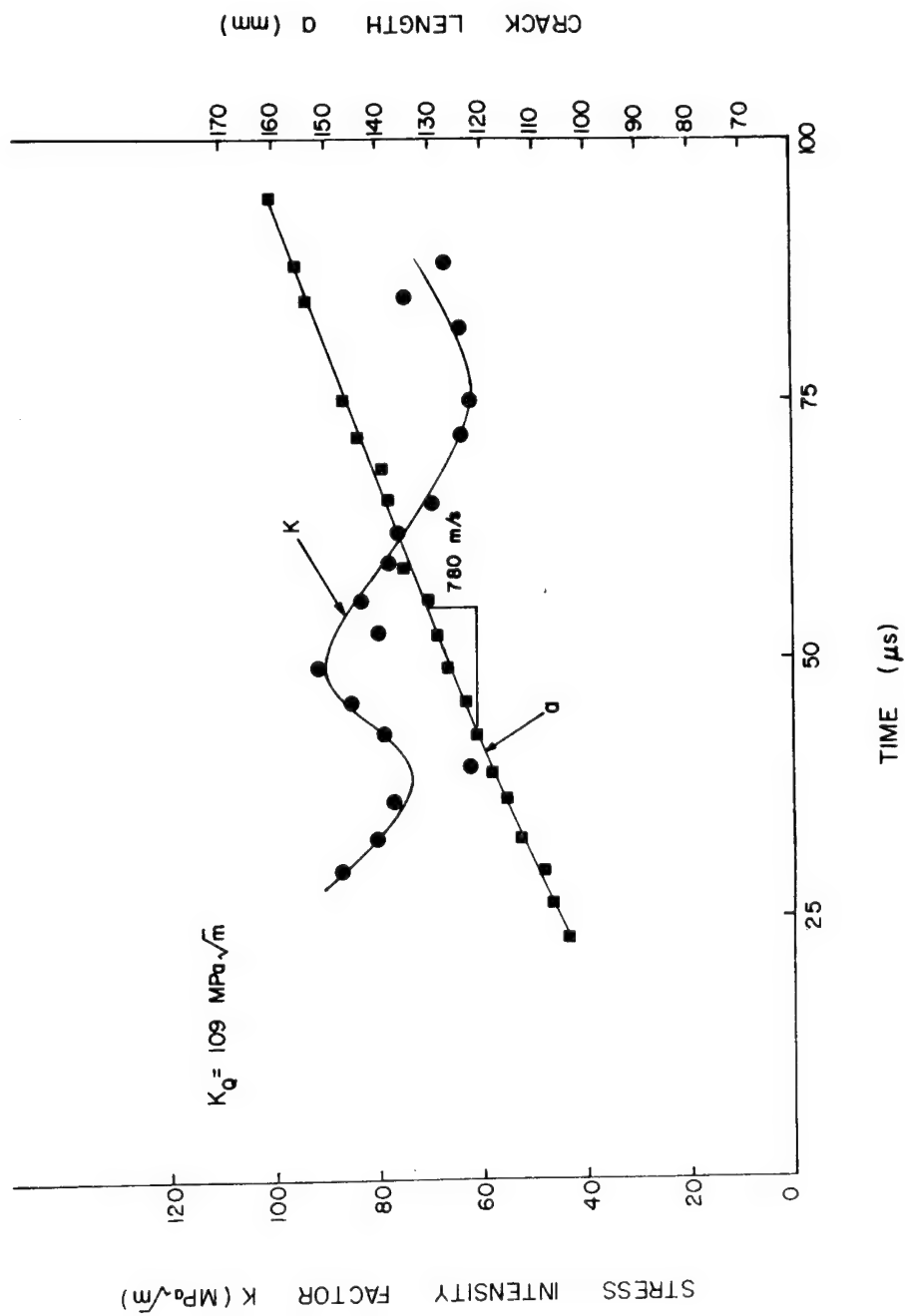


Fig. 3.9 Stress Intensity Factor and Crack Length as a Function of Time for Model No. 333.

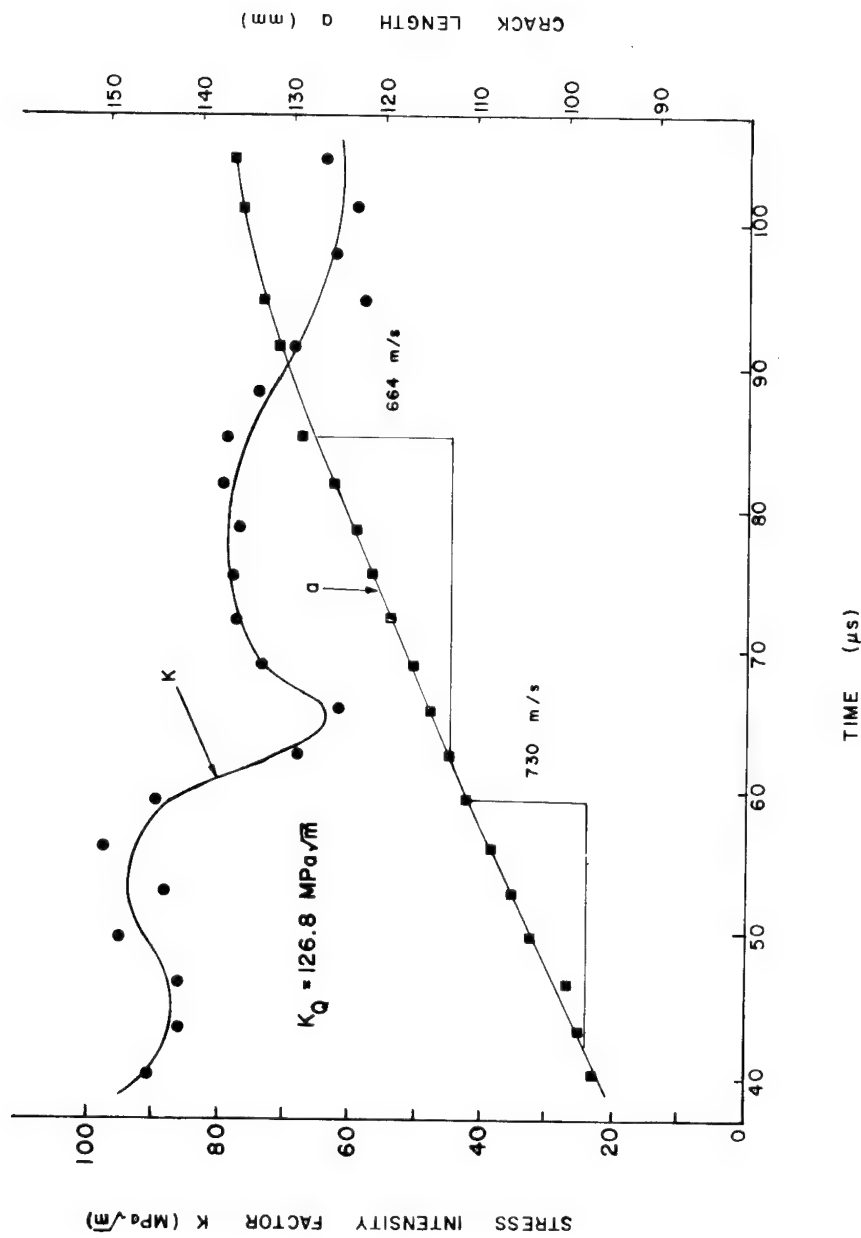


Fig. 3.10 Stress Intensity Factor and Crack Length as a Function of Time for Model No. 348.

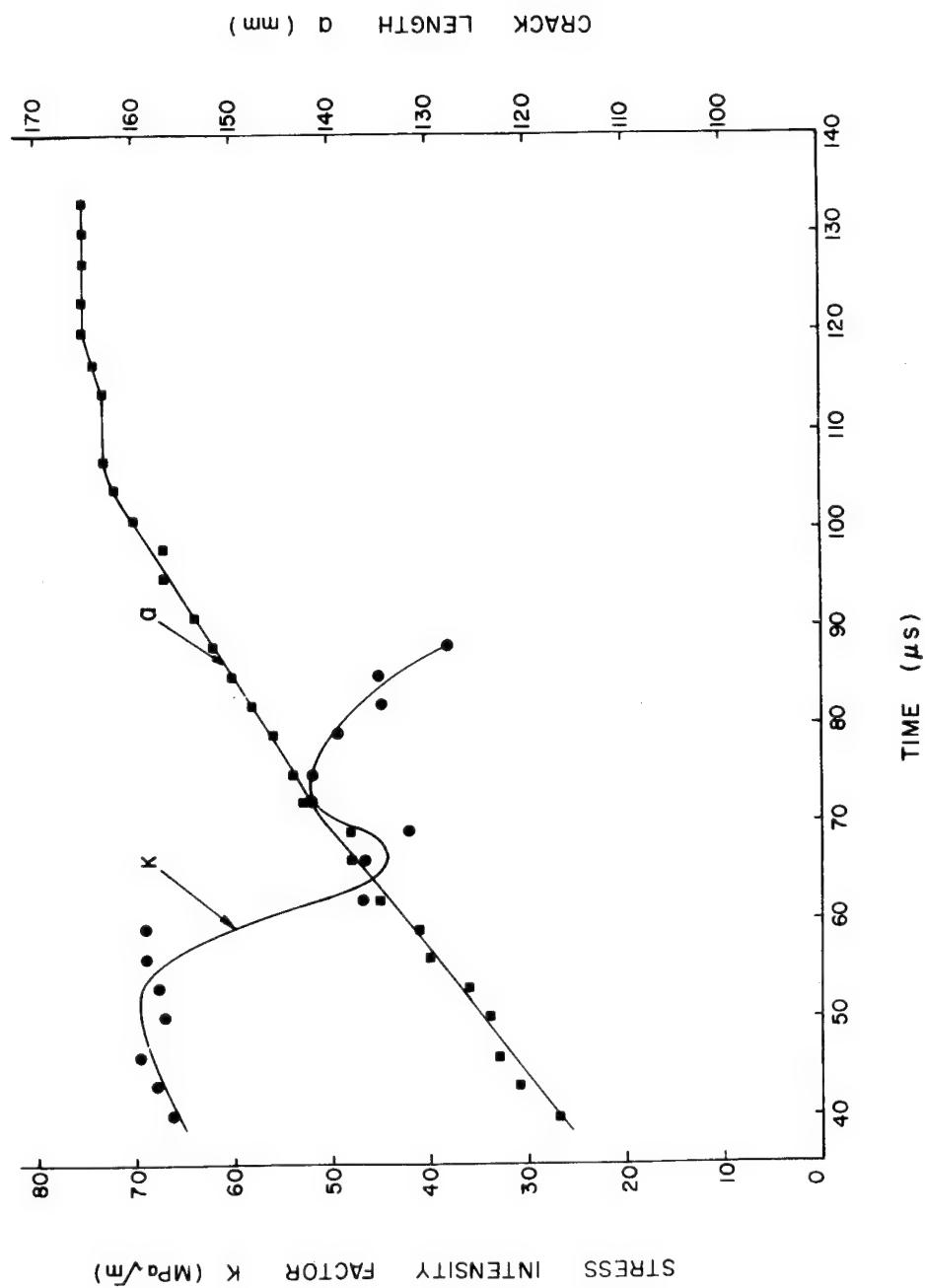


Fig. 3.11 Stress Intensity Factor and Crack Length as a Function of Time for Model No. 349.

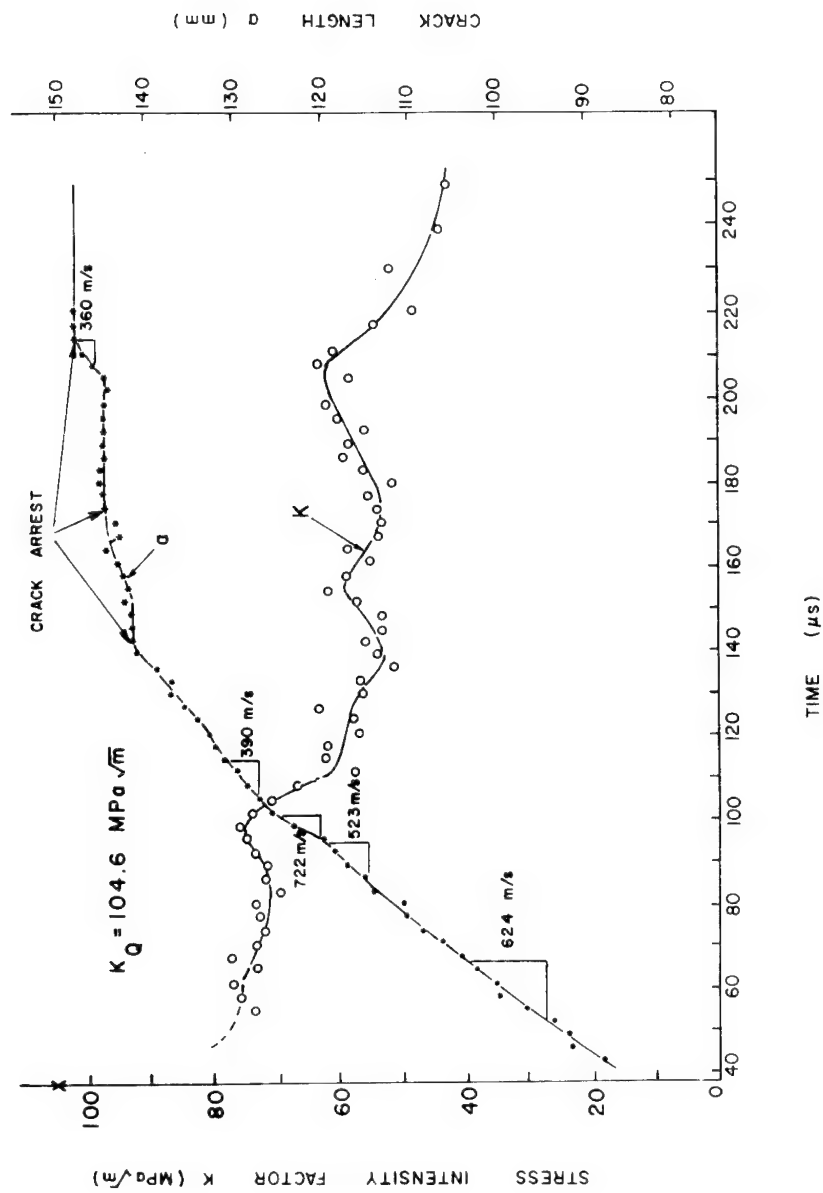


Fig. 3.12 Stress Intensity Factor and Crack Length as a Function of Time for Model No. 362.

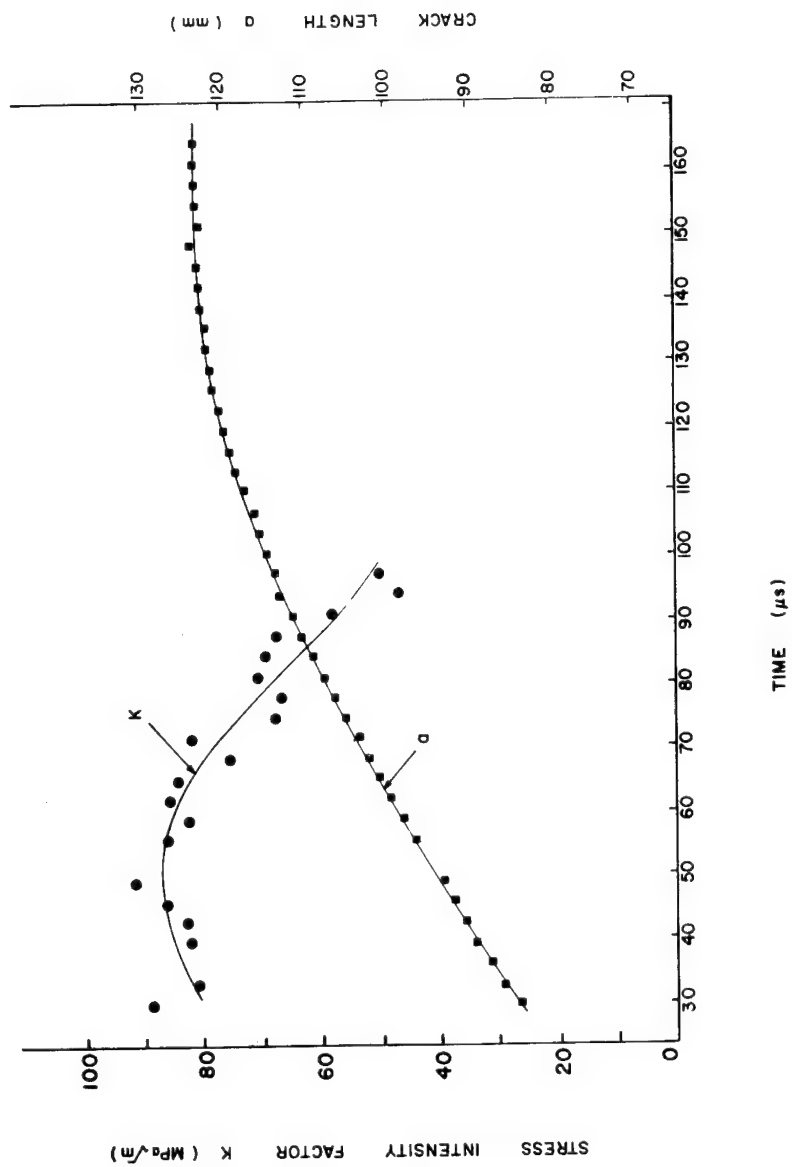


Fig. 3.13 Stress Intensity Factor and Crack Length as a Function of Time for Model No. 375.

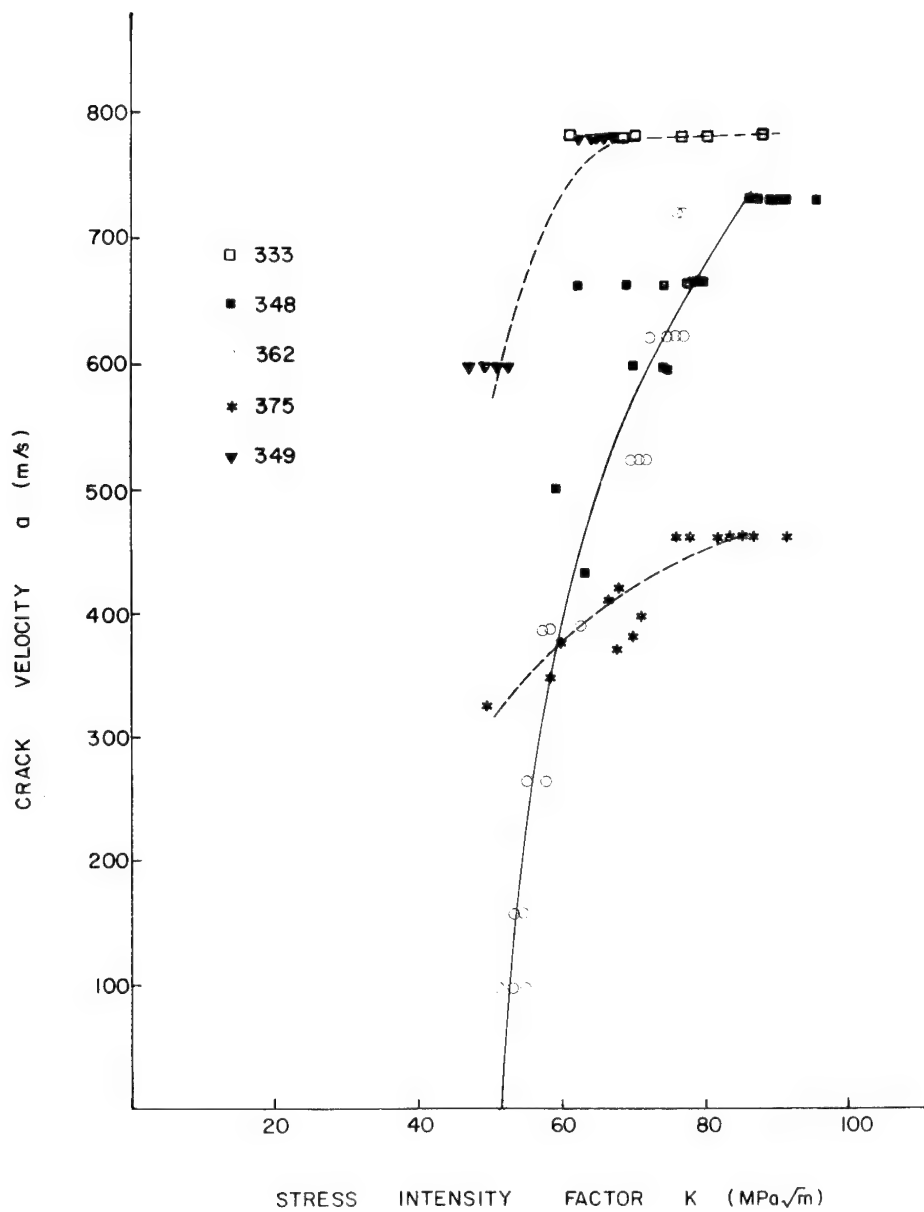


Fig. 3.14 Crack Velocity as a Function of Stress Intensity Factor for 4340 Steel.

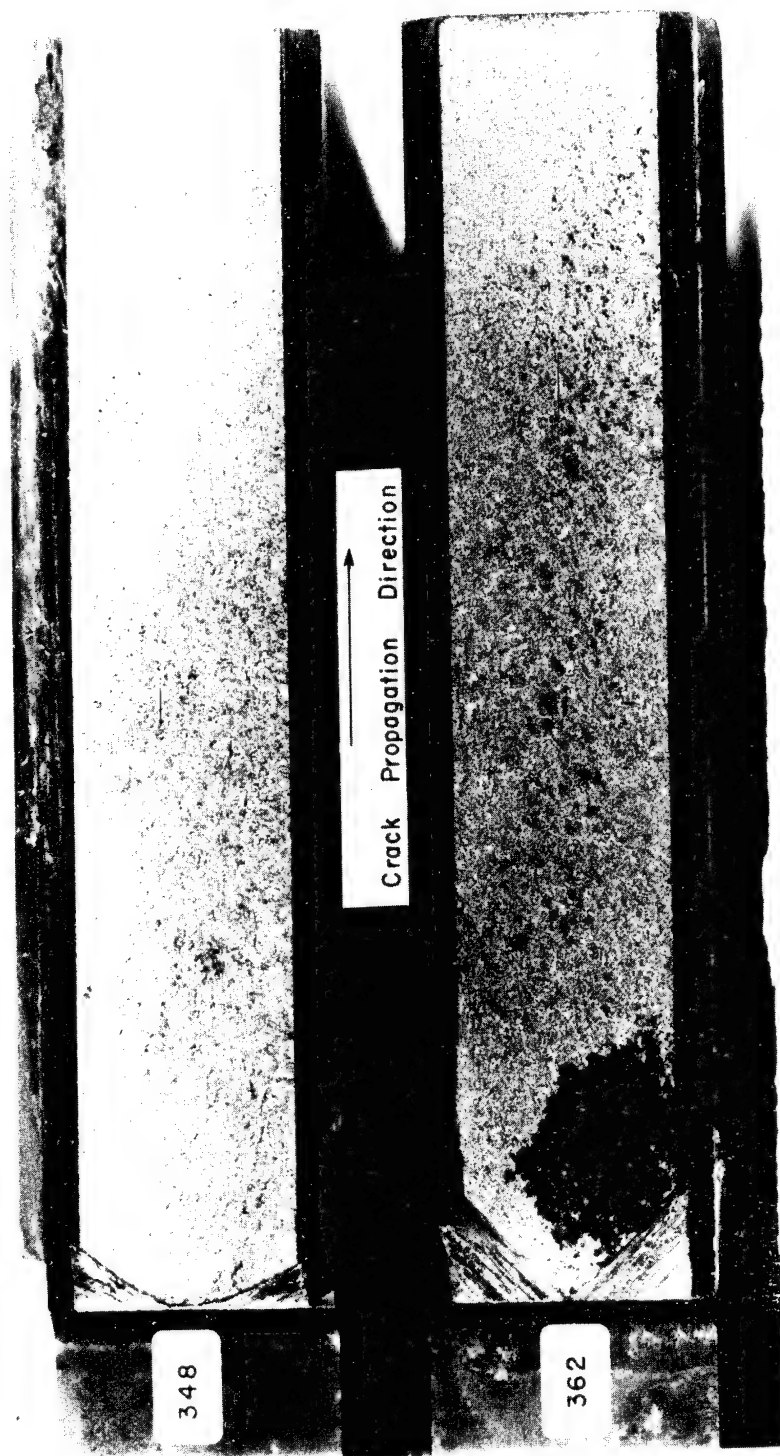


Fig. 3.15 Fracture Surface Characteristics for Model Nos. 348 and 362.

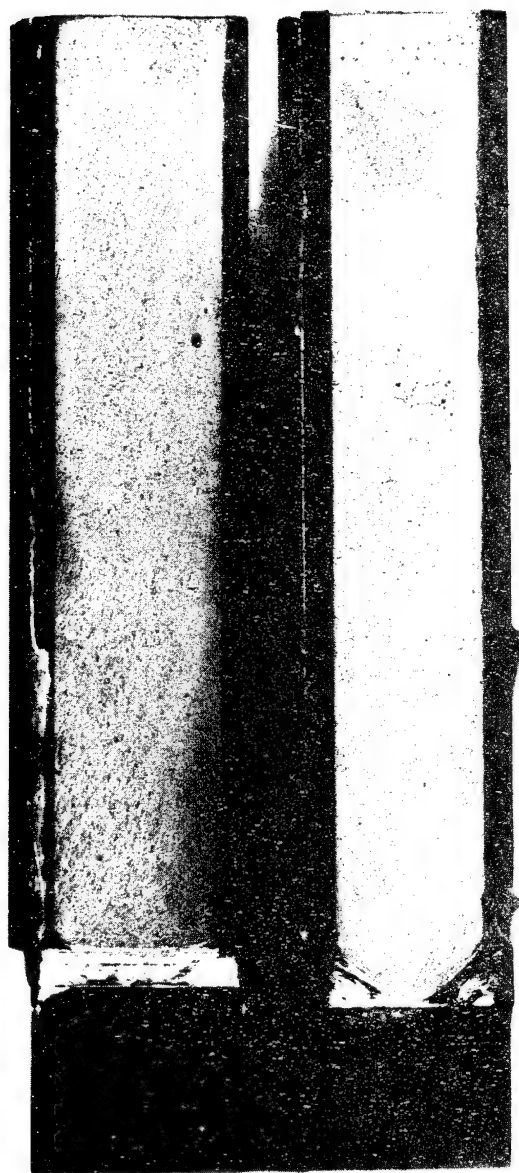


Fig. 3.16 Fracture Surface Characteristics for Model Nos. 333 and 375.

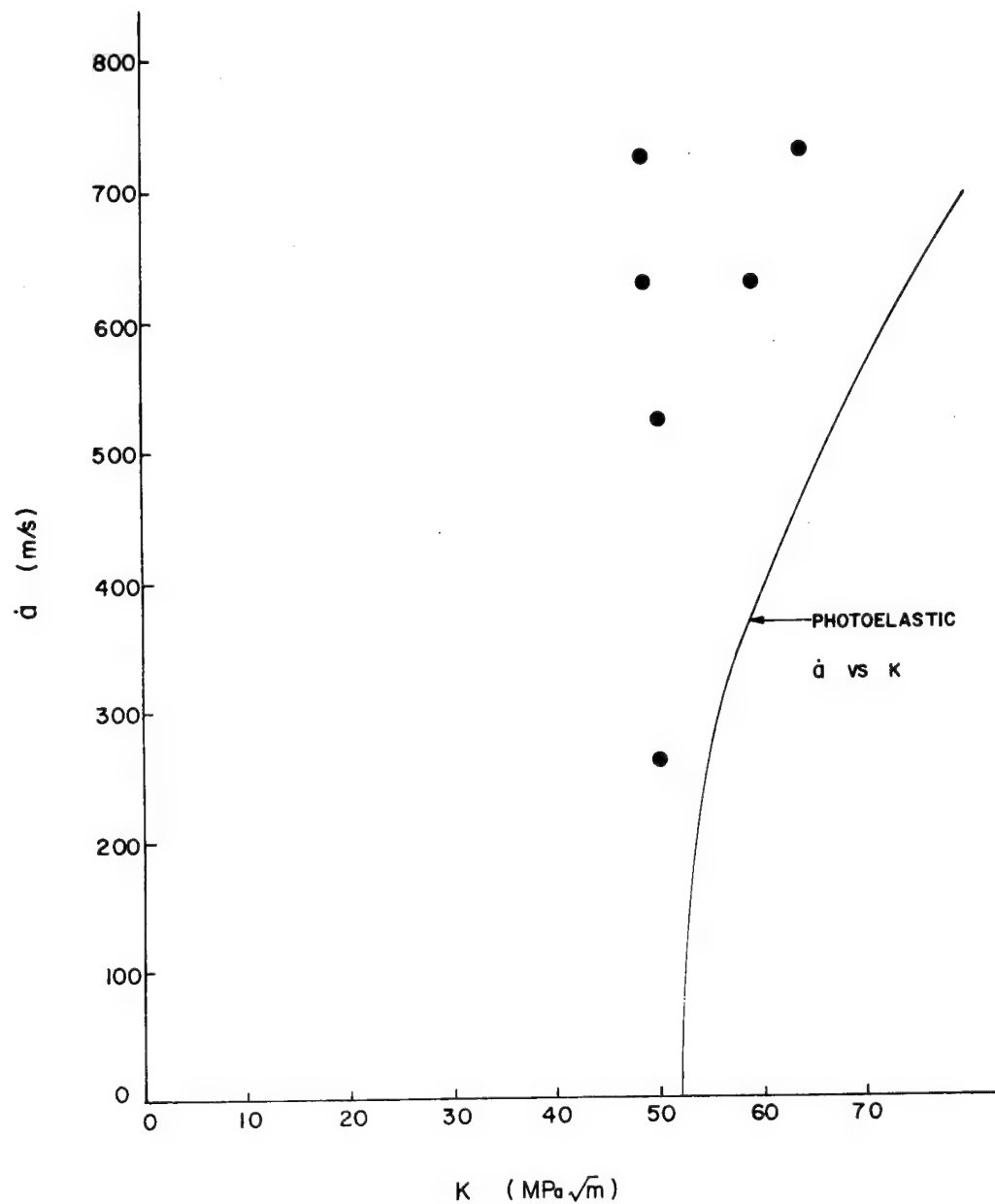


Fig. 3.17 Comparison between Photoelastic and BCL Determination of the \dot{a} vs K Relation for 4340 Steel.

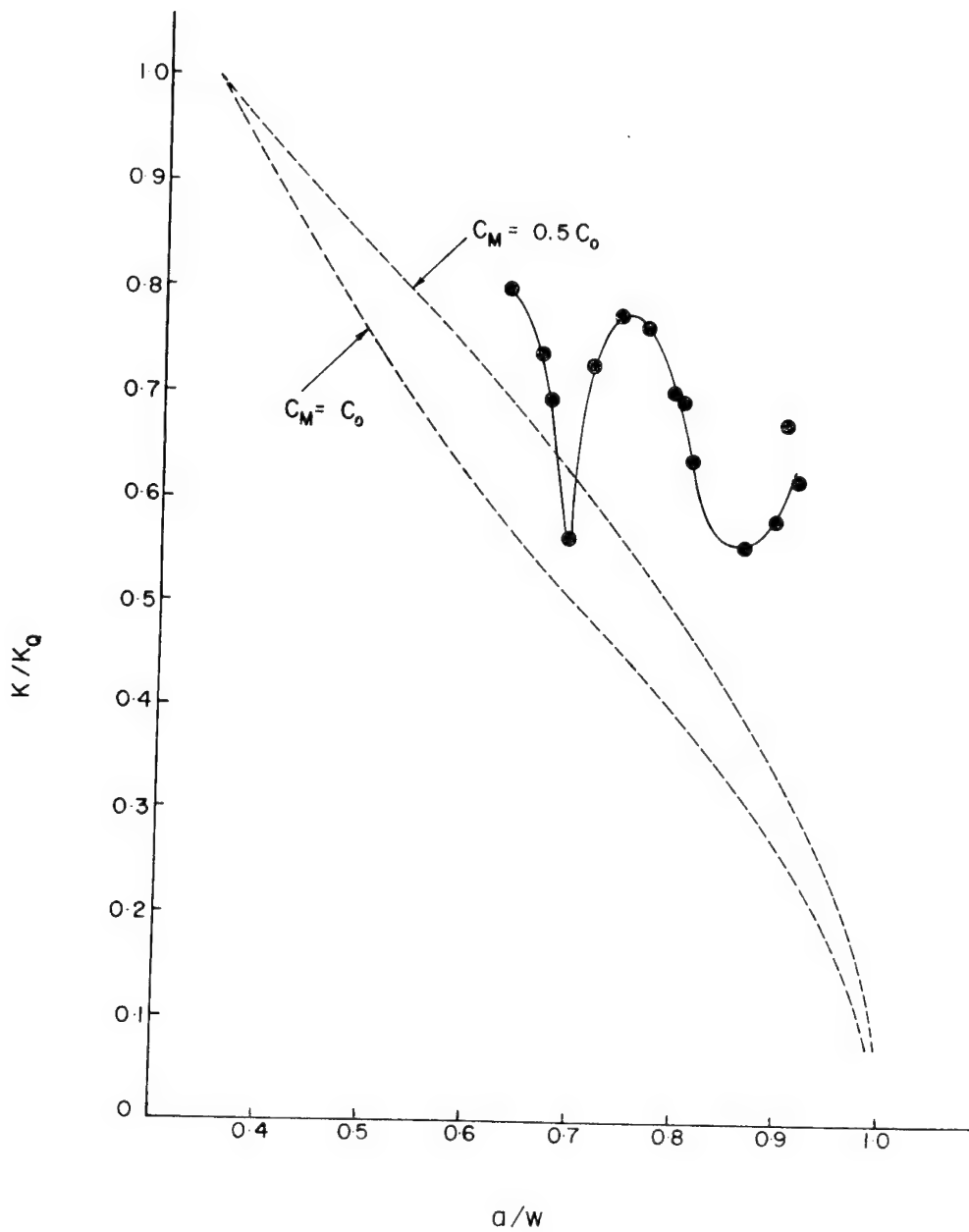


Fig. 3.18 K/K_Q vs a/w for Model No. 333.

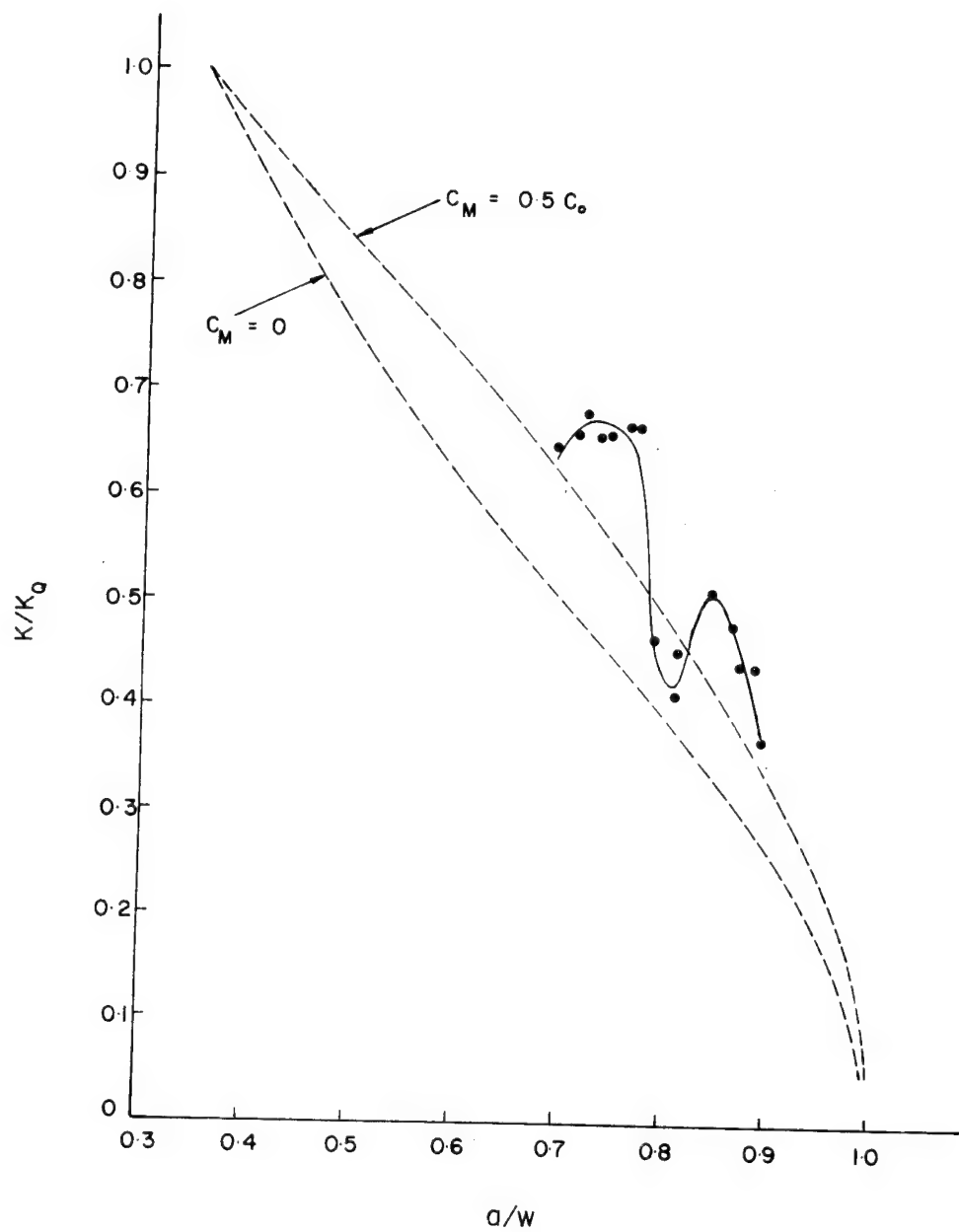


Fig. 3.19 K/K_Q vs a/W for Model No. 348.

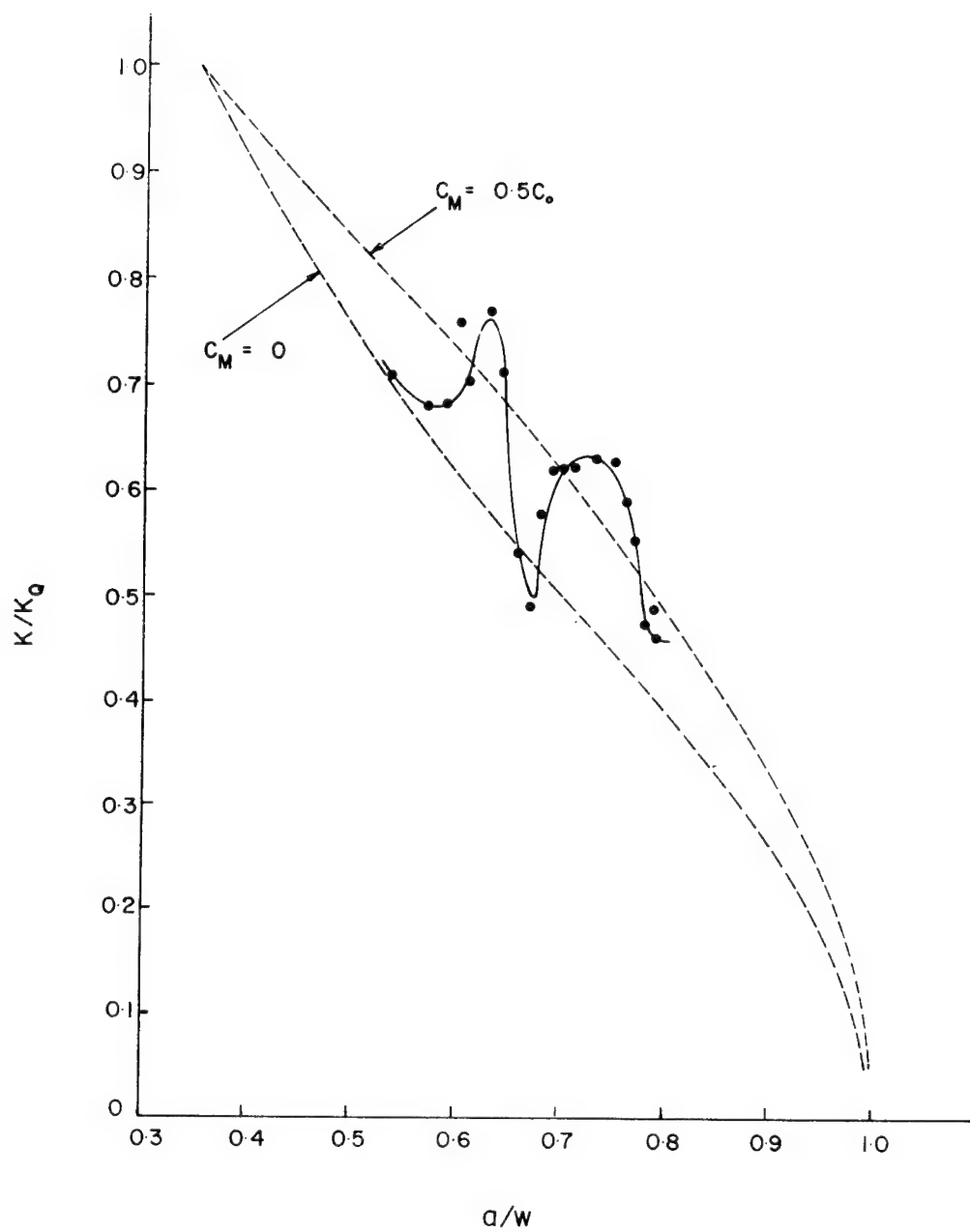


Fig. 3.20 K/K_Q vs a/w for Model No. 349.

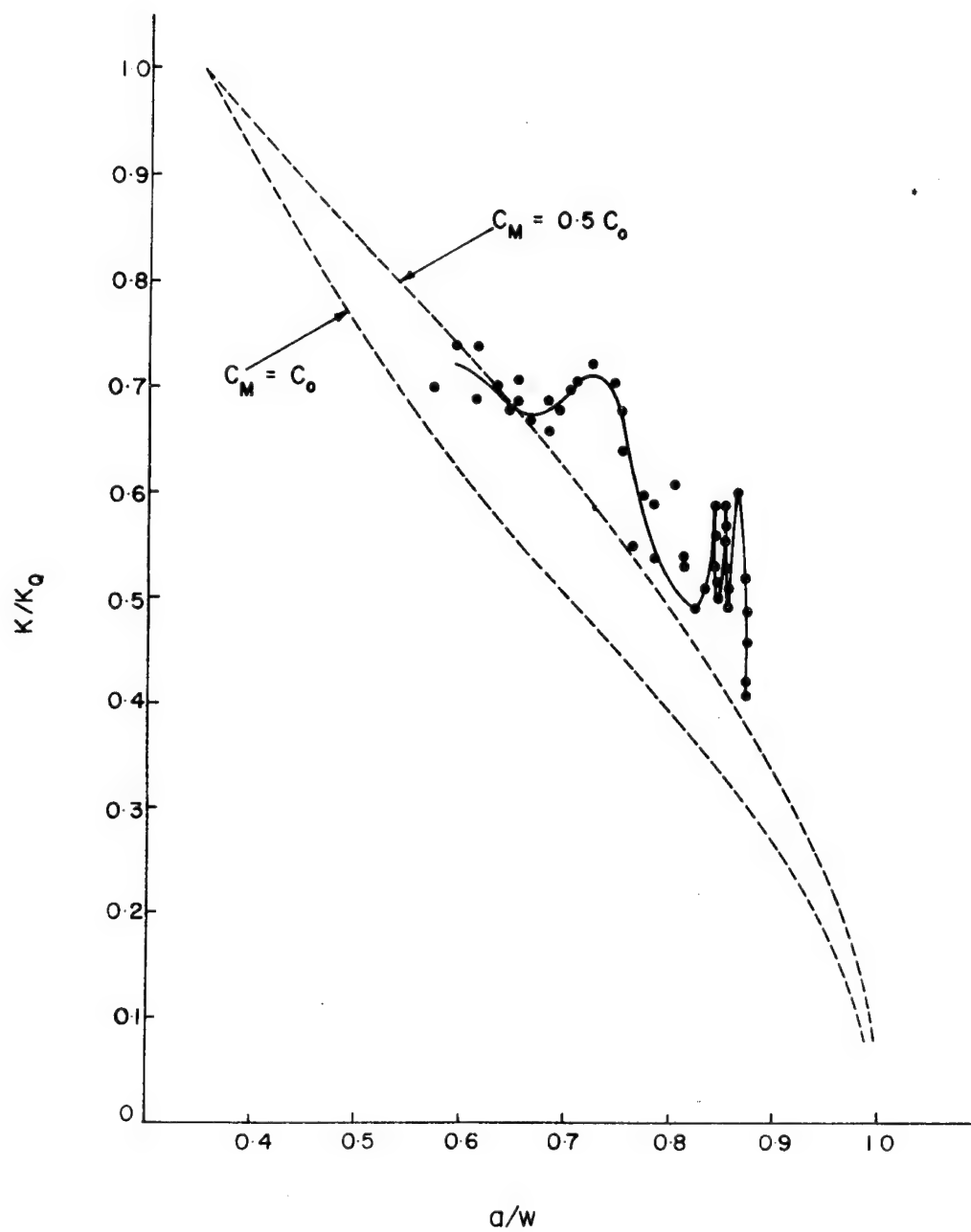


Fig. 3.21 K/K_Q vs a/w for Model No. 362.

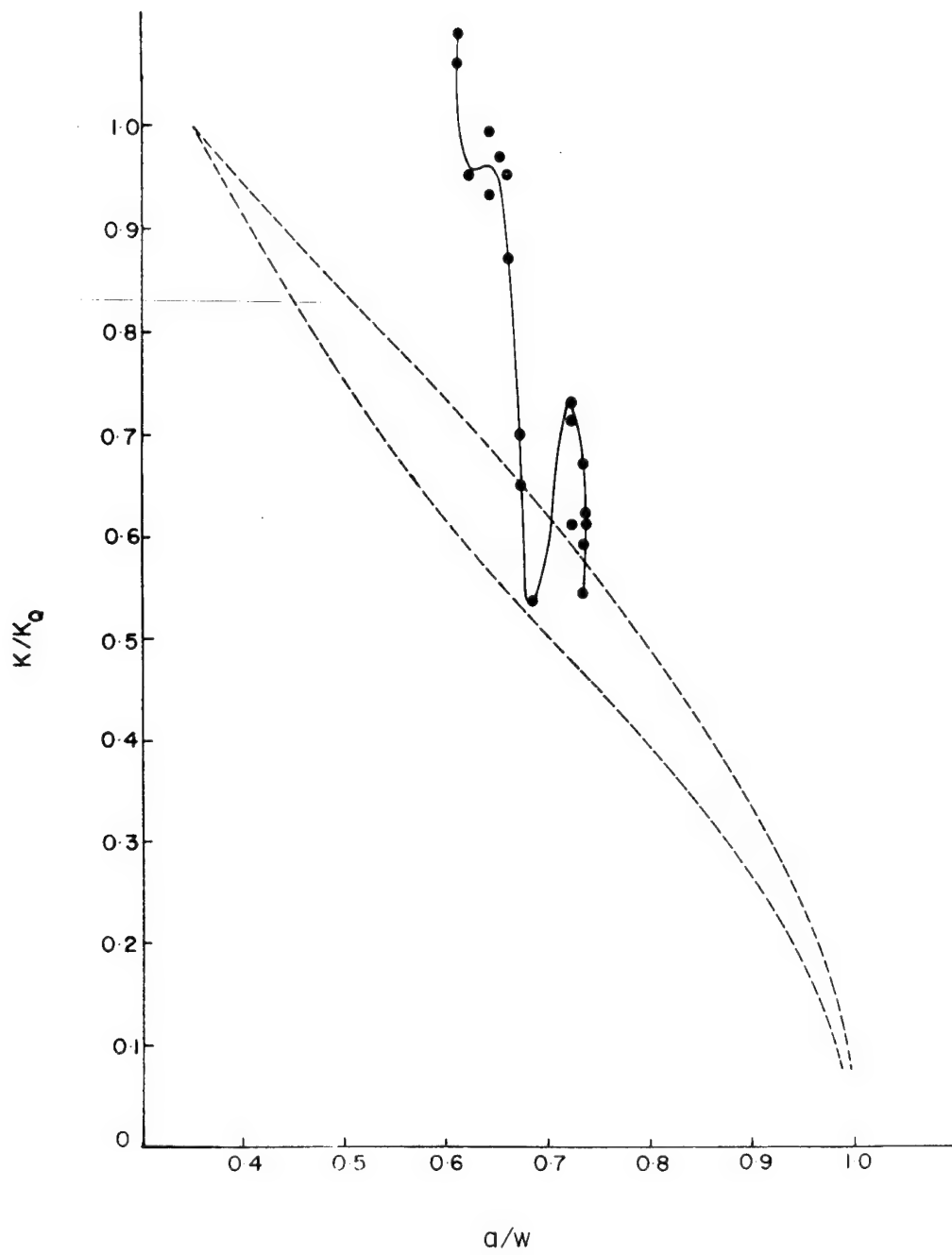


Fig. 3.22 K/K_Q vs a/W for Model No. 375.

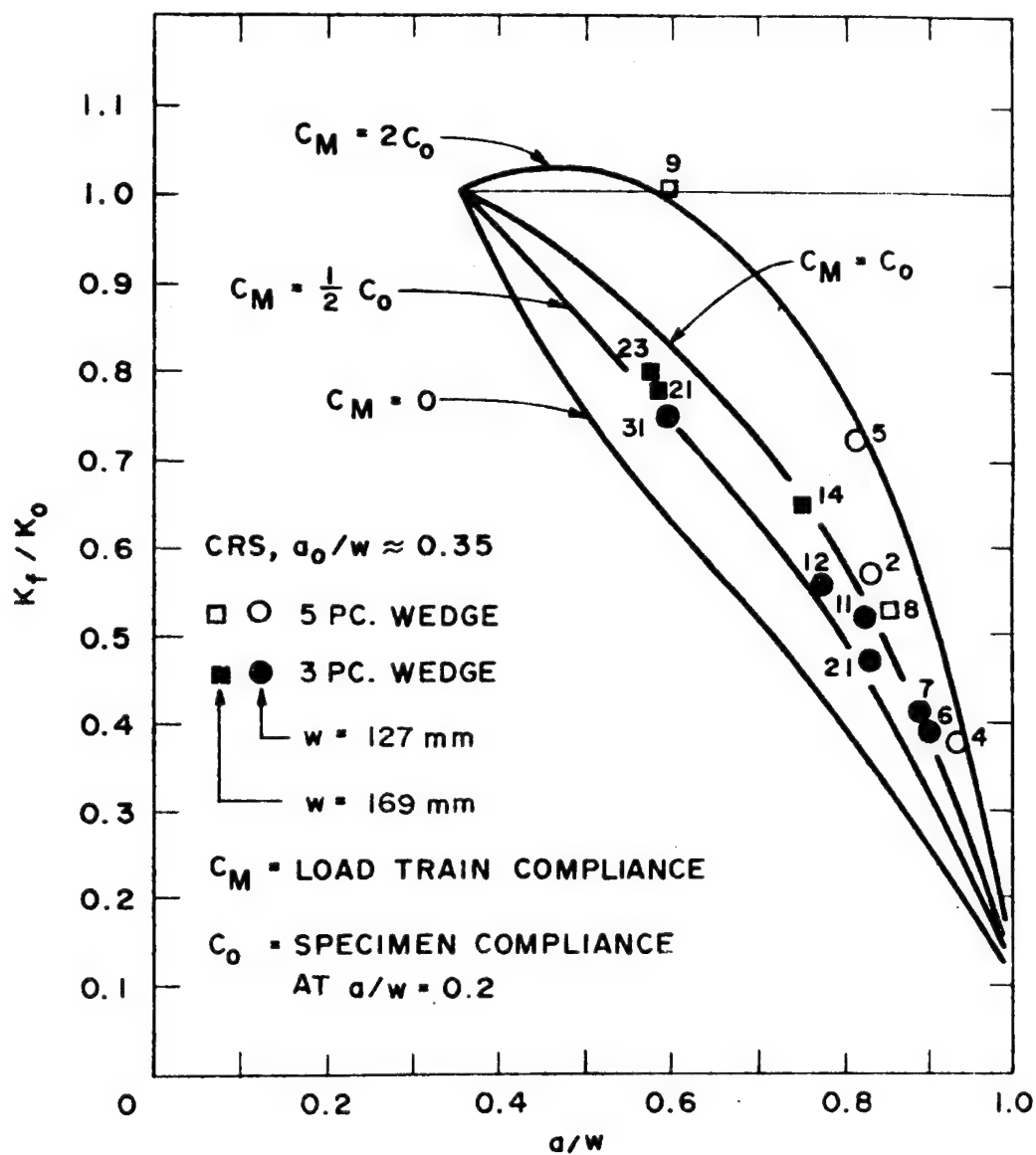


Fig. 3.23 Influence of Loading Machine Compliance on the K/K_0 vs a/w Relation.

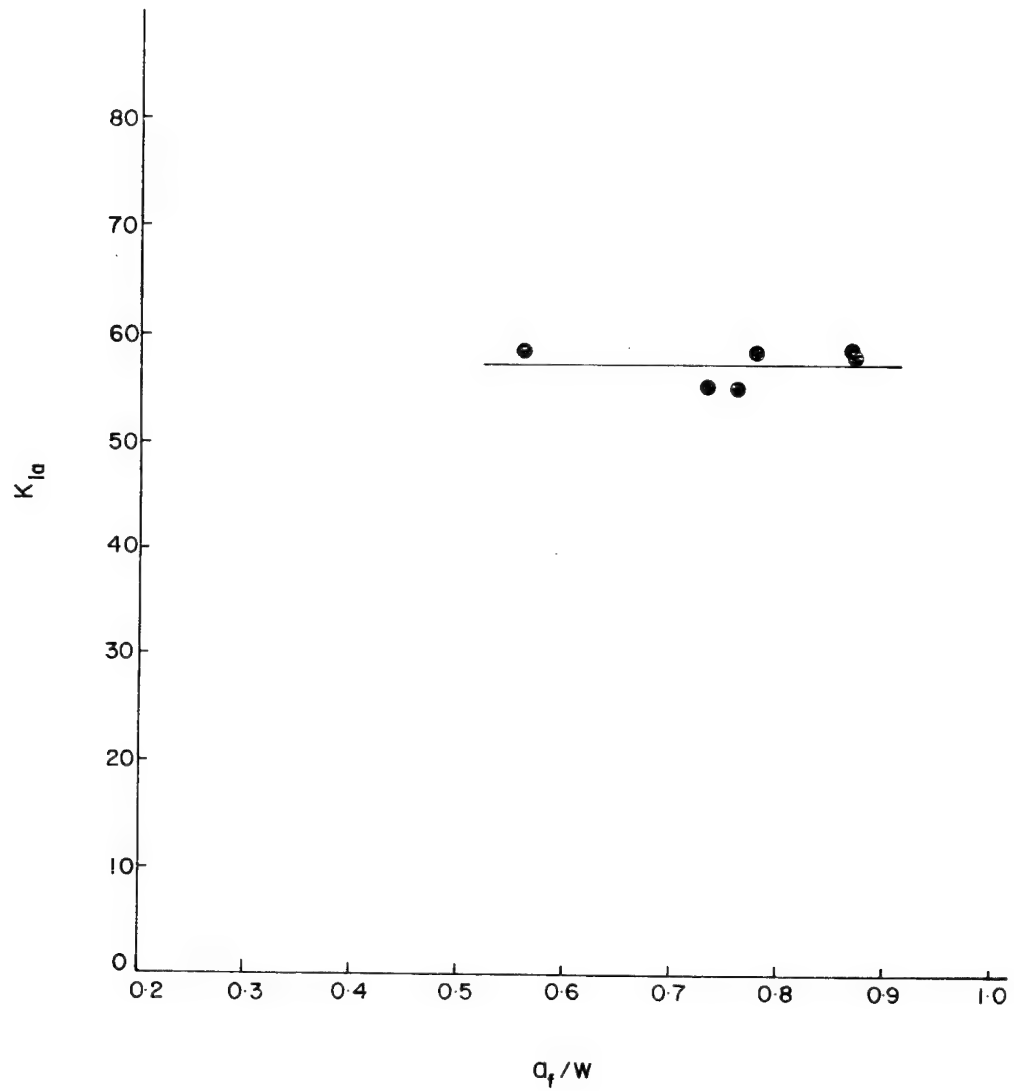


Fig. 3.24 Crack Arrest Toughness as a Function of Normalized Crack Jump Distance a_f/W for 4340 M-CT Specimens.

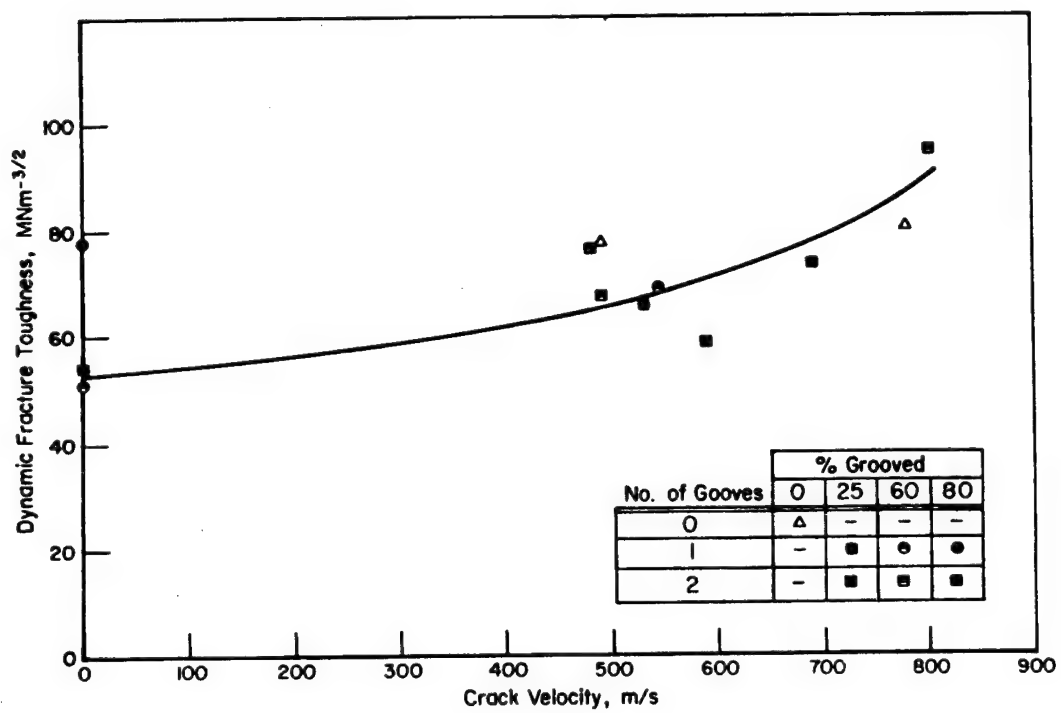


Fig. 3.25 Relation of \dot{a} to K_{Id} obtained using BCL Method of Data Analysis.

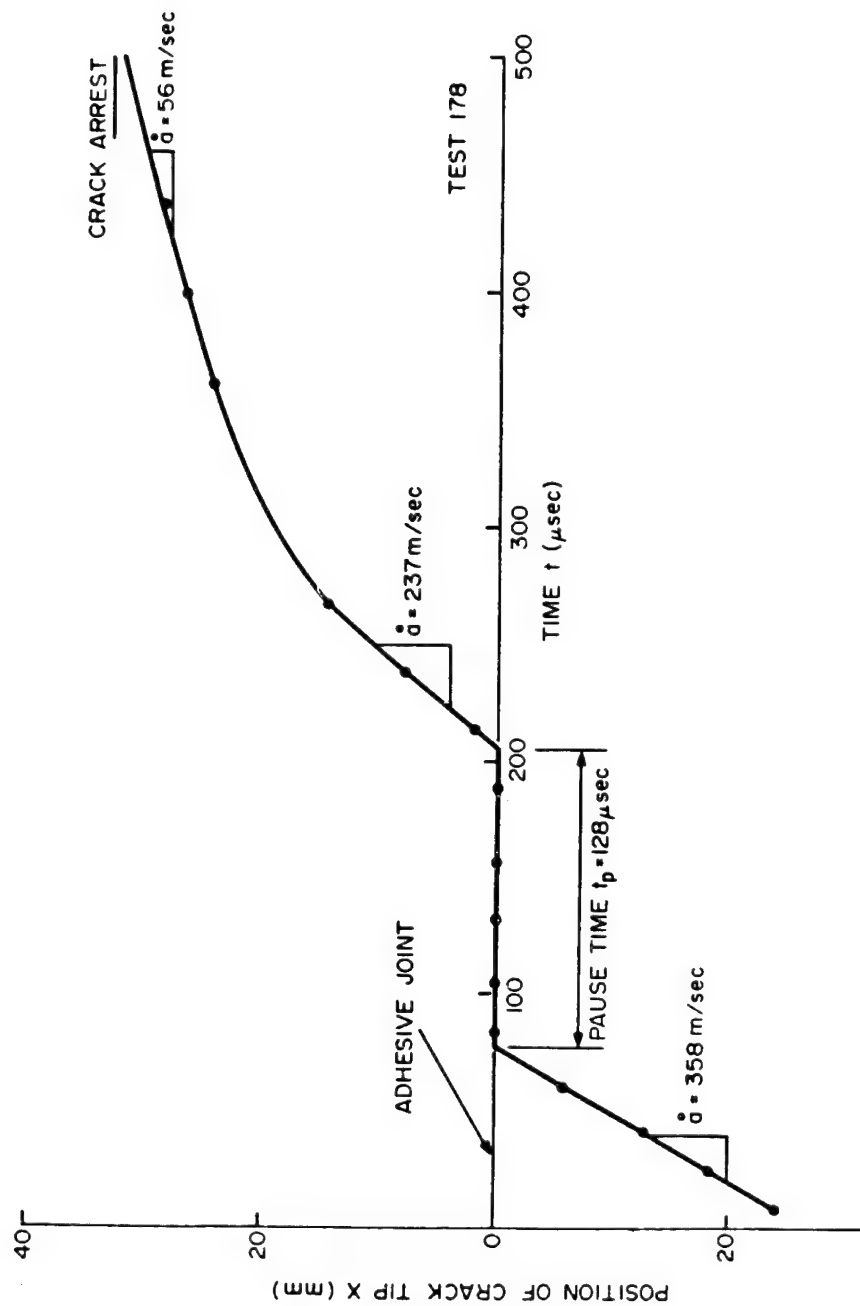


Fig. 4.1 Crack Position - Time Function Describing Crack Propagation Across the Duplex M-CT Specimen.

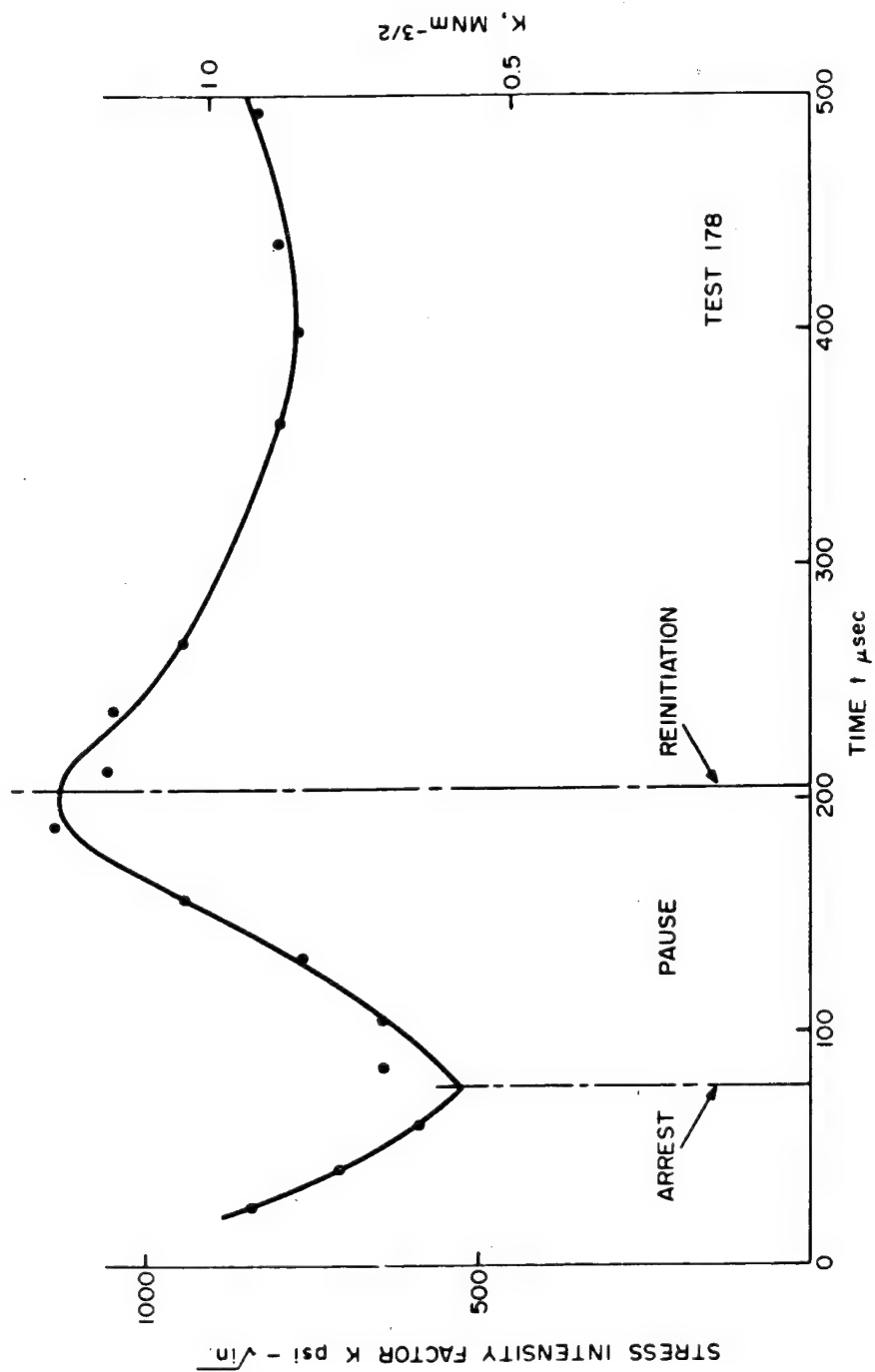


Fig. 4.2 Stress Intensity Factor as a Function of Time in a Duplex M-CT Specimen with Crack Reinitiation.

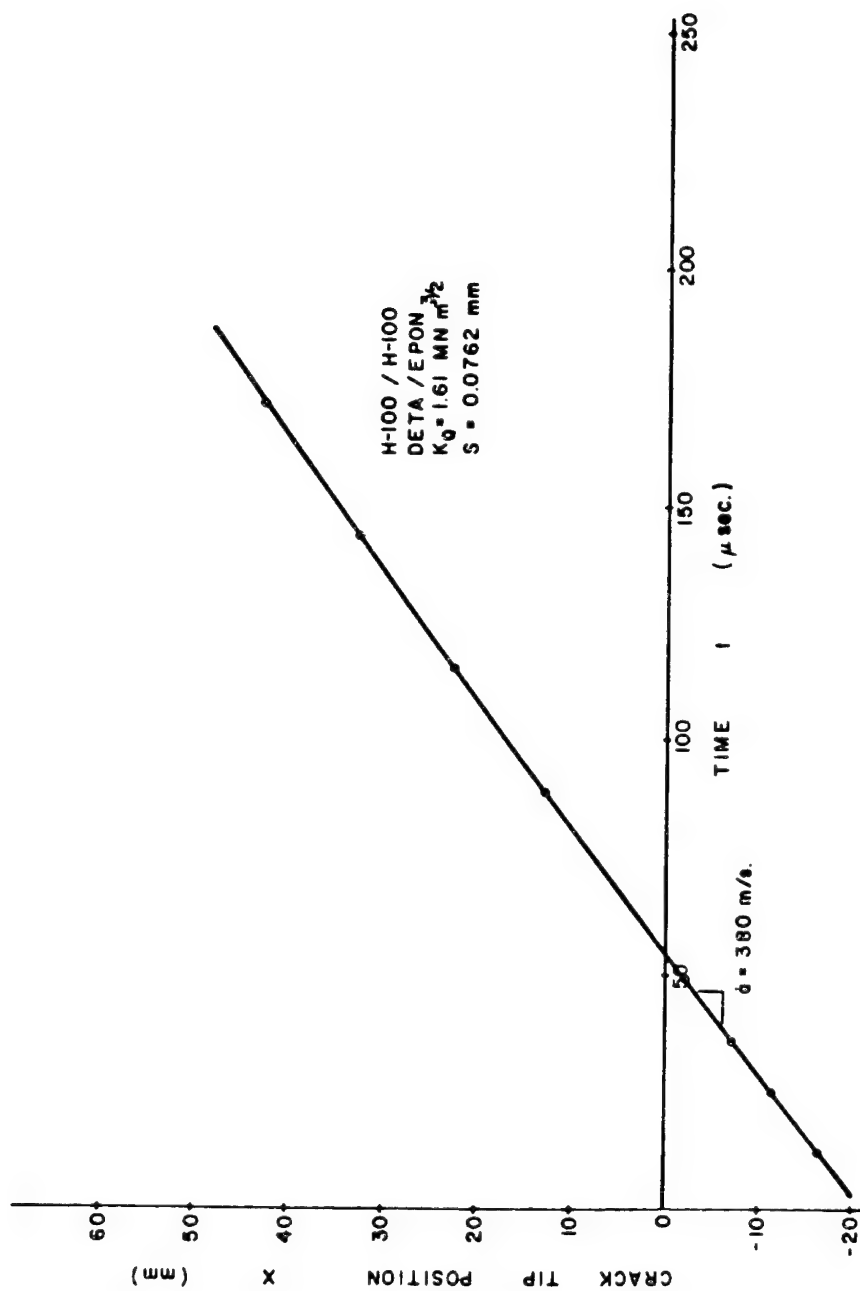


Fig. 4.3 Stress Intensity Factor as a Function of Time for a Duplex M-CT Specimen with a Brittle Adhesive Joint.

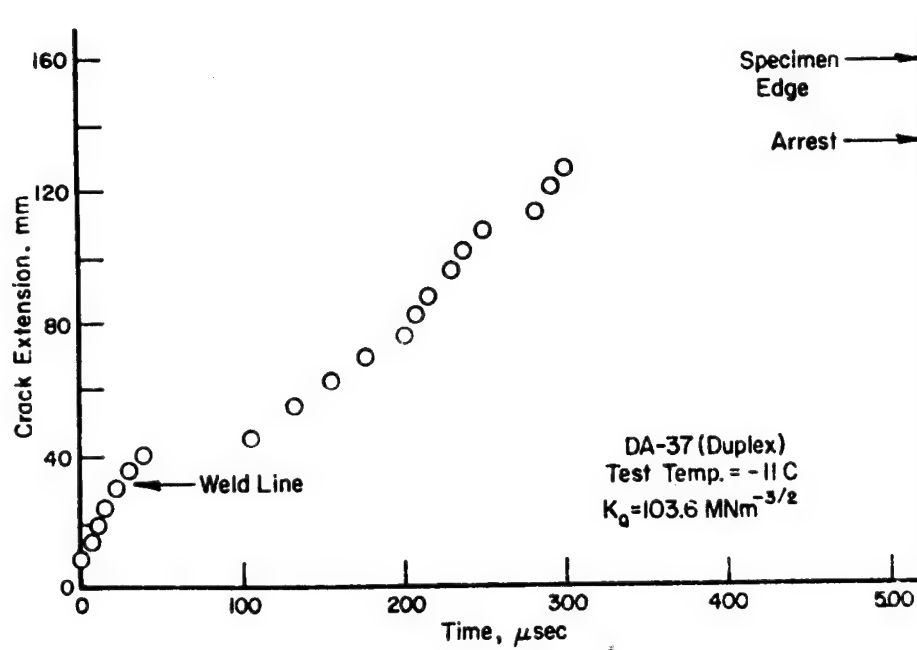


Fig. 4.4 Crack Extension - Time Records for the Duplex SEN Test No. DA-37.

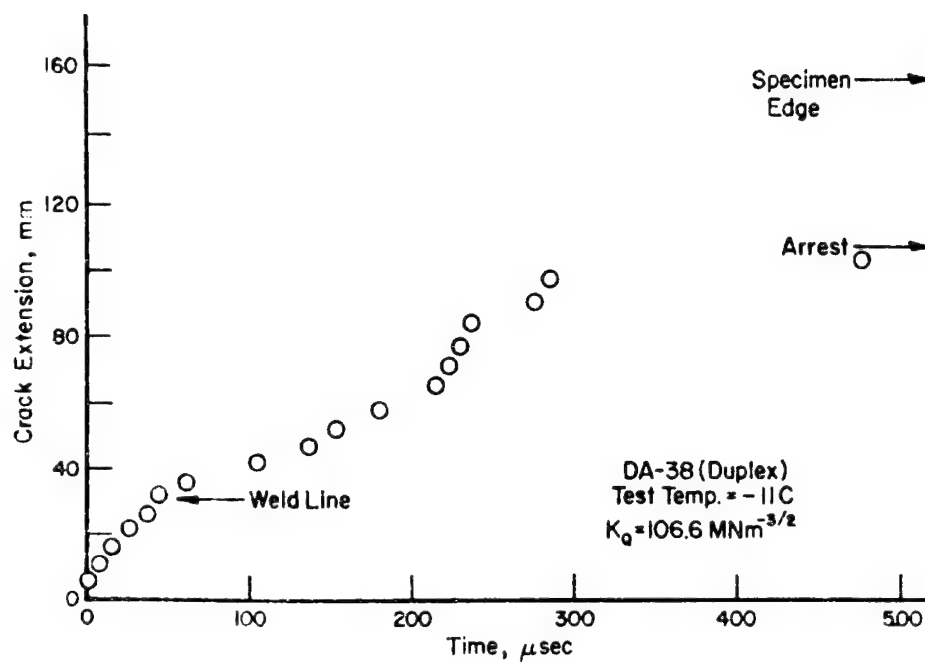


Fig. 4.5 Crack Extension - Time Records for the Duplex SEN Test No. DA-38.

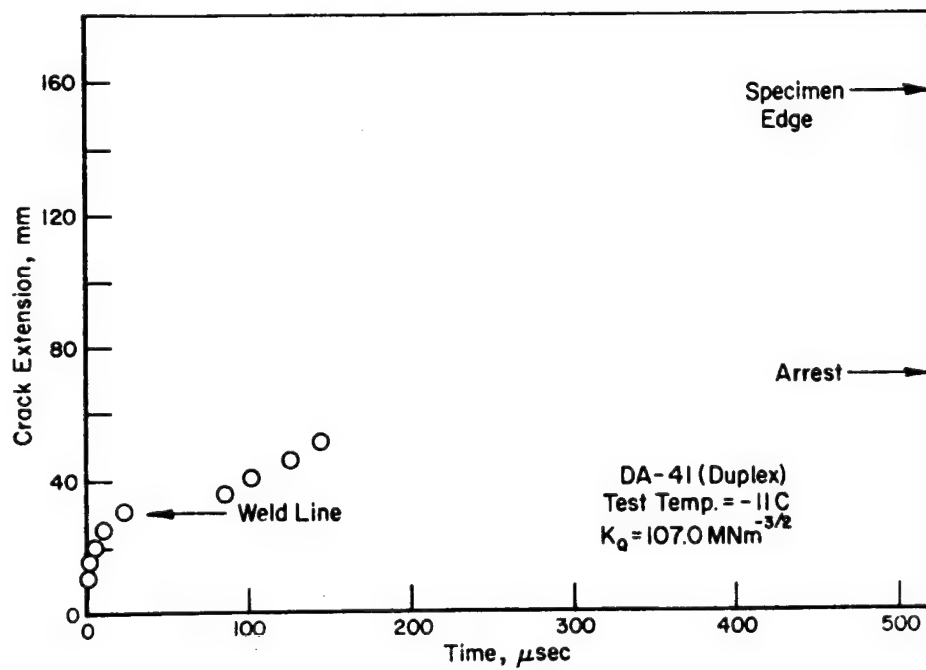


Fig. 4.6 Crack Extension - Time Records for the Duplex SEN Test No. DA-41.

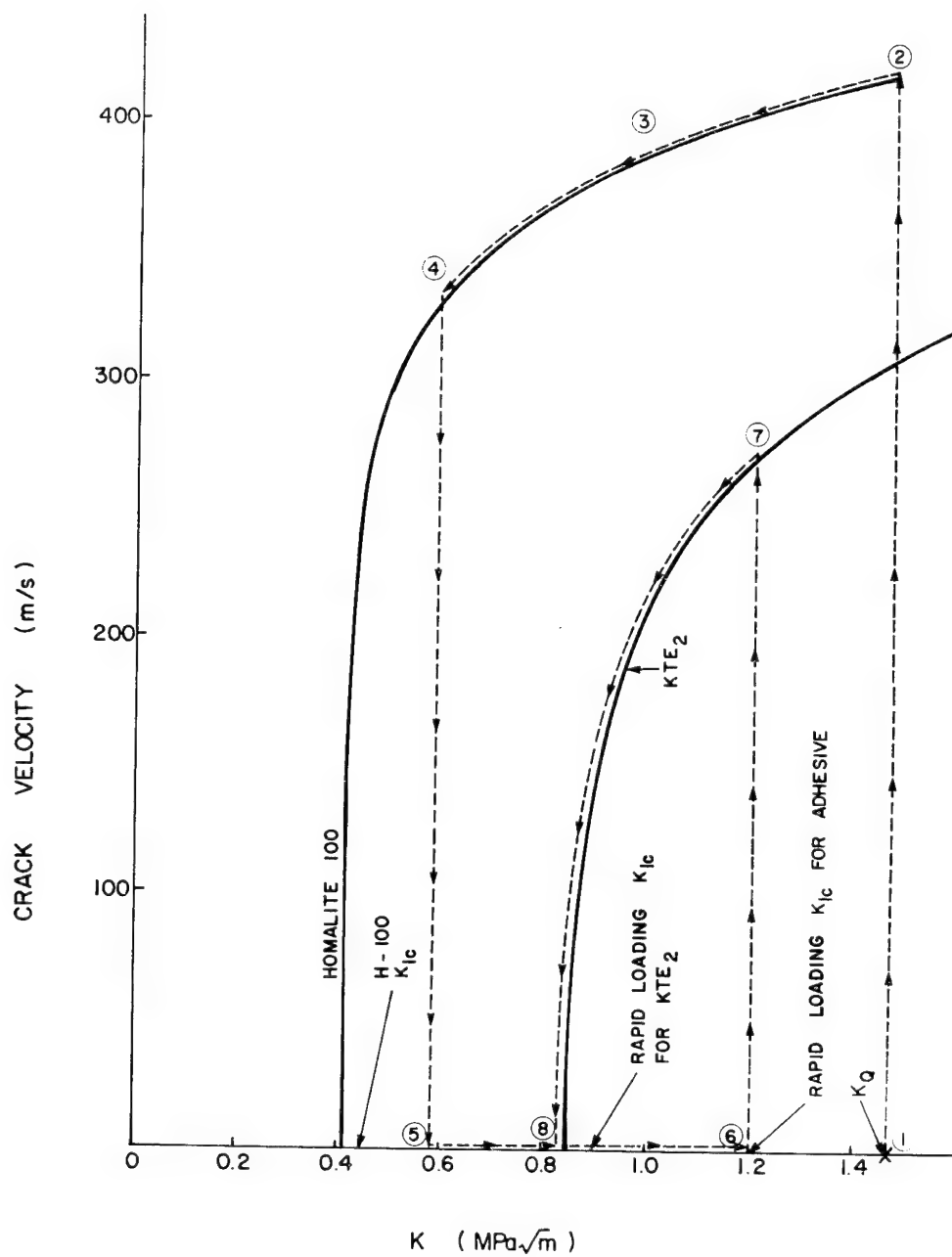


Fig. 4.7 \dot{a} vs K Relationship for Homalite 100 (starter section) and KTE₂ (arrest section) and the Crack Propagation History in the Duplex Specimen.

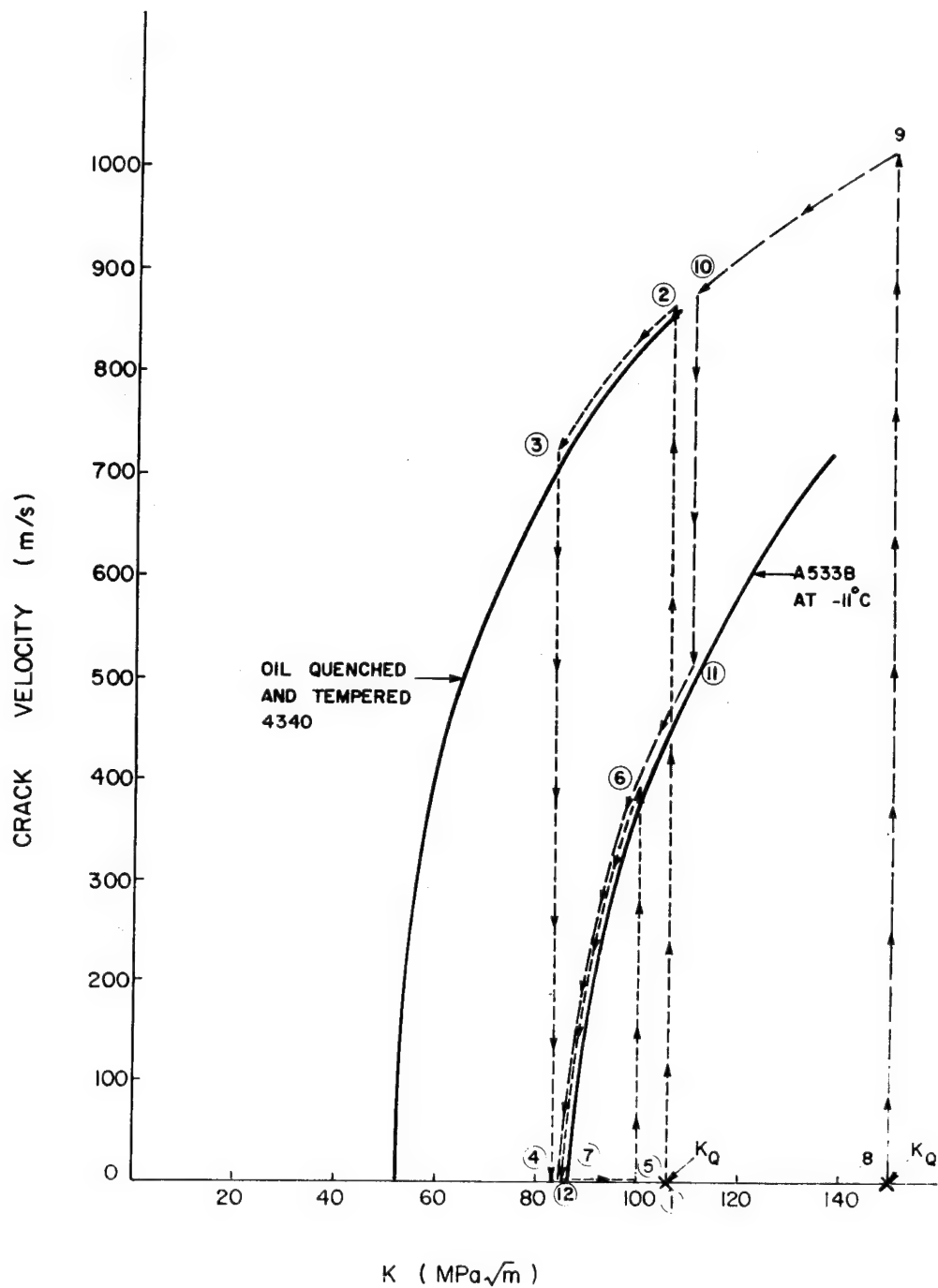


Fig. 4.8 Schematic \dot{a} vs K Relationships for 4340 and A 533 B Steels at -11°C .

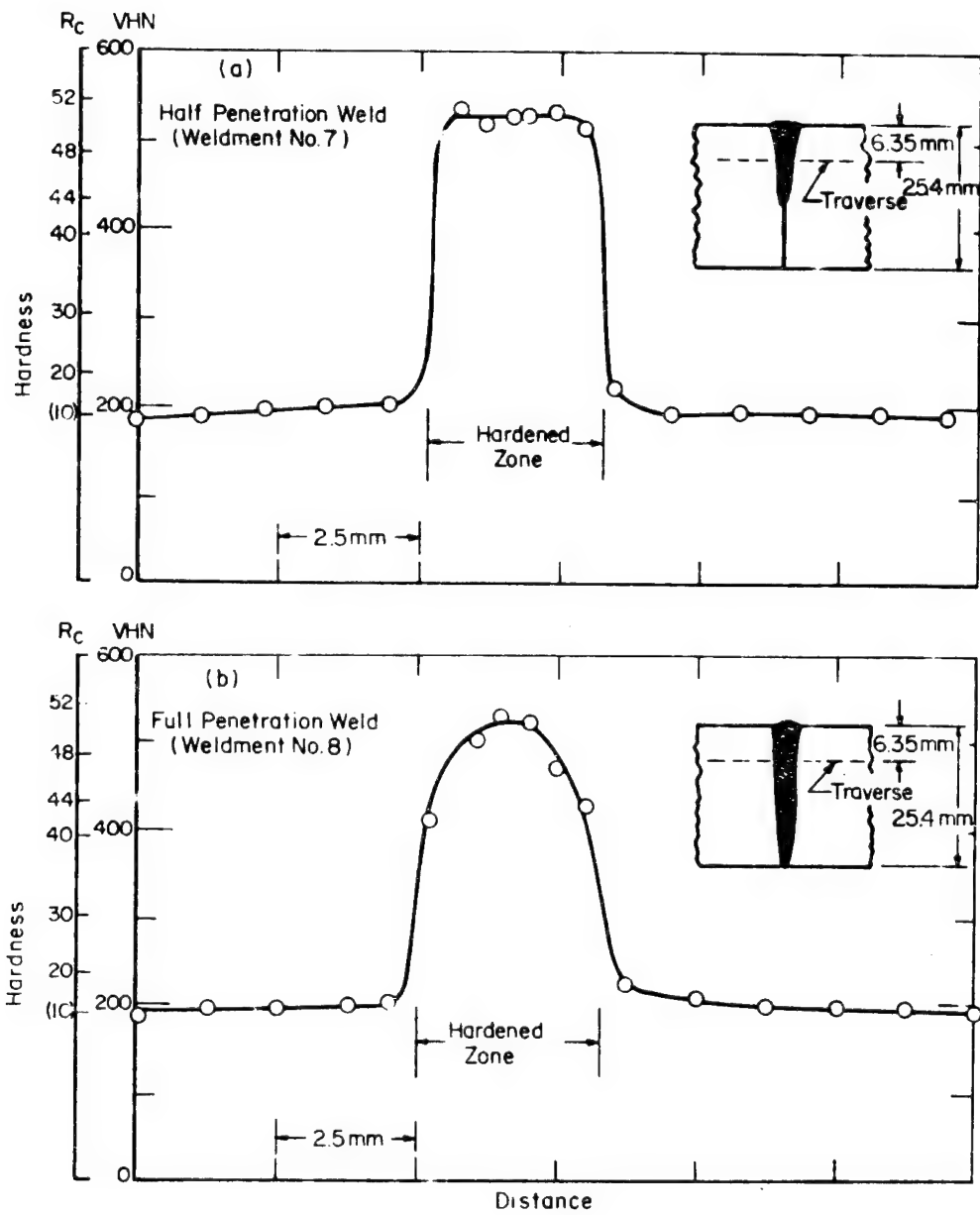


Fig. 4.9 Hardness Profiles for Electron Beam Welded A 533 B Specimen.

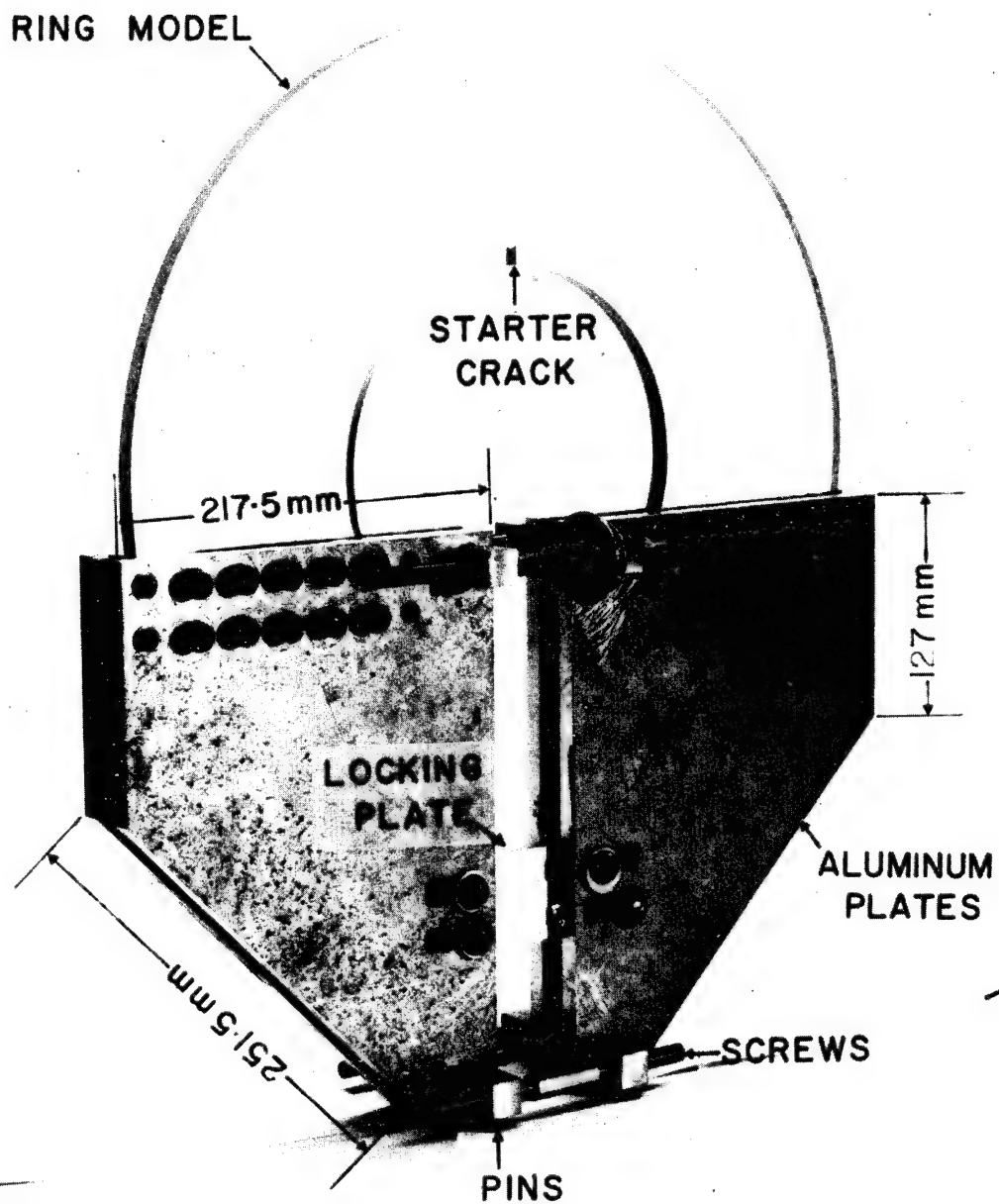


Fig. 5.1 Loading Fixture Attached to the Ring Specimen.

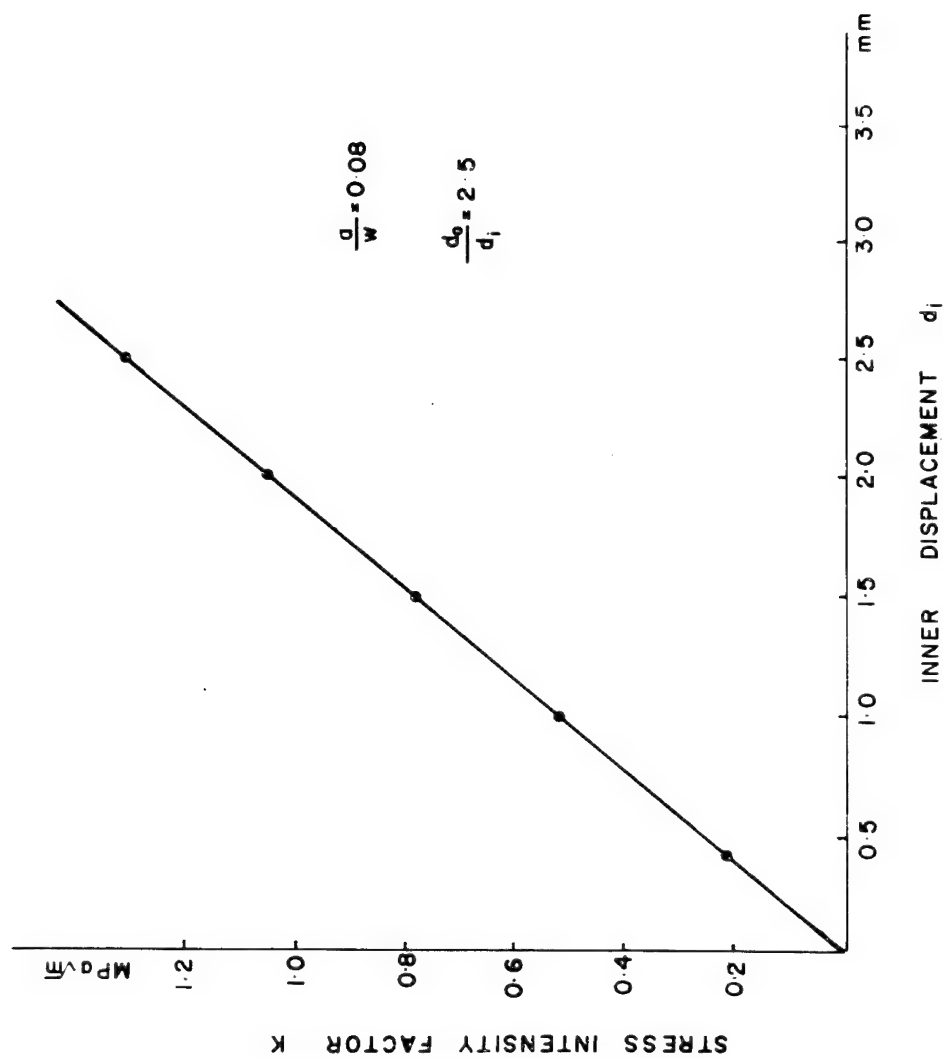


FIG. 5.2 Stress Intensity Factor K as a Function of Inner Pin Displacement d_i .

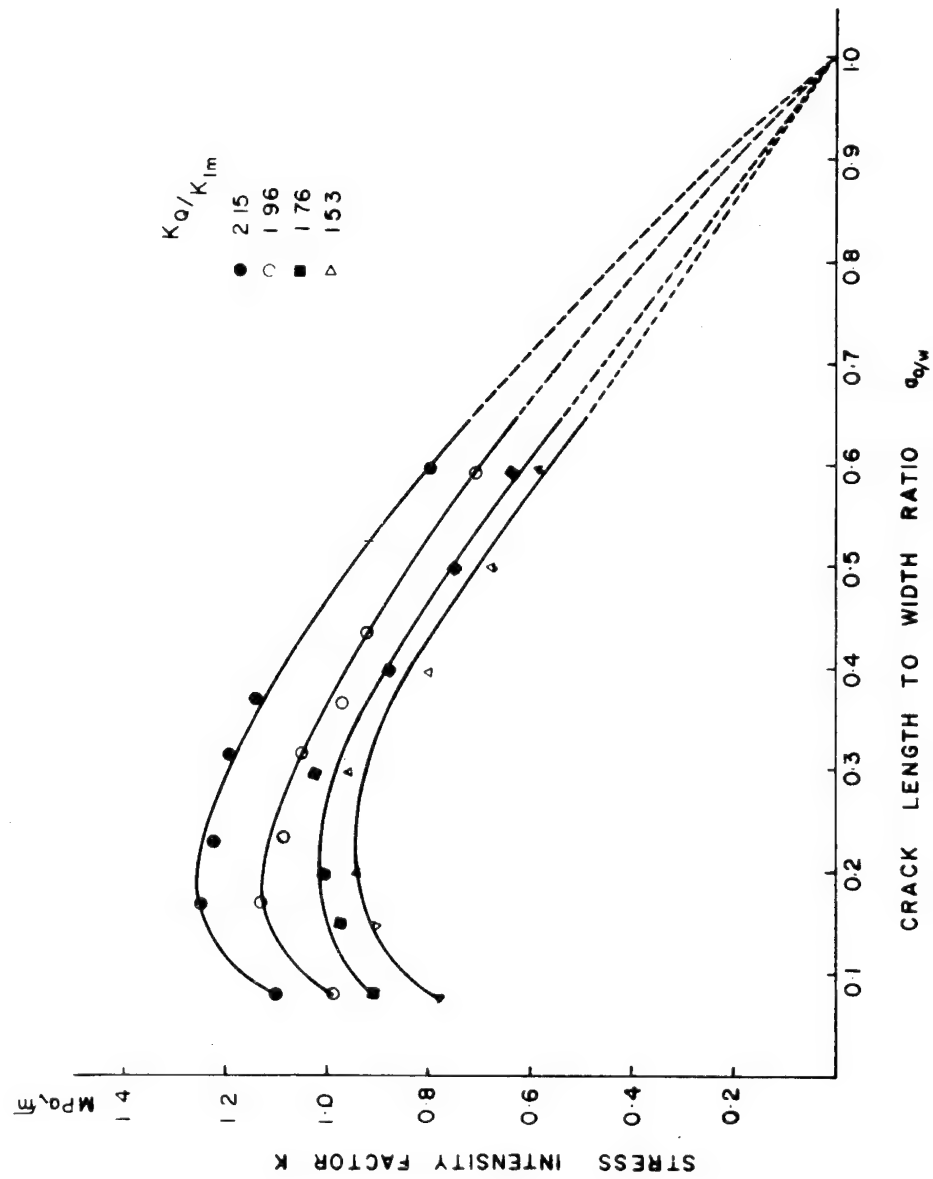


Fig. 5.3 Stress Intensity Factor K as a Function of Starter Crack Length to Width Ratio a_0/w .

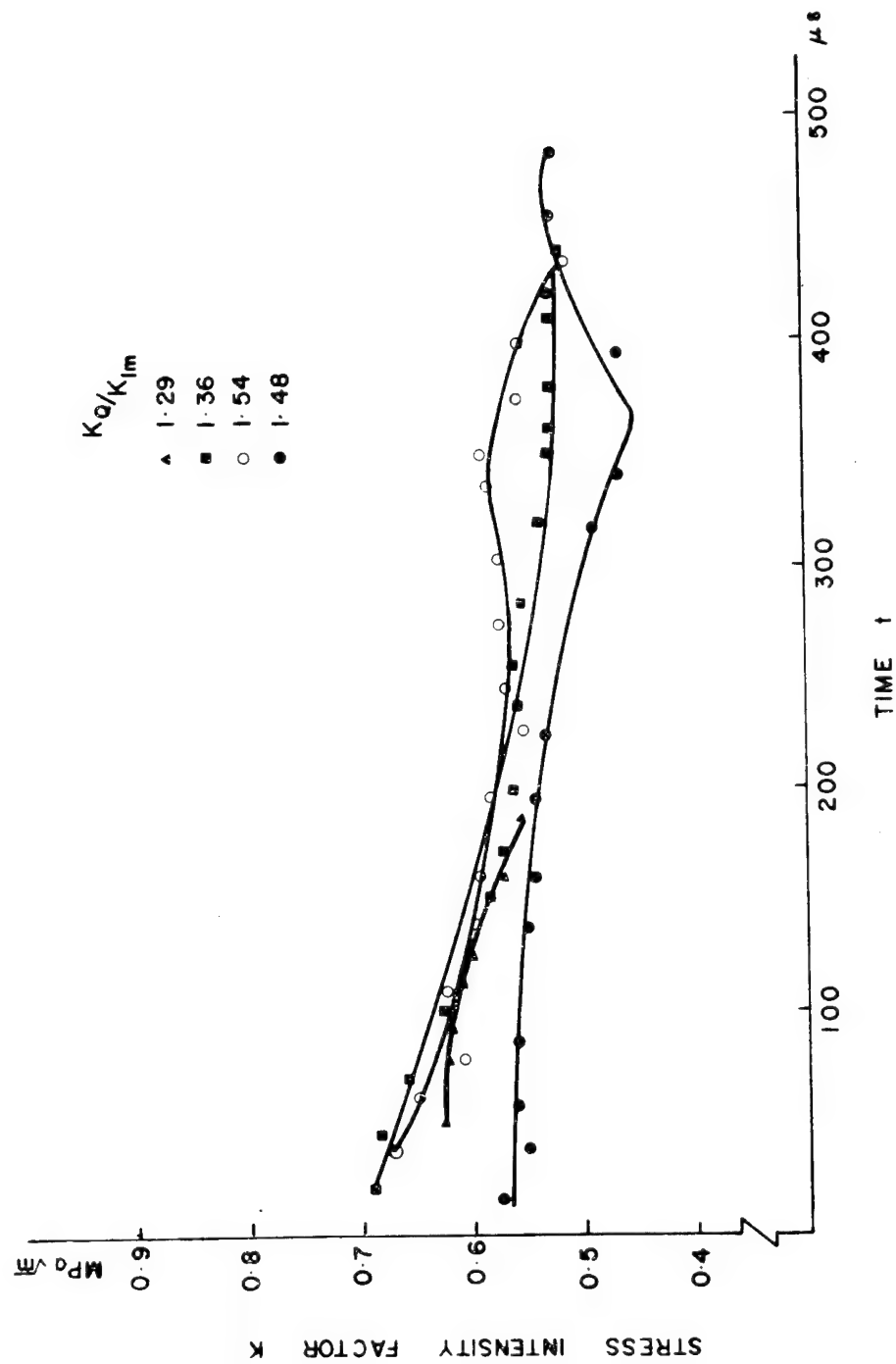


Fig. 5.4 Stress Intensity Factor K as a Function of Time t for Models R-2 through R-5.

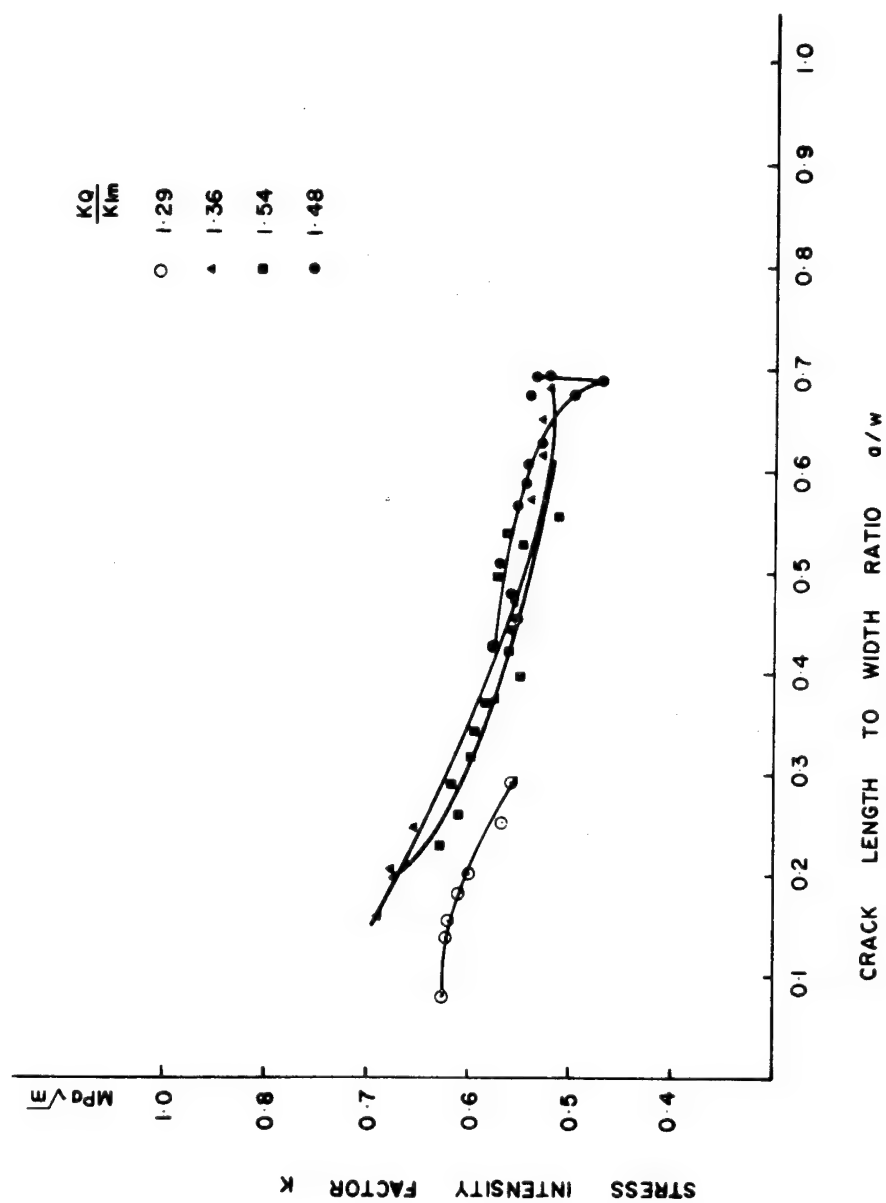


Fig. 5.5 Stress Intensity Factor K as a Function of Crack Length to Width Ratio a/w for Model R-2 through R-5.

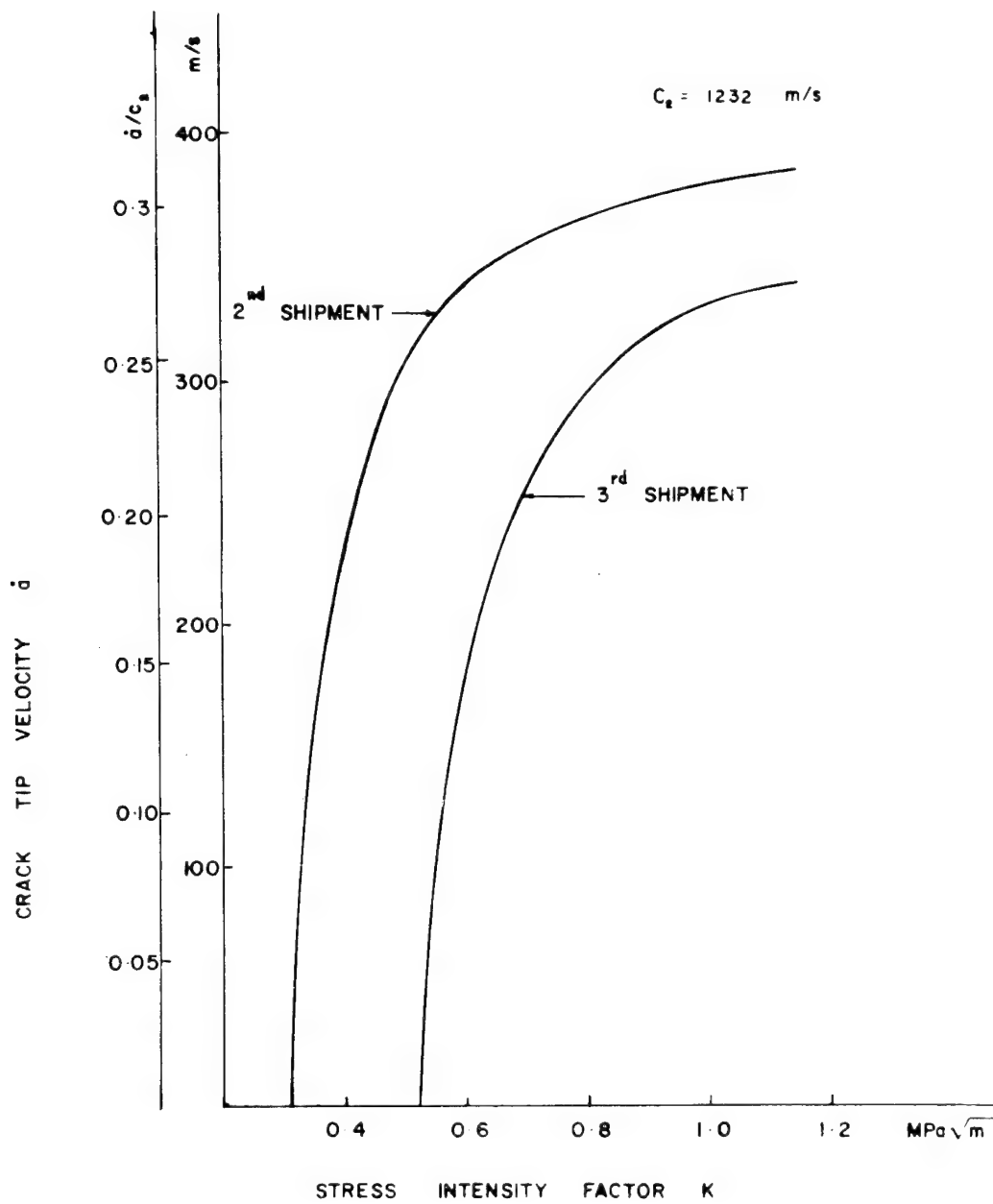


Fig. 5.6 Stress Intensity Factor K as a Function of Crack Velocity \dot{a} - Homalite 100 - 2nd Shipment and 3rd Shipment.

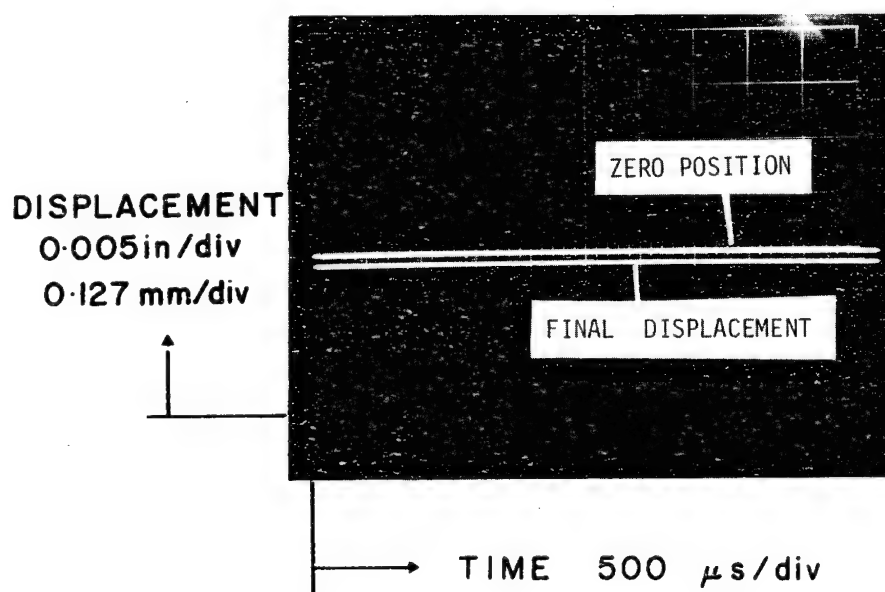
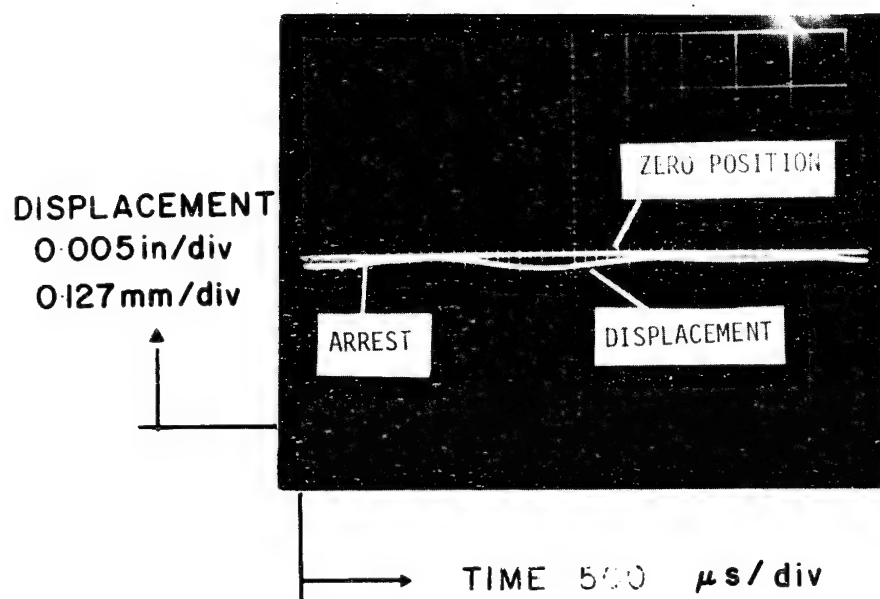


Fig. 5.7 Outer Pin Displacement as a Function of Time for Model R-6.

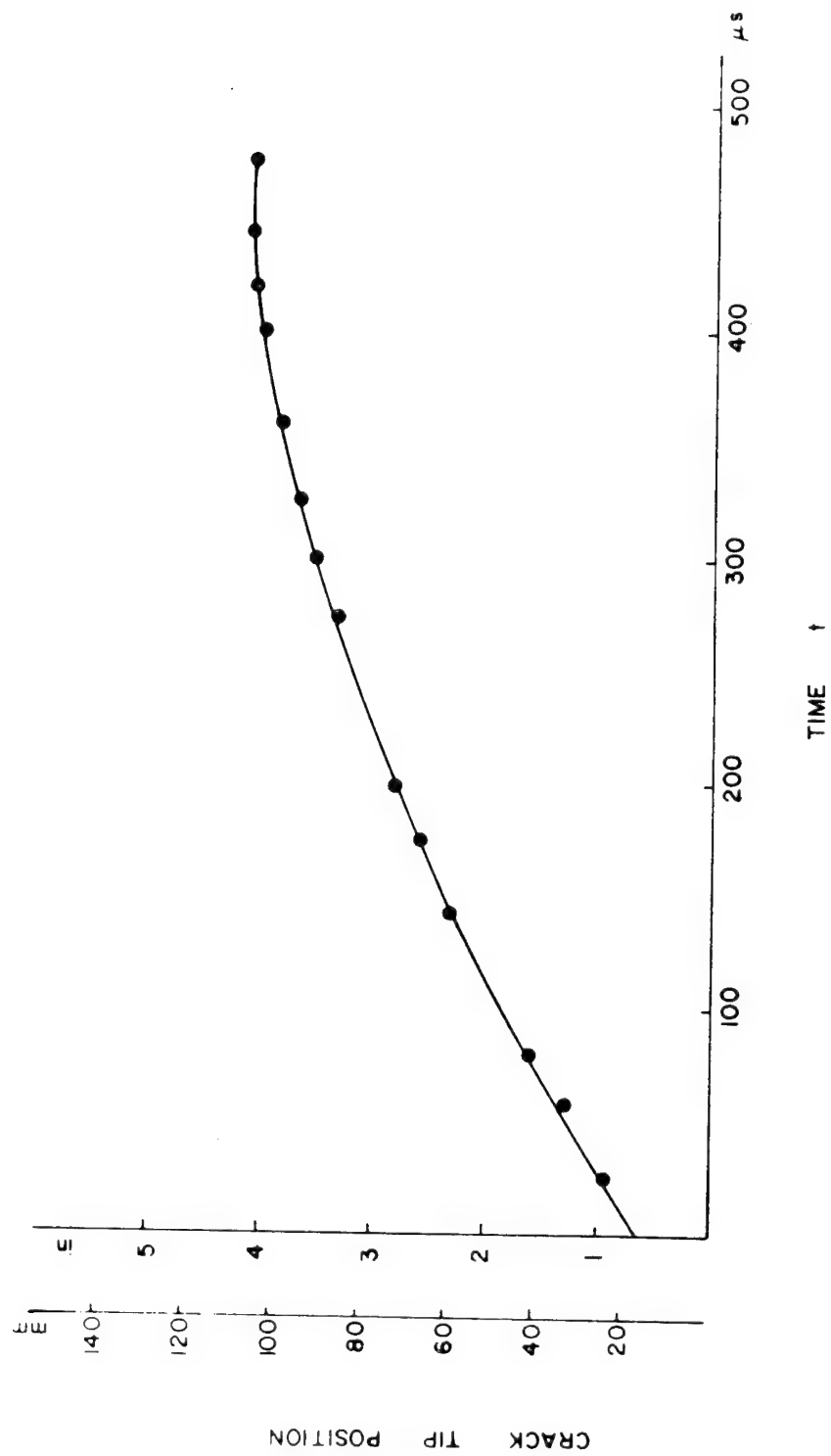


Fig. 5.8 Crack Tip Position a as a Function of Time t for Model R-6.

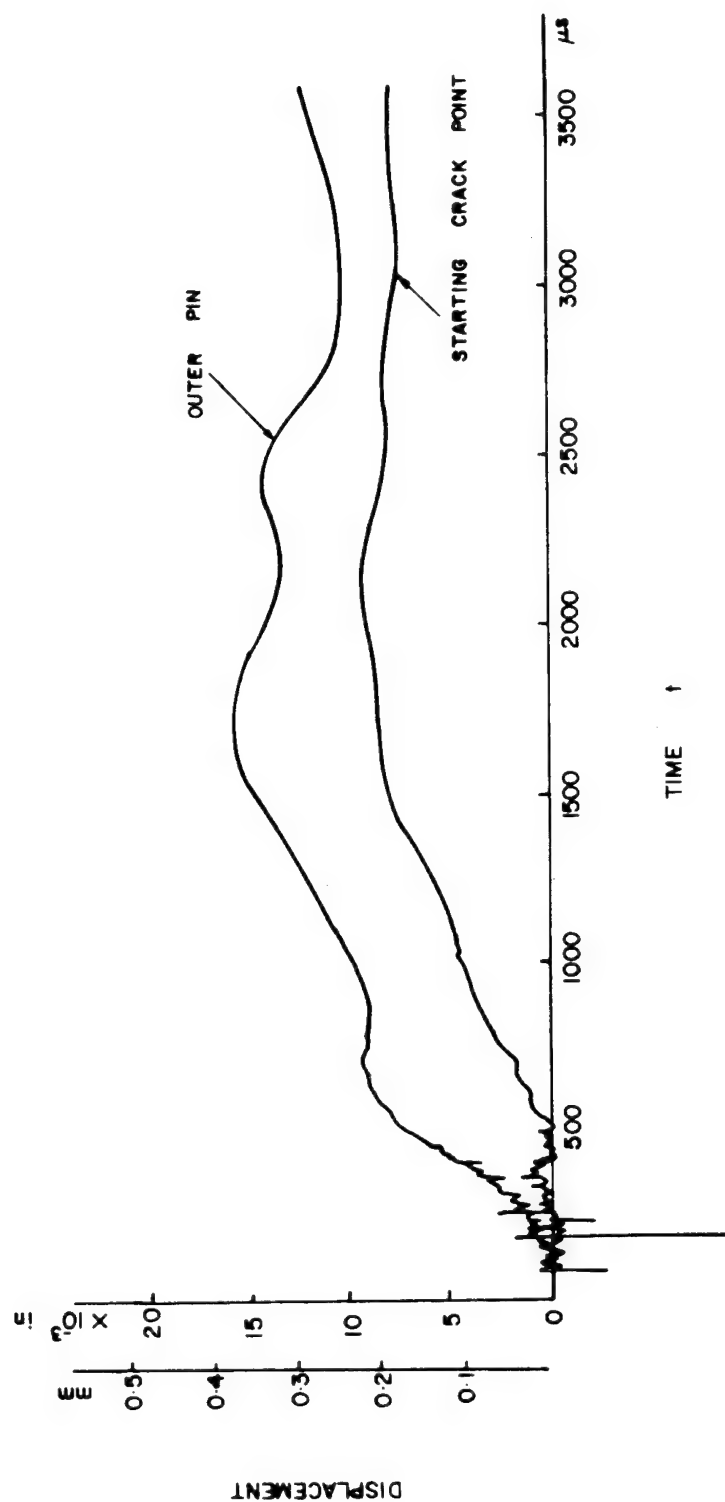


Fig. 5.9 Outer Pin and Starting Crack Point Displacement as a Function of Time for Model R-7.

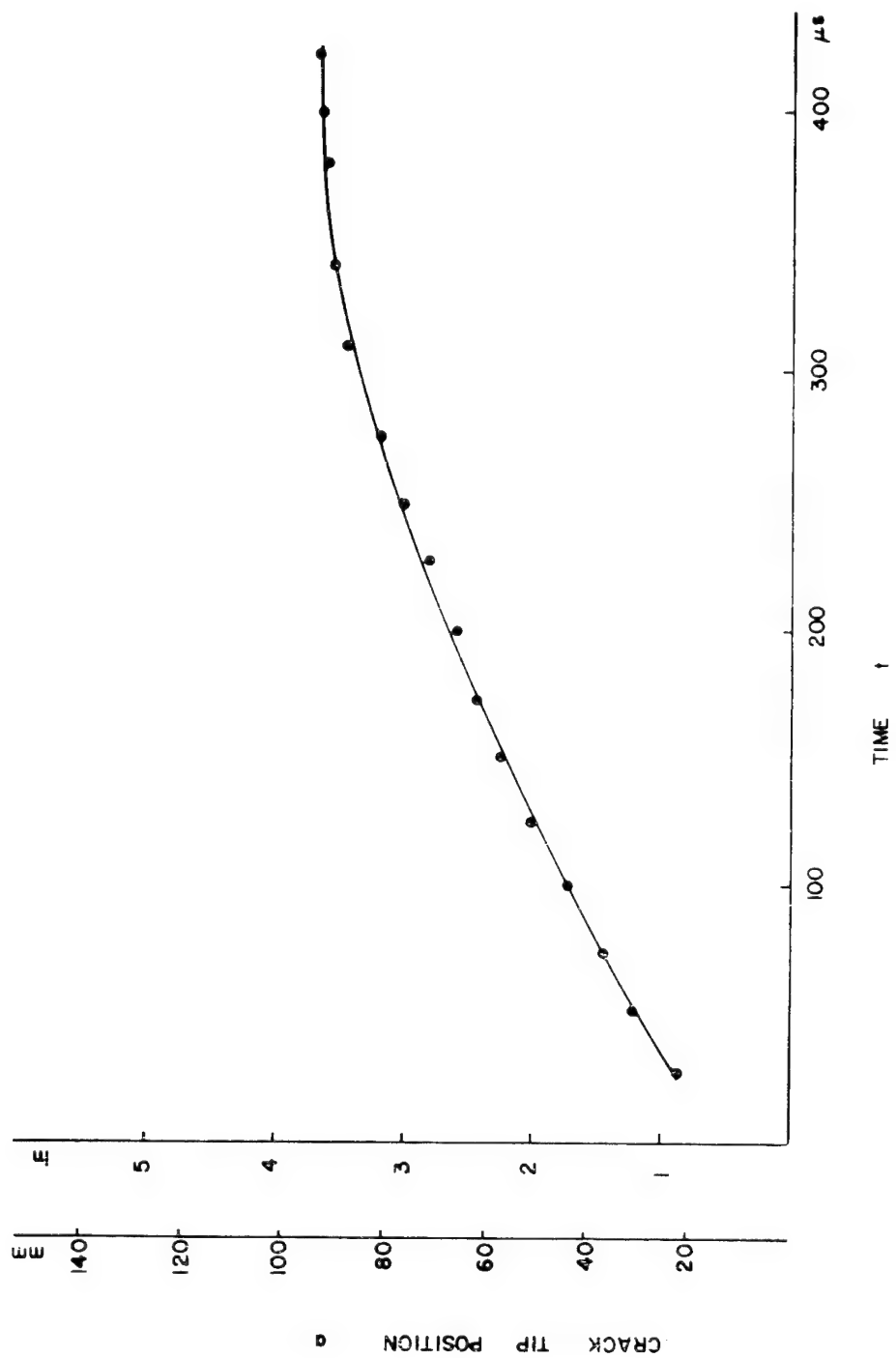


Fig. 5.10 Crack Tip Position a as a Function of Time t for Model R-7.

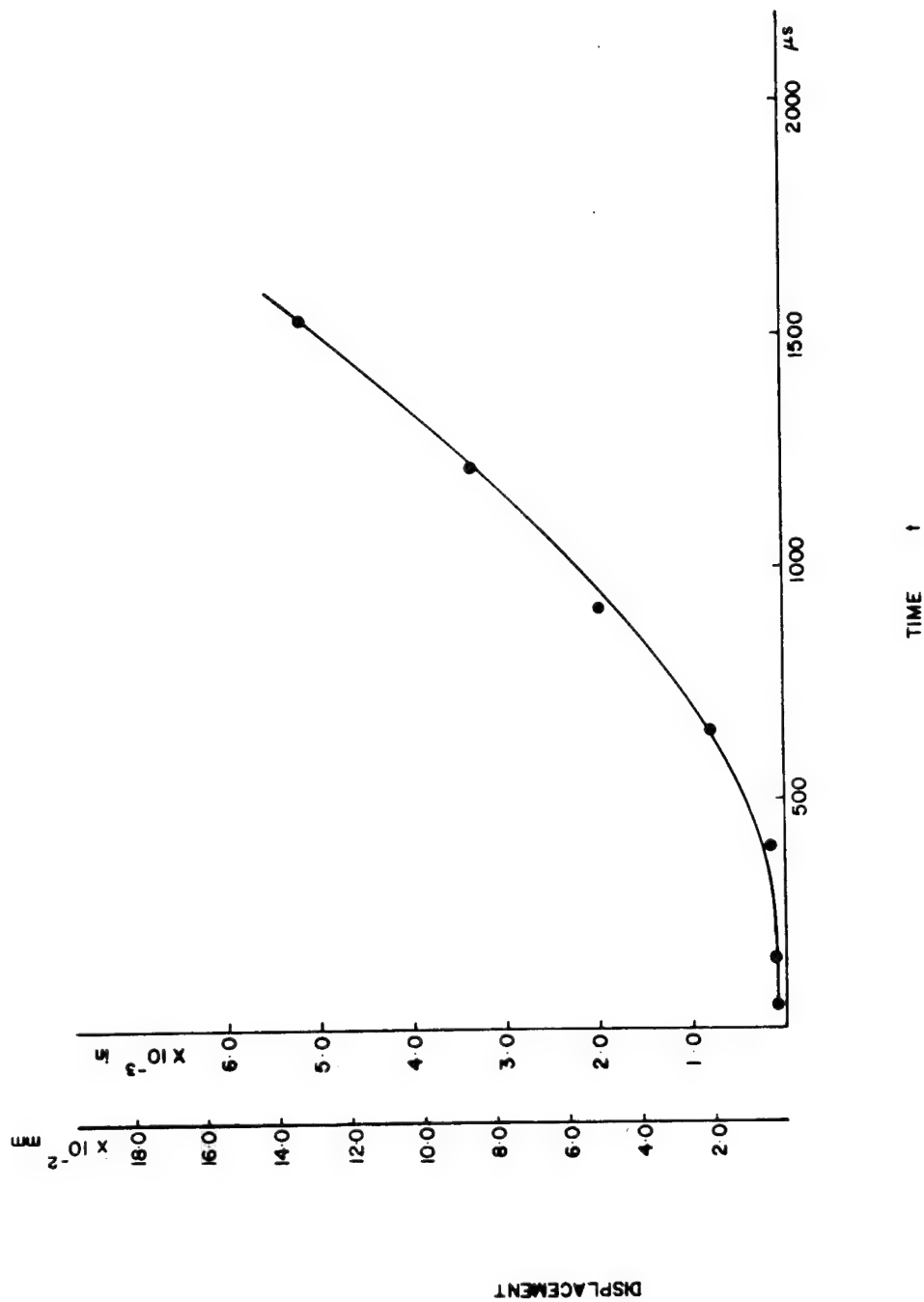


Fig. 5.11 Inner Pin Displacement as a Function of Time for Model R-8.

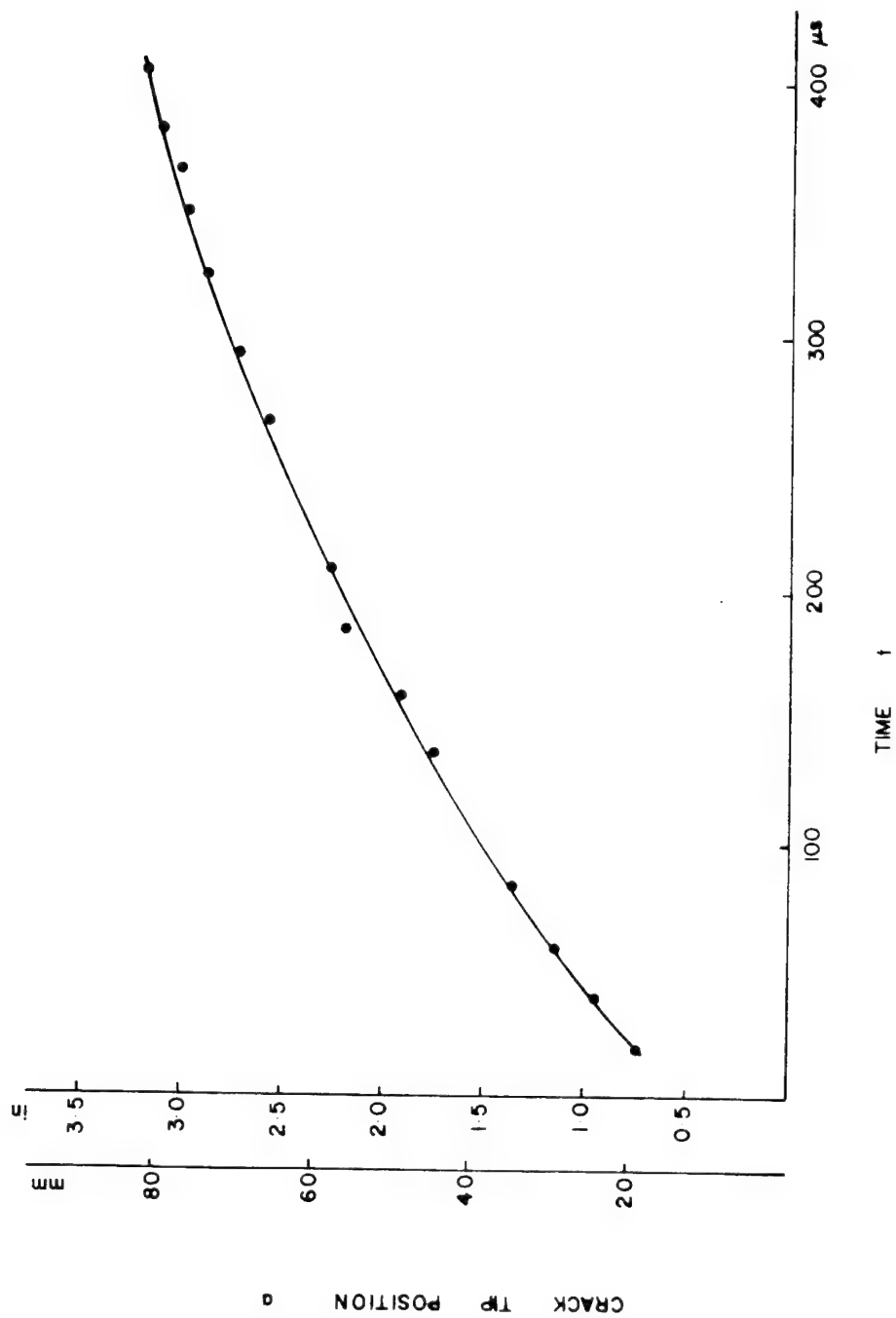


Fig. 5.12 Crack Tip Position as a Function of Time for Model R-8.

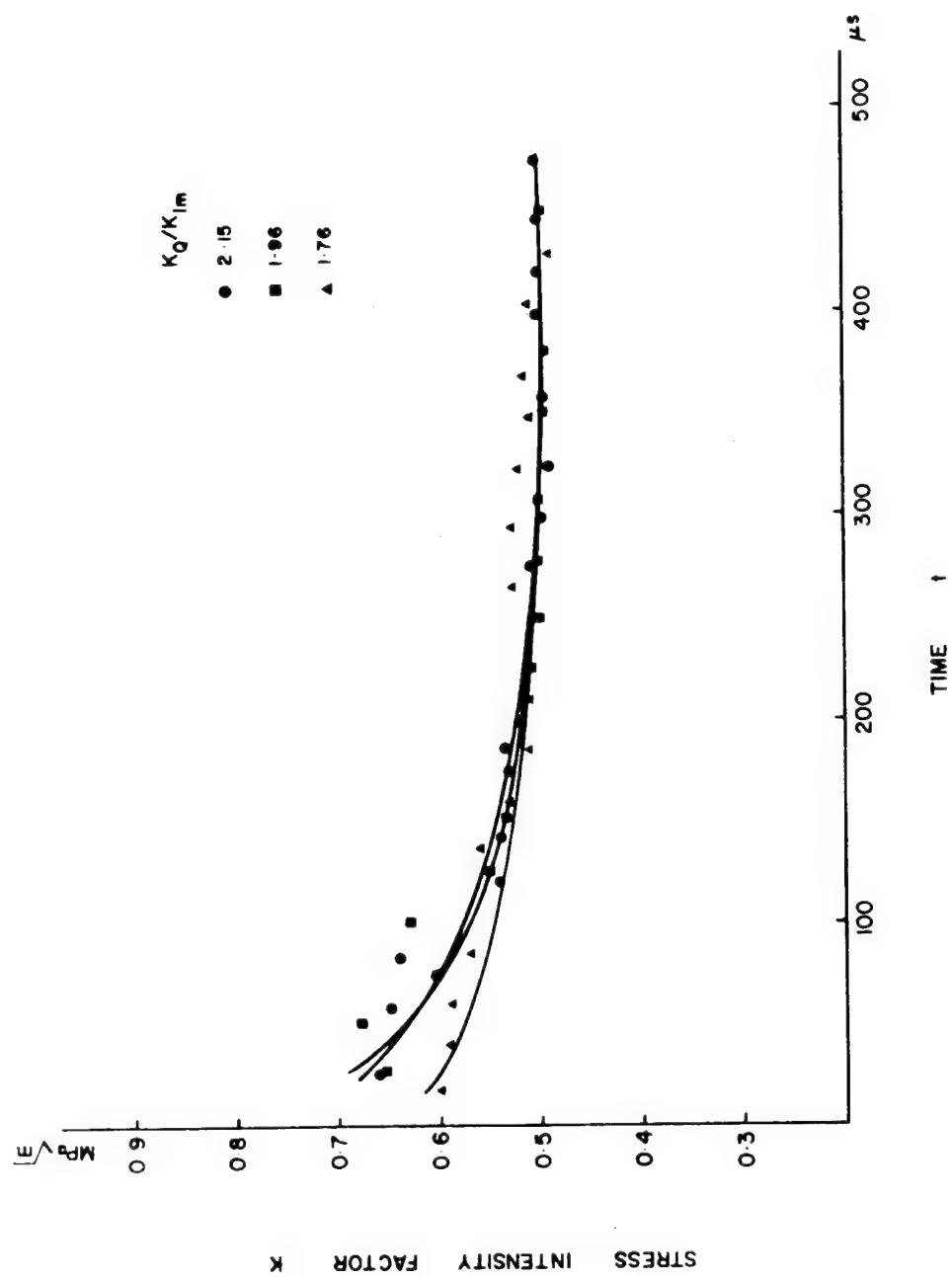


Fig. 5.13 Stress Intensity Factor K as a Function of Time t for Models R-6 through R-8.

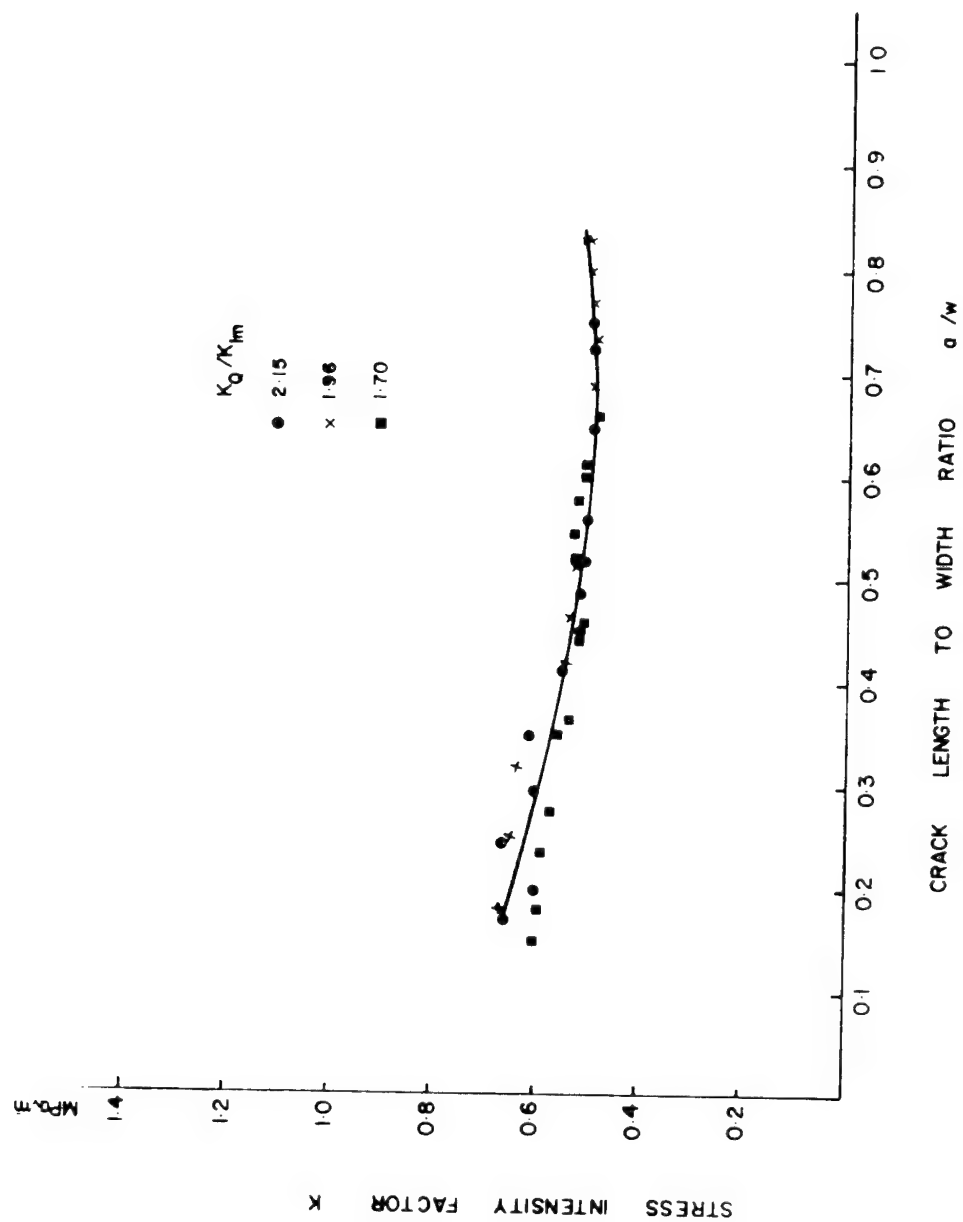


Fig. 5.14 Stress Intensity Factor K as a Function of a/w for Models R-6 through R-8.

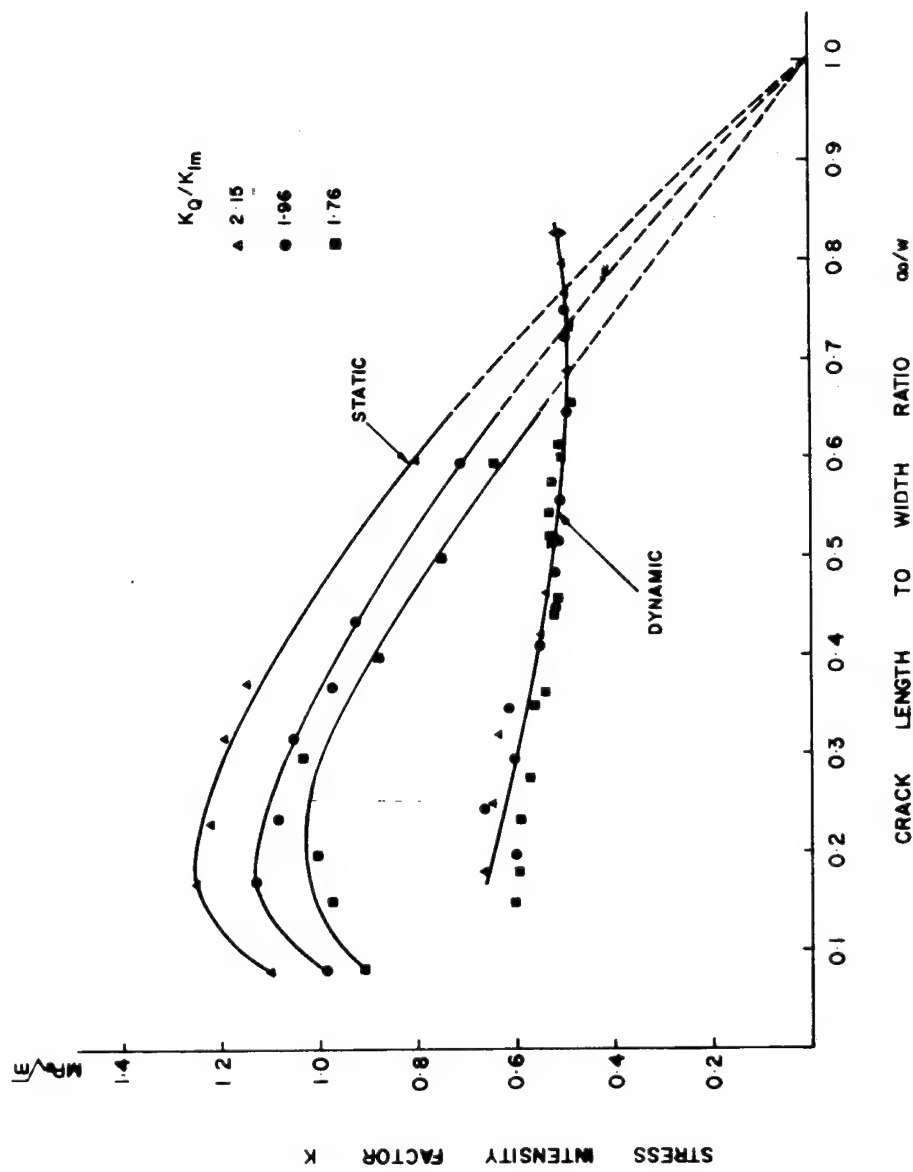


Fig. 5.15 Static and Dynamic Stress Intensity Factor K as a Function of a/w .

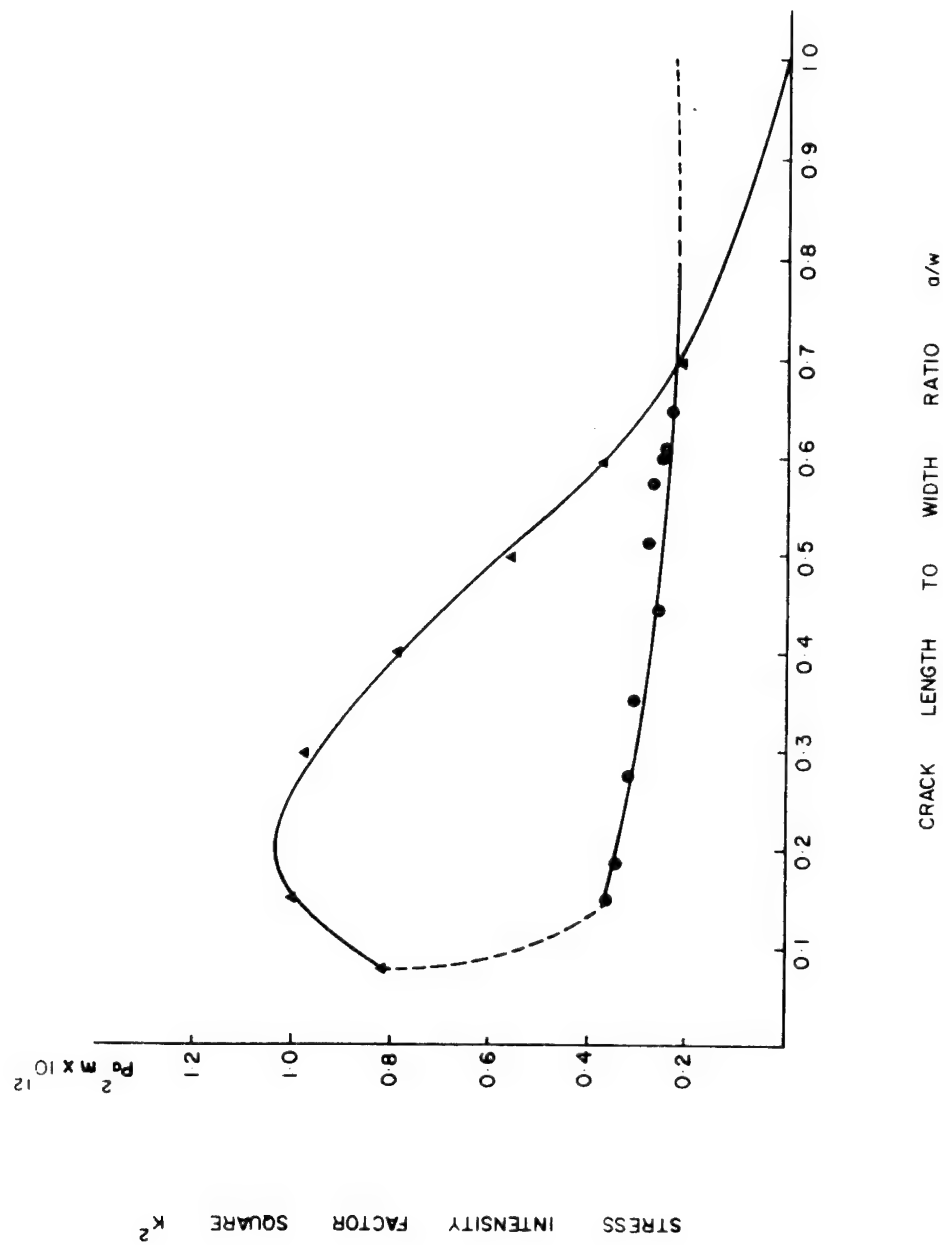


Fig. 5.16 Static and Dynamic Stress Intensity Factor Square K^2 as a Function of a/w .

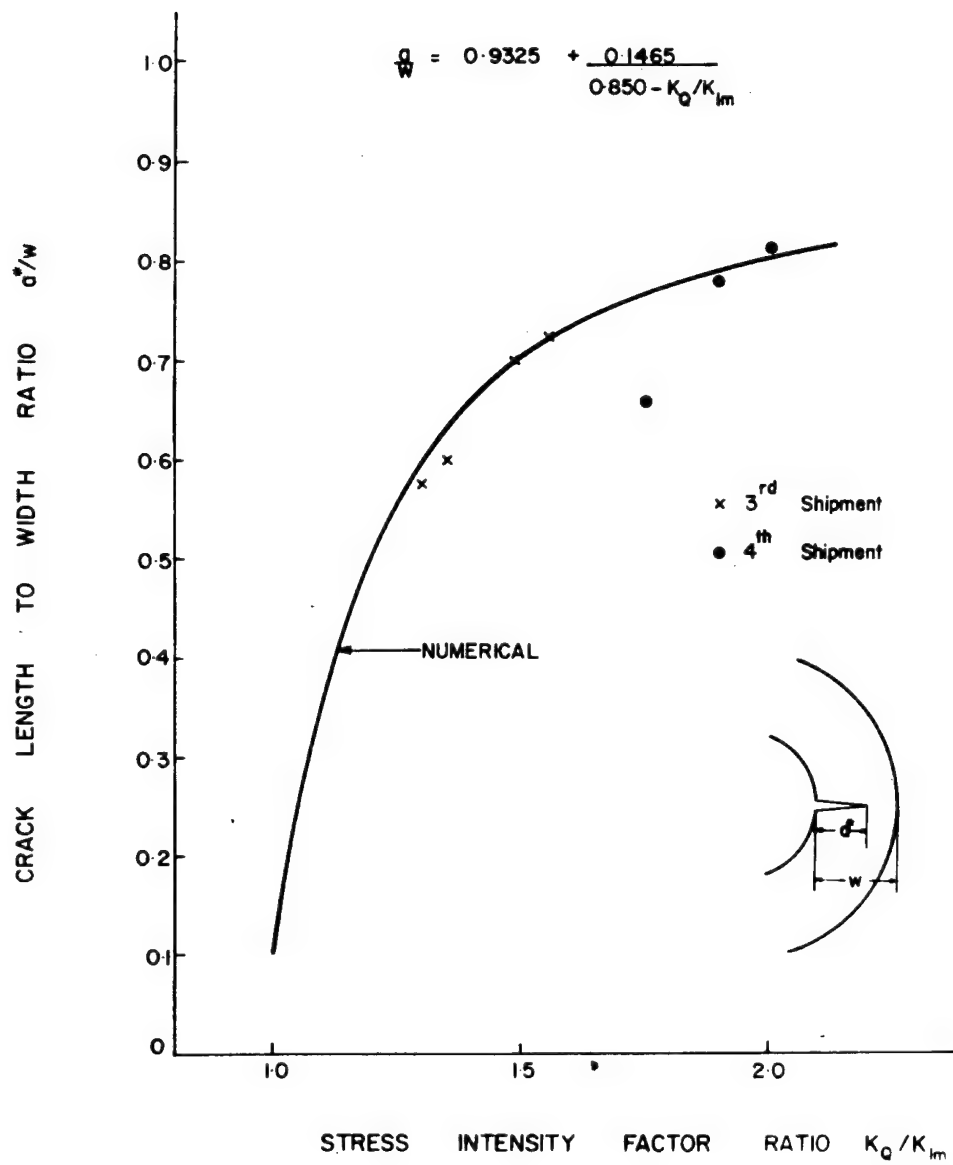


Fig. 5.17 Crack Jump Distance a^*/W as a Function of K_Q/K_{Im} .

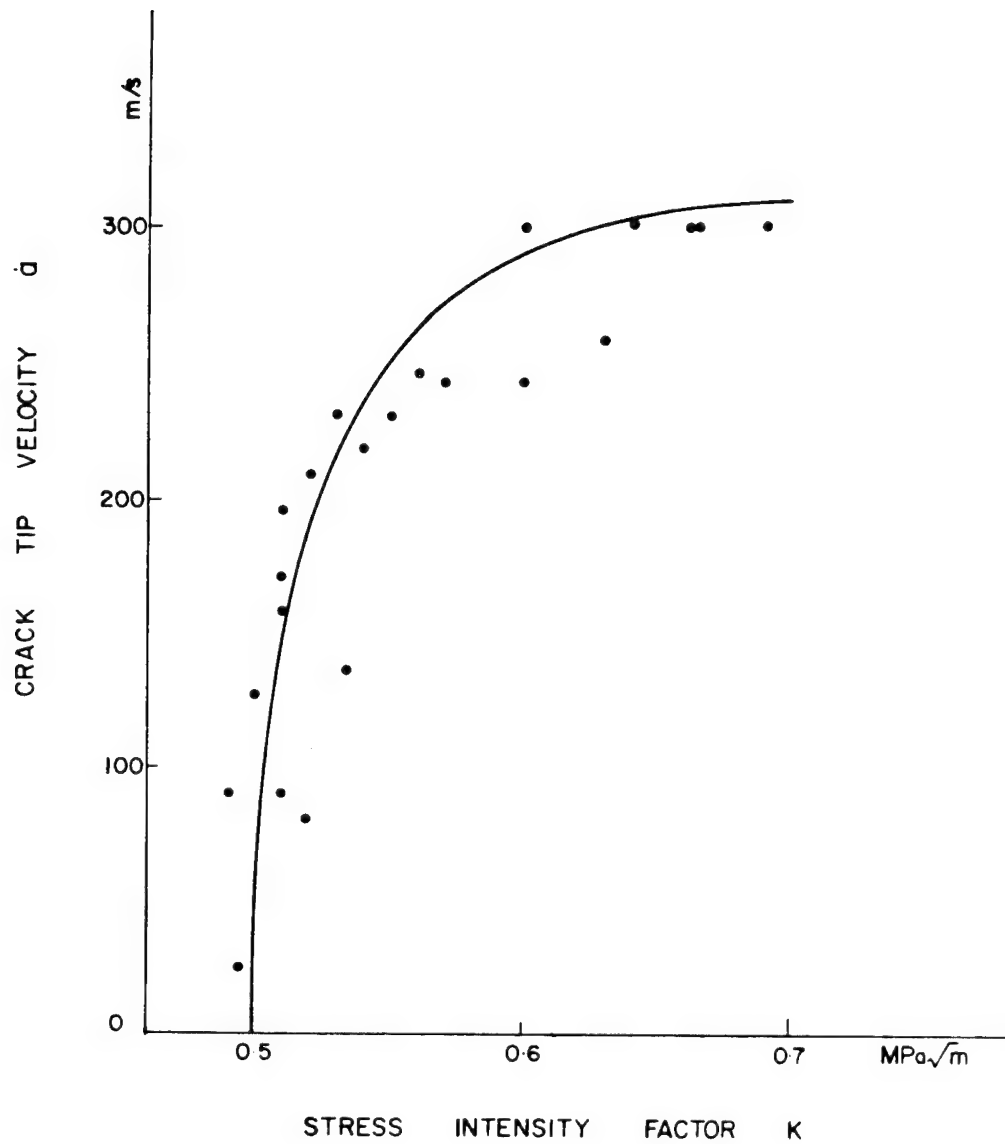


Fig. 5.18 Stress Intensity Factor K as a Function of Crack Velocity \dot{a} for 4th Shipment of Homalite 100.

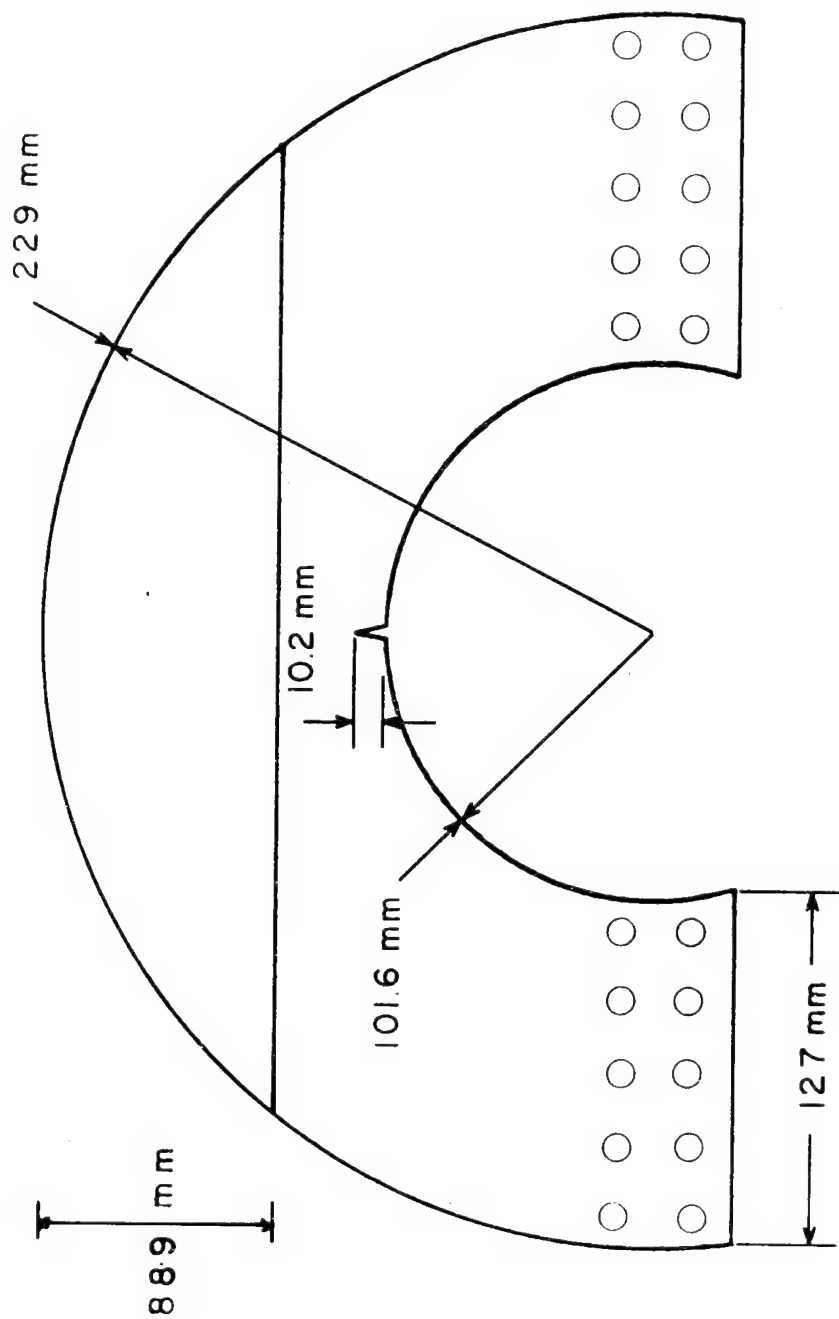


Fig. 5.19 Geometry of the Duplex Specimen.

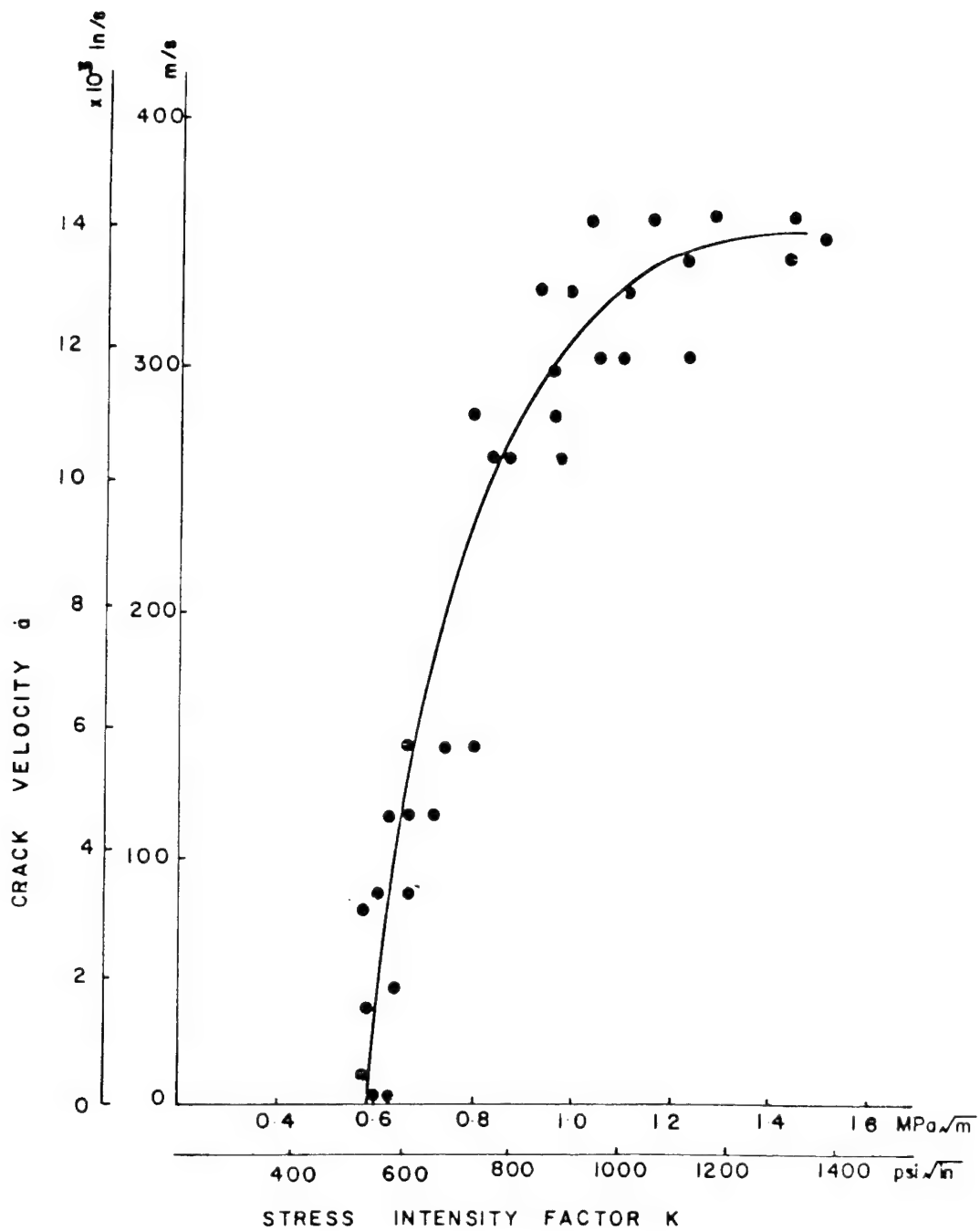
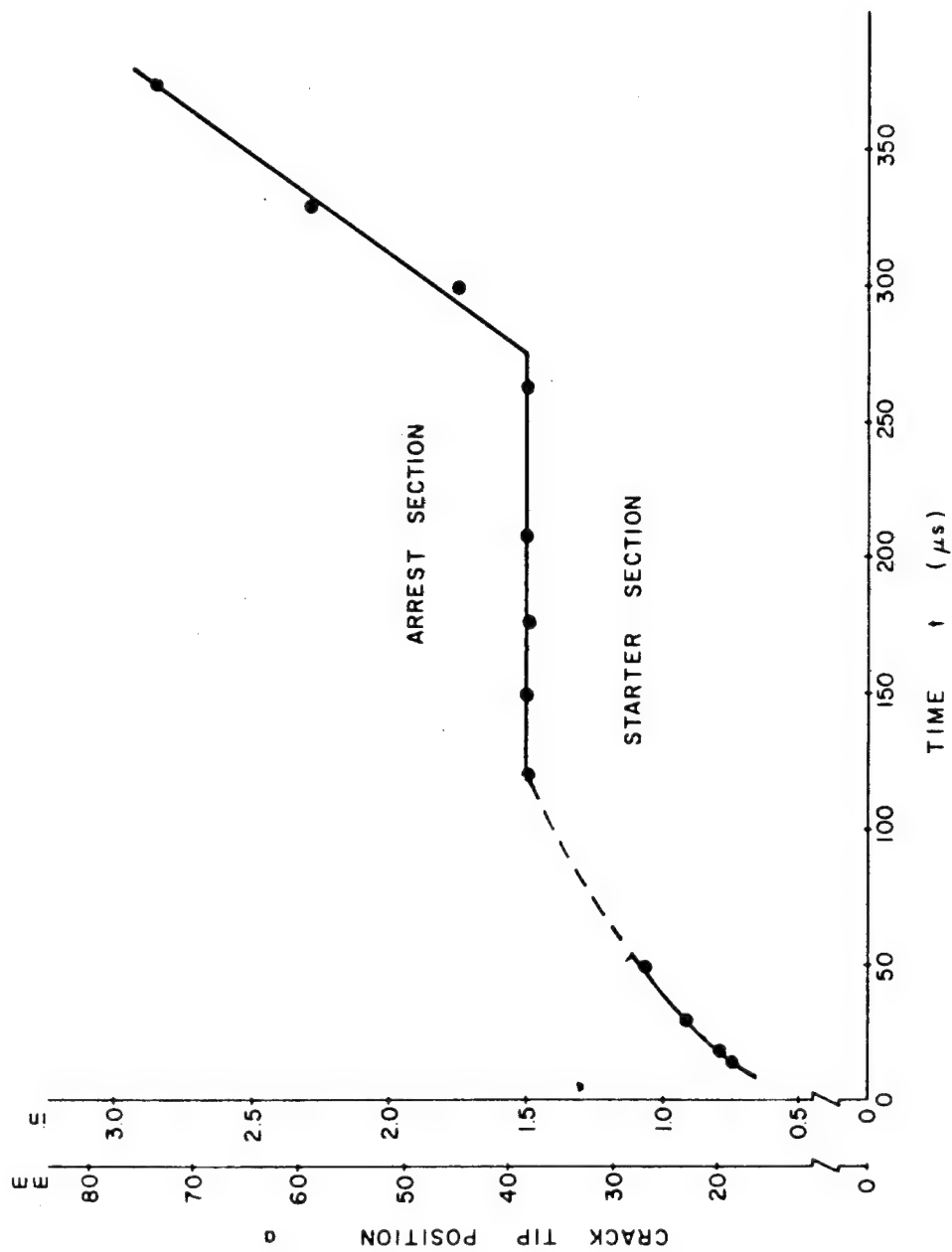


Fig. 5.20 Stress Intensity Factor K as a Function of Crack Velocity for Araldite B.



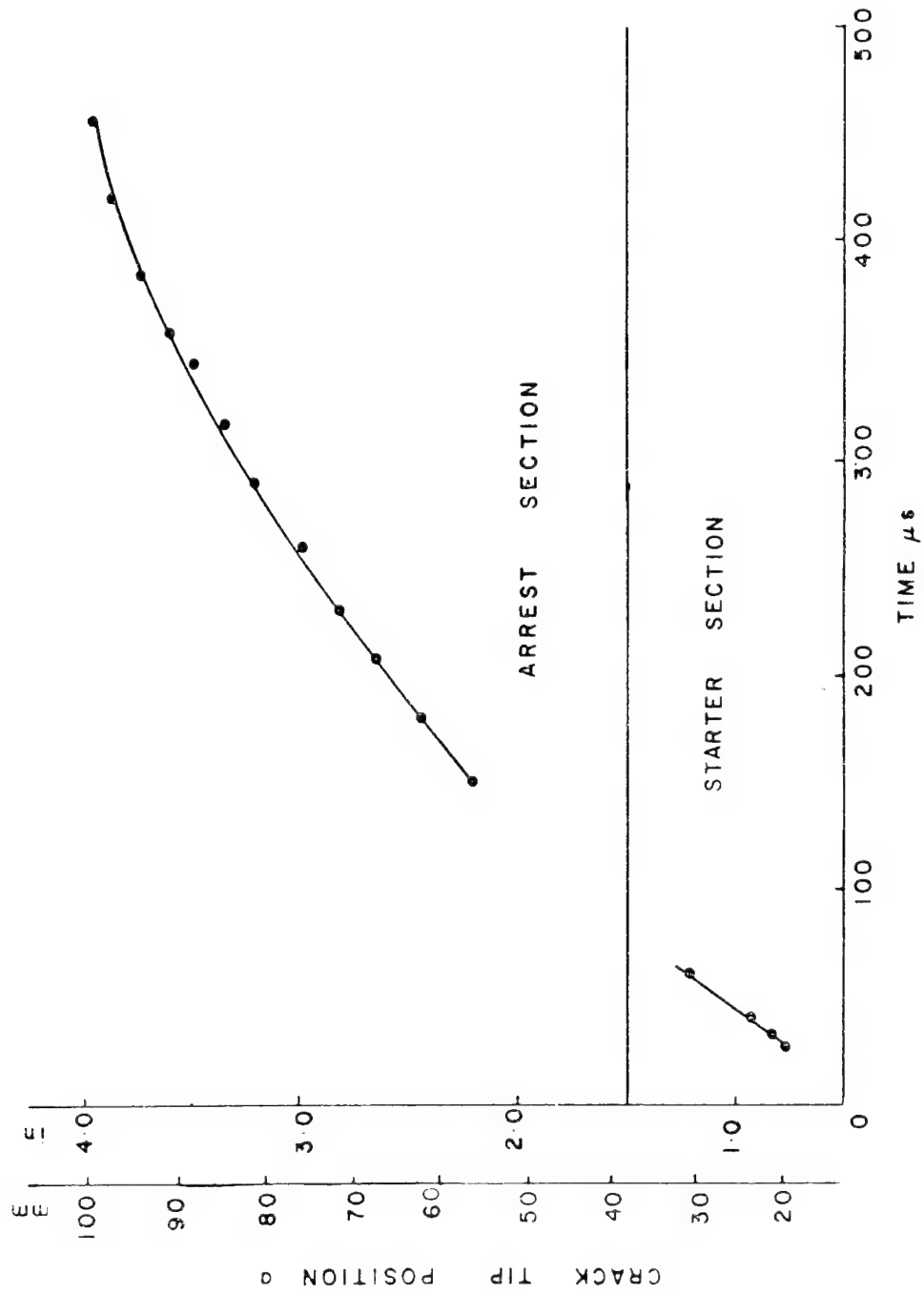


Fig. 5.22 Crack Tip Position as a Function of Time for Model R-10.

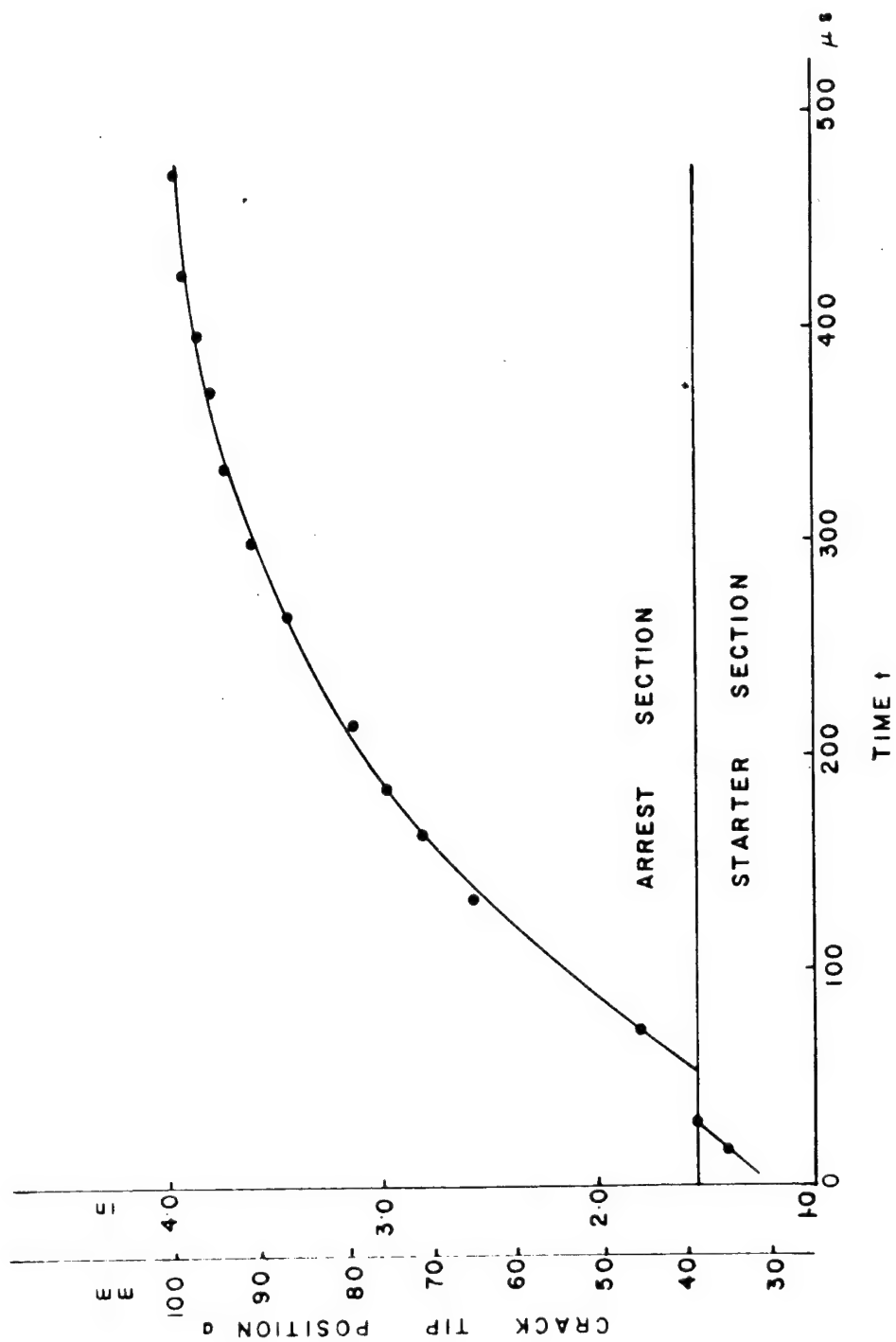


Fig. 5.23 Crack Tip Position as a Function of Time for Model R-11.

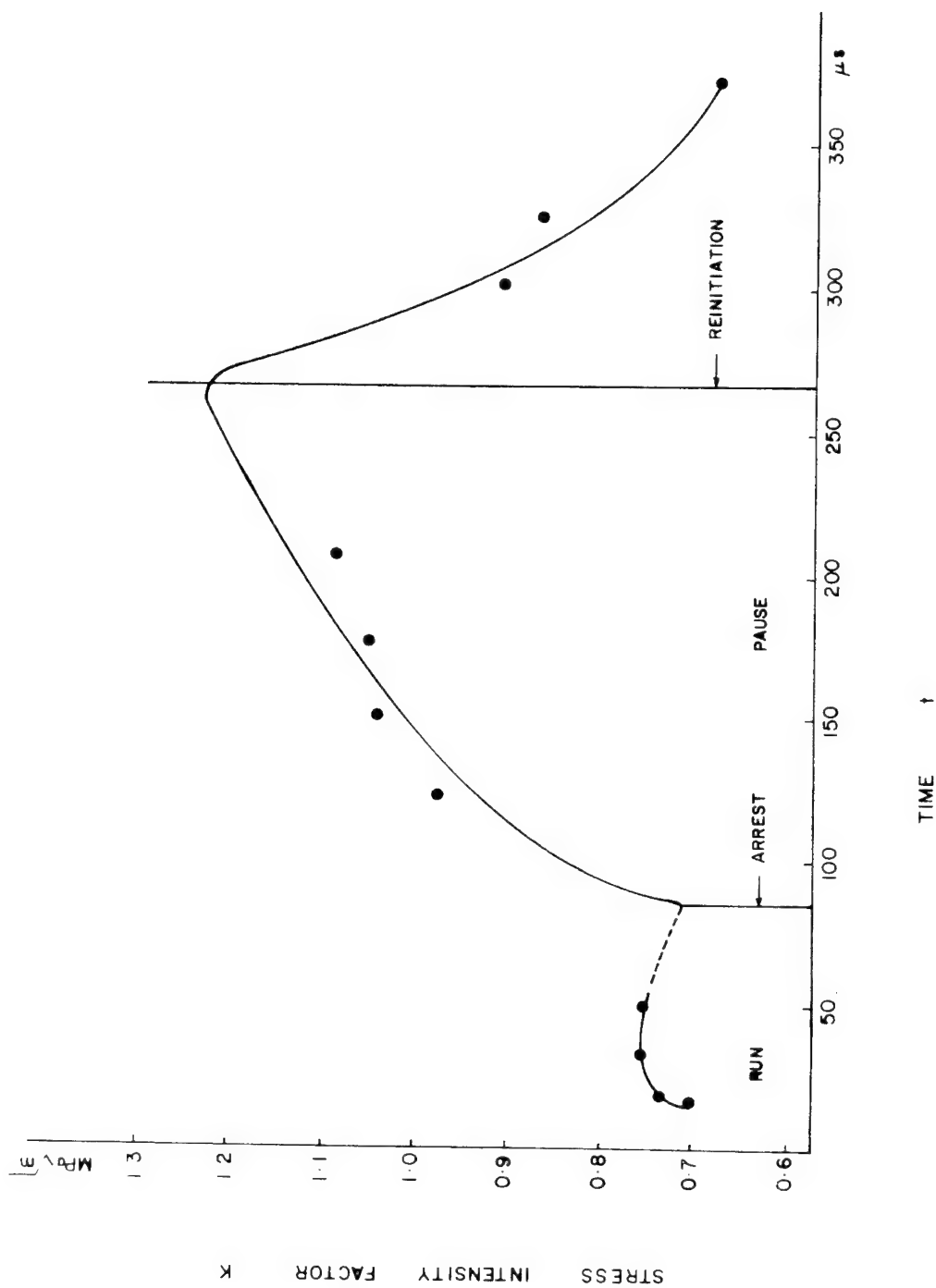


Fig. 5.24 Stress Intensity Factor K as a Function of Time for Model R-9.

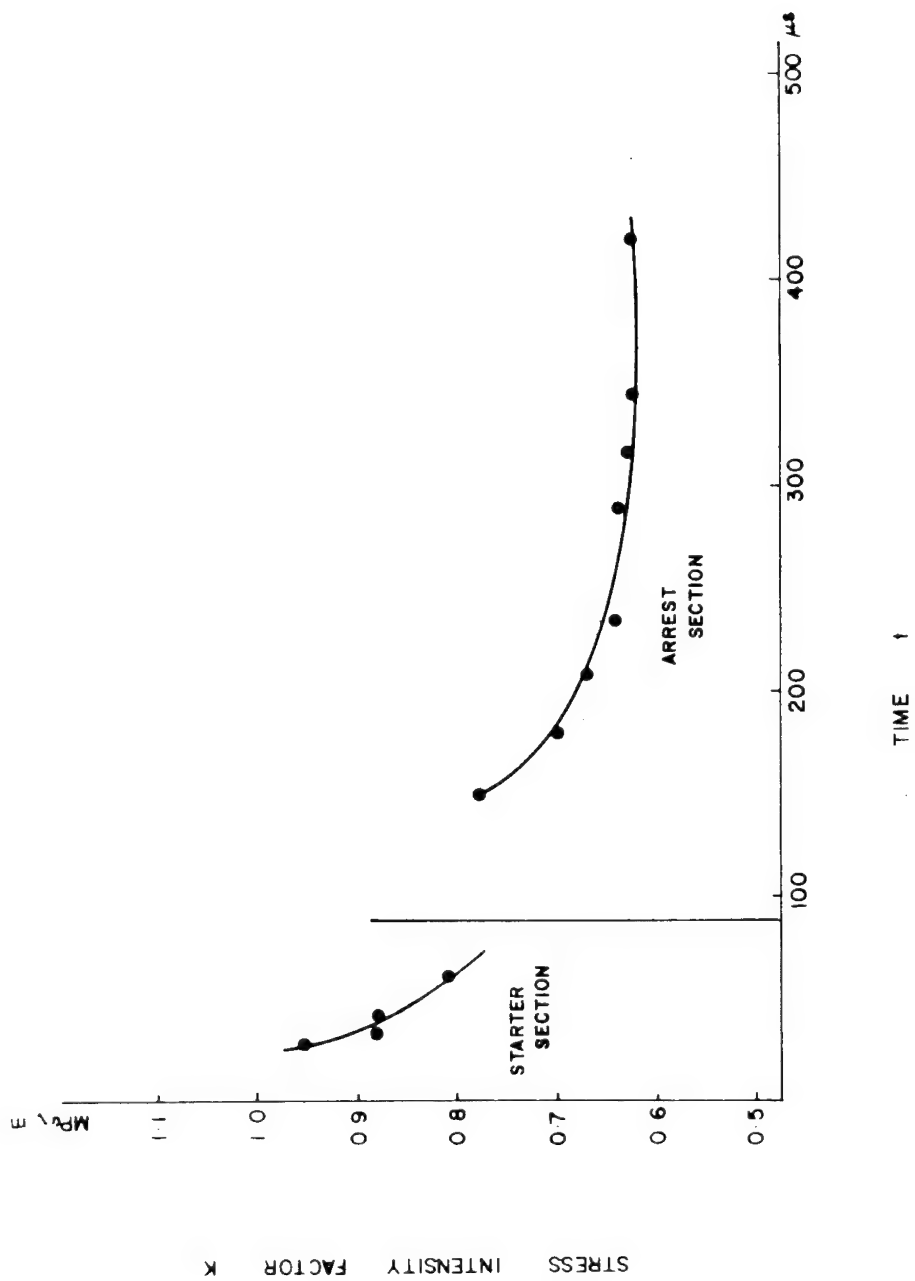


Fig. 5.25 Stress Intensity Factor K as a Function of Time for Model R-10.

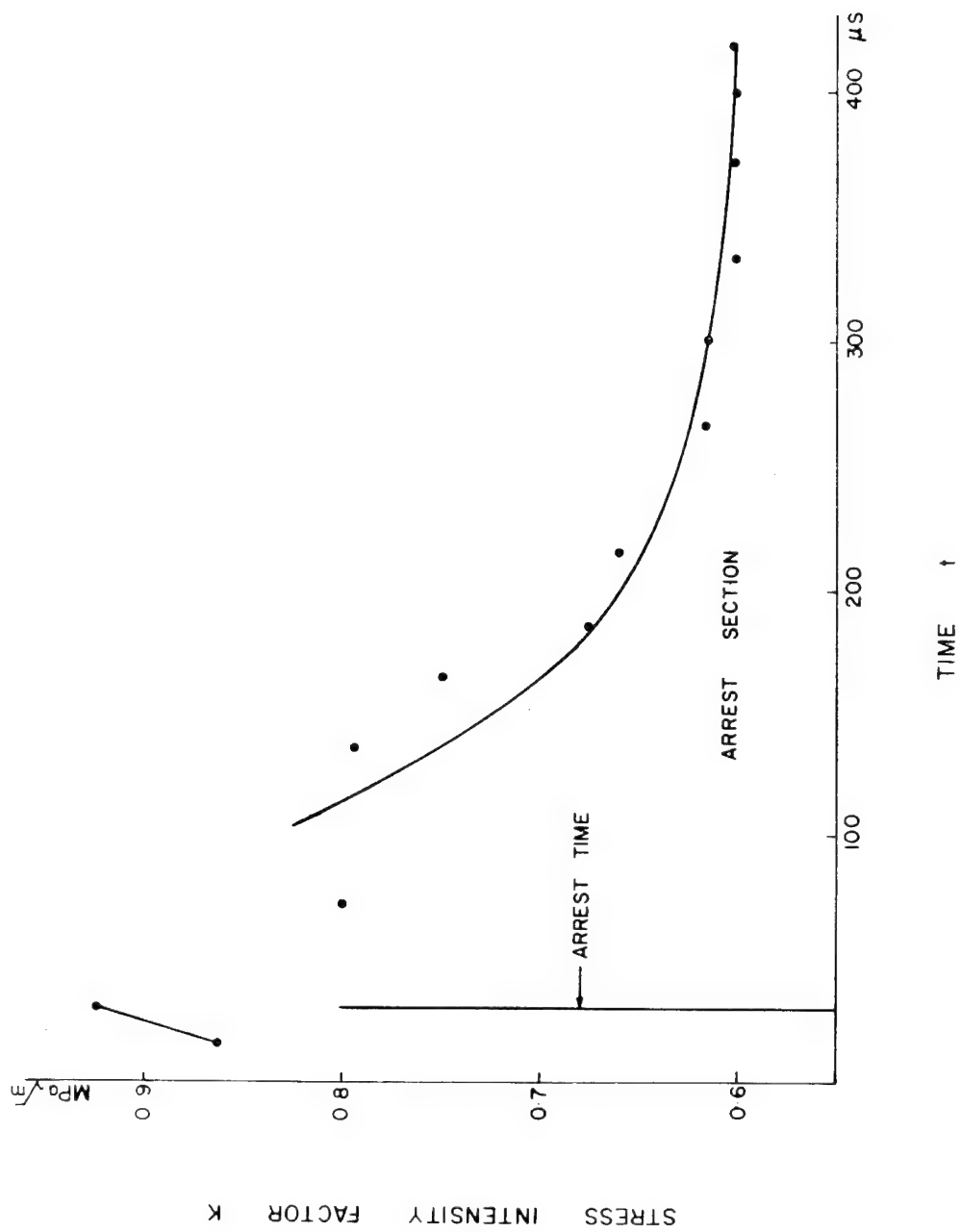


Fig. 5.26 Stress Intensity Factor K as a Function of Time for Model R-11.

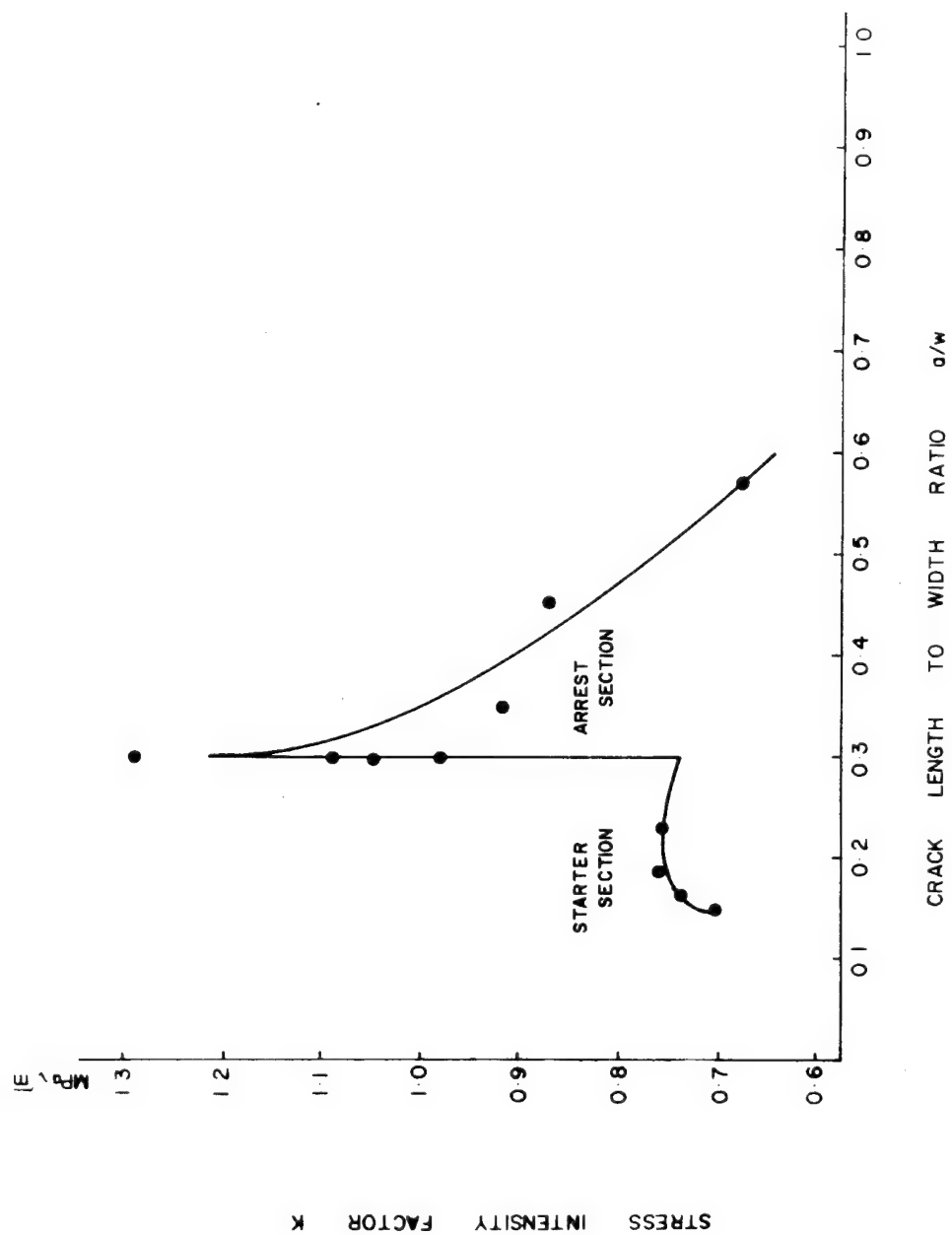


Fig. 5.27 Stress Intensity Factor K as a Function of a/w for Model R-9.

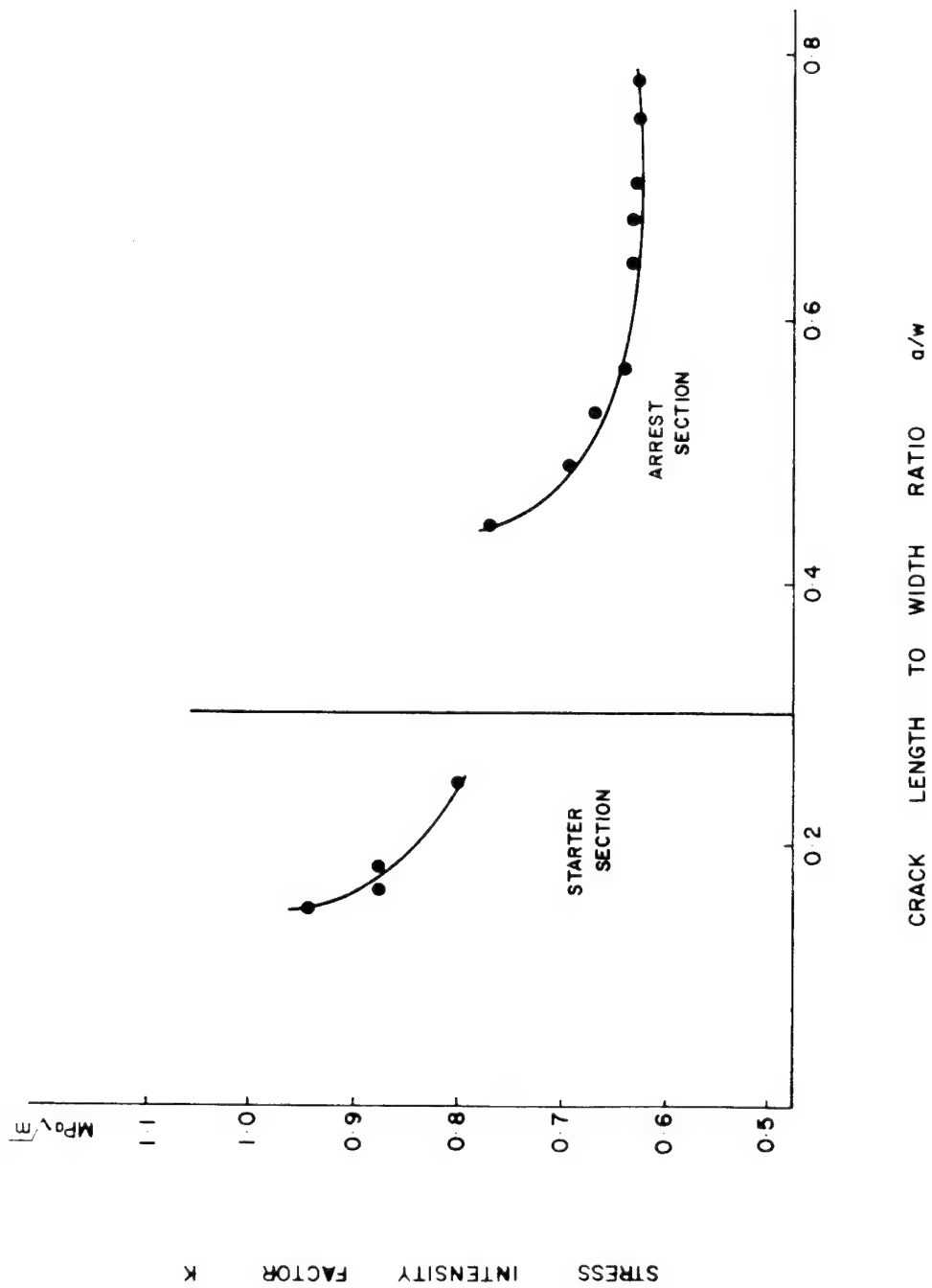


Fig. 5.28 Stress Intensity Factor K as a Function of a/w for Model R-10.

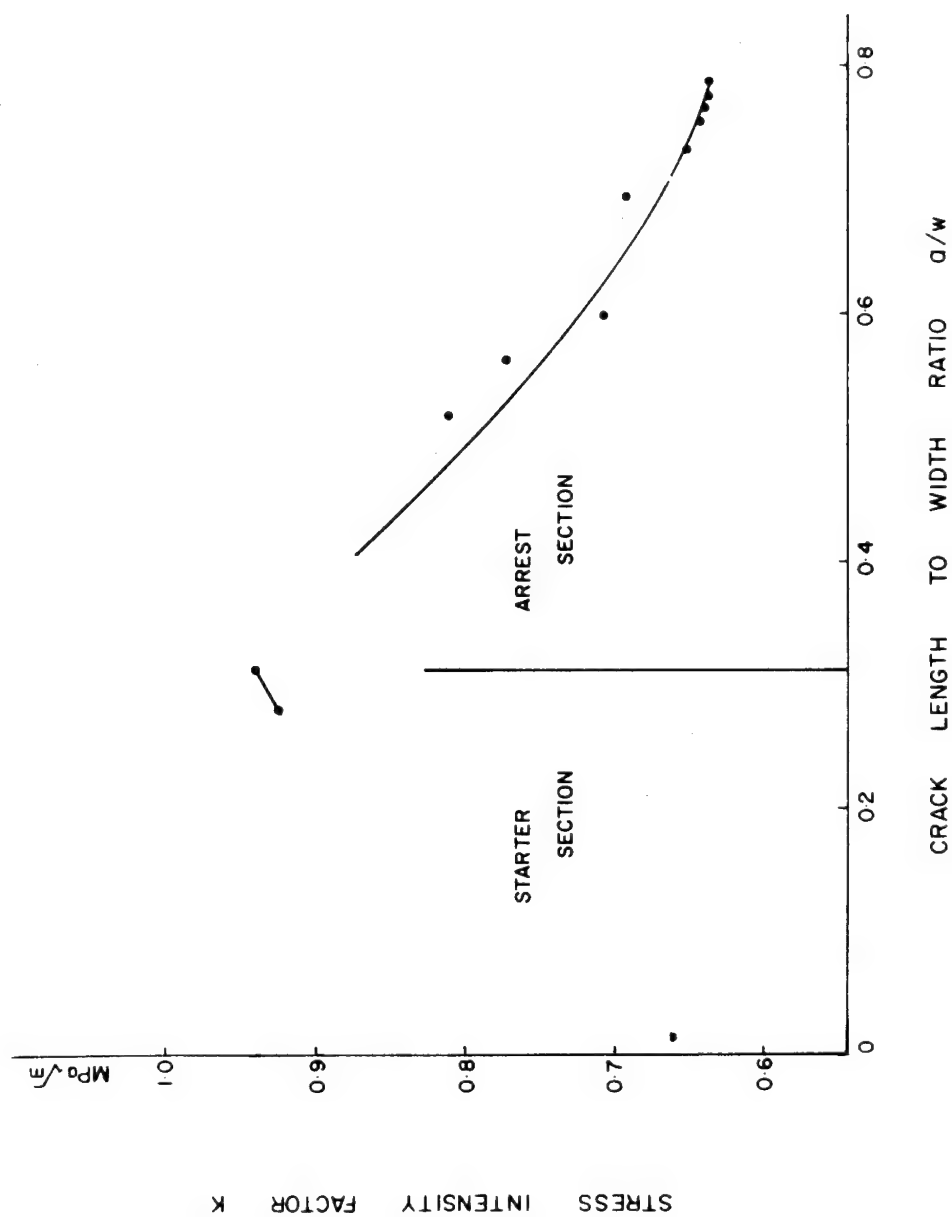


Fig. 5.29 Stress Intensity Factor K as a Function of a/w for Model R-11.

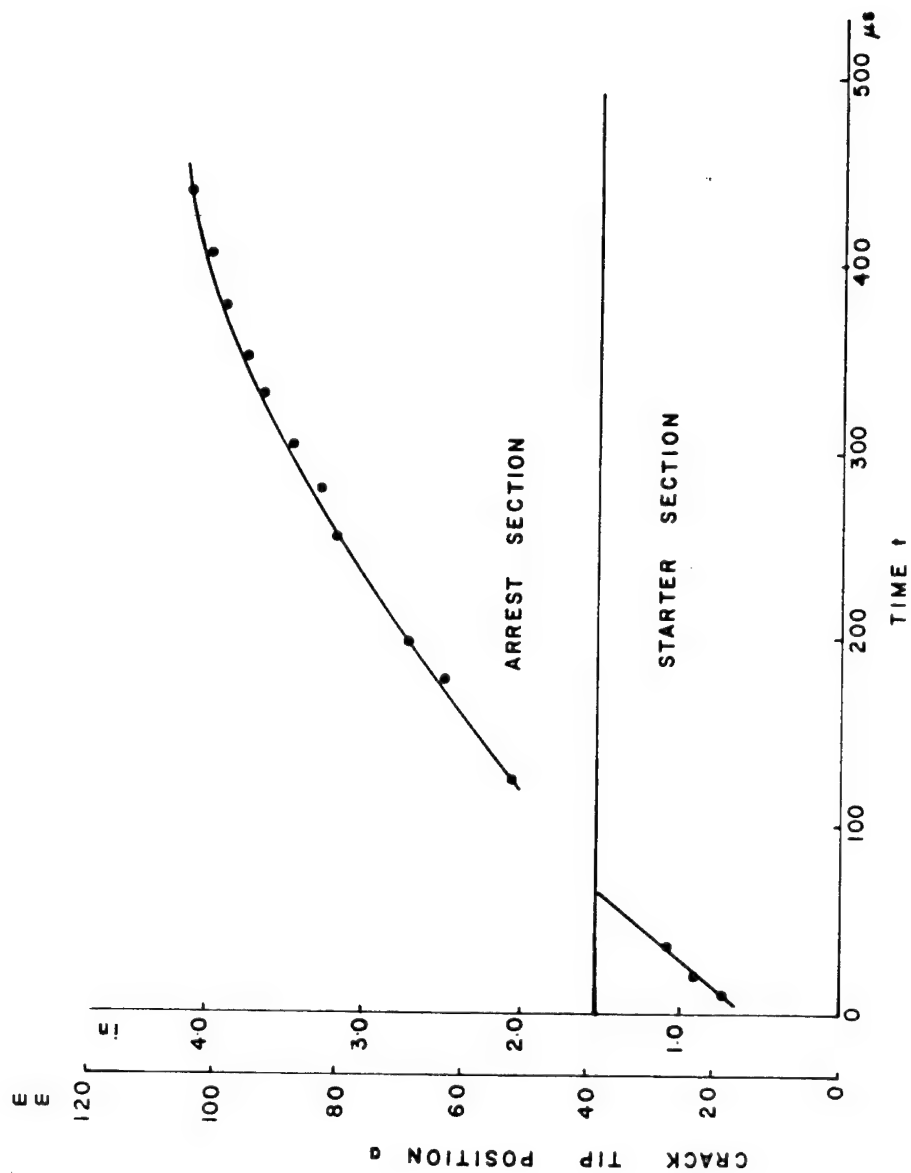


Fig. 5.30 Crack Tip Position as a Function of Time for Model R-12.

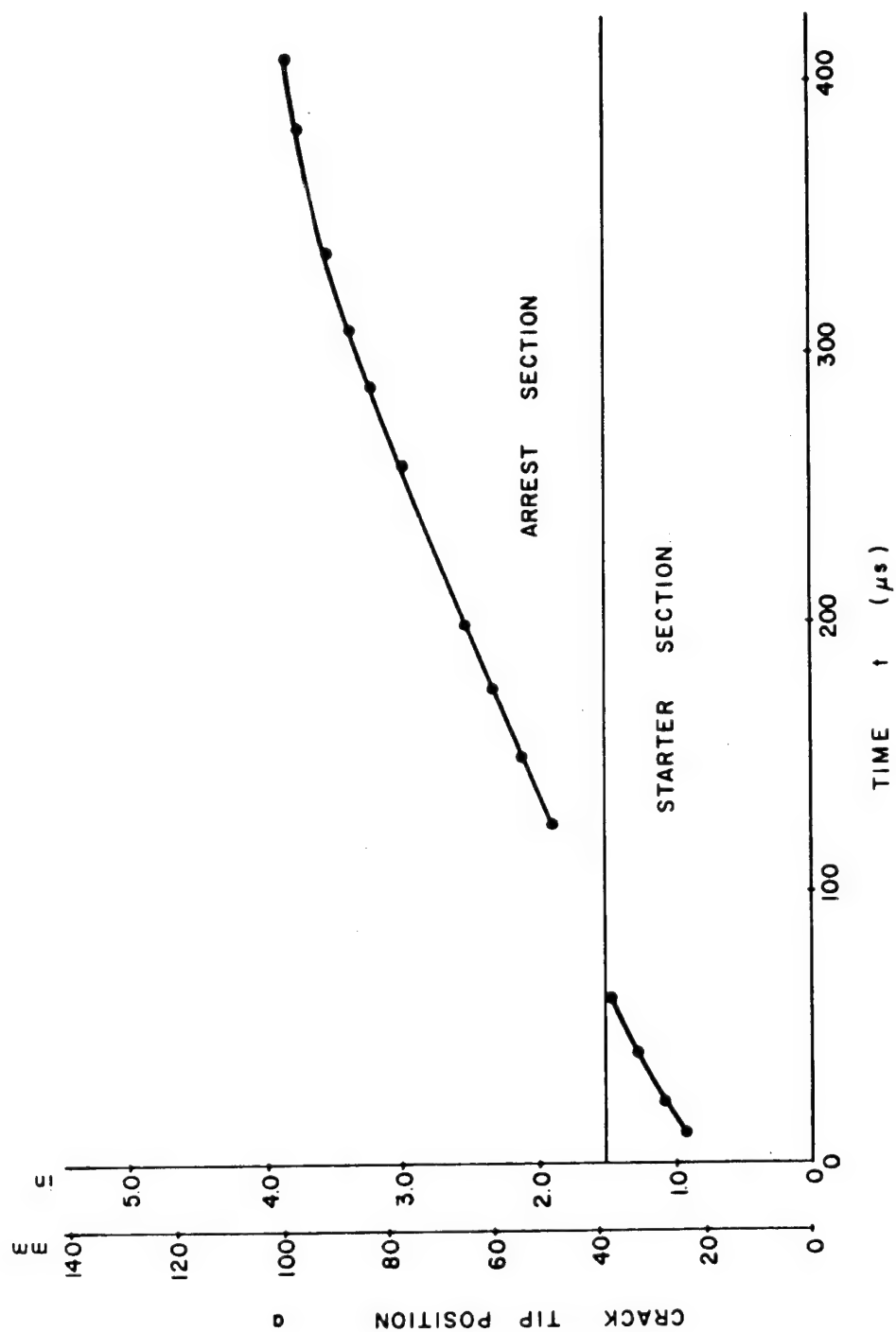


Fig. 5.31 Crack Tip Position as a Function of Time for Model R-13.

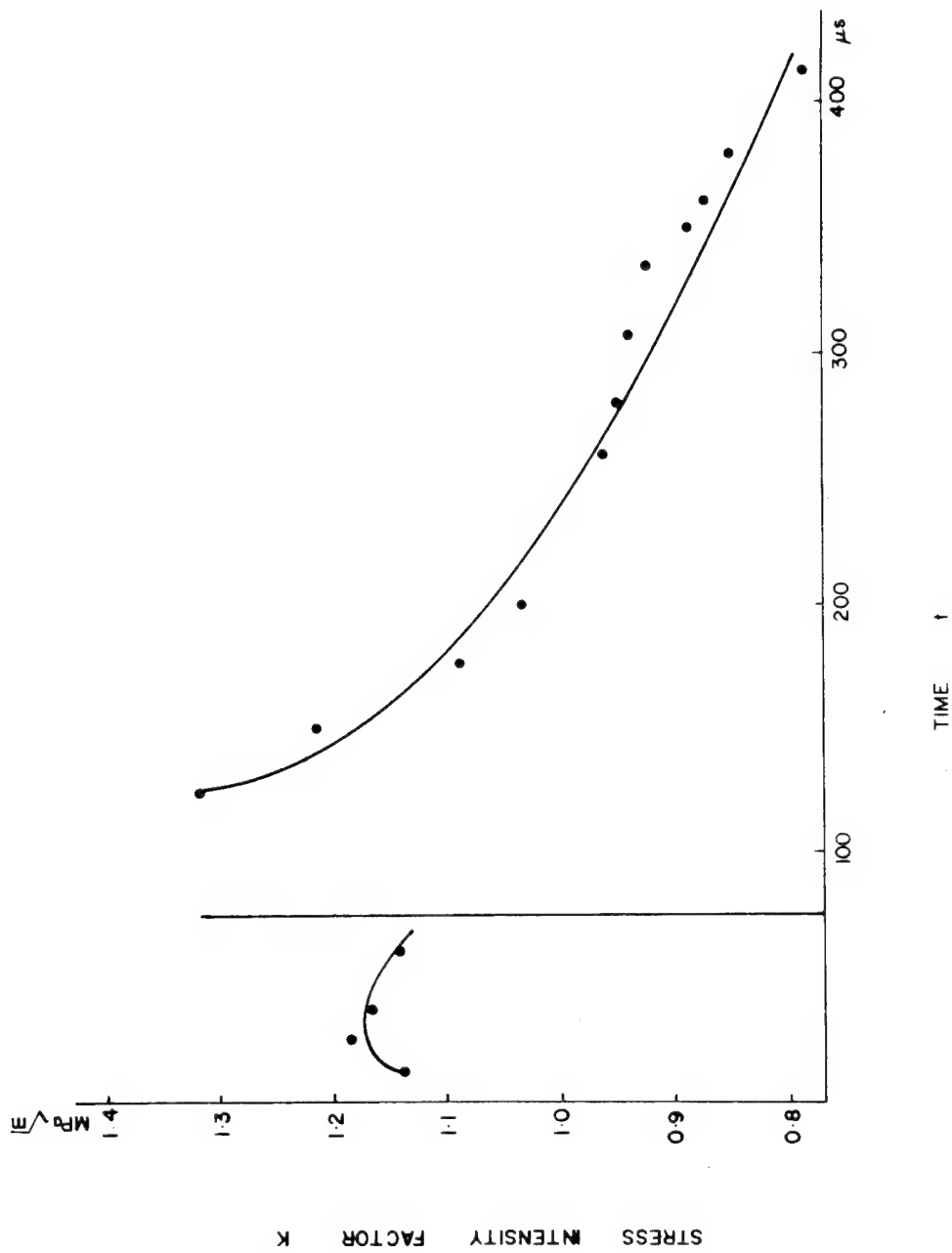


Fig. 5.32 Stress Intensity Factor as a Function of Time for Model R-12.

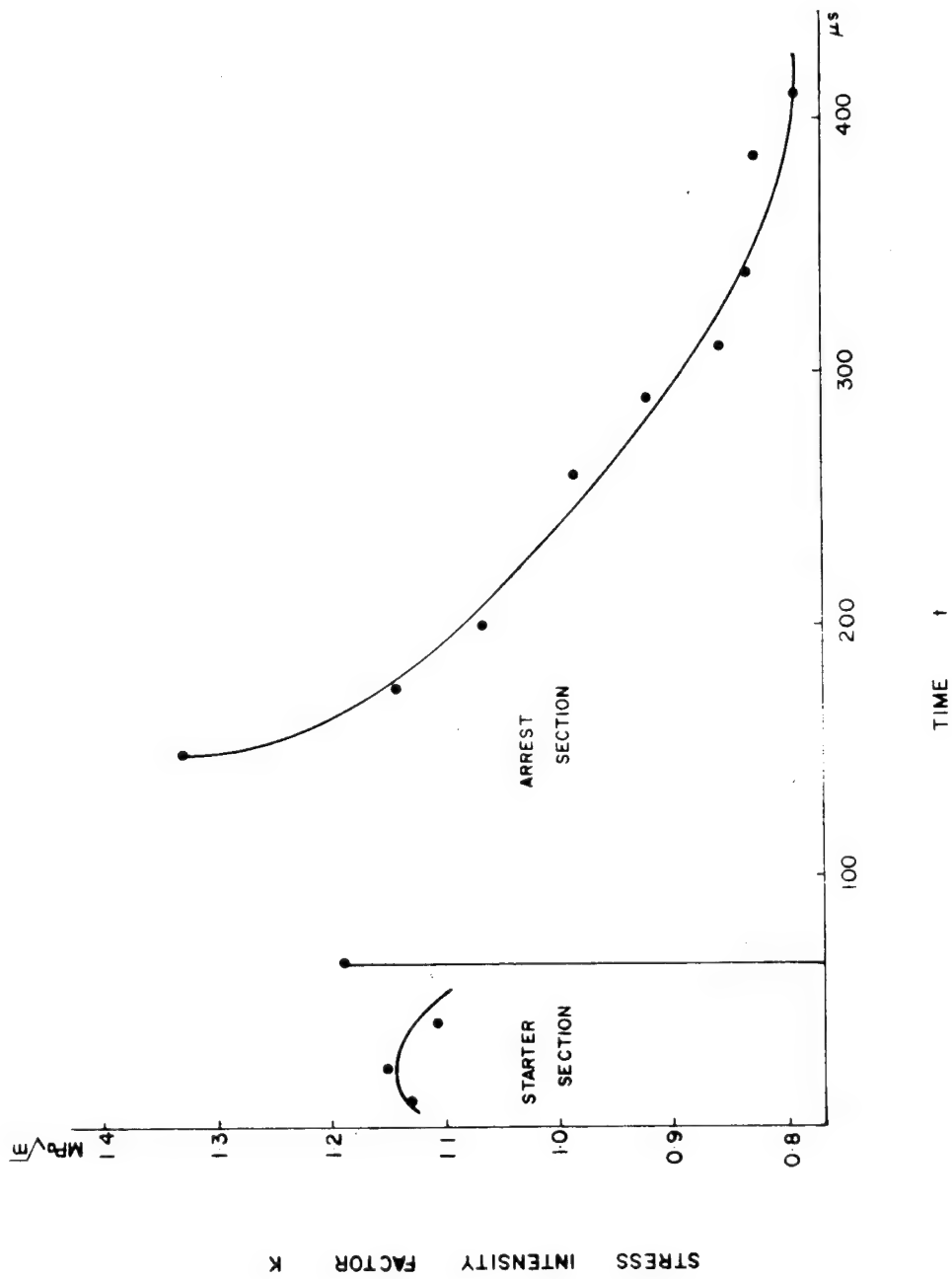


Fig. 5.33 Stress Intensity Factor as a Function of Time for Model R-13.

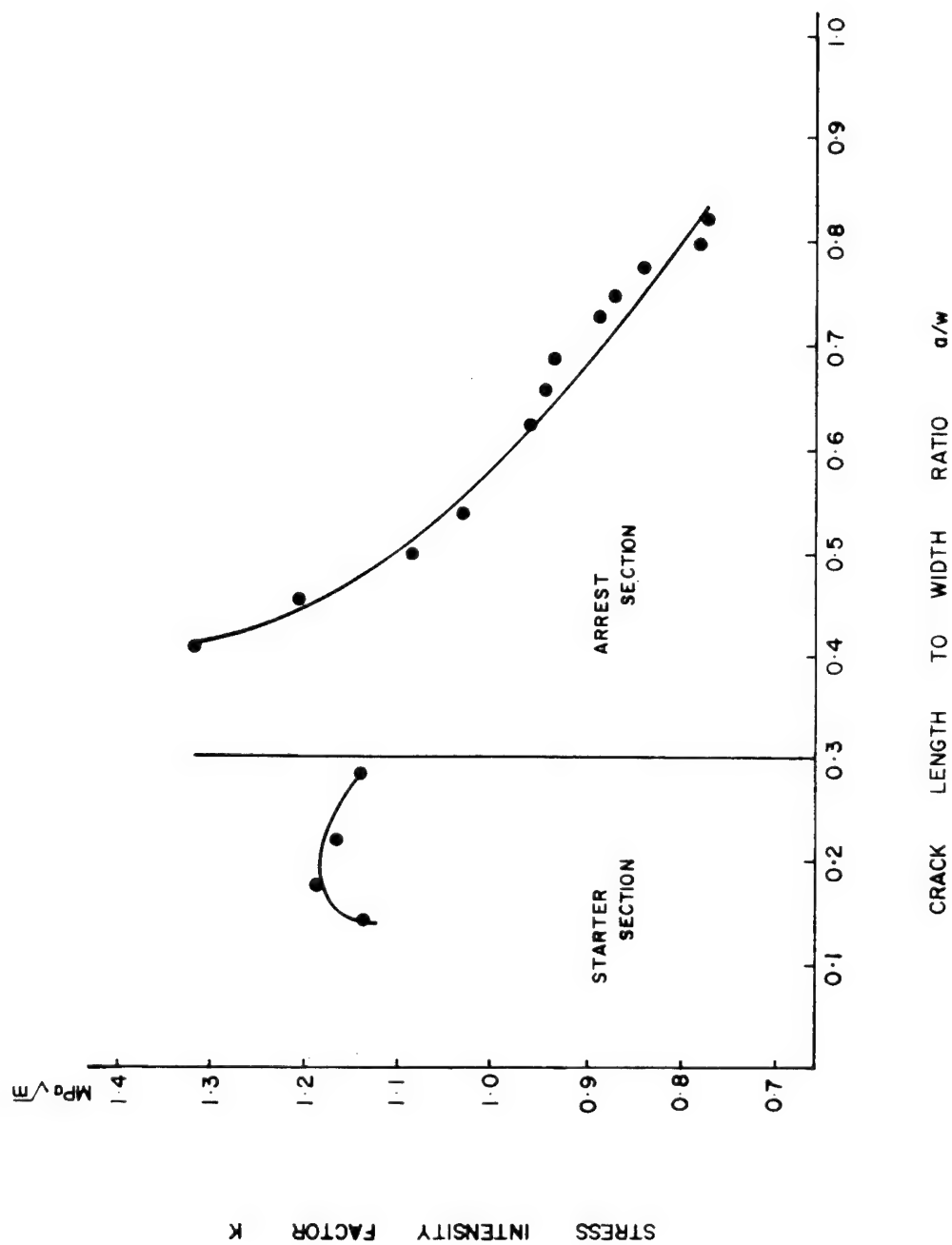


Fig. 5.34 Stress Intensity Factor as a Function of a/w for Model R-12.

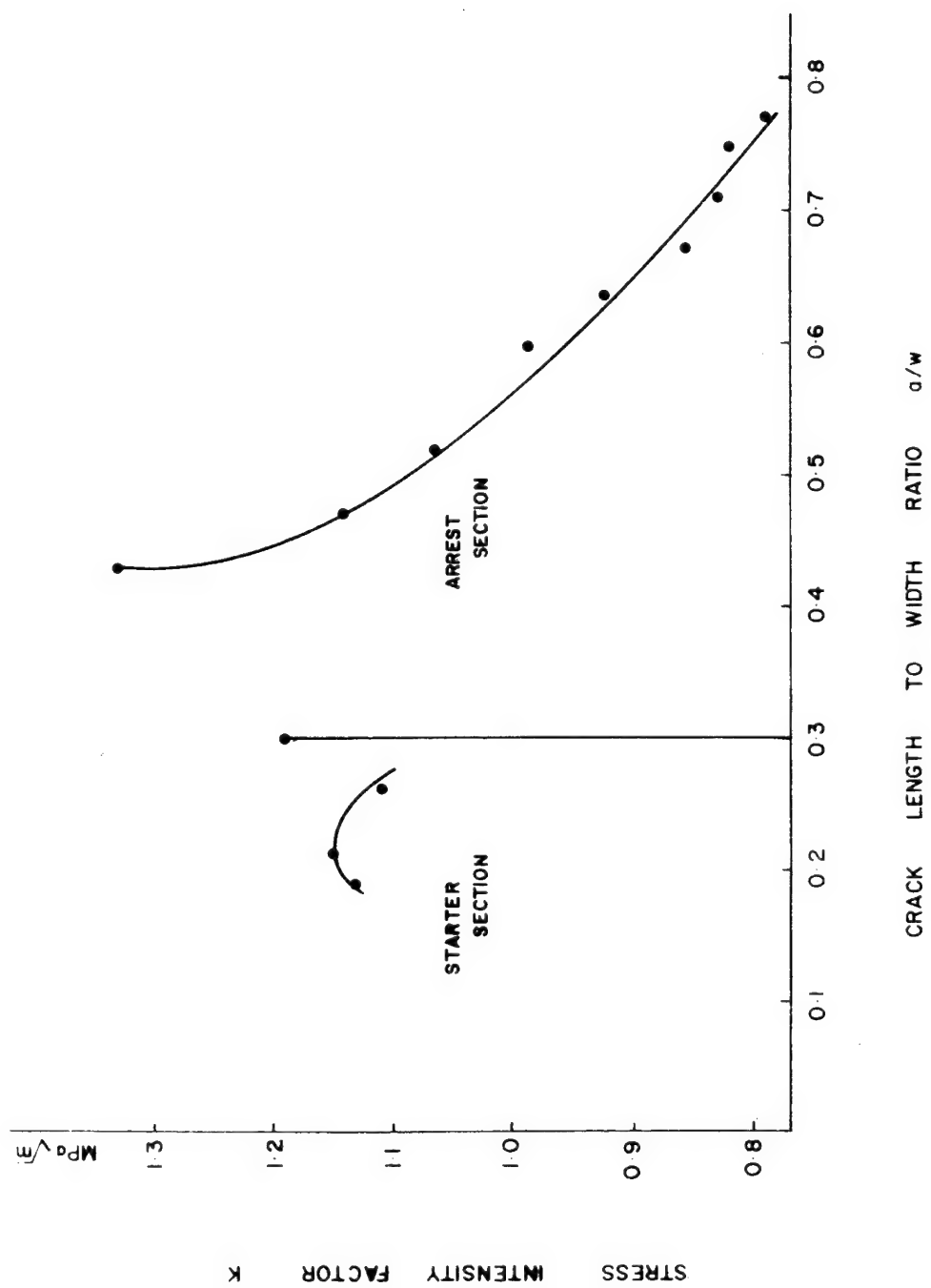


Fig. 5.35 Stress Intensity Factor as a Function of a/w for Model R-13.

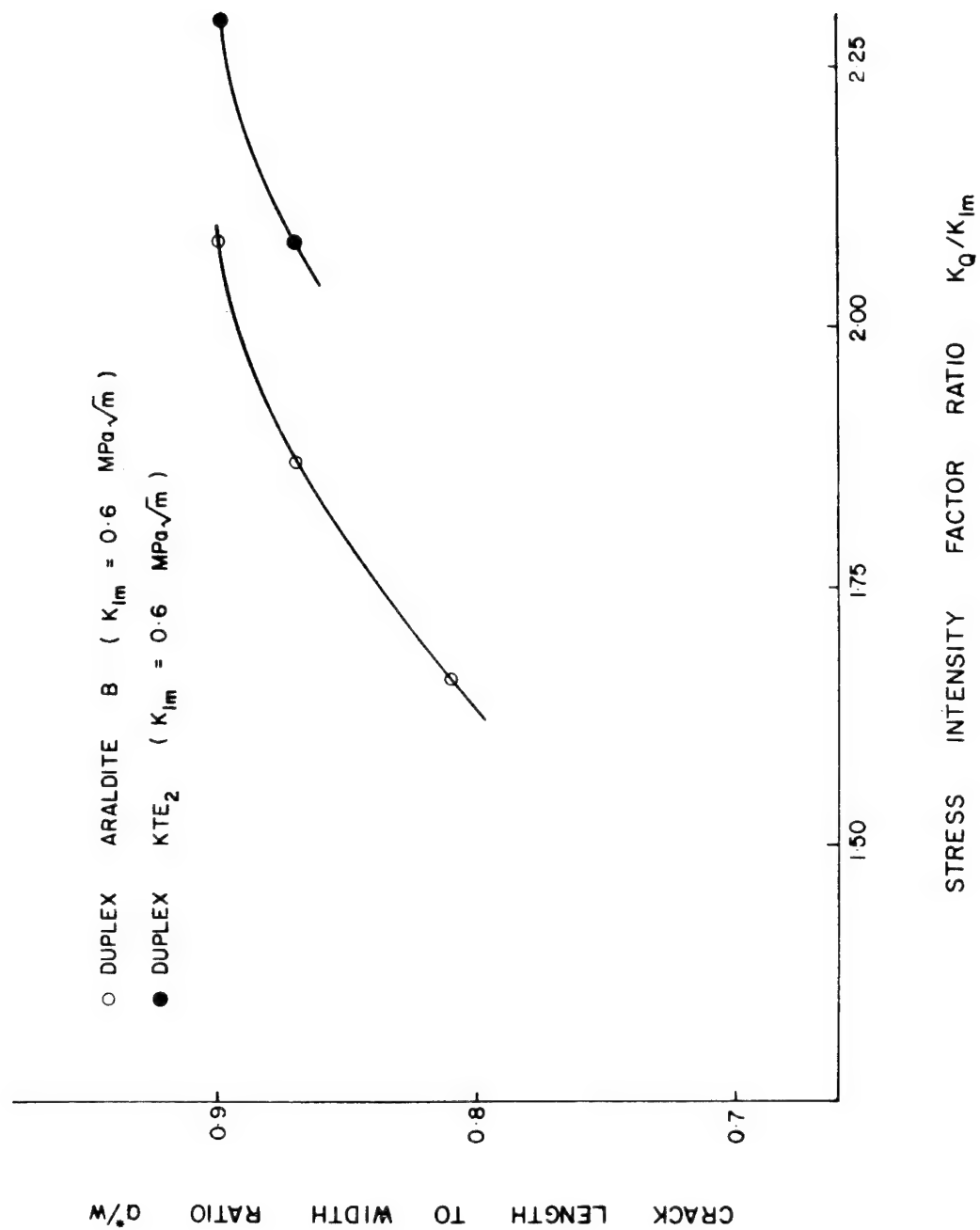


Fig. 5.36 Crack Jump Distance a^*/W as a Function of K_Q/K_{Im} .

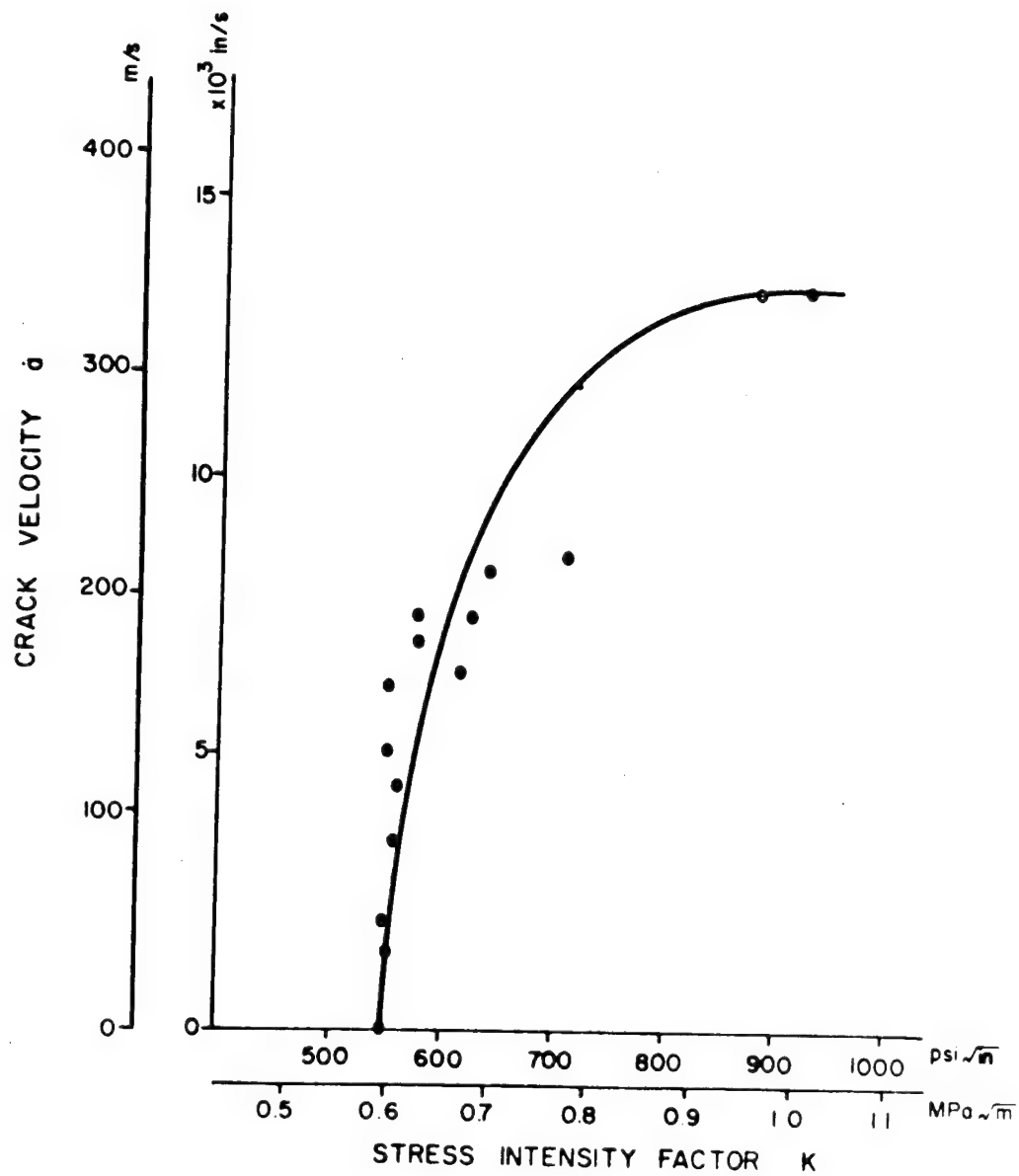


Fig. 5.37 Stress Intensity Factor K as a Function of Crack Velocity \dot{a} for Araldite B.

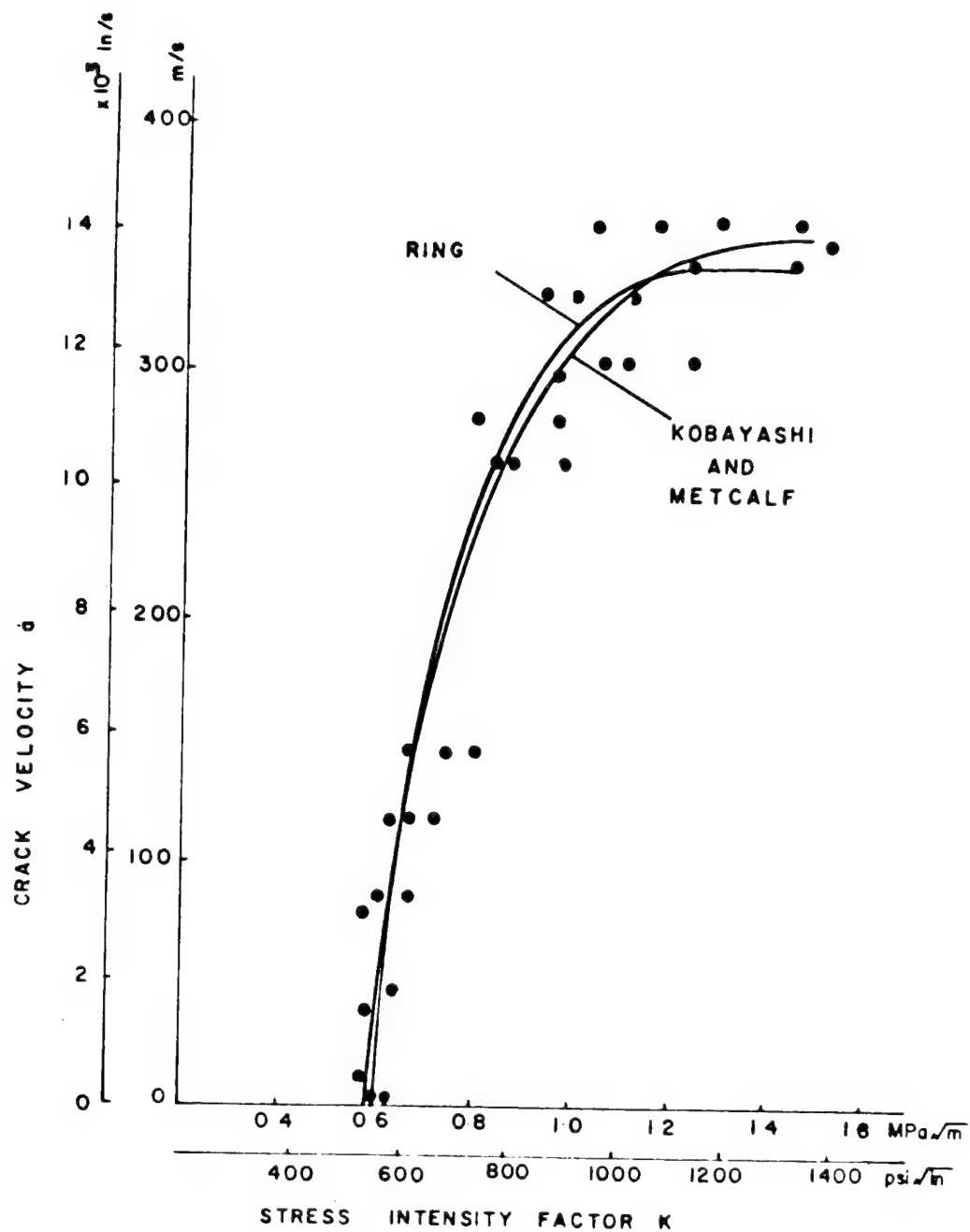


Fig 5.38 Comparison of Stress Intensity Factor K as a Function of Crack Velocity \dot{a} for Araldite B.

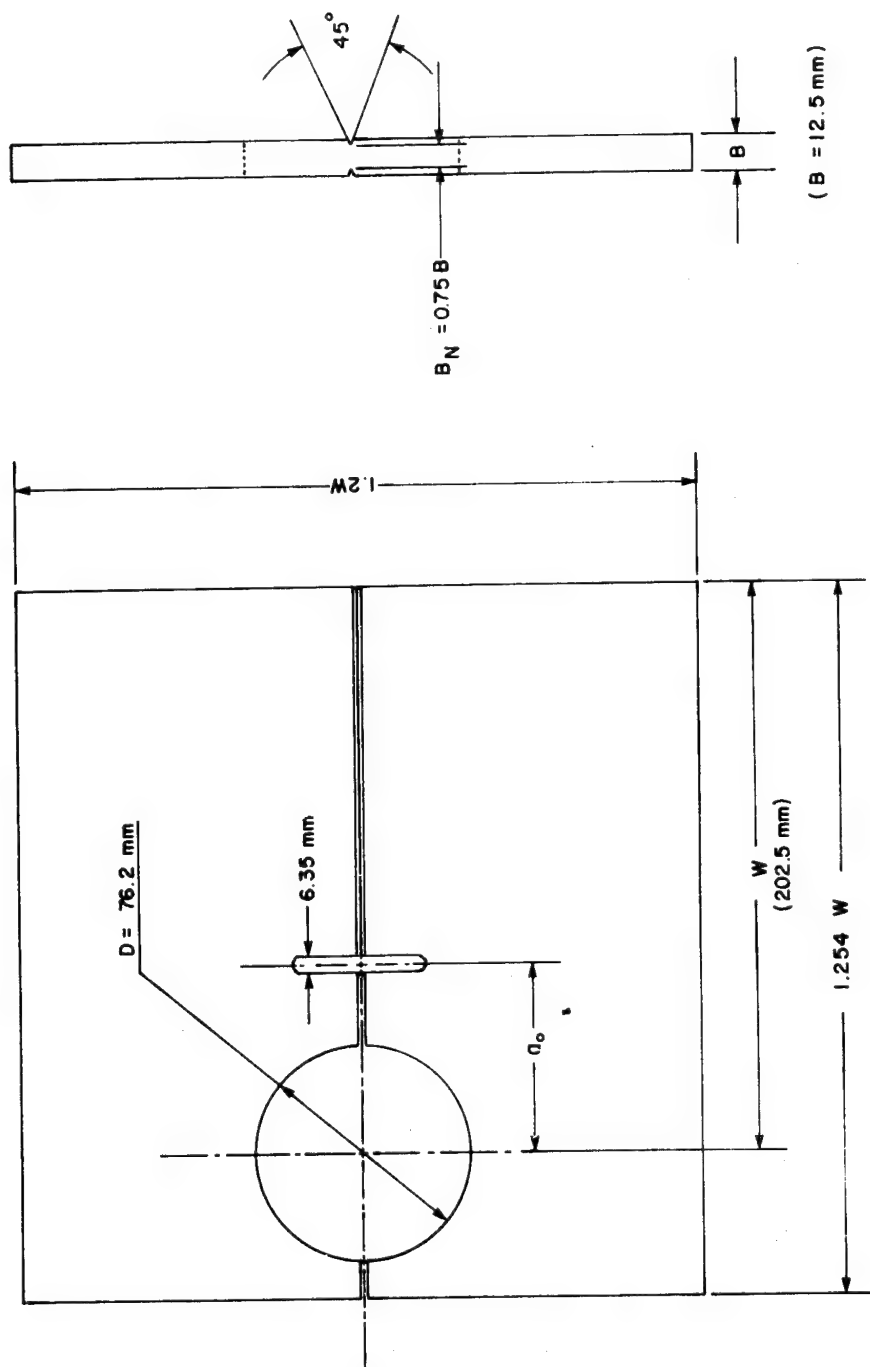


Fig. 6.1 Geometry of Face-Grooved Specimen.

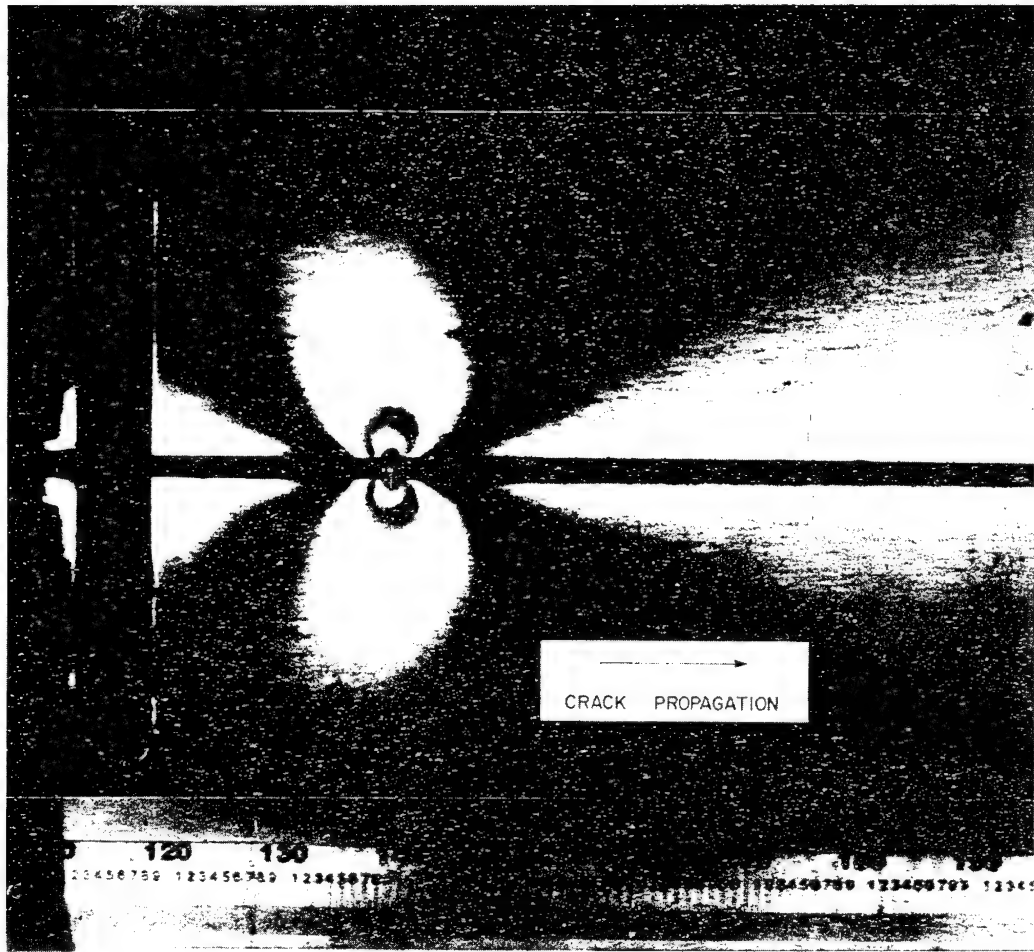


Fig. 6.2 Typical Isochromatic Fringes Observed in the Face-Grooved Compact Specimen.

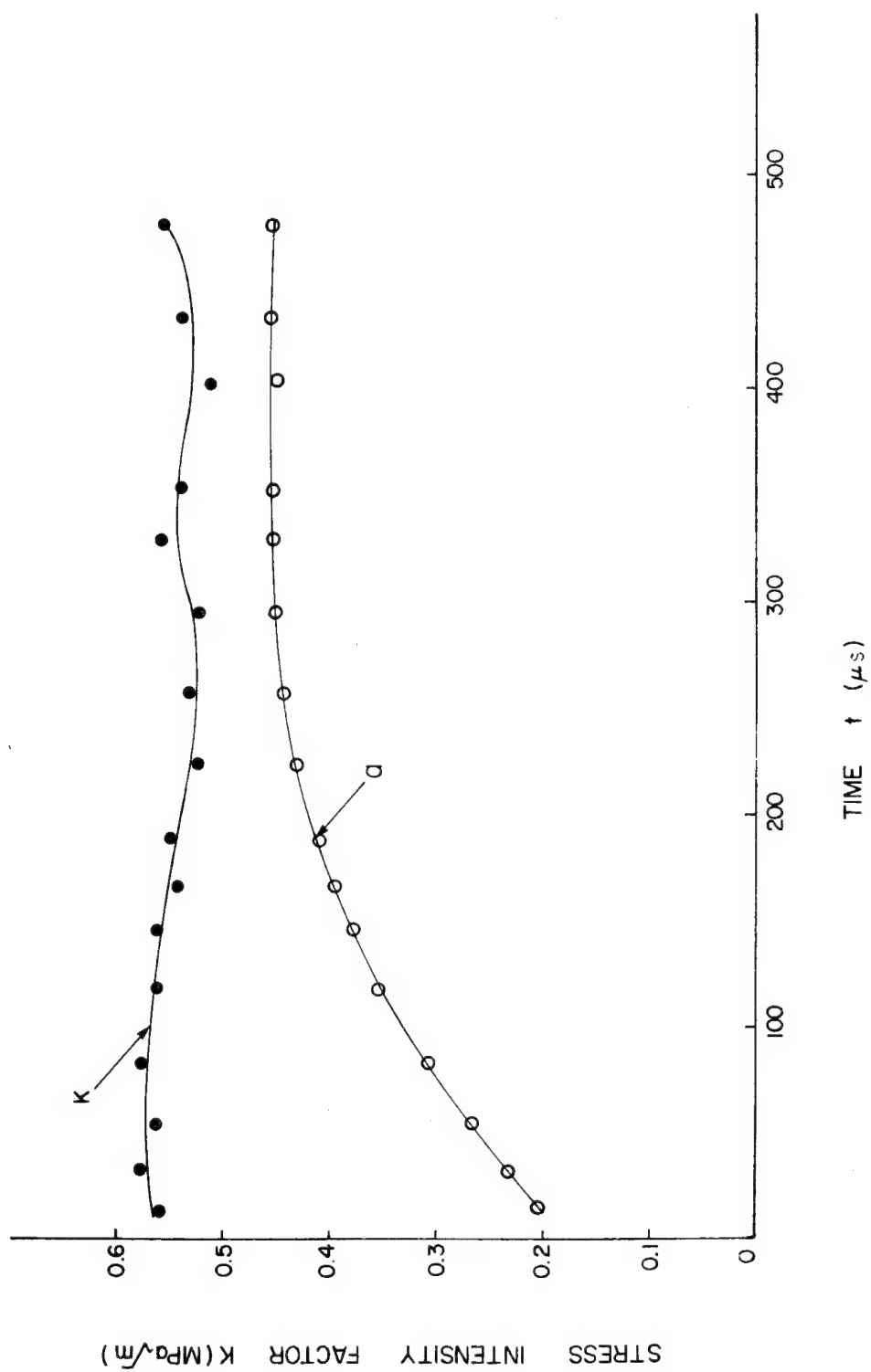


Fig. 6.3 Dynamic Stress Intensity Factor and Crack Position as a Function of Time for Model Nos. 311 and 312.

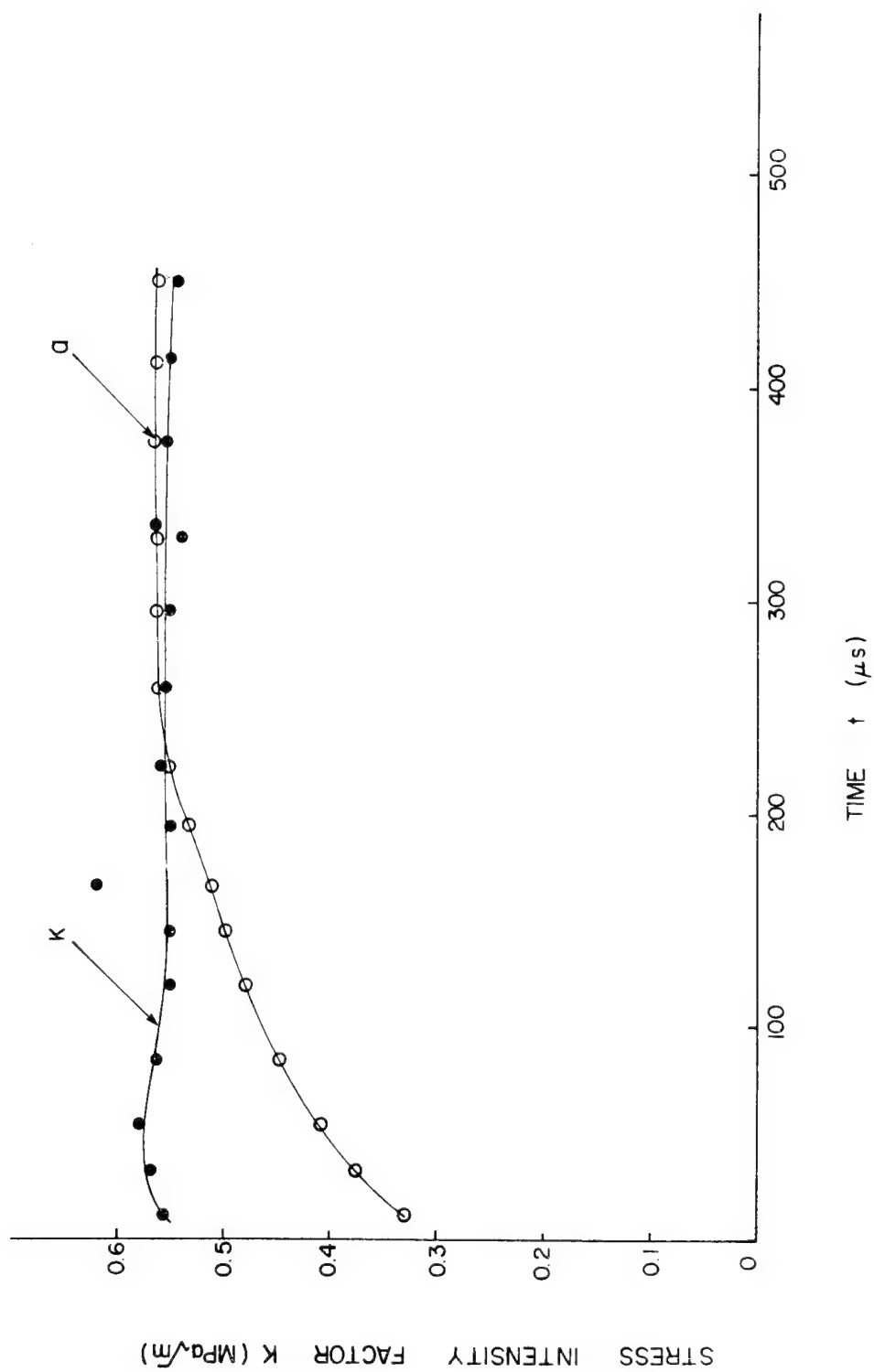


Fig. 6.4 Dynamic Stress Intensity Factor vs a/W for Model Nos. 311 and 312.

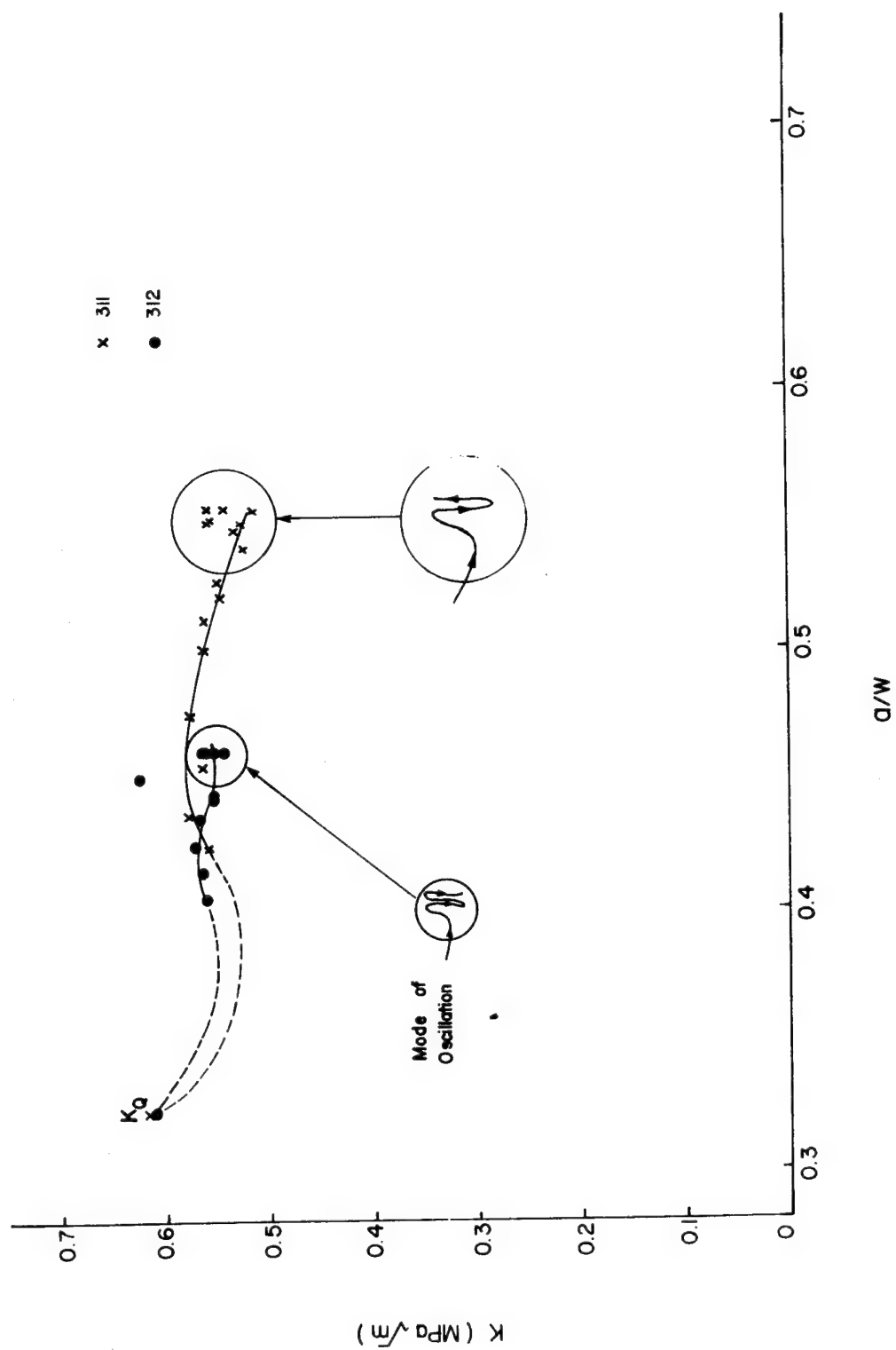


Fig. 6.5 Dynamic Stress Intensity Factor vs a/W for Model No. 144.

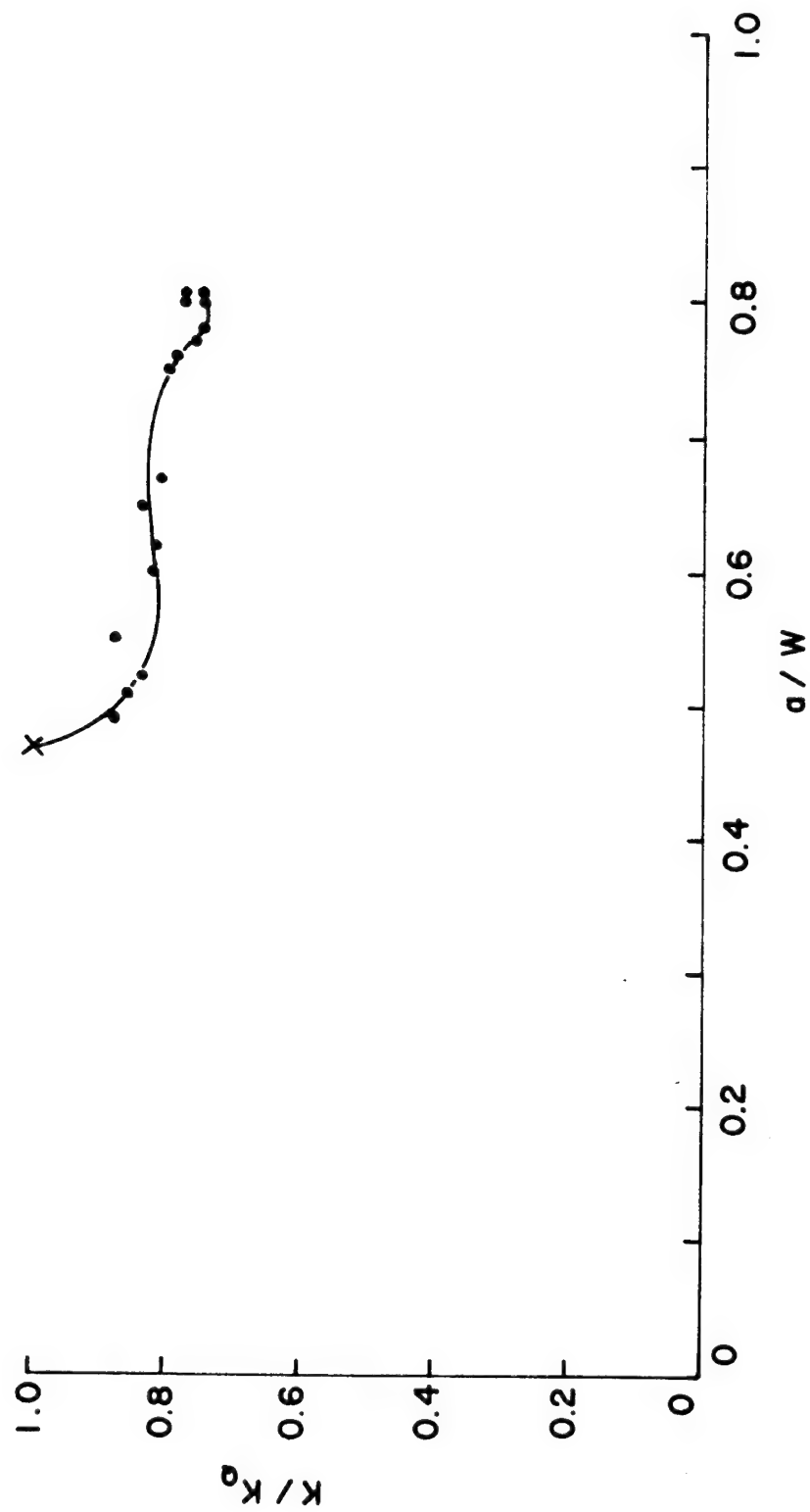


Fig. 6.6 Normalized Static Stress Intensity Factor vs. a/W for Various Machine Compliance
(Ref. 6.2).

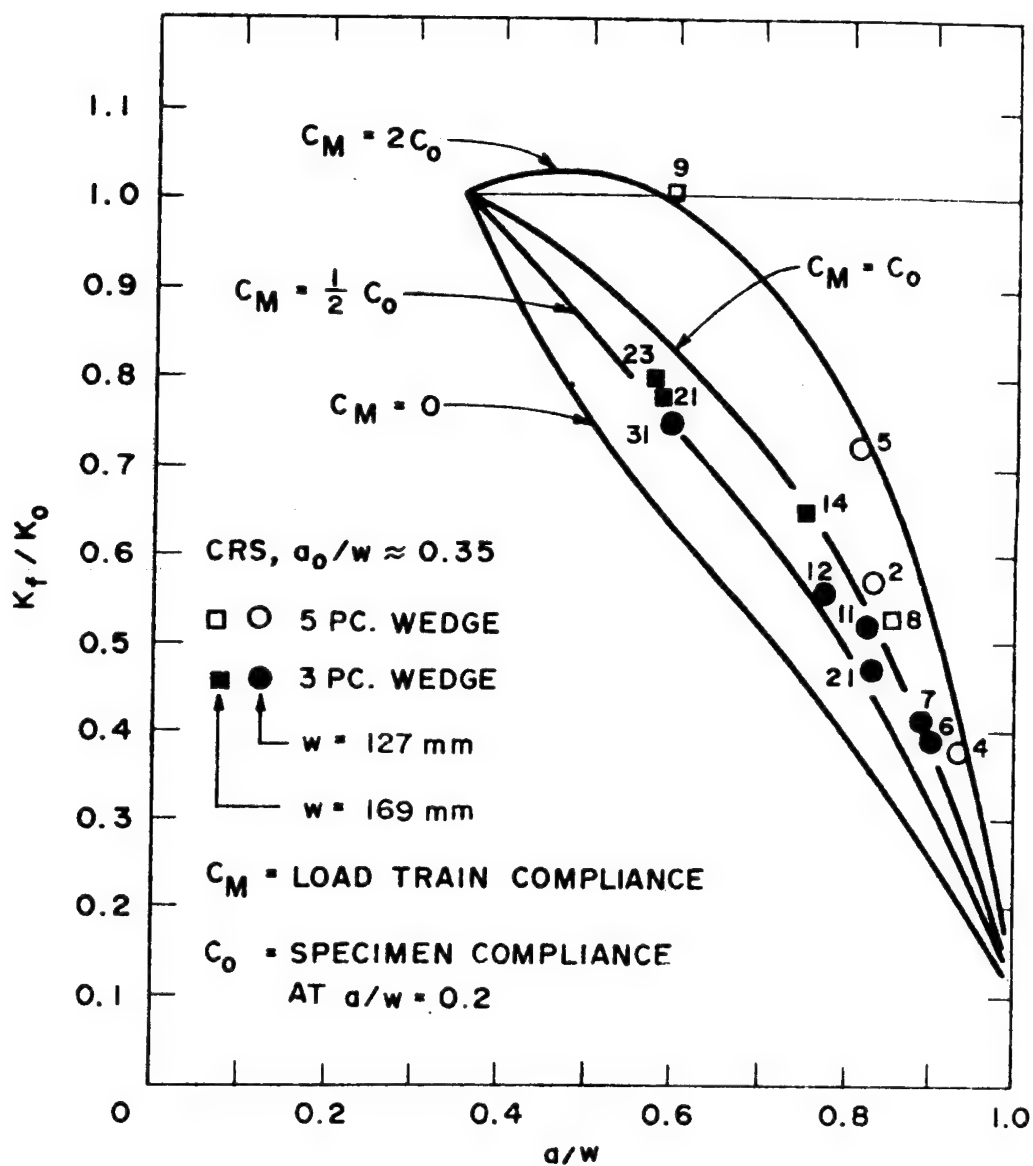


Fig. 6.7 ASTM E399 Compact Specimen and Load System.

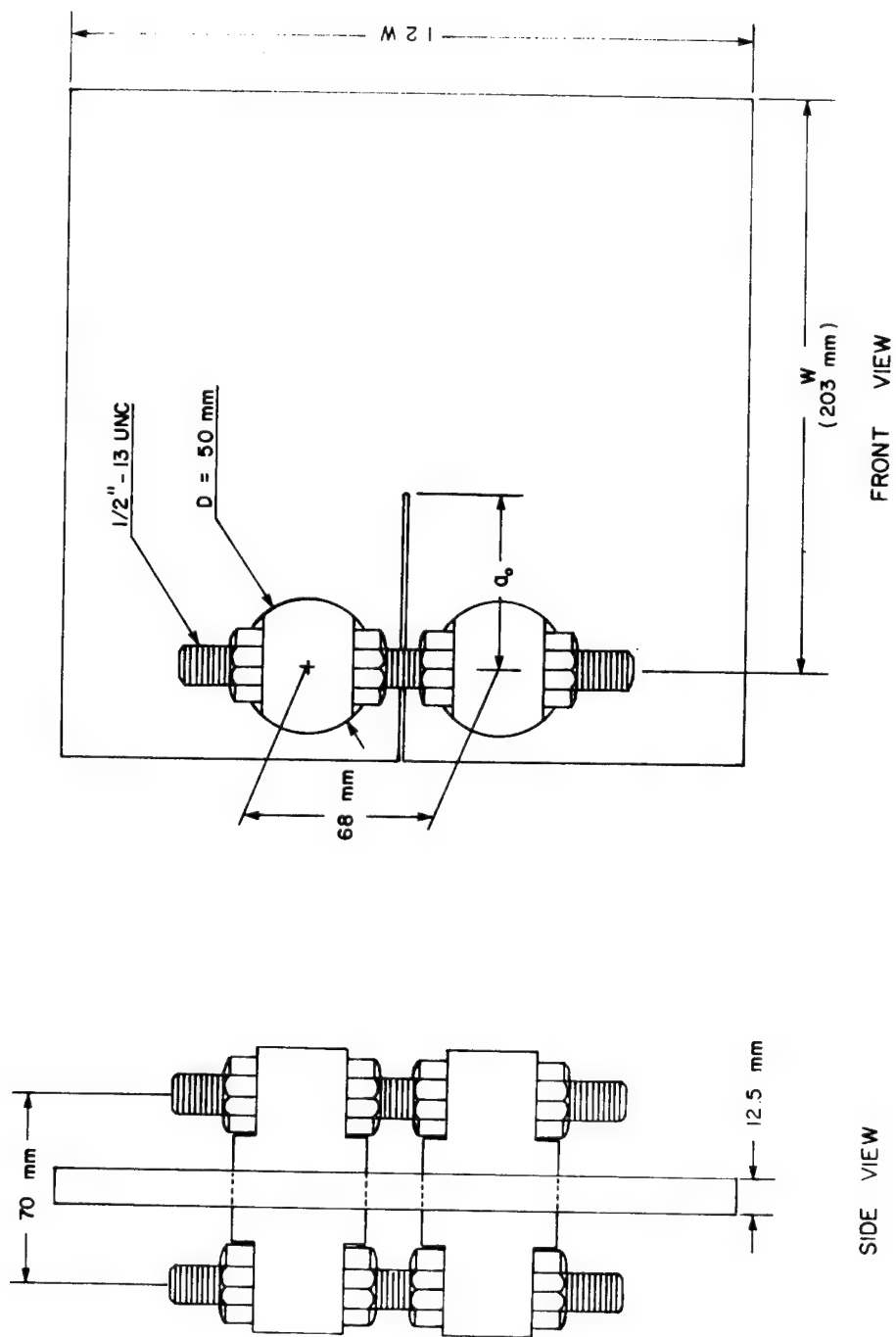


Fig. 6.8 Static K/K_0 vs a/W for Fixed-Pin Compact Specimen.

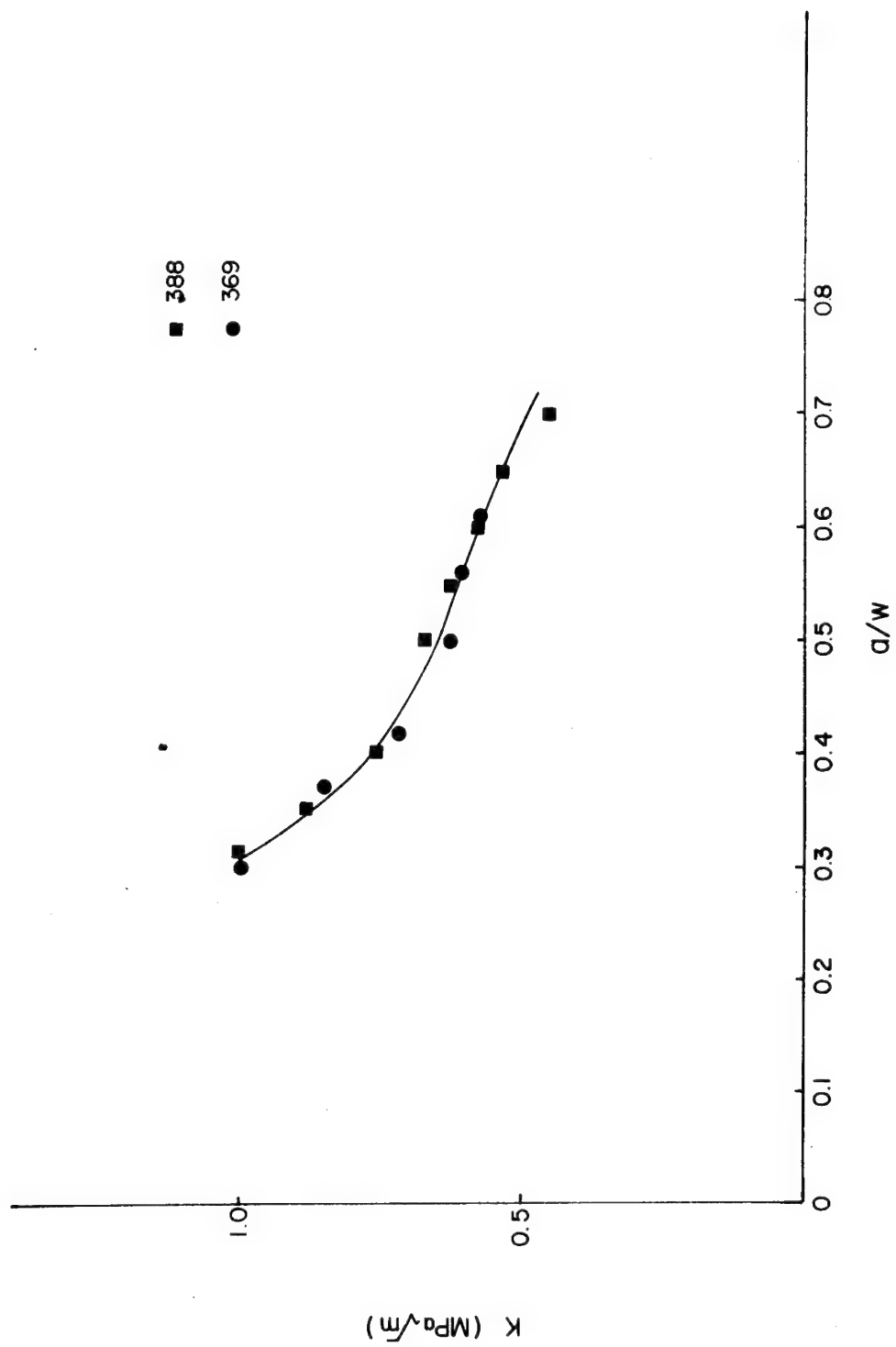


Fig. 6.9 K/K_Q vs a/W for Fixed Pin Compact Specimen.

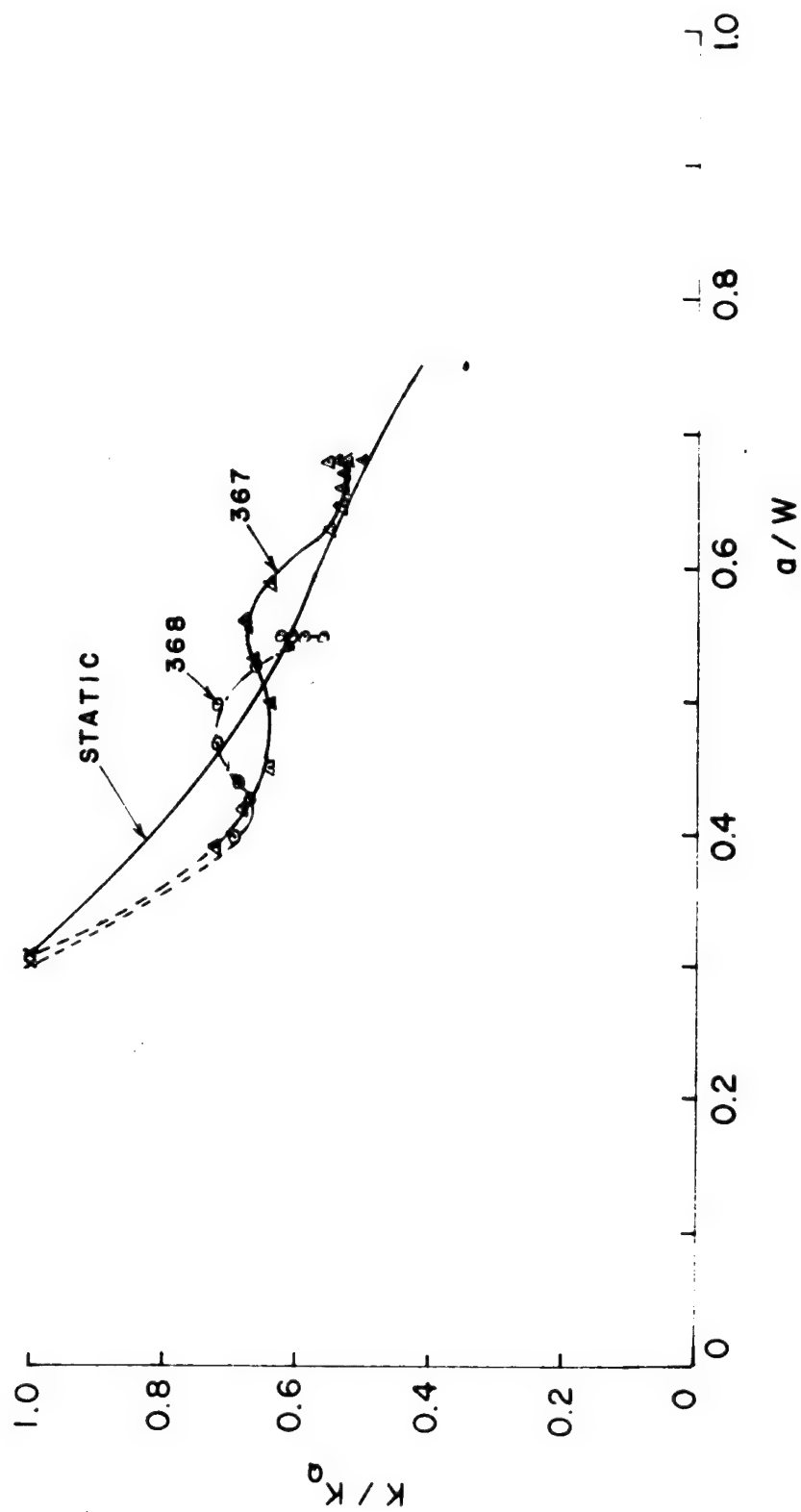


Fig. 6.10 K/K_Q vs a/W for Fixed-Pin Compact Specimen.

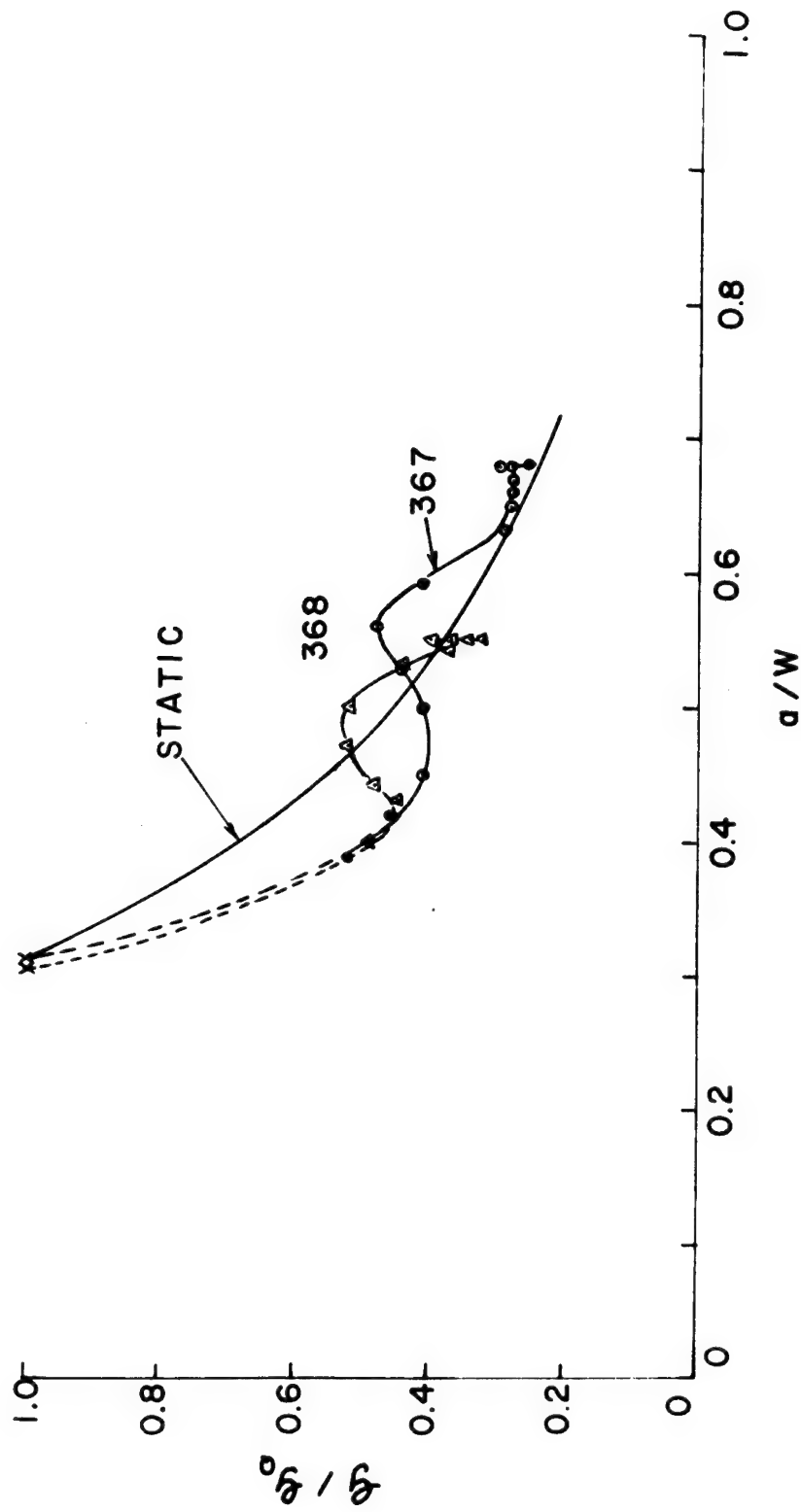


Fig. 6.11 G/G_Q vs a/W for Fixed-Pin Compact Specimen.

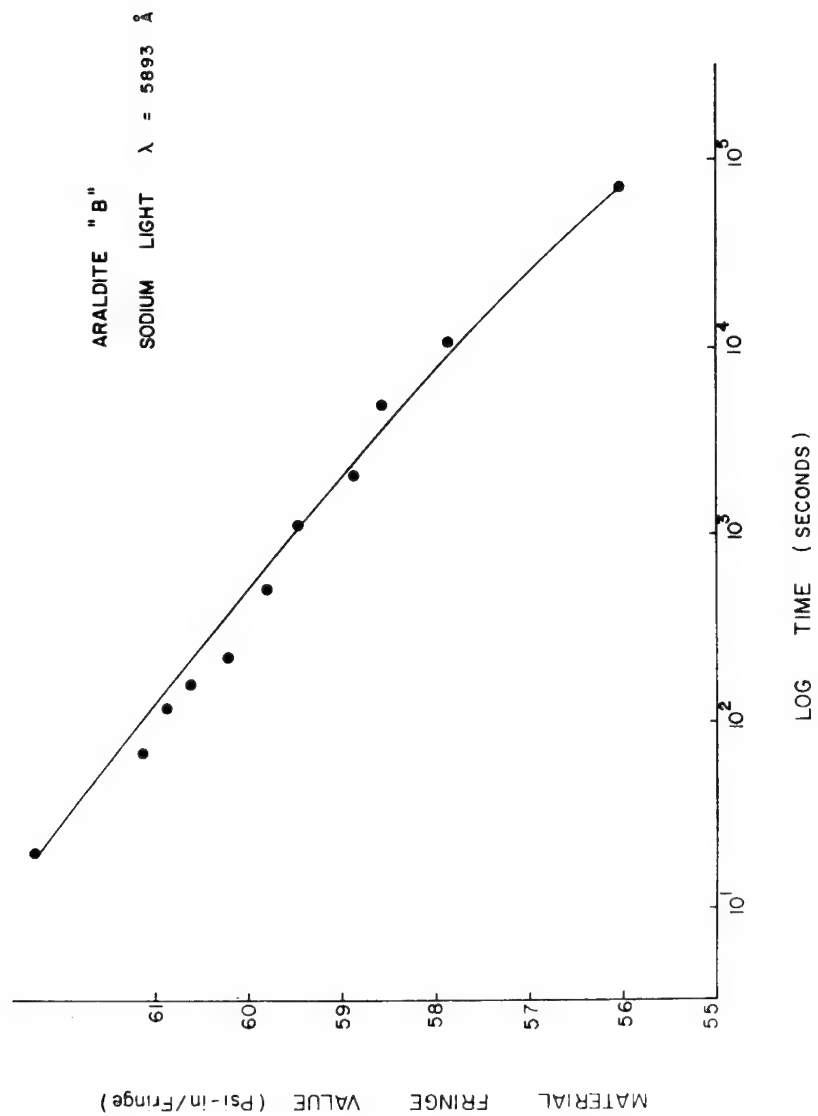


Fig. 7.1 Material Fringe Value as a Function of Time.

ARALDITE "B"

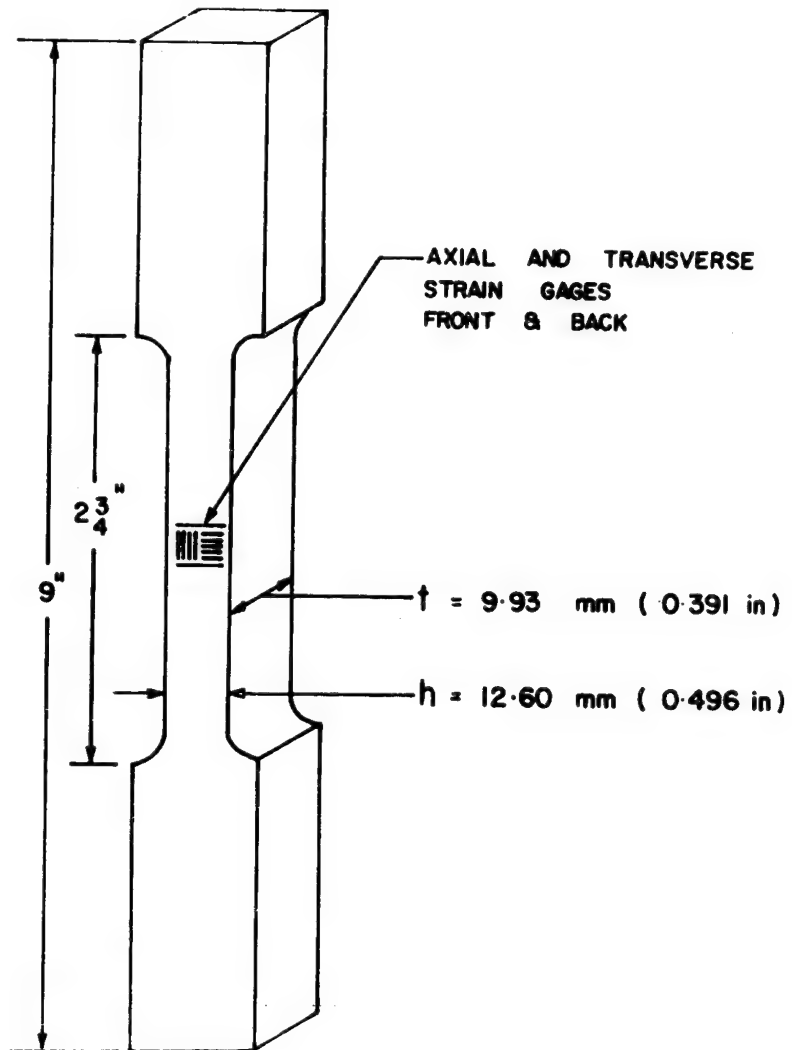


Fig. 7.2 Tension Test Specimen.

ARALDITE "B"

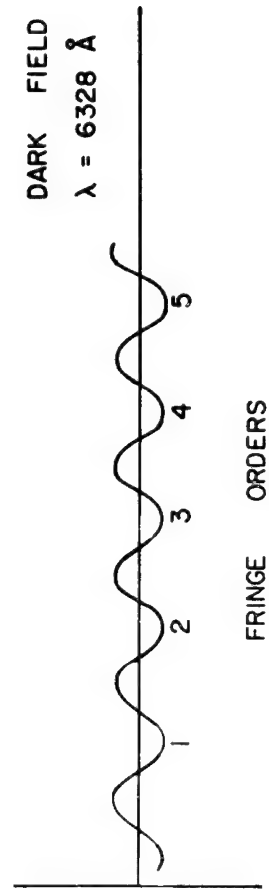
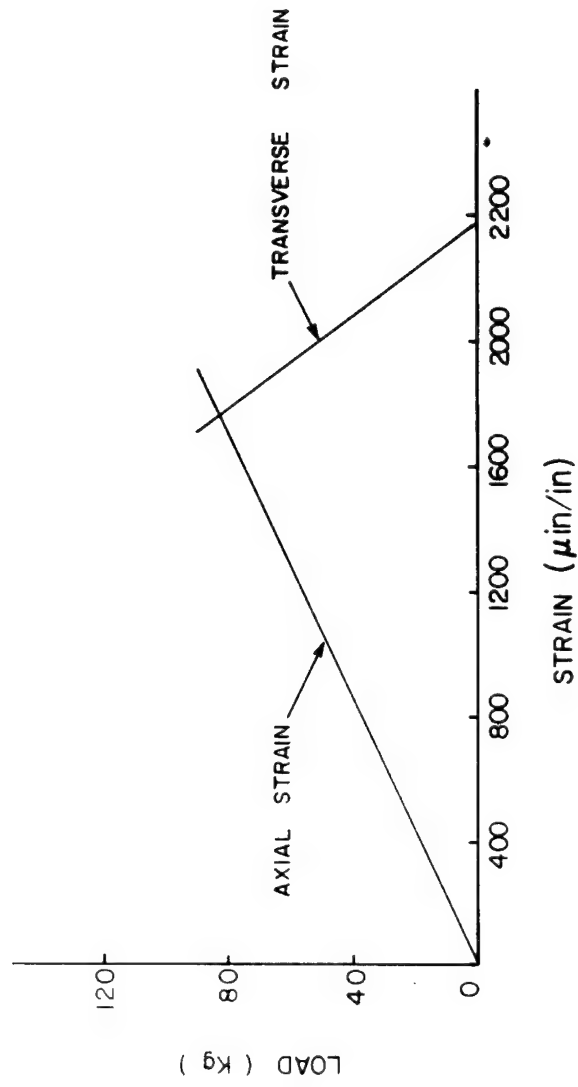


Fig. 7.3 X-Y Recorder Plot of Load vs Strain, Tension Test, Araldite B.

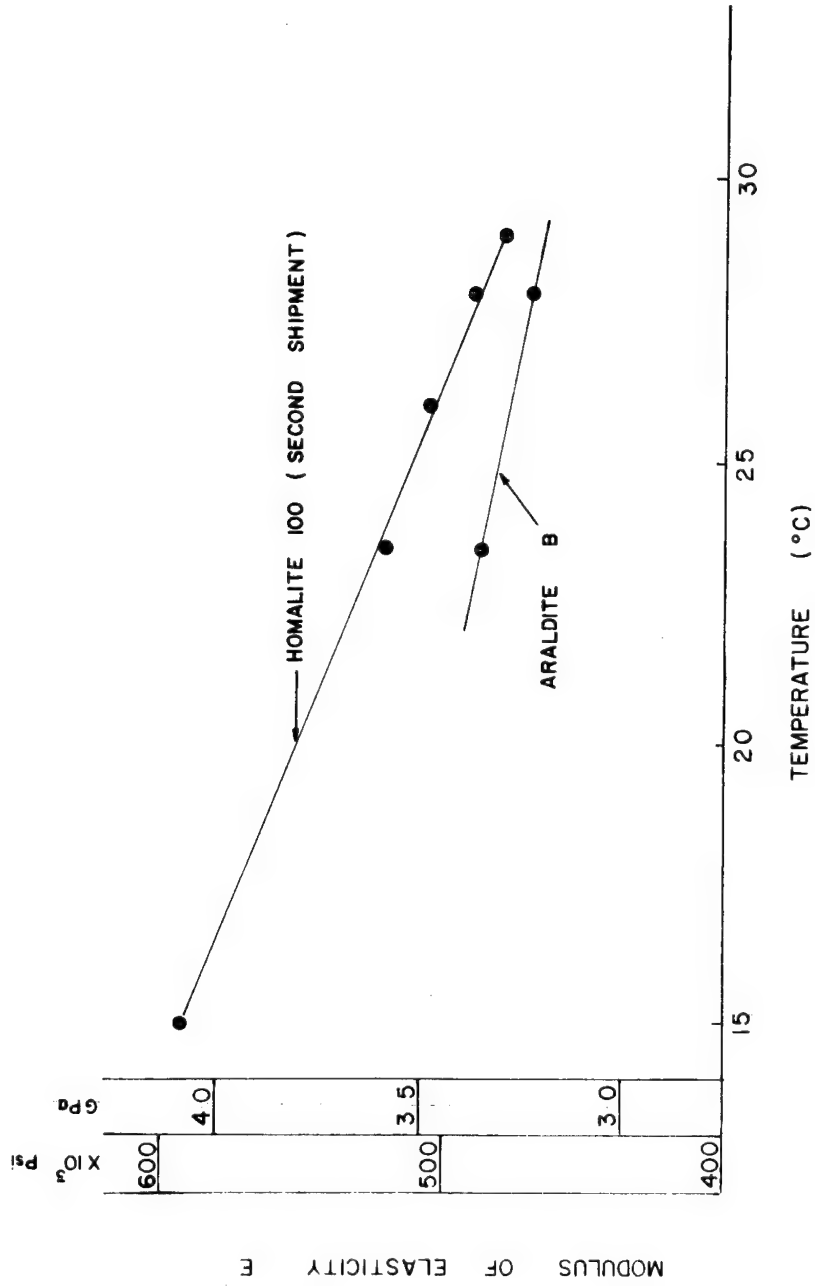


Fig. 7.4 Modulus of Elasticity as a Function of Temperature, Araldite B and Homalite 100 (2nd Shipment).

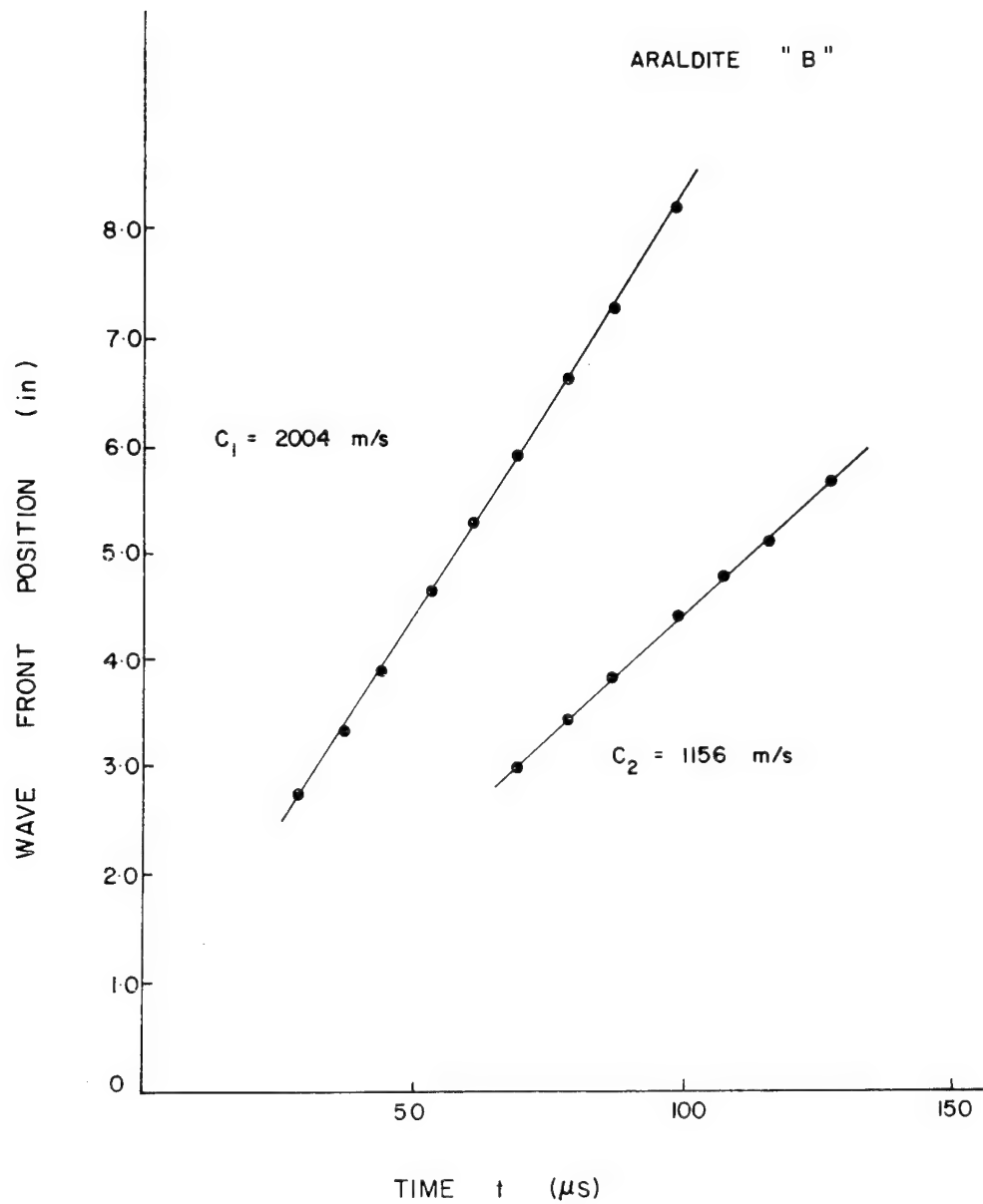


Fig. 7.5 Plate and Shear Wave Location with Time, Half Plane Model Test, Araldite B.



Fig. 7.6 Plate and Shear Wave, Half Plane Test No. 294, Araldite B.

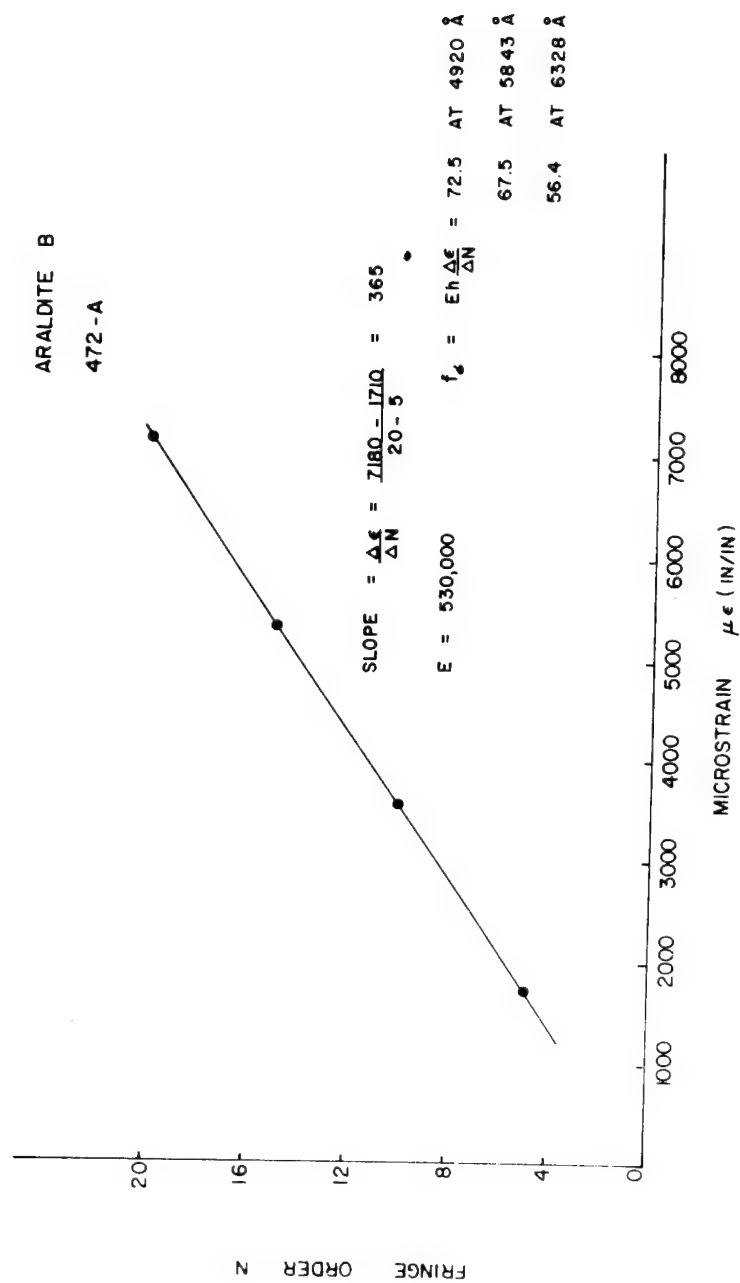


Fig. 7.7 Fringe Order vs Strain to Obtain $\Delta\epsilon/\Delta N$, Test No. 472A, Araldite B.

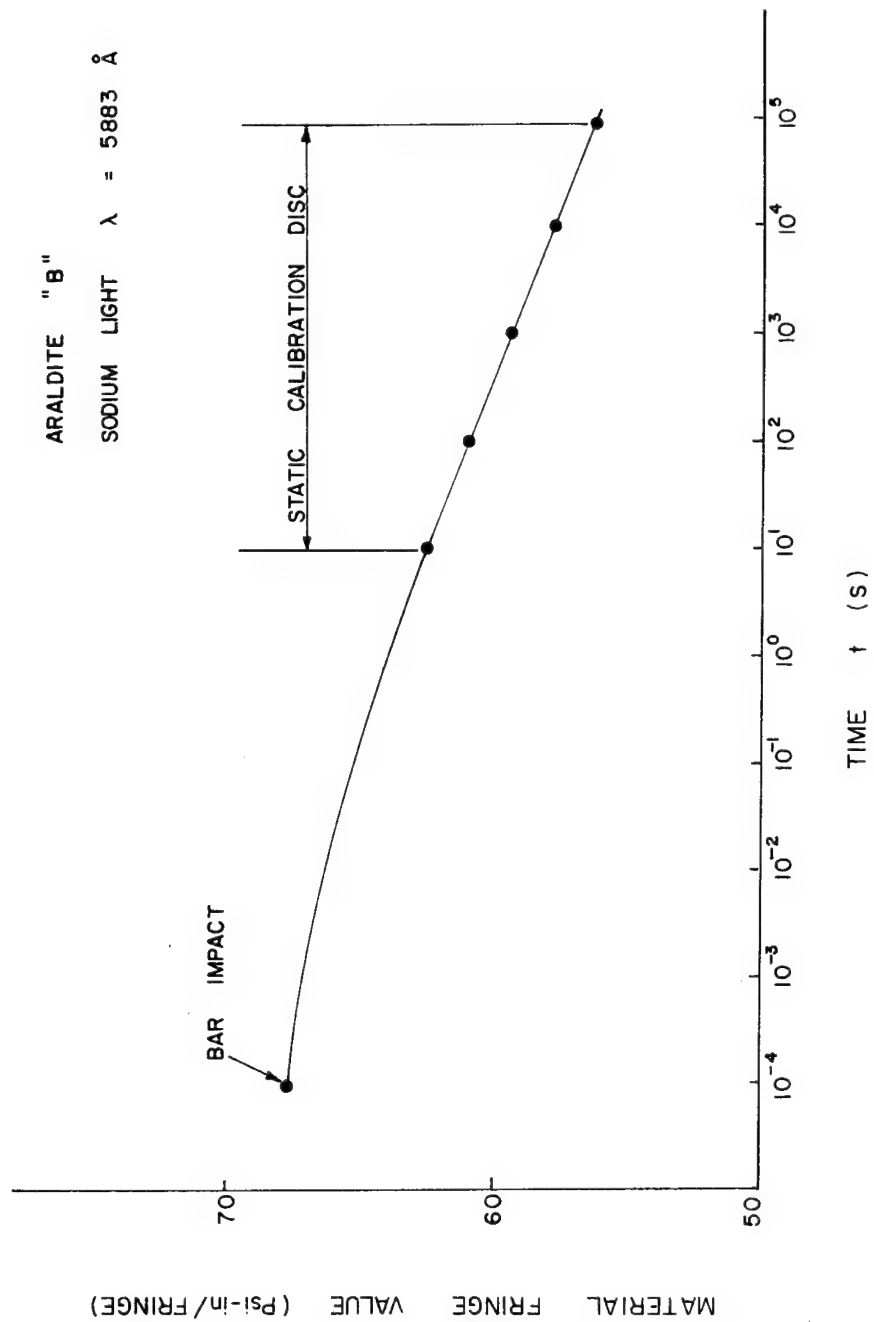


Fig. 7.8 Material Fringe Variation with loading Time, Araldite B.

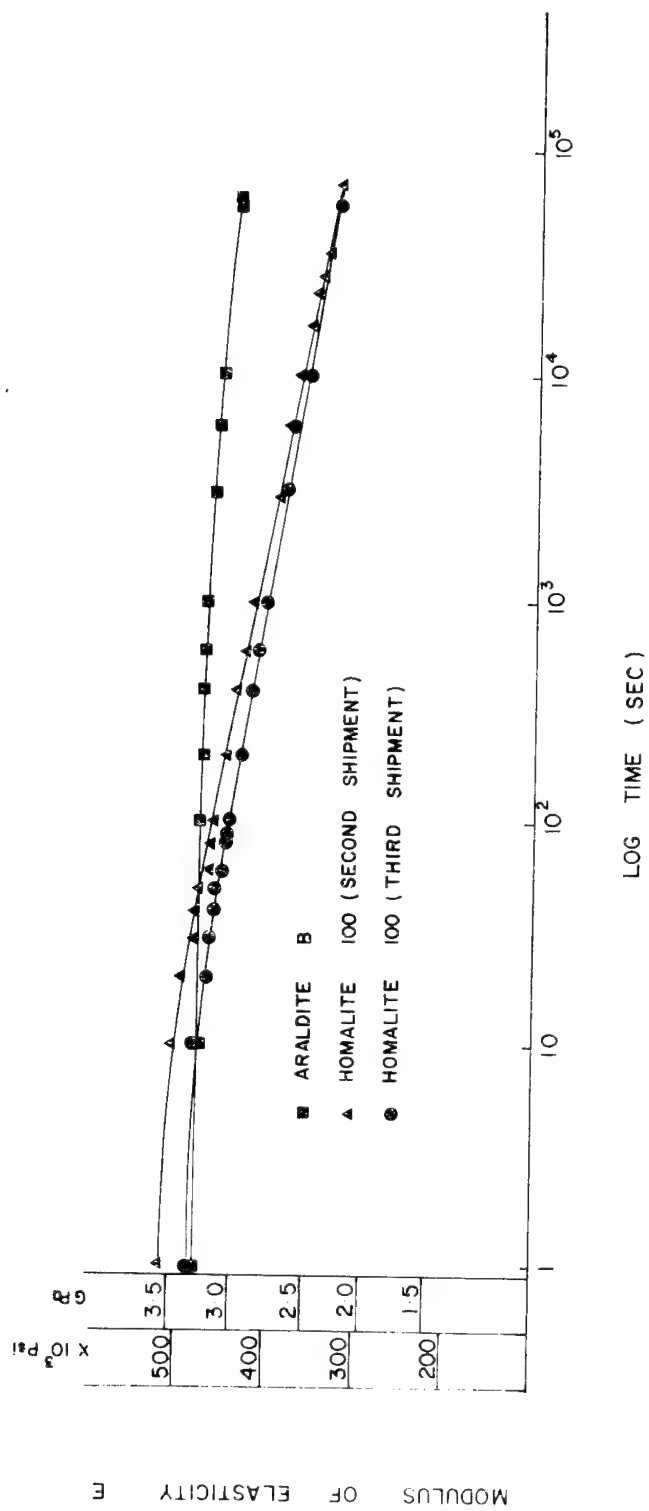


Fig. 7.9 Elastic Modulus as a Function of Time, Araldite B and Homalite 100.

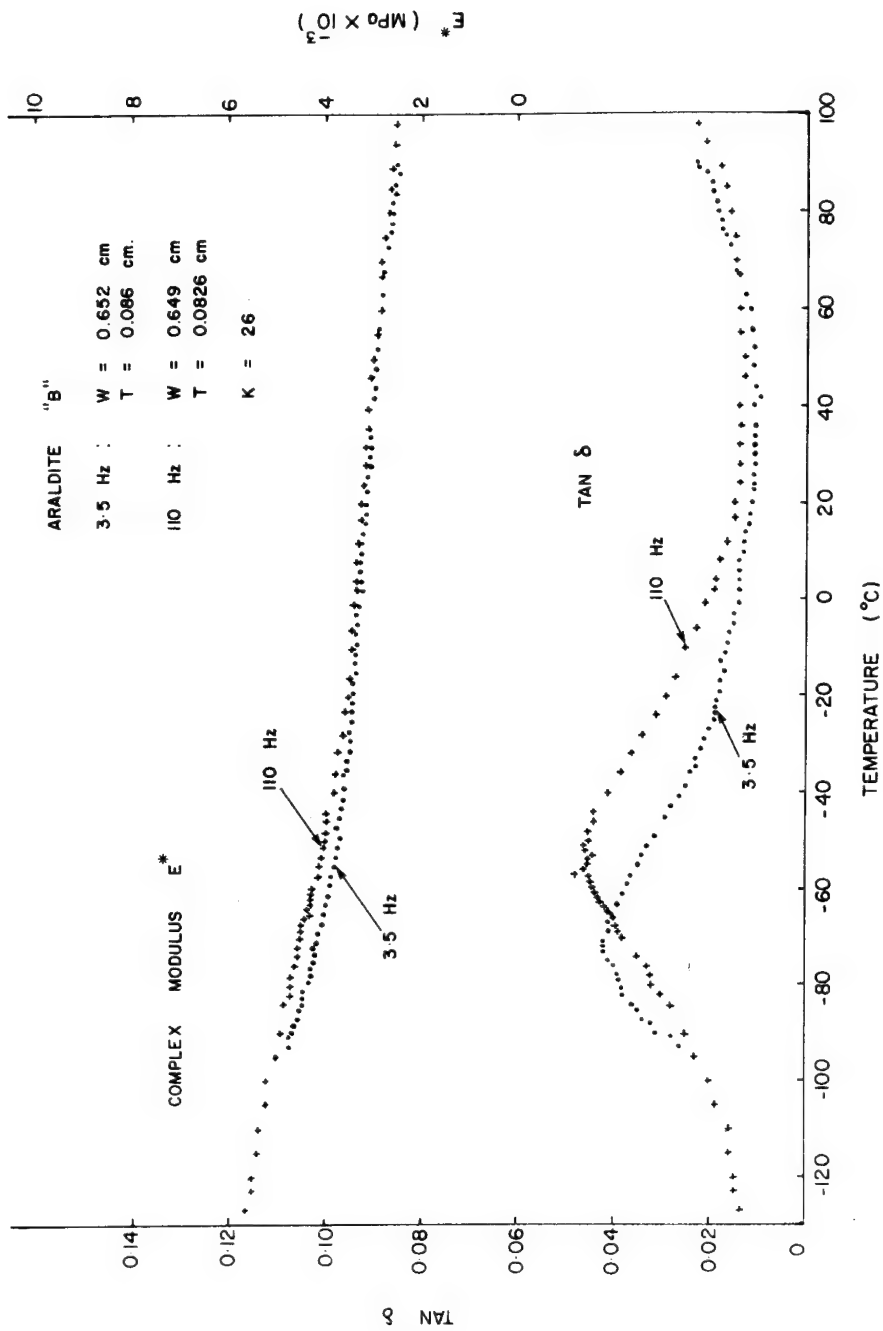


Fig. 7.10 Tangent δ and Complex Modulus E^* as a Function of Temperature and Frequency, Araldite B.

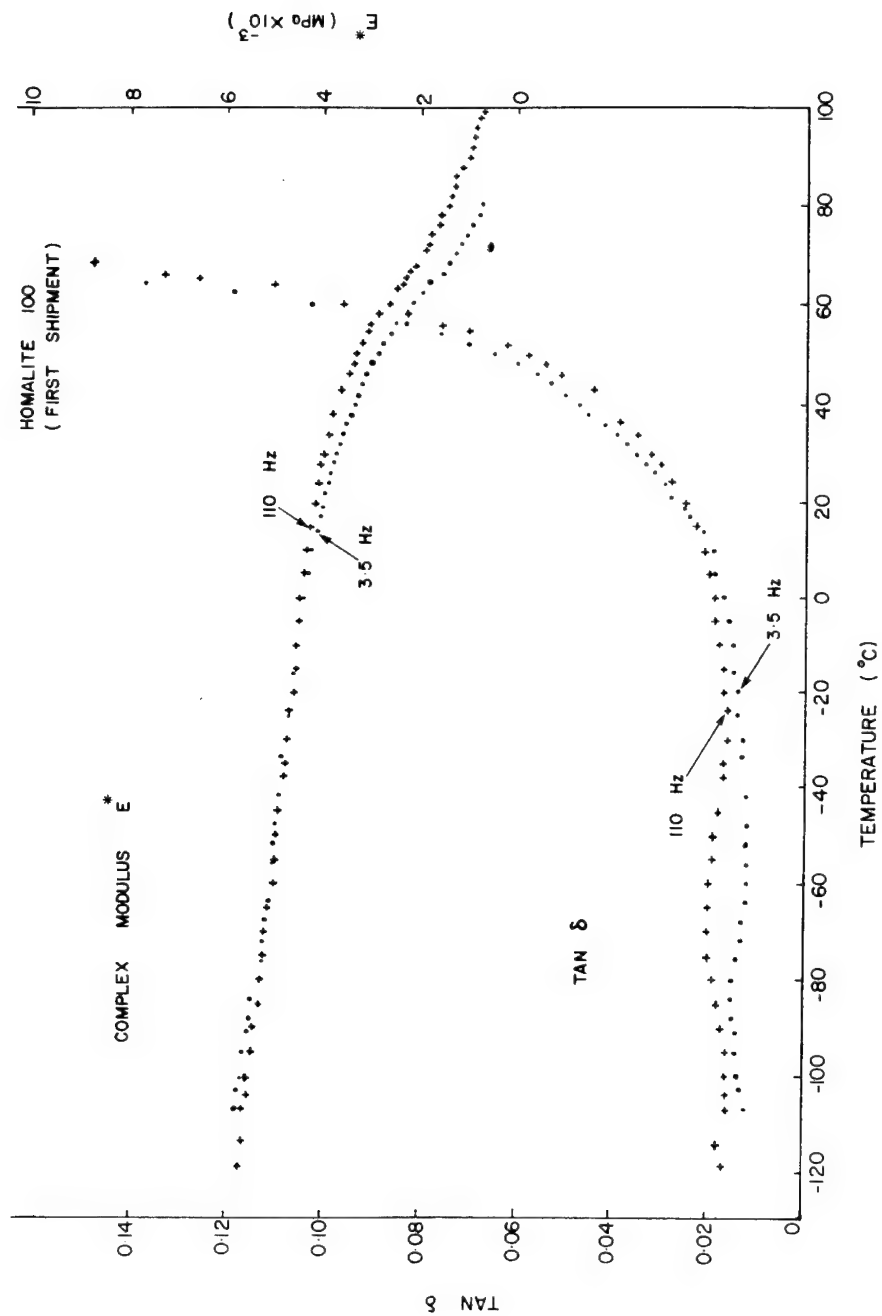


Fig. 7.11 Tangent δ and Complex Modulus E^* as a Function of Temperature and Frequency, Homalite 100 (1st Shipment).

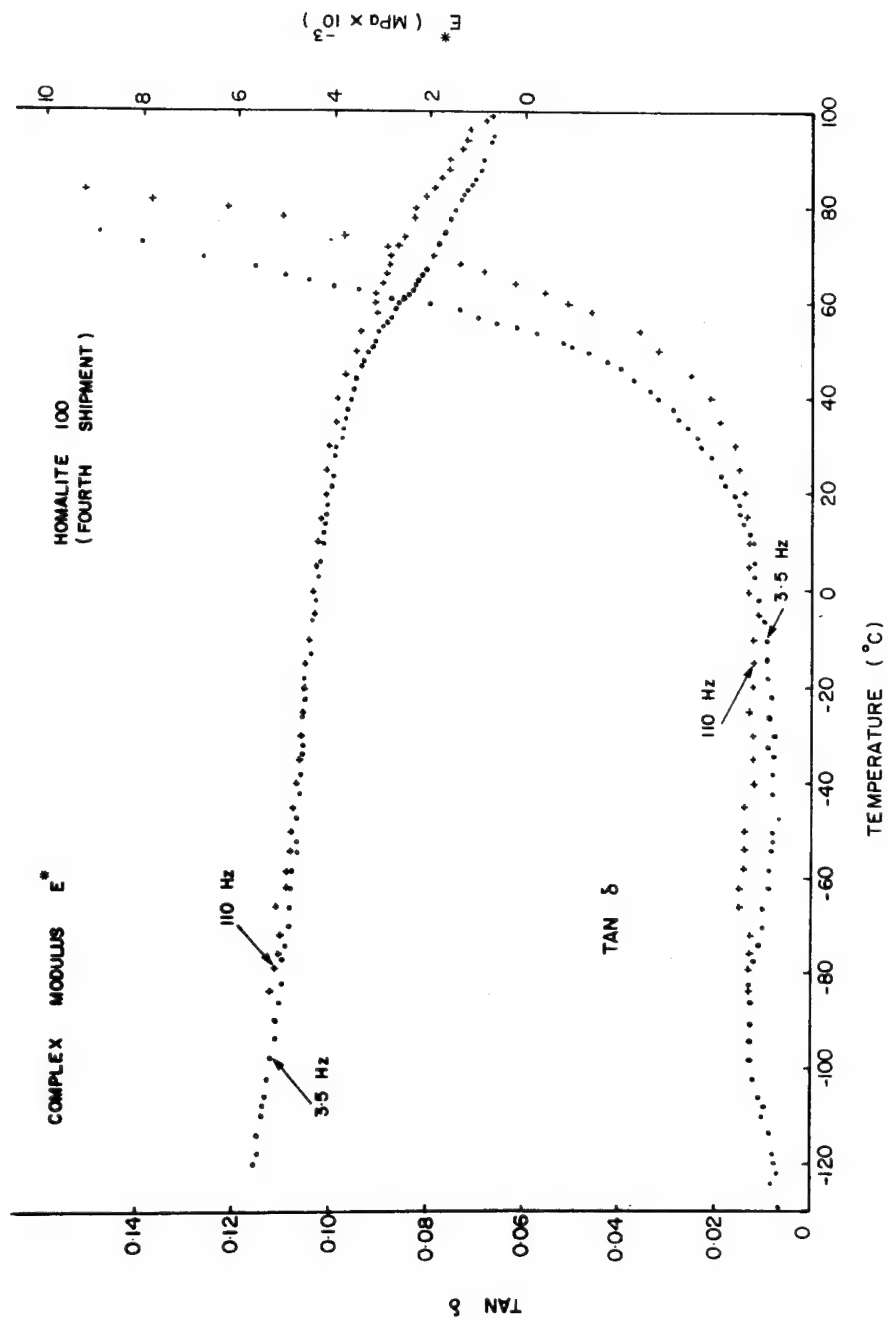


Fig. 7.12 Tangent δ and Complex Modulus E^* as a Function of Temperature and Frequency, Homalite 100 (4th Shipment).

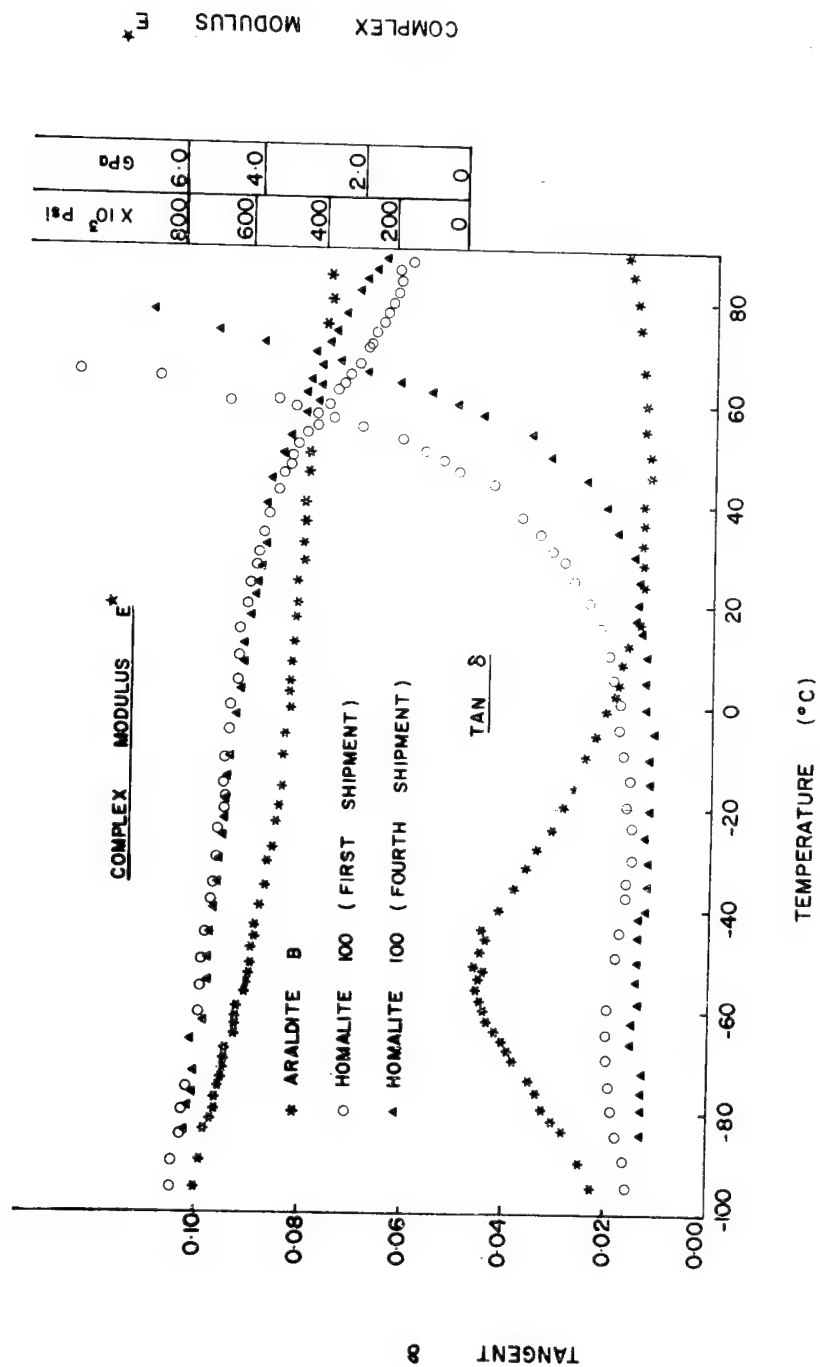


Fig. 7.13 Tangent δ and Complex Modulus E^* as a Function of Temperature, Araldite B and Homalite 100 (1st and 4th Shipments).

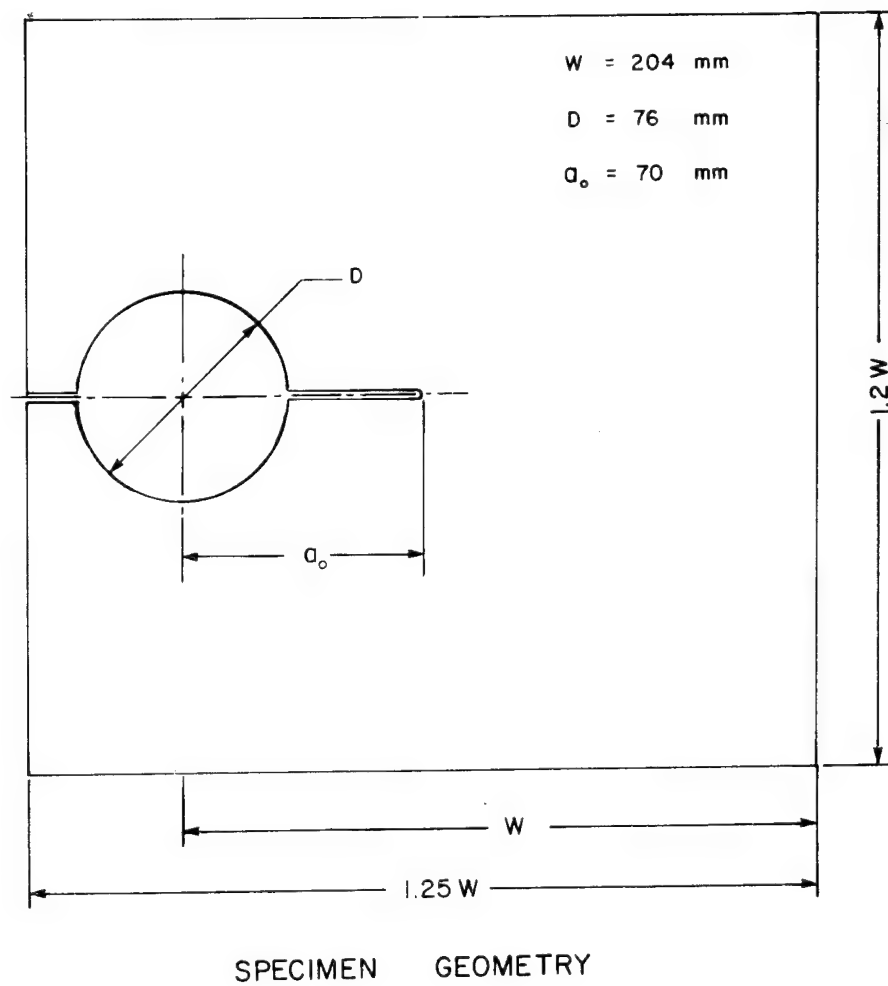
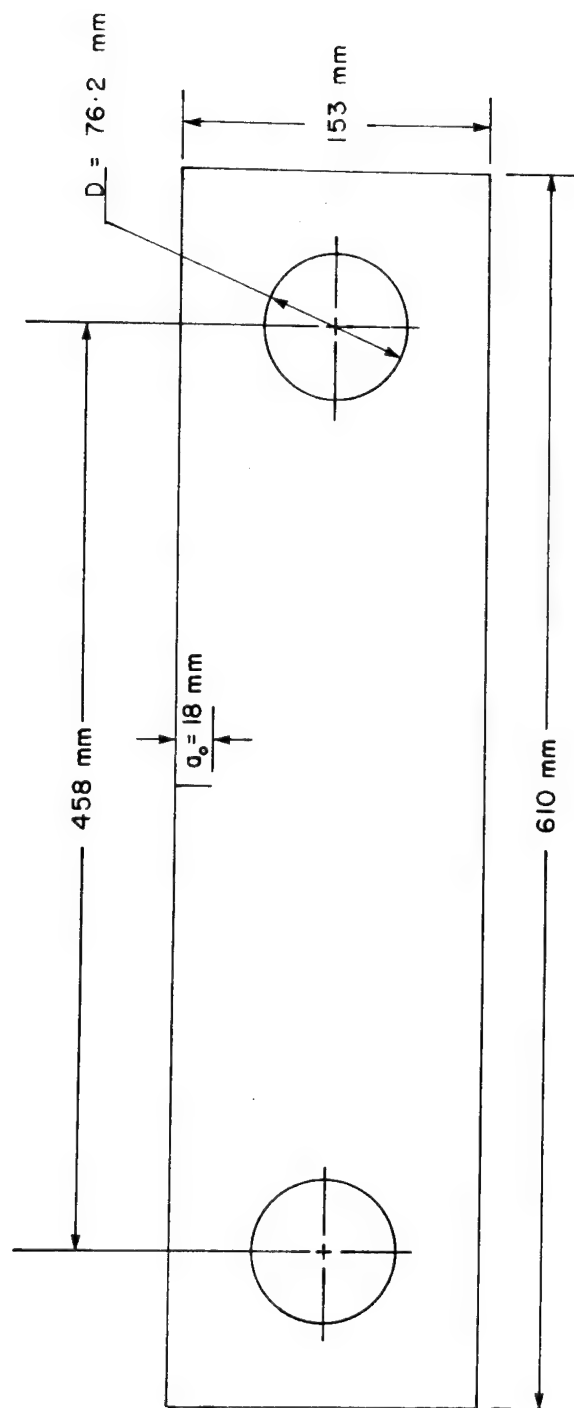
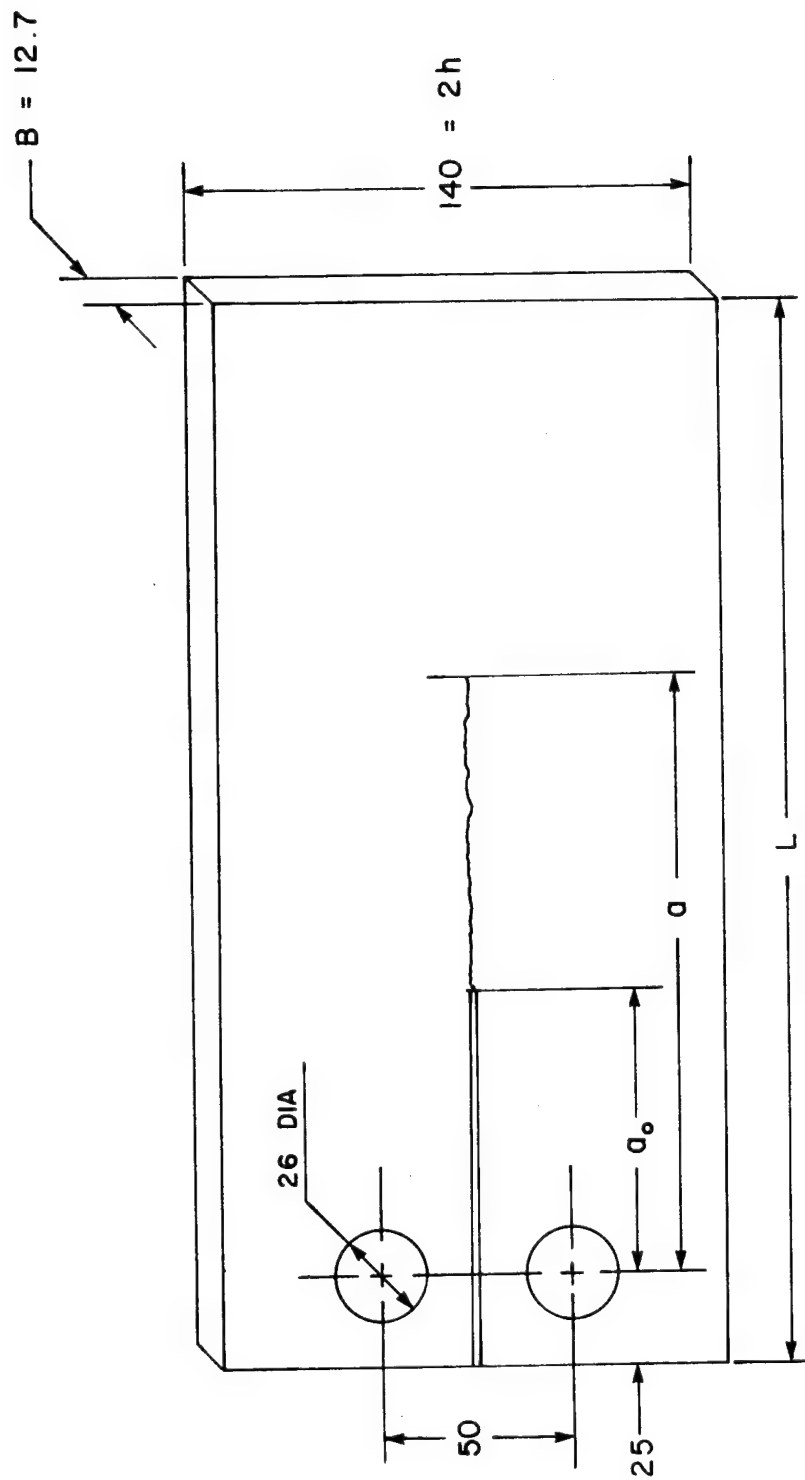


Fig. 7.14 Modified Crack Arrest Compact Specimen Geometry.



SPECIMEN GEOMETRY

Fig. 7.15 Center Pin Loading SEN Specimen Geometry.



SPECIMEN GEOMETRY

Fig. 7.16 Rectangular Double Cantilever Beam Specimen Geometry.

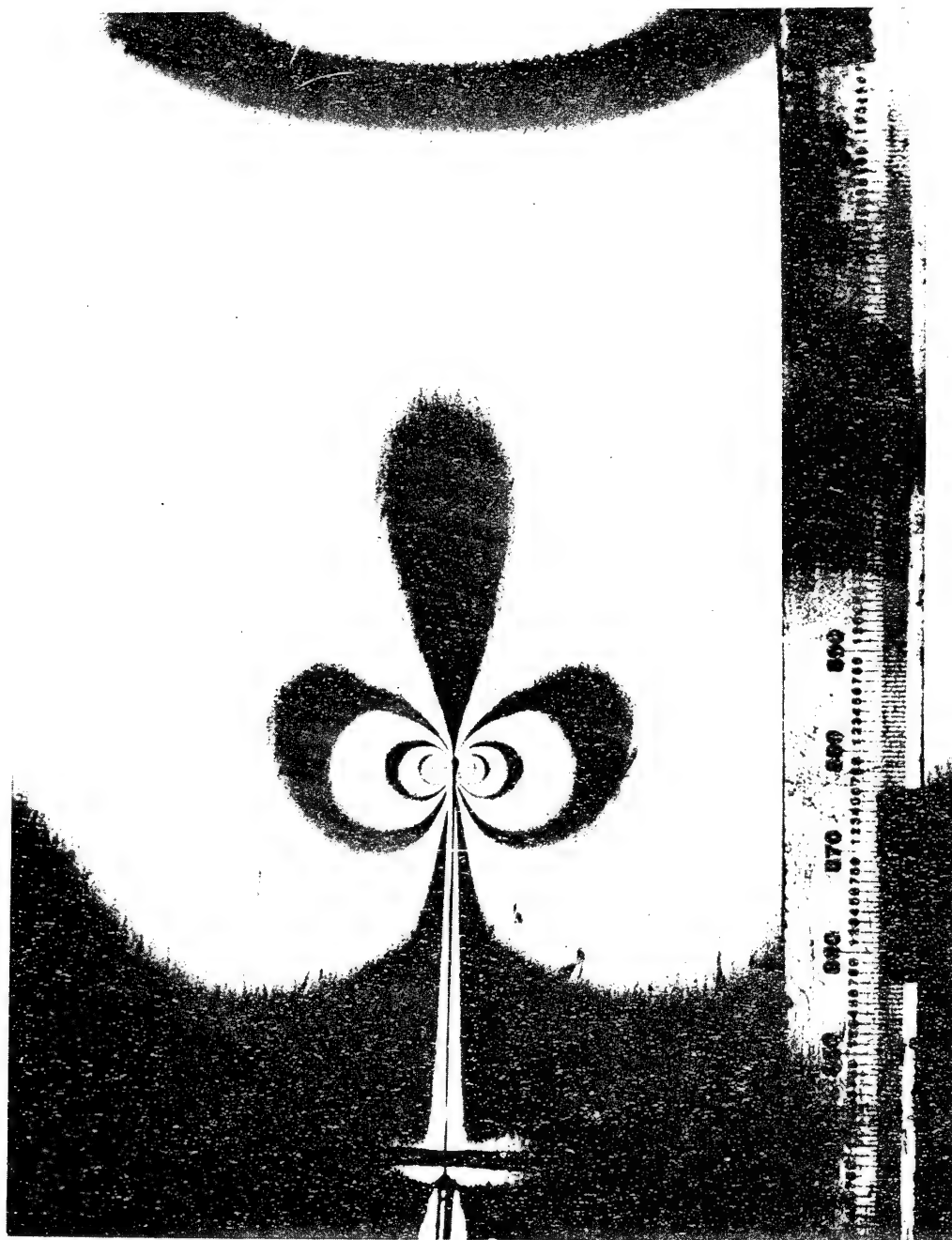


Fig. 7.17 Stress Intensity at Crack Tip, Test No. 287, AralditeB.

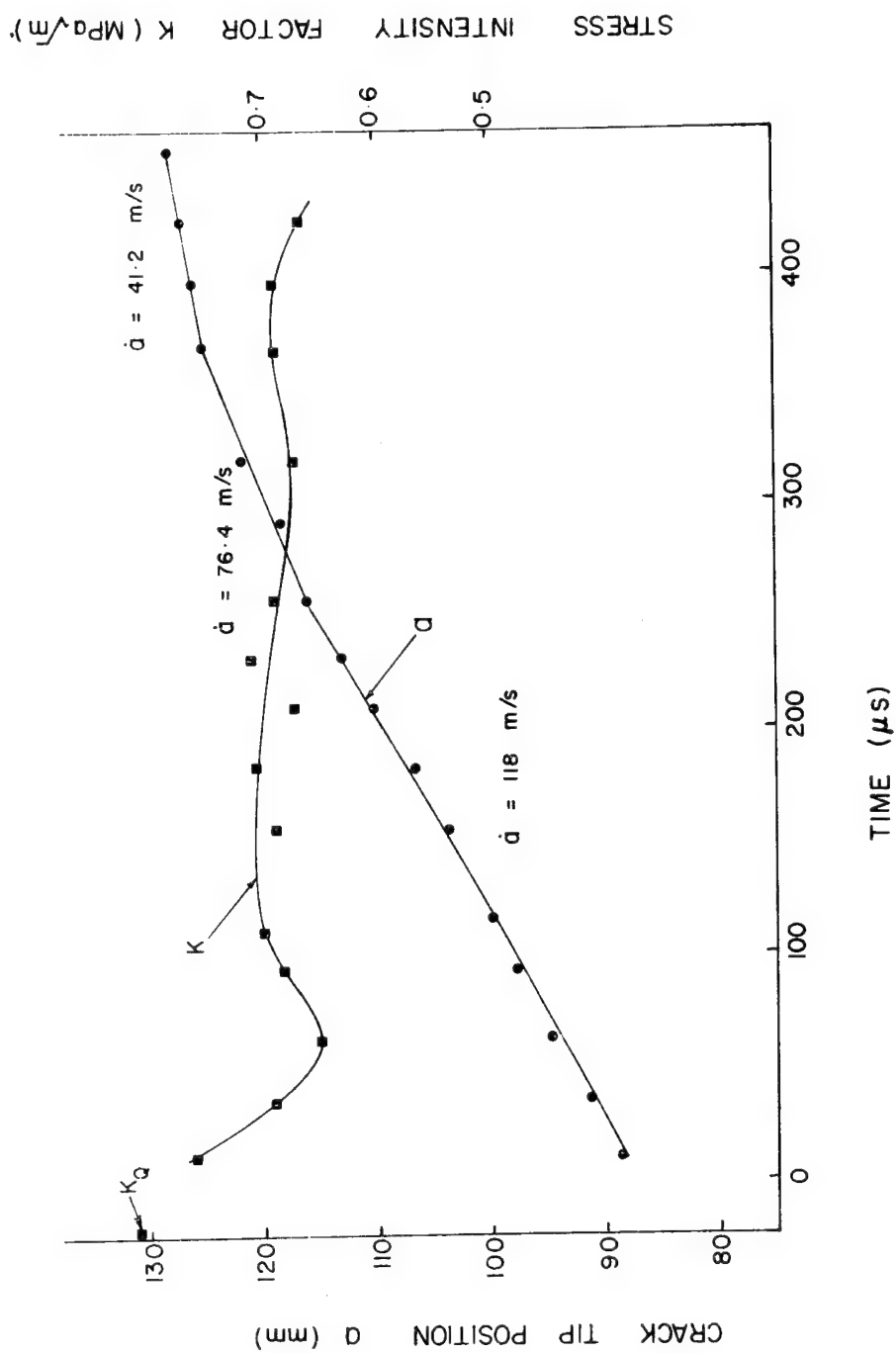


Fig. 7.18 Crack Tip Position and Stress Intensity Factor as a Function of Time, Test No. 287, Araldite B.

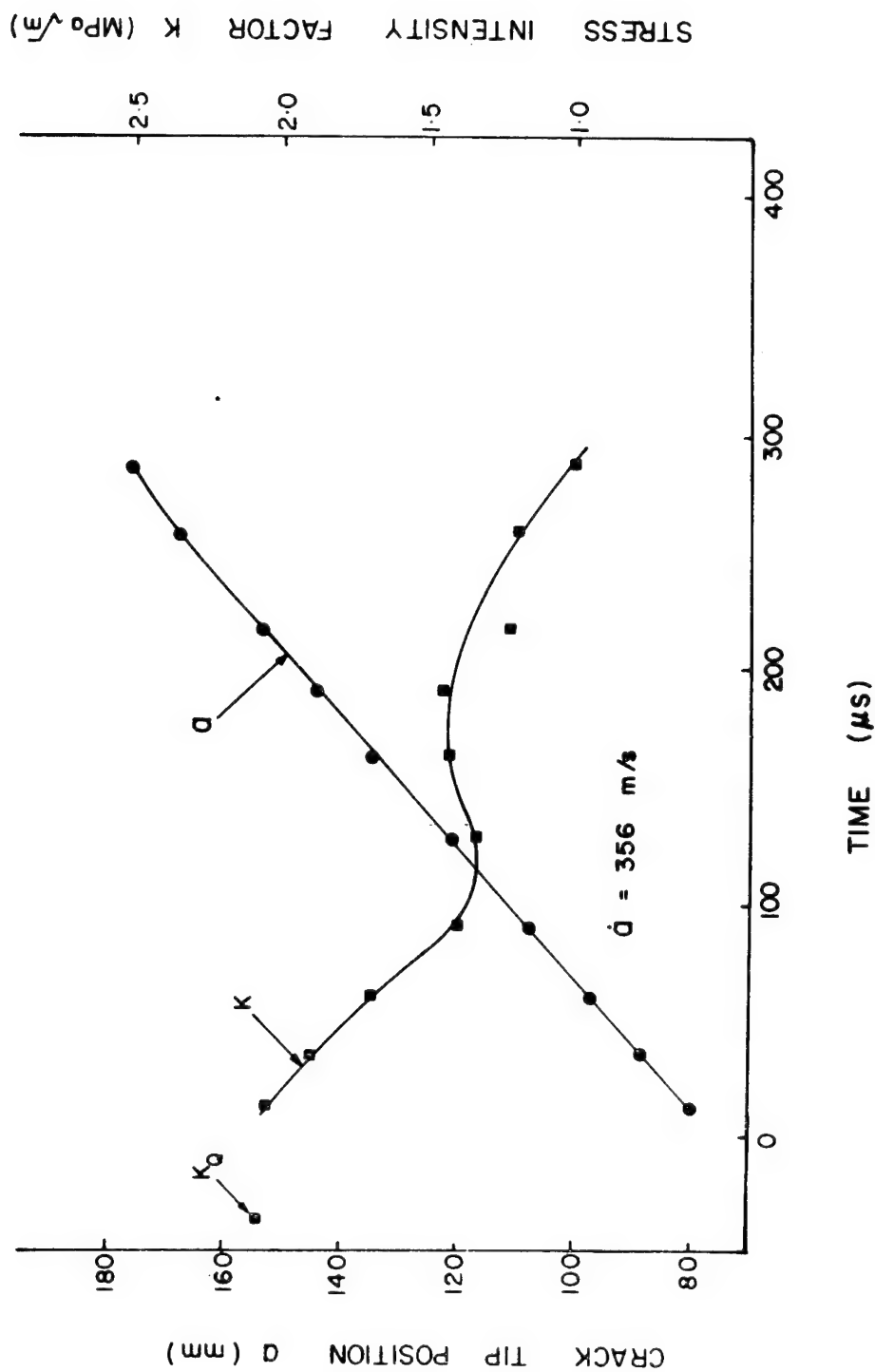


Fig. 7.19 Crack Tip Position and Stress Intensity Factor as a Function of Time, Test No. 293, Araldite B.

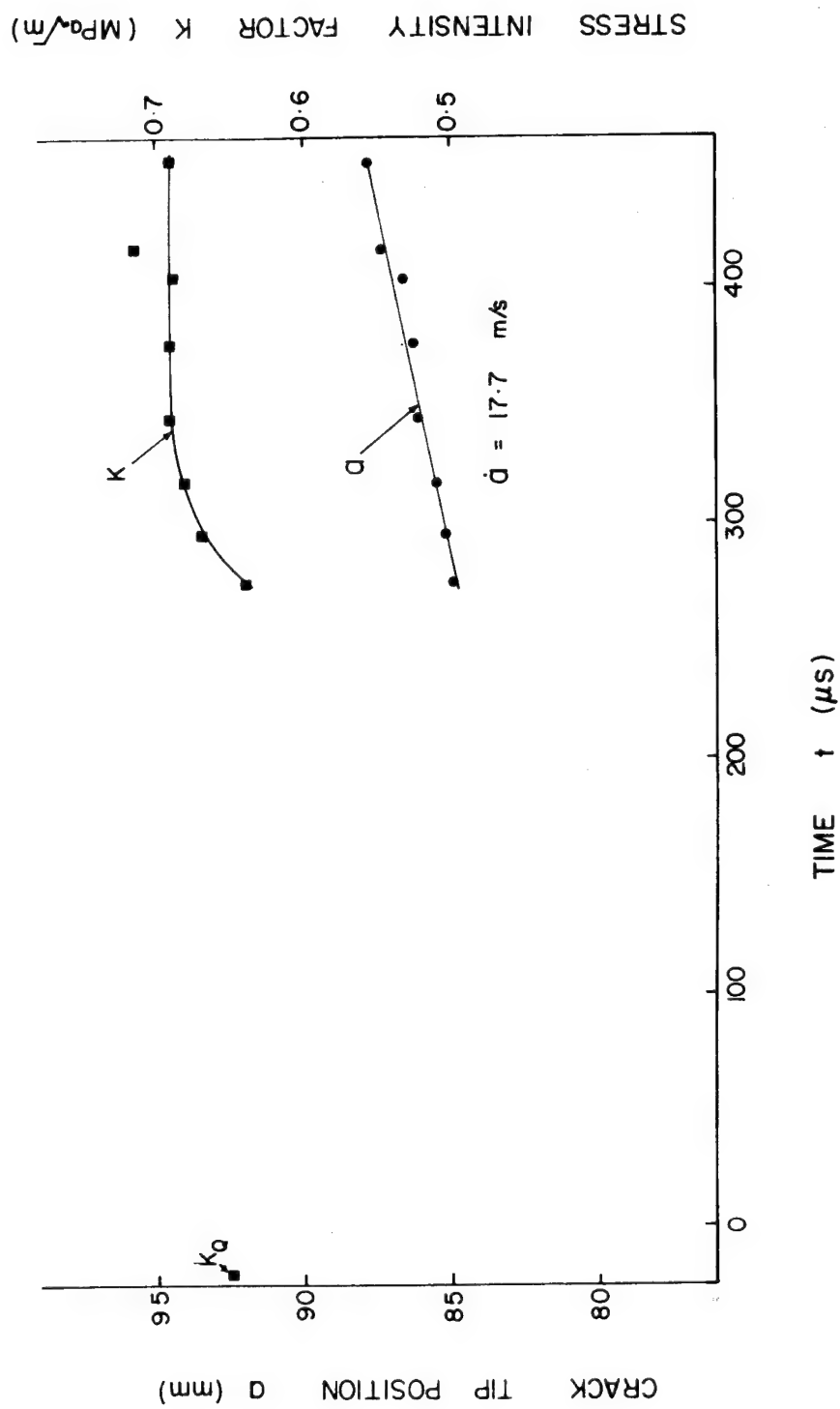


Fig. 7.20 Crack Tip Position and Stress Intensity Factor as a Function of Time, Test No. 313, Araldite B.

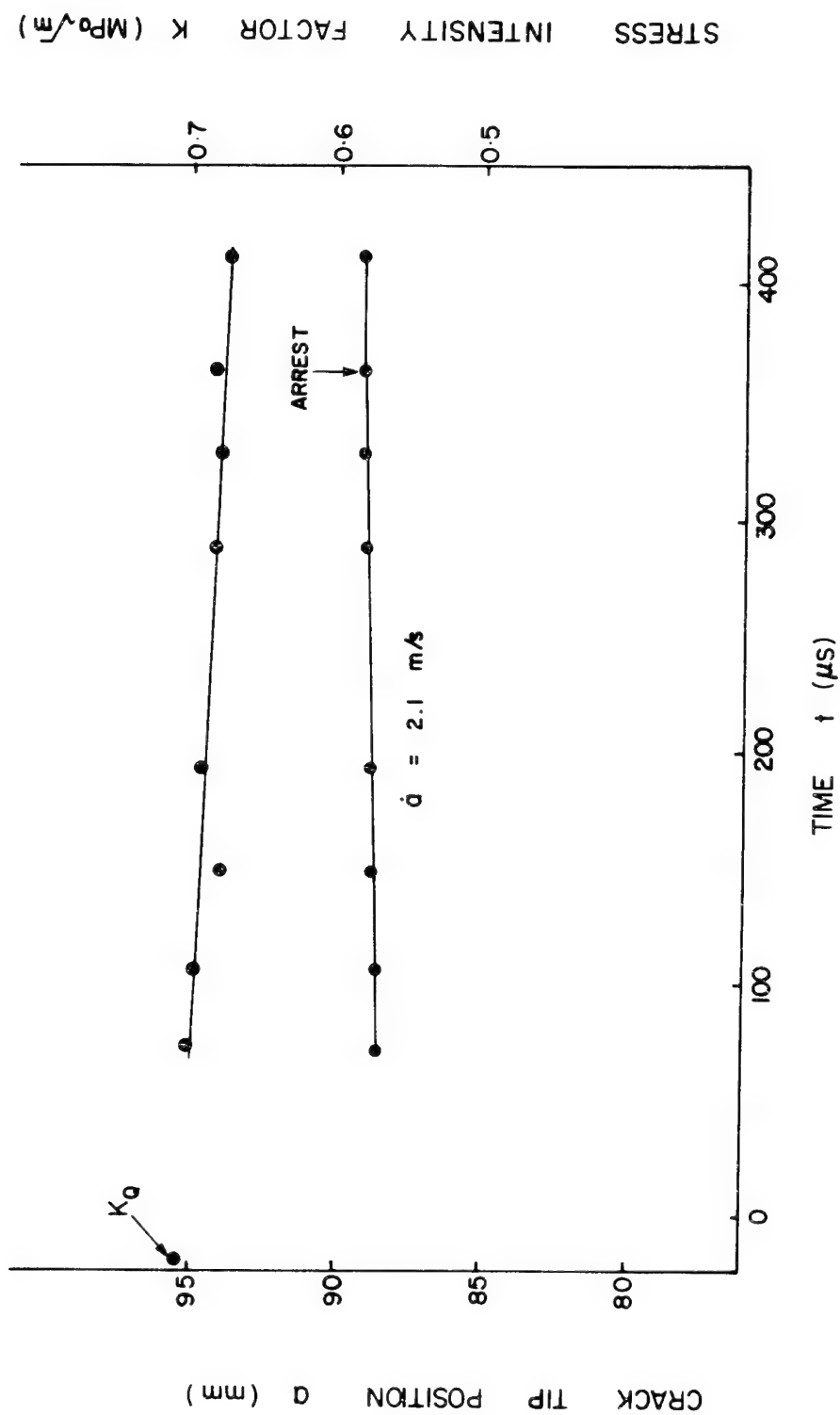


Fig. 7.21 Crack Tip Position and Stress Intensity Factor as a Function of Time, Test No. 314, Araldite B.

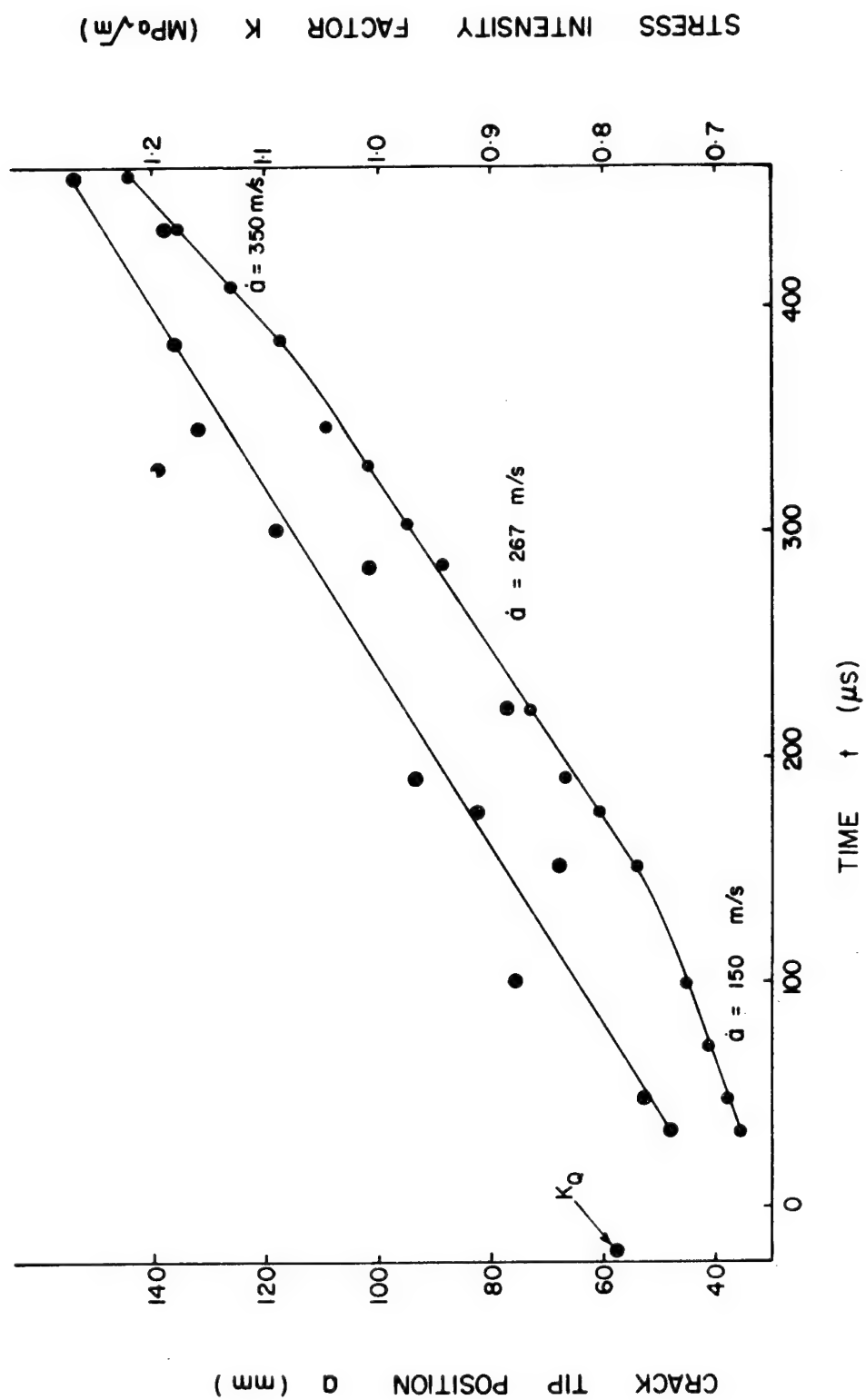


Fig. 7.22 Crack Tip Position and Stress Intensity Factor as a Function of Time, Test No. 308, Araldite B.

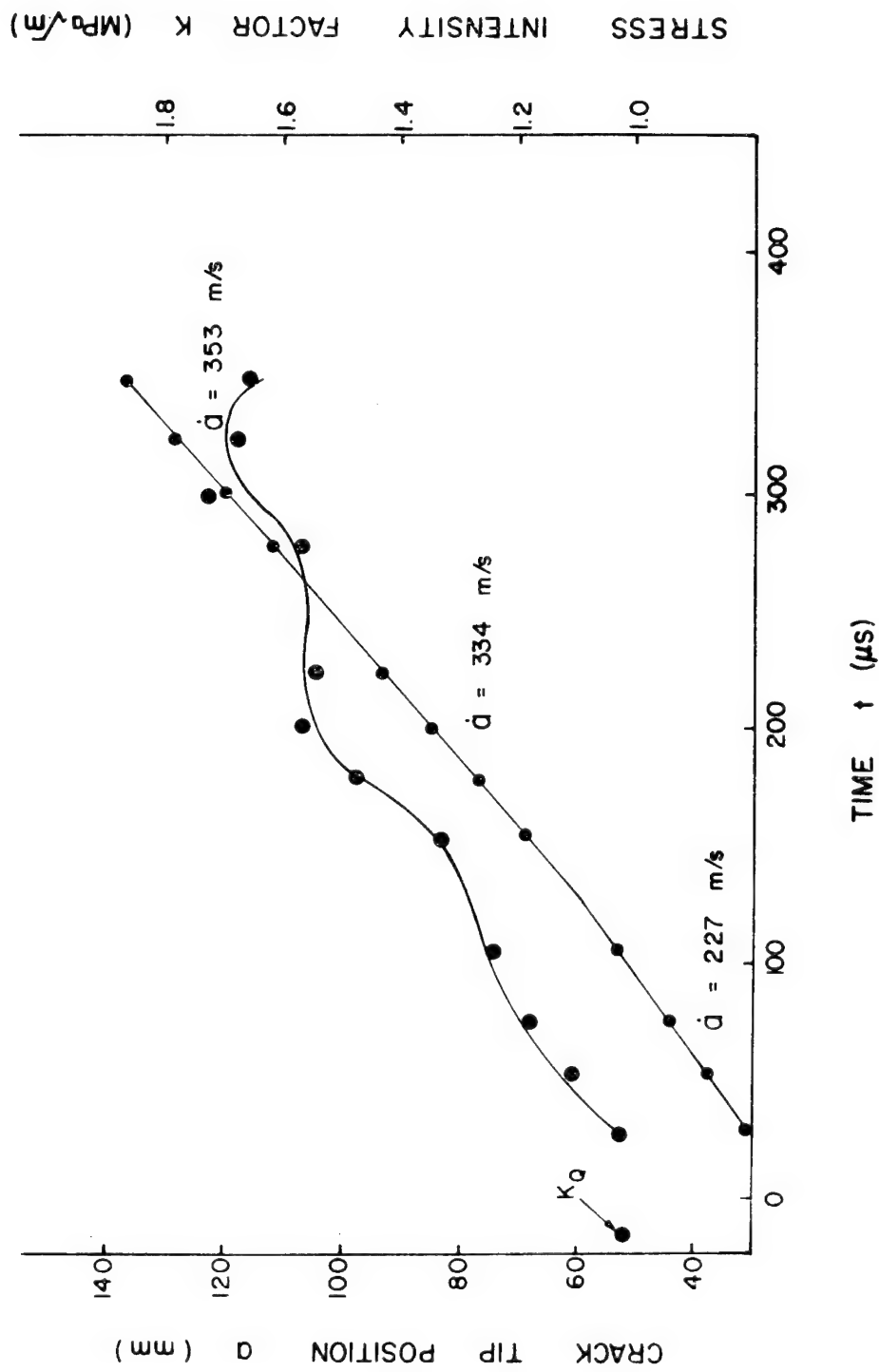


Fig. 7.23 Crack Tip Position Stress Intensity Factor as a Function of Time, Test #309, Araldite B.

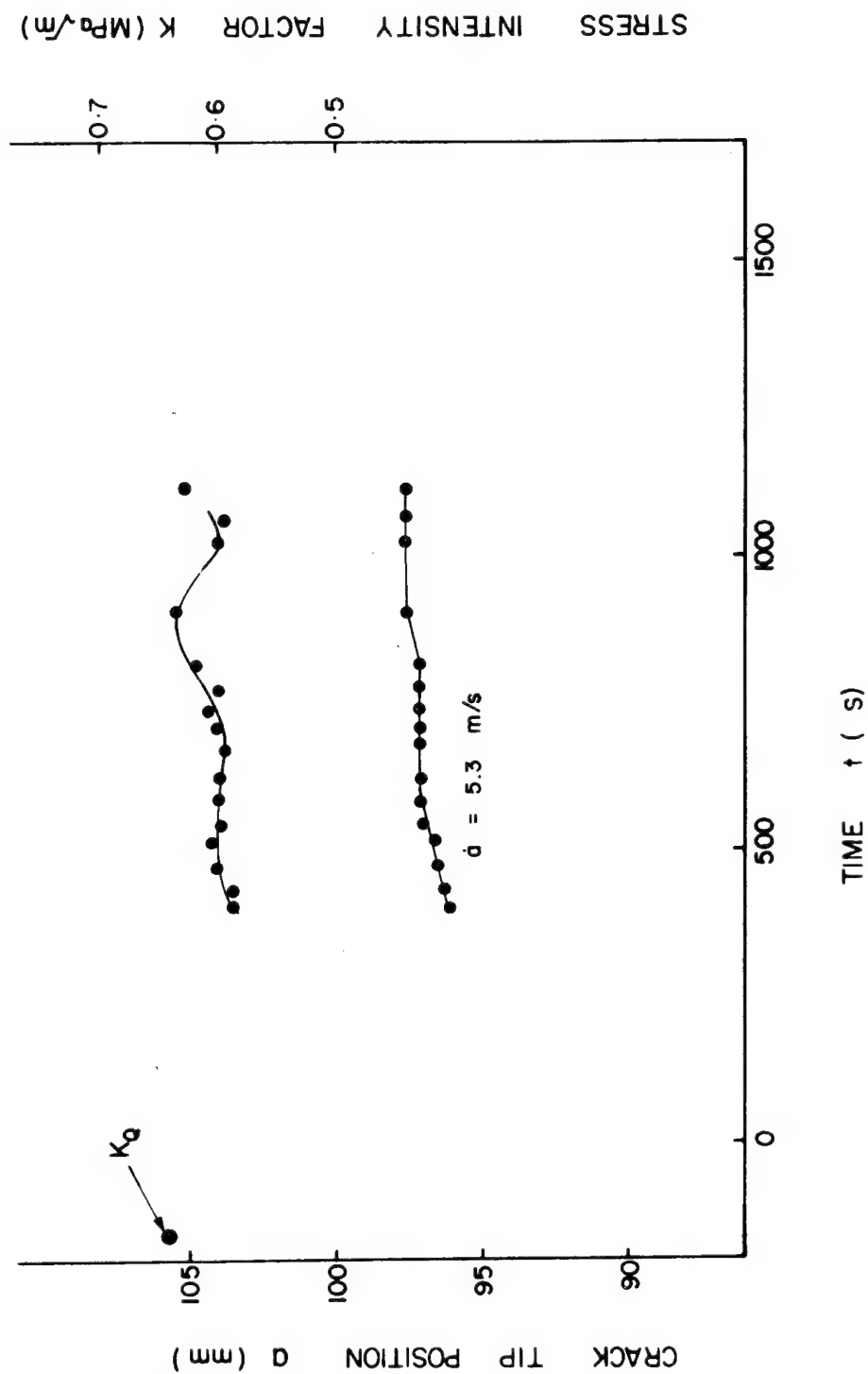


Fig. 7.24 Crack Tip Position and Stress Intensity Factor as a Function of Time, Test No. 331.
Araldite B.

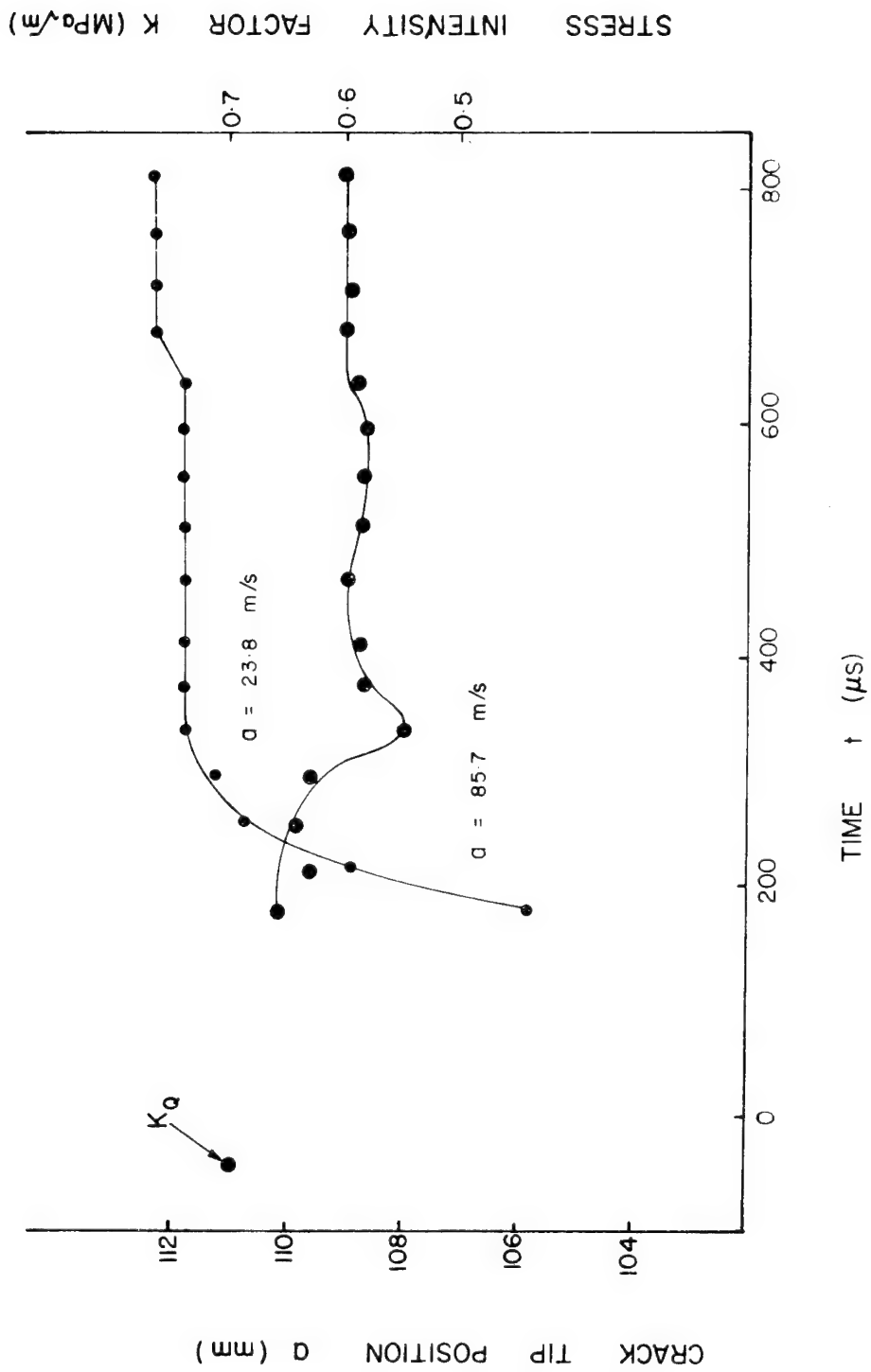


Fig. 7.25 Crack Tip Position and Stress Intensity Factor as a Function of Time, Test No. 332, Araldite B.

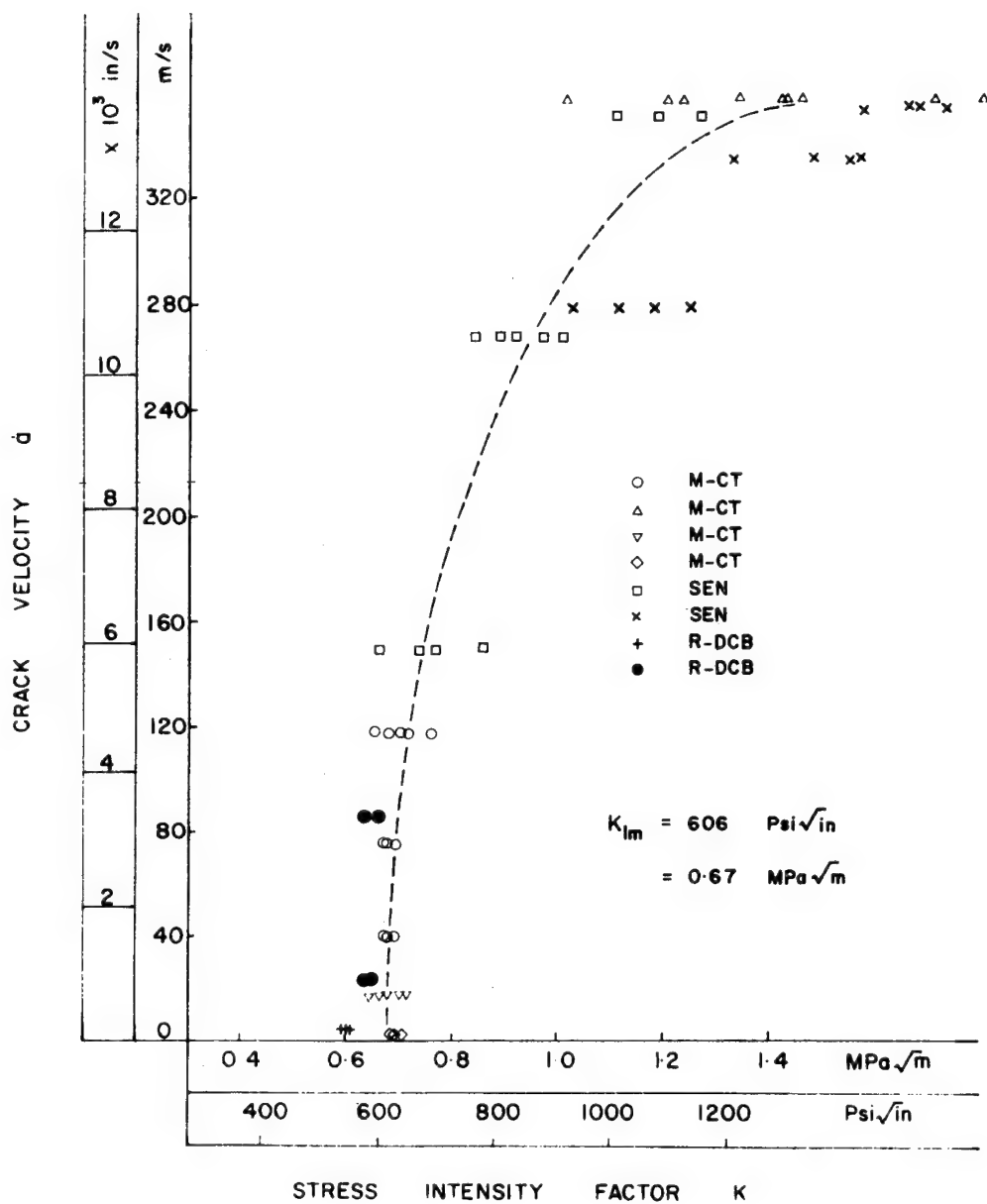


Fig. 7.26 Crack Velocity as a Function of Stress Intensity Factor, Araldite B.

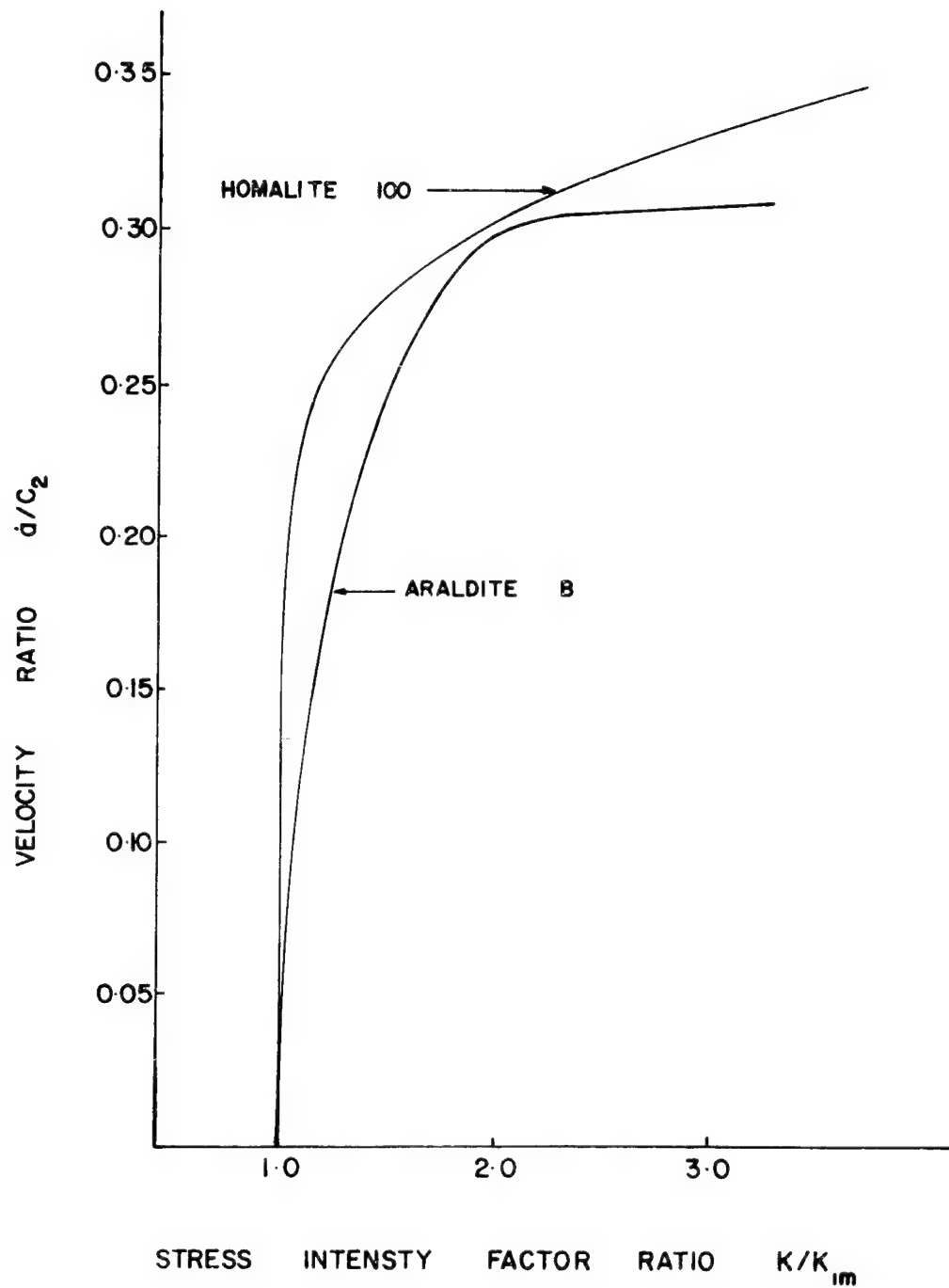


Fig. 7.27 Normalized \dot{a} vs K Relationship, Homalite 100 and Araldite B.

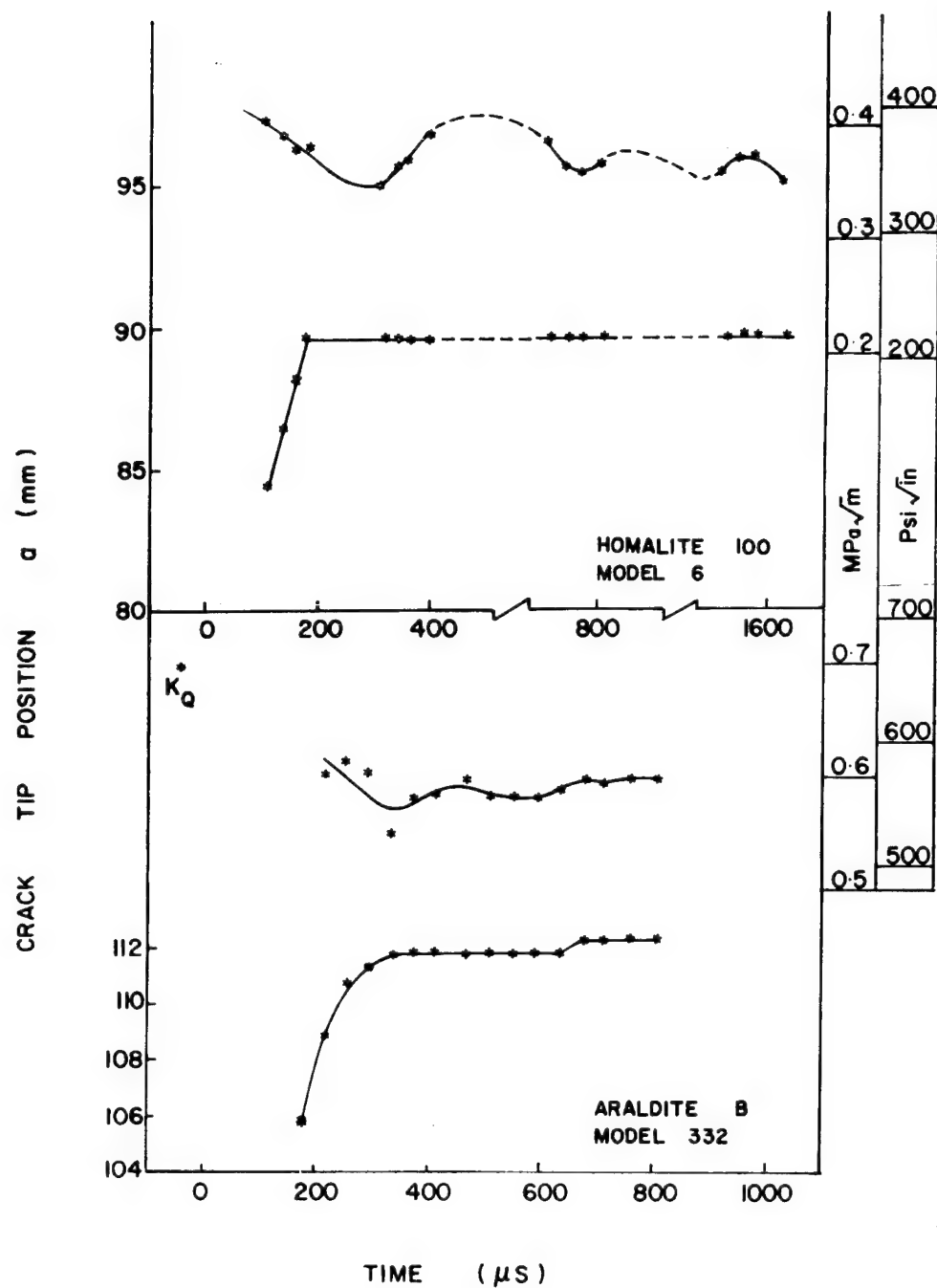


Fig. 7.28 Post Arrest Oscillations in Stress Intensity Factor, R-DCB, Araldite B and Homalite 100.

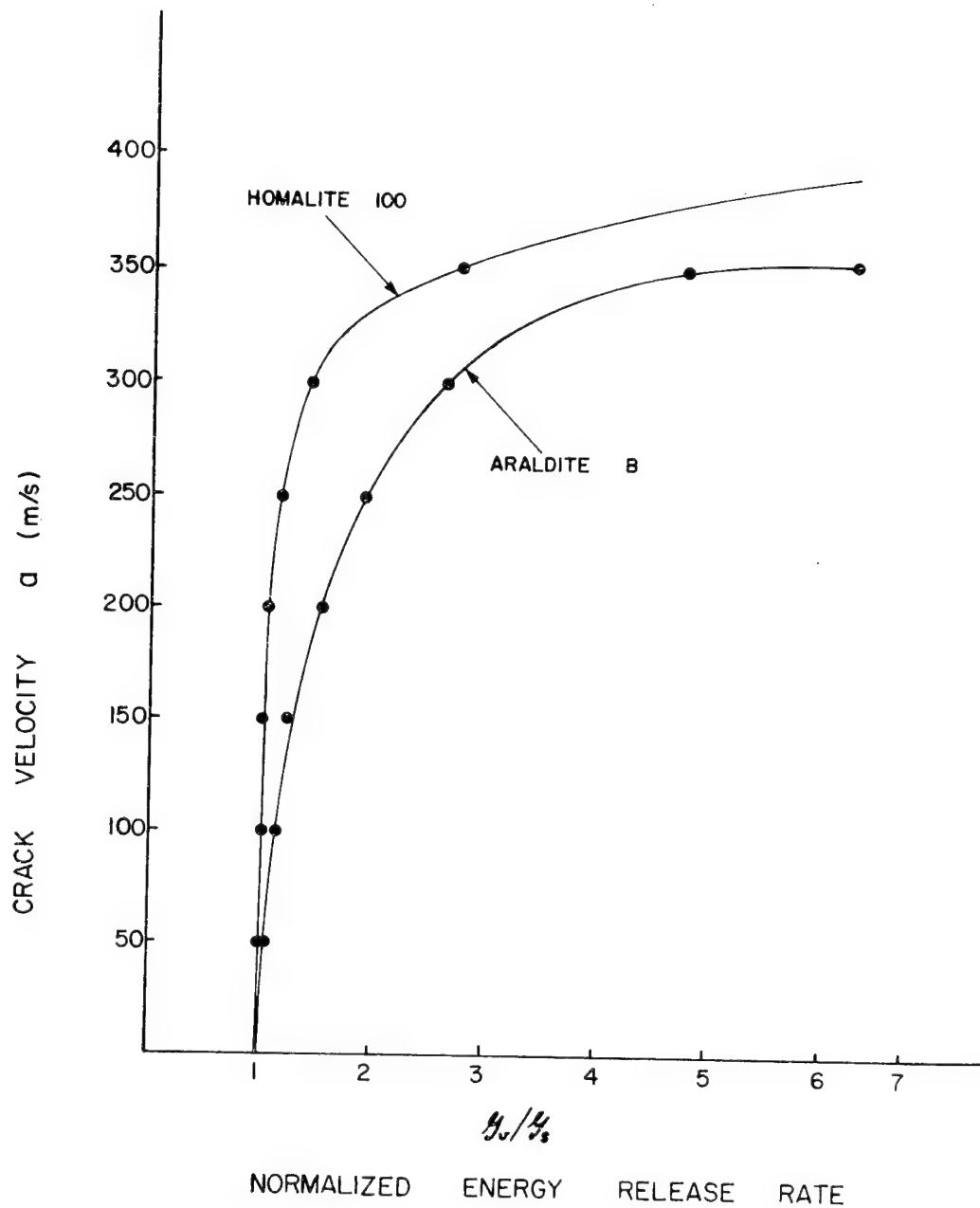


Fig. 7.29 Normalized Energy Release Rate as a Function of Crack Velocity, Homalite 100 and Araldite B.

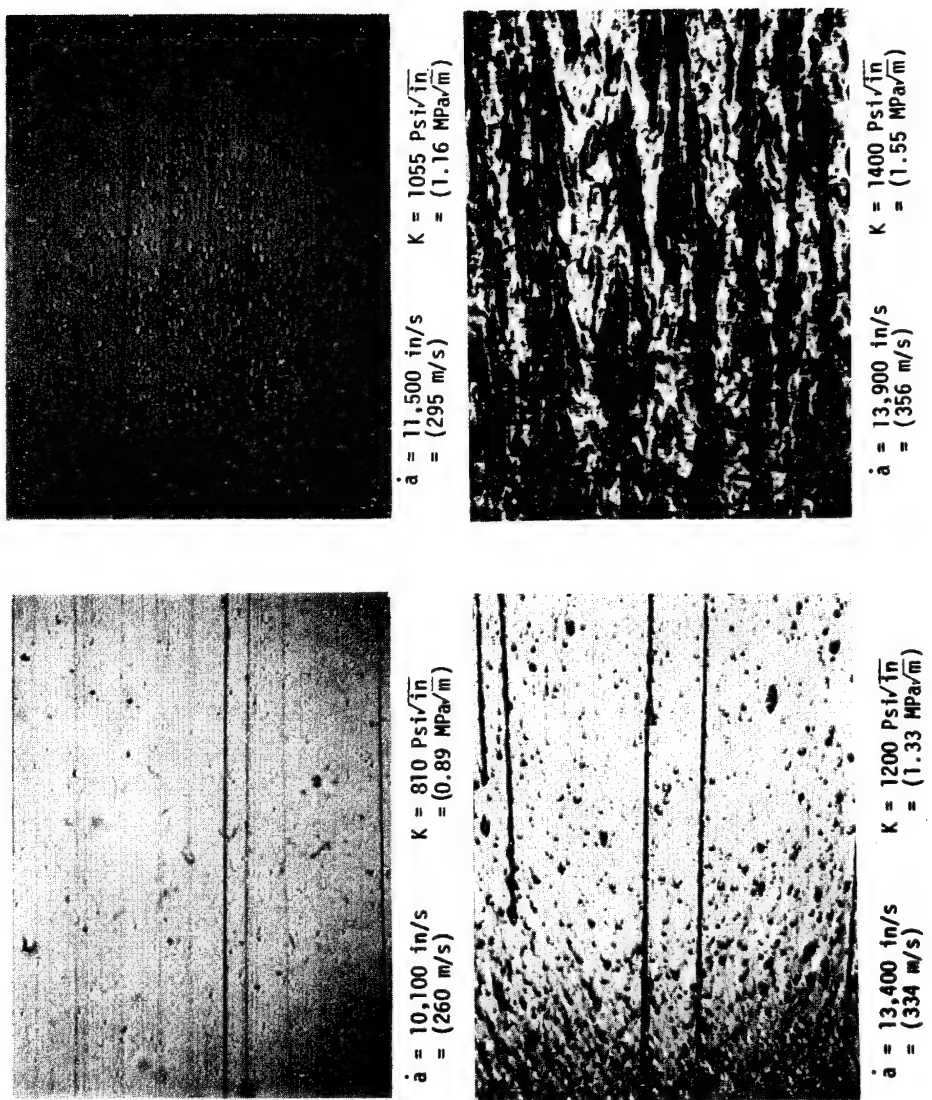
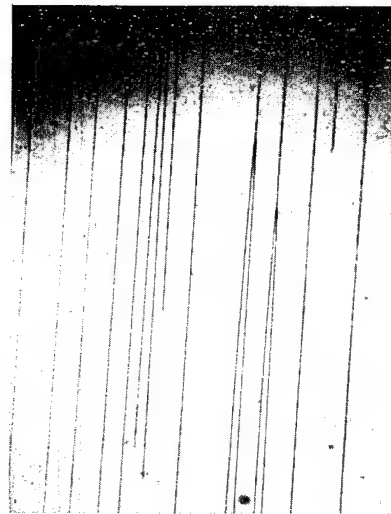
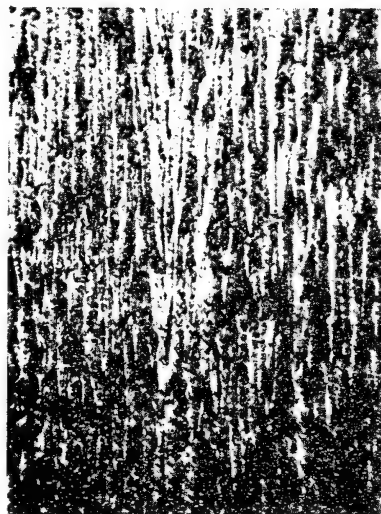


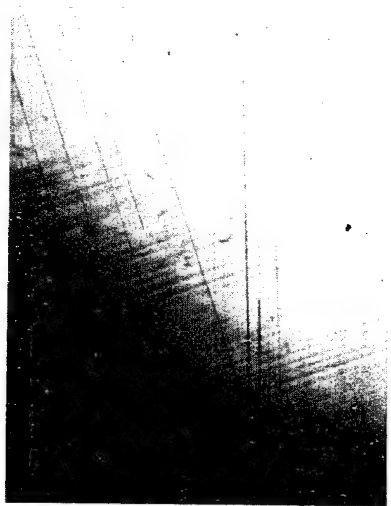
Fig. 7.30 Surface Features, Araldite B.



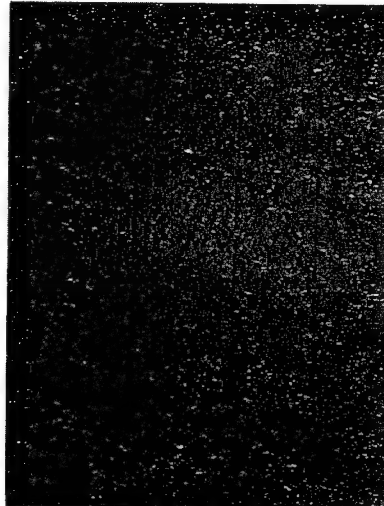
$\dot{a} = 10,200 \text{ in/s}$
 $= (262 \text{ m/s})$
 $K = 400 \text{ Psi}/\sqrt{\text{in}}$
 $= (0.442 \text{ MPa}/\sqrt{\text{m}})$



$\dot{a} = 15,700 \text{ in/s}$
 $= (402 \text{ m/s})$
 $K = 880 \text{ Psi}/\sqrt{\text{in}}$
 $= (0.875 \text{ MPa}/\sqrt{\text{m}})$



$\dot{a} = 13,300 \text{ in/s}$
 $= (341 \text{ m/s})$
 $K = 382 \text{ Psi}/\sqrt{\text{in}}$
 $= (0.422 \text{ MPa}/\sqrt{\text{m}})$



$\dot{a} = 13,300 \text{ in/s}$
 $= (341 \text{ m/s})$
 $K = 580 \text{ Psi}/\sqrt{\text{in}}$
 $= (0.641 \text{ MPa}/\sqrt{\text{m}})$

Fig. 7.31 Surface Features, Homalite 100

APPENDIX A - DATA SUMMARIES FOR RING SPECIMEN

TABLE A-1
Summary of Results for Model R-6
($K_Q = 1.075 \text{ MPa}\sqrt{\text{m}}$)

Fr. No.	Time (μs)	a mm	\dot{a} m/s	\dot{a} in/s	K MPa $\sqrt{\text{m}}$	K psi $\sqrt{\text{in}}$
1	26	23.62	304.8	12,000	0.660	601
2	58	32.00	304.8	12,000	0.650	592
3	79	40.39	304.8	12,000	0.640	582
4	120	52.98	304.8	12,000	0.541	492
5	142	59.33	212.0	8,350	0.538	490
6	173	65.28	203.0	8,000	0.532	484
7	200	70.87	177.8	7,000	0.517	471
8	275	85.98	158.7	6,250	0.507	461
9	300	90.30	154.9	6,100	0.495	451
10	325	93.85	138.4	5,450	0.485	441
11	360	97.54	88.9	3,500	0.493	449
12	400	101.60	76.2	3,000	0.506	460
13	420	104.65	63.5	2,500	0.503	458
14	445	105.16	33.0	1,300	0.502	457
15	475	105.66	0.0	0.0	0.507	461

TABLE A-2

Summary of Results for Model R-7

$$(K_Q = 1.032 \text{ MPa}\sqrt{\text{m}})$$

Fr. No.	Time (μs)	a mm	\dot{a} m/s	\dot{a} in/s	K MPa $\sqrt{\text{m}}$	K psi $\sqrt{\text{in}}$
1	30	22.35	304.8	12,000	0.663	603
2	50	31.39	304.8	12,000	0.689	627
3	72	37.46	304.8	12,000	0.608	553
4	100	44.70	259.6	10,220	0.632	575
5	122	52.43	226.1	8,900	0.549	500
6	148	57.58	226.1	8,900	0.524	477
7	171	62.28	221.0	8,700	0.533	485
8	200	65.79	210.8	8,300	0.524	477
9	228	71.65	198.1	7,800	0.516	470
10	250	77.04	177.8	7,000	0.509	463
11	278	81.79	177.8	7,000	0.508	462
12	308	87.76	127.0	5,000	0.498	453
13	341	90.40	88.9	3,500	0.492	448
14	380	91.97	45.7	1,800	0.490	446
15	400	93.29	25.4	1,000	0.494	450
16	425	94.87	0.0	0.0	0.491	447

TABLE A-3

Summary of Results for Model R-8

 $(K_Q = 0.88 \text{ MPa}\sqrt{\text{m}})$

Fr. No.	Time (μs)	a mm	\dot{a} m/s	\dot{a} in/s	K MPa $\sqrt{\text{m}}$	K psi $\sqrt{\text{in}}$
1	18	18.80	244.0	9,600	0.600	546
2	40	23.62	244.0	9,600	0.590	537
3	60	29.21	244.0	9,600	0.590	537
4	84	34.80	244.0	9,600	0.570	519
5	137	44.70	184.0	7,250	0.560	510
6	160	48.77	166.0	6,550	0.532	485
7	185	56.59	166.0	6,550	0.510	464
8	210	57.88	165.0	6,500	0.508	462
9	268	65.28	133.4	5,250	0.535	487
10	295	69.34	127.0	5,000	0.532	484
11	325	73.41	104.1	4,100	0.525	478
12	350	75.84	88.9	3,500	0.509	463
13	368	76.96	82.6	3,250	0.522	475
14	382	79.48	78.7	3,100	0.520	473
15	406	81.96	--	--	0.515	467
16	430	82.68	--	--	0.486	442

TABLE A-4

Summary of Results for Model R-9

 $(K_Q = 0.998 \text{ MPa}\sqrt{\text{m}})$

Fr. No.	Time (μs)	a mm	\dot{a} m/s	\dot{a} in/s	K MPa $\sqrt{\text{m}}$	K psi $\sqrt{\text{in}}$
1	15	19.0	279.4	11,000	0.687	625
2	17	19.8	279.4	11,000	0.725	660
3	30	23.4	228.6	9,000	0.747	680
4	50	29.5	172.7	6,800	0.747	680
5	122	38.1	0	0	0.983	895
6	150	38.1	0	0	1.055	960
7	177	38.1	0	0	1.055	960
8	208	38.1	0	0	1.099	1,000
9	263	38.1	0	0	1.319	1,200
10	300	44.2	340.4	13,400	0.910	828
11	330	58.7	340.4	13,400	0.870	792
12	375	72.6	340.4	13,400	0.681	620

TABLE A-5
Summary of Results for Model R-10
($K_Q = 1.123 \text{ MPa } \sqrt{\text{m}}$)

Fr. No.	Time (μs)	a mm	\dot{a} m/s	\dot{a} in/s	K $\text{MPa}\sqrt{\text{m}}$	K $\text{psi}\sqrt{\text{in}}$
1	28	19.6	340	13,300	0.949	864
2	32	21.6	340	13,300	0.870	792
3	42	23.6	340	13,300	0.870	792
4	60	31.2	340	13,300	0.791	720
5	150	56.4	240	8,200	0.765	696
6	180	62.7	204	8,200	0.676	615
7	207	67.6	190	7,500	0.648	590
8	235	71.9	190	7,500	0.615	560
9	262	76.2	178	7,000	0.615	560
10	290	81.8	178	7,000	0.615	560
11	318	85.6	159	6,250	0.604	550
12	344	89.4	159	6,250	0.604	550
13	358	91.9	127	5,000	0.604	550
14	385	95.5	117	4,600	-	-
15	418	99.1	89	3,500	-	-
16	455	101.1	64	2,500	-	-

TABLE A-6

Summary of Results for Model R-11

 $(K_Q = 1.248 \text{ MPa}\sqrt{\text{m}})$

Fr. No	Time (μs)	a mm	\dot{a} m/s	\dot{a} in/s	K $\text{MPa}\sqrt{\text{m}}$	K $\text{psi}\sqrt{\text{in}}$
1	15	35.6	340	13,300	0.862	785
2	30	39.1	340	13,300	0.928	845
4	72	45.5	340	13,300	0.802	730
5	135	65.8	262.9	10,350	0.791	720
6	163	71.9	218.4	8,600	0.749	682
7	185	76.2	190.5	7,500	0.675	615
8	215	80.5	163.8	6,450	0.659	600
9	267	87.9	113.0	4,450	0.615	560
10	300	93.0	81.3	3,200	0.615	560
11	333	95.8	65.5	2,580	0.604	550
12	372	96.8	53.3	2,100	0.604	550
13	398	98.3	37.6	1,480	0.604	550
14	428	99.8	-	-	0.604	550

TABLE A-7

Summary of Results for Model R-12

$$(K_Q = 1.373 \text{ MPa}\sqrt{\text{m}})$$

Fr. No.	Time (μs)	a mm	\dot{a} m/s	\dot{a} in/s	K MPa $\sqrt{\text{m}}$	K psi $\sqrt{\text{in}}$
1	11	18.3	340	13,350	1.137	1,035
2	22	22.4	340	13,350	1.187	1,080
3	38	27.6	340	13,350	1.165	1,060
4	60	35.6	203	8,000	1.143	1,040
5	125	51.8	203	8,000	1.319	1,200
6	150	57.9	203	8,000	1.215	1,106
7	175	63.0	203	8,000	1.088	990
8	200	68.8	203	8,000	1.033	940
9	260	80.5	203	8,000	0.962	875
10	282	83.3	145	5,700	0.961	875
11	308	87.6	145	5,700	0.956	870
12	335	92.2	133	5,250	0.896	815
13	358	95.3	133	5,250	0.879	800
14	380	98.3	133	5,250	0.852	775
15	408	100.9	86	3,400	0.780	710
16	440	104.4	86	3,400	0.786	715

TABLE A-8

Summary of Results for Model R-13

$$(K_Q = 1.248 \text{ MPa}/\sqrt{\text{m}})$$

Fr. No.	Time (μs)	a mm	\dot{a} m/s	\dot{a} in/s	K MPa/ $\sqrt{\text{m}}$	K psi/ $\sqrt{\text{in}}$
1	12	23.6	305	12,000	1.129	1,028
2	23	27.2	305	12,000	1.149	1,046
3	39	32.8	305	12,000	1.104	1,005
4	61	37.1	240	9,500	1.187	1,080
5	125	48.3	225	8,750	--	--
6	150	55.1	225	8,750	1.329	1,210
7	175	59.7	225	8,750	1.143	1,040
8	200	65.5	225	8,750	1.066	970
9	260	76.2	190	7,500	0.989	900
10	288	81.8	190	7,500	0.923	840
11	310	85.8	160	6,400	0.857	780
12	338	90.2	160	6,400	0.835	760
13	385	95.3	91	3,600	0.826	755
14	410	98.0	91	3,600	0.791	720

APPENDIX E - DATA SUMMARIES FOR ARALDITE B AND HOMALITE 100

TABLE E-1

TENSION TEST ARALEDITE B

Test No. 370, T = 23.5°C

LOAD POUNDS	TUCKERMAN		MODULUS		STRAIN GAGES		MODULUS	
	FRONT	REAR	PSI	MPa	AXIAL	TRANS	PSI	MPa
0	20.0	20.0	482,000	3,300	0	0	489,000	3,380
10	18.0	17.8			440	140		
20	16.0	15.6			880	310		
30	13.6	13.4			1330	460		
40	11.2	11.1			1775	620		
50	8.9	8.9			2240	780		
60	6.4	6.5			2700	940		
0	20.0	20.0	483,500	3,350	0	0	492,200	3,290
10	17.8	17.8			440	150		
20	15.6	15.5			890	310		
30	13.2	13.5			1320	500		
40	10.8	11.1			1780	650		
50	8.3	8.9			2240	820		
60	5.4	6.9			2700	1000		

Poisson's Ratio: 0.353

Tuckerman Strain Gage Factor: 2×10^{-4}

Load Frame Factor: 4.36

Specimen Dimensions: .398" X .495" A = 0.197 in²

TABLE E-2

TENSION TEST

ARALDITE B

TEST NO. 370, T = 28°C

LOAD POUNDS	TUCKERMAN FRONT	TUCKERMAN REAR	ELASTIC MODULUS PSI	MPa
0	20	20	464,800	3,320
10	17.7	17.6		
20	15.2	15.2		
30	12.8	12.7		
40	10.4	10.2		
50	7.8	7.7		
60	5.3	5.1		
0	20	20	473,800	3,270
10	17.7	17.8		
20	15.1	15.1		
30	13.7	13.8		
40	12.7	12.6		
50	10.2	9.9		
60	7.8	7.3		

Tuckerman Strain Gage Factor: 2×10^{-4}

Load Frame Factor: 4.36

Specimen Dimensions: .484" x .391" A = .189 in.²

TABLE E-3

TENSION TEST, HOMALITE 100, (SECOND SHIPMENT), TEST NO. 370

T = 16°C

LOAD POUNDS	TUCKERMAN		MODULUS		STRAIN GAGE		MODULUS	
	FRONT	REAR	PSI	MPa	AXIAL	TRANS	PSI	MPa
0	20	20	602,600	4,150	0	0	583,100	4,020
10	18.3	18.4			280	100		
20	17.0	16.9			600	210		
30	15.7	15.5			900	300		
40	14.2	14.0			1,210	400		
50	12.5	12.8			1,520	500		

Poisson's Ratio: 0.340

Tuckerman Strain Gage Factor: 2×10^{-4}

Load Frame Factor: 4.36

Specimen Dimensions: 0.484" x 0.510", A = 0.246 in²

TABLE E-4

TENSION TEST, HOMALITE 100 (SECOND SHIPMENT), TEST NO. 370, T = 23.5°C

LOAD POUNDS	TUCKERMAN FRONT	TUCKERMAN REAR	MODULUS PSI	MODULUS MPa	STRAIN GAGE AXIAL	STRAIN GAGE TRANS	MODULUS PSI	MODULUS MPa
0	20.0	20.0	536,200	3,700	0	0	526,000	3,630
10	18.5	18.5			325	120		
20	17.0	17.0			650	225		
30	15.4	15.5			960	340		
40	13.8	13.8			1300	450		
50	12.0	12.1			1630	550		
60	10.3	10.4			1990	675		
0	20.0	20.0	533,700	3,680	0	0	488,300	3,370
10	18.4	18.4			325	100		
20	16.8	17.0			606	250		
30	15.1	15.2			1010	350		
40	13.4	13.5			1350	450		
50	11.6	12.2			1700	600		
60	9.8	10.4			2100	700		

Poisson's Ratio: .348

Tuckerman Strain Gage Factor: 2×10^{-4}

Load Frame Factor: 4.36

Specimen Dimensions: 0.484" x 0.510", A = 0.246 in²

TABLE E-5

TENSION TEST HOMALITE 100 (SECOND SHIPMENT)

TEST NO. 320, T = 26°C

LOAD POUNDS	TUCKERMAN		MODULUS	
	FRONT	REAR	PSI	MPa
0	20.0	20.0	540,600	3,480
10	18.4	18.3		
20	16.7	16.5		
30	14.8	14.8		
40	13.1	13.1		
50	11.3	11.2		
60				

Tuckerman Strain Gage Factor: 2×10^{-4}

Load Frame Factor: 4.36

Specimen Dimensions: 0.484 x 0.510, A - 0.246 in²

TABLE E-6

TENSION TEST HOMALITE 100 (SECOND SHIPMENT)

TEST NO. 370, T = 28°C

LOAD POUNDS	TUCKERMAN		MODULUS	
	FRONT	REAR	PSI	MPa
0	20.0	20.0		
10	18.3	18.3	475,800	3,280
20	16.4	16.5		
30	14.6	14.6		
40	12.5	12.6		
50	10.8	10.9		
60	8.8	9.0		
0	20.0	20.0	504,300	3,480
10	18.4	18.3		
20	16.6	16.5		
30	14.9	14.8		
40	13.0	13.0		
50	11.2	11.2		
60	9.3	9.3		

Tuckerman Strain Gage Factor: 2×10^{-4}

Load Frame Factor: 4.36

Specimen Dimensions: .484" X .510", $A = 0.246 \text{ in}^2$

TABLE E-7

TENSION TEST HOMALITE 100 (SECOND SHIPMENT) TEST NO. 320, T = 29°C

LOAD POUNDS	TUCKERMAN		MODULUS		STRAIN GAGE		MODULUS	
	FRONT	REAR	PSI	MPa	AXIAL	TRANS	PSI	MPa
0	24.0	24.0	496,800	3,430	0	0	462,400	3,120
10	22.3	22.5			325	110		
20	20.4	20.6			750	250		
30	18.8	19.0			1100	360		
40	16.8	17.0			1500	500		
50	15.2	15.3			1900	650		
60	13.2	13.4			2300	800		
0	24.1	24.1	488,200	3,370	0	0	466,400	3,220
10	22.4	22.4			400	120		
20	20.2	20.7			750	250		
30	18.9	18.9			1150	400		
40	17.0	17.0			1500	525		
50	15.2	15.1			1900	650		
60	13.4	13.3			2250	800		

Poisson's Ratio: 0.331

Tuckerman Strain Gage Factor: 2×10^{-4}

Load Frame Factor: 4.36

Specimen Dimensions: 0.484" X 0.510", $A = 0.246 \text{ in}^2$

TABLE E-8

TIME, STRAIN AND ELASTIC MODULUS DATA FOR ARALDITE B

TIME (SEC)	STRAIN GAGE READING	ELASTIC MODULUS PSI
0	24.00	-----
1	9.50	476,700
100	9.40	473,800
200	9.40	473,800
400	9.30	470,600
600	9.20	469,000
1000	9.15	467,400
3000	9.00	465,800
6000	8.90	461,200
10,000	8.70	458,100
57,000	8.00	432,300
62,000	8.10	435,300

LOAD - 60 LBS (MECHANICAL ADVANTAGE = 4.36)

SPECIMEN DIMENSIONS: .484" X .391", $A = .189 \text{ in}^2$

TEMPERATURE: 28°C

TUCKERMAN STRAIN GAGE FACTOR: 2×10^{-4}

TABLE E-9

TIME, STRAIN AND ELASTIC MODULUS DATA FOR HOMALITE 100 (SECOND SHIPMENT)

TIME (SEC)	STRAIN GAGE READING	ELASTIC MODULUS PSI
0	24.00	----
1	14.50	519,900
10	14.20	504,000
20	14.00	493,900
30	13.70	479,500
40	13.65	477,200
50	13.55	472,600
60	13.40	466,900
80	13.30	461,600
100	13.20	457,300
200	12.90	445,000
400	12.60	433,300
600	12.25	420,400
1,000	12.00	411,600
3,000	11.30	388,913
6,000	10.85	375,600
10,000	10.58	368,000
16,900	9.95	351,500
23,000	9.70	345,400
27,000	9.52	341,100
33,000	9.30	336,000
72,000	8.75	324,000

Load = 50 lb. (MA 4.36)

Dimensions: .484' X .510' A = .246

Tuckerman Gage Factor: 2×10^{-4}

T = 26.5°C

TABLE E-10

TIME, STRAIN AND ELASTIC MODULUS HOMLITE 100 (THIRD SHIPMENT)

TIME SEC	STRAIN GAGE READING	ELASTIC MODULUS PSI	MPa
0	22.00	----	
1	12.80	----	
10	12.00	476,700	
20	11.80	467,300	
30	11.70	462,700	
40	11.60	458,300	
50	11.50	453,900	
60	11.40	449,600	
80	11.30	445,400	
90	11.25	443,400	
100	11.20	441,300	
200	10.90	429,400	
400	10.60	418,100	
600	10.40	410,900	
1,000	10.20	403,900	
3,180	9.68	386,900	
6,000	9.30	375,300	
10,000	8.70	358,400	
57,000	7.65	325,300	

Load = 60 lb. Mechanical Advantage 4.36

Specimen Dimensions = .487" x .516" A = .251 m²

Temperature = 28.5°C

Tuckerman Strain Gage Factor = 2×10^{-4}

TABLE E-11

SUMMARY FOR COMPACT TENSION SPECIMEN, TEST NO. 287, ARALEDITE B

FRAME NO. 287	TIME t(U SEC)	POSITION a(mm)	S.I.F. K(MPa \sqrt{m})
1	9	88.6	0.760
2	34	91.6	0.692
3	62	94.7	0.650
4	91	97.9	0.681
5	128	101.1	0.702
6	155	103.7	0.690
7	182	106.8	0.706
8	209	110.4	0.674
9	230	113.0	0.709
10	258	116.4	0.691
11	289	118.8	0.678
12	318	121.4	0.672
13	366	124.8	0.682
14	394	125.9	0.689
15	423	127.0	0.670
16	454	128.3	0.679

$$a_0/w = 85.9/203.1 = 0.423$$

$$h = 8.128 \text{ mm}$$

$$K_Q = 0.813 \text{ MPa } \sqrt{m}$$

TABLE E-12

SUMMARY FOR COMPACT TENSION SPECIMEN, TEST NO. 293, ARALEDITE B

FRAME NO. 287	TIME t(U SEC)	POSITION a(mm)	S.I.F. K(MPa \sqrt{m})
1	12	79.6	2.075
2	34	88.1	1.921
3	60	97.7	1.708
4	90	108.3	1.495
5	127	121.7	1.340
6	166	135.0	1.426
7	191	143.8	1.458
8	218	153.5	1.233
9	258	168.4	1.208
10	286	176.0	1.009

$$a_0/w = 76.4/203.1 = 0.376$$

$$h = 8.077 \text{ mm}$$

$$K_Q = 2.088 \text{ MPa } \sqrt{m}$$

TABLE E-13

SUMMARY FOR COMPACT TENSION SPECIMEN, TEST NO. 313, ARALEDITE B

FRAME NO. 313	TIME t(U SEC)	POSITION a(mm)	S.I.F. K(MPa \sqrt{m})
1	275	84.8	0.643
2	295	85.1	0.671
3	317	85.5	0.679
4	345	86.1	0.695
5	376	86.2	0.692
6	402	86.6	0.690
7	415	87.3	0.716
8	453	87.9	0.689
9	1365	94.7	0.701
10	1392	94.7	0.705
11	1412	94.7	0.695
12	1464	94.7	0.671
13	3715	105.4	0.671
14	3737	105.4	0.671
15	3764	105.4	0.660
16	3795	105.4	0.670

$$a_0/w = 75.1/203.1 = 0.370$$

$$h = 9.96 \text{ mm}$$

$$K_Q = 0.627 \text{ MPa } \sqrt{m}$$

TABLE E-14

SUMMARY FOR COMPACT TENSION SPECIMEN, TEST NO. 314, ARALEDITE B

FRAME NO. 314	TIME t(U SEC)	POSITION a(mm)	S.I.F. K(MPa \sqrt{m})
1	72	88.5	0.703
2	105	88.6	0.699
3	147	88.8	0.680
4	192	88.8	0.695
5	289	89.1	0.682
6	327	89.1	0.680
7	368	89.2	0.684
8	410	89.2	0.676
9	3128	97.8	0.692
10	3166	98.5	0.693
11	3208	98.8	0.692
12	3254	98.8	0.693
13	9774	926.9	0.688
14	9825	126.9	0.682
15	9863	126.9	0.688
16	9909	126.9	0.693

$$a_0/w = 85.1/203.1 = 0.419$$

$$h = 9.957 \text{ mm}$$

$$K_Q = 0.622 \text{ MPa}\sqrt{m}$$

TABLE E-15

SUMMARY FOR SEN SPECIMEN, TEST NO. 308, ARALEDITE B

FRAME NO. 308	TIME t(U SEC)	POSITION a (mm)	S.I.F. K(MPa \sqrt{m})
1	32.4	34.8	0.739
2	47.5	37.9	0.765
3	71.5	40.9	0.659
4	99.6	45.1	0.858
5	153	54.3	0.840
6	175	60.7	0.914
7	190	66.8	0.968
8	223	72.8	0.888
9	284	88.9	1.011
10	304	95.2	1.093
11	329	102.2	1.194
12	345	109.5	1.162
13	384	117.5	1.181
14	409	126.4	1.109
15	433	135.9	1.190
16	460	144.4	1.269

$$a_0/w = 31.4/152.5 = 0.206$$

$$h = 7.747 \text{ mm}$$

$$K_Q = 0.790 \text{ MPa } \sqrt{m}$$

TABLE E-16

SUMMARY FOR SEN SPECIMEN, TEST NO. 309, ARALEDITE B

FRAME NO. 309	TIME t(U SEC)	POSITION a (mm)	S.I.F. K(MPa \sqrt{m})
1	28.4	30.8	1.033
2	52.6	37.7	1.110
3	75.0	44.1	1.186
4	104	53.3	1.250
5	152	69.0	1.333
6	176	77.3	1.479
7	198	84.7	1.569
8	222	92.7	1.550
9	278	112	1.573
10	300	120	1.734
11	323	129	1.683
12	348	137	1.664

$$a_0/w = 22.7/152.5 = 0.149$$

$$h = 7.747 \text{ mm}$$

$$K_Q = 1.02 \text{ MPa}\sqrt{m}$$

TABLE E-17

SUMMARY FOR R-DCB SPECIMEN, TEST NO. 331, ARALEDITE B

FRAME NO. 331	TIME t(U SEC)	POSITION a (mm)	S.I.F. K(MPa \sqrt{m})
1	399	96.1	0.587
2	431	96.4	0.587
3	471	96.4	0.600
4	514	96.6	0.603
5	545	97.0	0.593
6	587	97.1	0.599
7	627	97.1	0.600
8	681	97.1	0.594
9	703	97.1	0.603
10	742	97.1	0.608
11	778	97.1	0.598
12	815	97.1	0.620
13	909	97.6	0.636
14	1026	97.6	0.602
15	1068	97.6	0.595
16	1115	97.6	0.629

$$a_0/w = 91.3/276.2 = 0.331$$

$$h = 7.930 \text{ mm}$$

$$K_Q = 0.645 \text{ MPa}\sqrt{m}$$

TABLE E-18

SUMMARY FOR R-DCB SPECIMEN, TEST NO. 332, ARALEDITE B

FRAME NO. 332	TIME t(U SEC)	POSITION a (mm)	S.I.F. K(MPa \sqrt{m})
1	177	105.8	0.658
2	212	108.8	0.633
3	254	110.8	0.643
4	296	111.2	0.633
5	338	111.8	0.548
6	377	111.8	0.582
7	417	111.8	0.590
8	470	111.8	0.599
9	516	111.8	0.583
10	554	111.8	0.583
11	594	111.8	0.579
12	636	112.3	0.598
13	680	112.3	0.598
14	718	112.3	0.593
15	760	112.3	0.598
16	811	112.3	0.578

$$a_0/w = 88.2/276.2 = 0.319$$

$$h = 7.930 \text{ mm}$$

$$K_Q = 0.697 \text{ MPa}\sqrt{m}$$

NRC FORM 335
(7-77)

U.S. NUCLEAR REGULATORY COMMISSION
BIBLIOGRAPHIC DATA SHEET

1. REPORT NUMBER (Assigned by DDC)

NUREG/CR-0542

4. TITLE AND SUBTITLE (Add Volume No., if appropriate)

Photoelastic Studies of Crack Propagation and Arrest in
Polymers and 4340 Steel

2. (Leave blank)

3. RECIPIENT'S ACCESSION NO.

7. AUTHOR(S)

G. R. Irwin and others

5. DATE REPORT COMPLETED

MONTH November YEAR 1978

9. PERFORMING ORGANIZATION NAME AND MAILING ADDRESS (Include Zip Code)

University of Maryland
Mechanical Engineering Department
College Park, MD 20742

DATE REPORT ISSUED

MONTH December YEAR 1978

6. (Leave blank)

8. (Leave blank)

12. SPONSORING ORGANIZATION NAME AND MAILING ADDRESS (Include Zip Code)

Metallurgy & Materials Research Branch
Division of Reactor Safety Research
US Nuclear Regulatory Commission
Mail Stop 1130 SS
Washington, DC 20555

10. PROJECT/TASK/WORK UNIT NO.

11. CONTRACT NO.

NRC-04-76-172

13. TYPE OF REPORT

Annual

PERIOD COVERED (Inclusive dates)

7/15/77 - 9/30/78

15. SUPPLEMENTARY NOTES

14. (Leave blank)

16. ABSTRACT (200 words or less)

This report describes the progress made during the fourth year on a research program dealing with the dynamic characterization of fracture.

17. KEY WORDS AND DOCUMENT ANALYSIS

17a. DESCRIPTORS

17b. IDENTIFIERS/OPEN-ENDED TERMS

18. AVAILABILITY STATEMENT

Unlimited

19. SECURITY CLASS (This report)
Unclassified

21. NO. OF PAGES

20. SECURITY CLASS (This page)
Unclassified

22. PRICE
\$